



UNIVERSITÀ DEGLI STUDI DI GENOVA

PHD IN MARINE AND SCIENCE TECHNOLOGIES  
CURRICULUM: MARINE AND NAUTICAL ENGINEERING,  
MARINE TECHNOLOGIES  
XXXVI CYCLE

---

**Guidance and motion control logic for Marine  
Autonomous Surface Ships**

---

*Candidate:*  
Camilla Fruzzetti

*Supervisor:*  
Prof. Michele Martelli

*After an opinion from:*  
Prof. Lokukaluge Prasad Perera & Prof. Jialun Liu

*In front of a jury composed of:*  
Prof. Lokukaluge Prasad Perera, Prof. Jialun Liu & Prof. Silvia  
Donnarumma

*Date:*  
March 6, 2024



*Rivers know this: there is no hurry.  
We shall get there some day.*  
A.A.Milne - *Winnie the Pooh*





This work was carried out between November 2020 and October 2023 inside the XXXVI cycle of the PhD course in Marine science and technologies – Marine and nautical engineering, marine technologies. This work belongs to the Italian academic discipline ING-IND/02 - Ship structures and marine engineering and the academic recruitment fields 09/A1 – Aeronautical and aerospace engineering and naval architecture.



# Abstract

The increasing maritime traffic and a major awareness regarding environmental pollution lead to a greater emphasis on the efficiency of operations and their costs. Improvements can be achieved with the progressive integration of automation tools to relieve humans from repetitive and complex tasks that might lead them to error or to non-optimal solutions. The promises are to enhance both human and environmental safety while also holding the potential for increased efficiency and reduced operational costs. The introduction of automated systems occurs at different levels with applications spanning from decision support systems to fully autonomous ships, defined as Marine Autonomous Surface Ships (MASS). Both academic institutions and industrial companies carried out various studies on this topic over the past decades, leading to the design and testing of pioneering prototypes of fully autonomous vessels. The above-mentioned studies focus on a broad spectrum of areas that contribute to the design of a decision support or autonomous system. The topics include situation awareness systems for obtaining information on the surrounding environment, systems for route planning or for following the desired path, systems for avoiding collisions with fixed or moving objects or for automatic mooring, and more. Different methodologies can be defined for each of the above mentioned tasks and can be organised through the well-known schematisation in the three independent modules of the Guidance, Navigation, and Control (GNC).

For the motivation explained above, the research carried out within this thesis fits into this context, leading to the guidance and control modules. The main objective is the development of systems for planning and controlling motions through the entire speed operational range of surface vessels. Different kind of vessels leading to model-scale to full scale vessels are adopted for this study. With respect to the state of the art, this work would like to propose an integrated motion control scenario suitable for all the MASS operation conditions, from berthing, track and station keeping, to path following, and target tracking operations. Controlling the motion at low or high speed involves different design approaches that can be schematised into 2 or 3 degree-of-freedom (DOF) controllers due to the effects of the actuators in the sway motion at high surge velocities.

The outlined 2 DOF motion control scenario, used for high speed, aims to follow a moving object controlling the desired heading and speed. The adopted guidance law is the target tracking one. It consists of reaching and following a target of which it is only possible to know the instantaneous position and velocity, hence when the future motion is unknown. In this context, the standard Line-Of-Sight, Pure Pursuit, and Constant Bearing laws are modified and deeply tested. The controller layout comprises an autopilot and a speed pilot, working together to establish the desired guidance setpoint, and the synthesis leads to provide the

stability of the closed-loop together with some performance characteristics.

The presented 3 DOF motion control scenario desires to maintain position or to follow a path at low speed. The chosen guidances enable smooth setting of the desired setpoint using reference models or to define a trajectory to be tracked for track keeping. Several control layouts are investigated, composed of a controller together with the force and thrust allocations. Controllers consist of both feedback contributions like PID or its variations and a feedforward component computed through a model-based approach or disturbance reconstruction. The allocation problem is deeply investigated and solved through both a simplified approach and optimization techniques.

Both 2 and 3 DOF motion control scenarios are applied to real test cases in both model and full scale, each characterised by different main dimensions, manoeuvrability capability, and propulsion system configurations. Each test case is described and their characteristics are shown. Specific key performance indicators, running from integral metrics to yearly operability and emission indexes, are selected for each motion control scenario to evaluate the effectiveness of the proposed GNC modules.

The proposed motion control scenarios are extensively tested using non-linear dynamic simulators representing the MASS test cases. Based on the results, the defined key performance indicators are used to assess the effectiveness of the proposed approaches across a spectrum of speeds and environmental conditions.

In conclusion, this thesis contributes to the field of autonomous marine vessels by providing motion control strategies suitable for the entire speed range.



# Contents

<b>List of Figures</b>	<b>15</b>
<b>List of Tables</b>	<b>19</b>
<b>1 Introduction</b>	<b>21</b>
1.1 Motivation . . . . .	23
1.2 Level of Automation and Taxonomy . . . . .	24
1.3 Guidance, Navigation & Control . . . . .	34
1.4 State of art . . . . .	37
1.5 Contributions . . . . .	39
<b>2 Vessel mathematical model</b>	<b>41</b>
2.1 Adopted reference frame . . . . .	41
2.2 Kinetics . . . . .	44
2.3 Hull Forces . . . . .	44
2.3.1 Oltmann & Sharma model . . . . .	44
2.3.2 MMG-like model . . . . .	45
2.4 Propulsion plant . . . . .	46
2.5 Manoeuvring device . . . . .	48
2.5.1 Azimuth propeller . . . . .	48
2.5.2 Transversal Thruster . . . . .	49
2.6 Environmental forces . . . . .	50
2.6.1 Wind . . . . .	50
2.6.2 Current . . . . .	51
2.6.3 Wave . . . . .	52
2.6.4 Disturbances cross relationships . . . . .	53
<b>3 Guidance</b>	<b>57</b>
3.1 Target Tracking . . . . .	57
3.1.1 Line Of Sight . . . . .	58
3.1.2 Pure Pursuit . . . . .	61
3.1.3 Constant Bearing . . . . .	62
3.2 Track keeping . . . . .	65
3.3 Reference models . . . . .	67

<b>4</b>	<b>Control: 2-DOF</b>	<b>69</b>
4.1	Autopilot . . . . .	70
4.2	Speed pilot . . . . .	70
4.3	Linearised model for synthesis purpose . . . . .	70
4.4	Synthesis . . . . .	74
4.4.1	Closed Loop Stability . . . . .	74
4.4.2	Decay Rate . . . . .	75
4.4.3	Peak Limit . . . . .	75
<b>5</b>	<b>Control: 3 DOF</b>	<b>77</b>
5.1	Controller . . . . .	77
5.1.1	Model-Base PID . . . . .	78
5.1.2	Environmental Feedforward . . . . .	78
5.2	Force Allocation Logic . . . . .	79
5.2.1	Simplified approach . . . . .	79
5.2.2	Optimized methods . . . . .	81
5.2.2.1	Nonlinear programming . . . . .	81
5.2.2.2	Lagrange Multiplier . . . . .	83
5.3	Thrust Allocation Logic . . . . .	84
<b>6</b>	<b>Key Performance Indicators</b>	<b>85</b>
6.1	Target Tracking KPIs . . . . .	85
6.2	Dynamic Positioning Capability Plot (DPCP) . . . . .	86
6.2.1	Static analysis . . . . .	86
6.2.2	Dynamic analysis . . . . .	87
6.3	Yearly operability . . . . .	87
6.4	Emission factor . . . . .	88
6.5	Integral metrics . . . . .	90
<b>7</b>	<b>Vessel test cases</b>	<b>91</b>
7.1	Tito-Neri tug model . . . . .	91
7.2	milliAmpere ferry prototype vessel . . . . .	96
7.3	Minehunter . . . . .	100
7.4	Platform Supply Vessel . . . . .	102
<b>8</b>	<b>Results</b>	<b>105</b>
8.1	Tito-Neri tug model . . . . .	106
8.1.1	Smart pilot synthesis results . . . . .	106
8.1.1.1	Scenario A . . . . .	108
8.1.1.2	Scenario B . . . . .	111
8.1.1.3	Scenario C . . . . .	114
8.1.2	Target Tracking parameters sensitivity analysis . . . . .	117
8.1.2.1	Line-Of-Sight analysis . . . . .	119
8.1.2.2	Pure Pursuit analysis . . . . .	121
8.1.2.3	Constant Bearing analysis . . . . .	122
8.1.2.4	Parameters selection and validation . . . . .	124
8.1.3	Human in the loop . . . . .	128
8.2	milliAmpere ferry prototype vessel . . . . .	130
8.2.1	Low Speed range scenario . . . . .	130
8.2.2	Higher Speed range scenario . . . . .	137

---

8.3	Minehunter . . . . .	139
8.3.1	DPCP . . . . .	142
8.3.2	Operability index . . . . .	143
8.3.3	Emission Factor . . . . .	144
8.4	Platform Supply Vessel . . . . .	147
8.4.1	Static Analysis . . . . .	148
8.4.2	Dynamic Analysis . . . . .	148
8.4.3	Real-Time Hardware in the loop . . . . .	151
<b>9</b>	<b>Conclusion and future developments</b>	<b>155</b>
	<b>List of publications</b>	<b>157</b>
	<b>Nomenclature</b>	<b>159</b>
	<b>List of Acronyms</b>	<b>169</b>
	<b>Bibliography</b>	<b>171</b>

---



# List of Figures

1.1	Introduction - EMSA report 2022. . . . .	24
1.2	Introduction - GNC architecture. . . . .	35
1.3	Introduction - Guidance architecture. . . . .	37
2.1	Vessel mathematical model - Layout. . . . .	42
2.2	Vessel mathematical model - Reference frames. . . . .	42
2.3	Vessel mathematical model - Propulsion Plant layout. . . . .	47
2.4	Vessel mathematical model - Propeller 4 quadrants coefficients. . . . .	49
2.5	Vessel mathematical model - Propeller coefficients. . . . .	50
2.6	Vessel mathematical model - Environmental - Wind. . . . .	51
2.7	Vessel mathematical model - Environmental - Current. . . . .	51
2.8	Vessel mathematical model - Environmental - Wave. . . . .	52
2.9	Vessel mathematical model - Environmental - Beaufort Wave-Wind relationship. . . . .	54
2.10	Vessel mathematical model - Environmental - $p_{\gamma_i}$ . . . . .	55
2.11	Vessel mathematical model - Environmental - Scatter diagram. . . . .	55
3.1	Guidance - Target Tracking - Layout. . . . .	58
3.2	Guidance - Target Tracking - Geometrical Sketch of the LOS Guidance. . . . .	59
3.3	Guidance - Target Tracking - Speed law for LOS Guidance. . . . .	61
3.4	Guidance - Target Tracking - Geometrical Sketch of the PP Guidance. . . . .	61
3.5	Guidance - Target Tracking - Geometrical Sketch of the CB Guidance. . . . .	63
3.6	Guidance - Target Tracking - Constant Bearing speed law. . . . .	64
3.7	Guidance - Target Tracking - Constant Bearing heading law. . . . .	65
3.8	Guidance - Track Keeping - Layout. . . . .	65
3.9	Guidance - Track Keeping - Reference frame. . . . .	66
3.10	Guidance - Track Keeping - Trapezium speed law. . . . .	66
3.11	Guidance - Track Keeping - Desired heading angle. . . . .	67
3.12	Guidance - Reference Model - Layout. . . . .	68
4.1	Control: 2-DOF - Controller layout. . . . .	69
4.2	Control: 2-DOF - Open Loop Layout. . . . .	72
4.3	Control: 2-DOF - Smart pilot layout. . . . .	73
4.4	Control: 2-DOF - Closed Loop Layout. . . . .	73
5.1	Control: 3-DOF - Controller layout. . . . .	77
5.2	Control: 3-DOF - (a) Actuators layout (b-d) Fixed Angles Allocations. . . . .	80
5.3	Control: 3-DOF - Allocation Switch condition. . . . .	81

5.4	Control: 3-DOF - Lagrange Multiplier. . . . .	84
6.1	KPI - DPCP - Example. . . . .	86
7.1	Test Case - Tito-Neri - Model. . . . .	92
7.2	Test Cases - Tito-Neri - Construction plan. . . . .	92
7.3	Test Cases - Tito-Neri - Hull. . . . .	92
7.4	Test Cases - Tito-Neri - Actuators layout. . . . .	93
7.5	Test Cases - Tito-Neri - Azimuthal combinator curve. . . . .	95
7.6	Test Cases - Tito-Neri - Bow thruster combinator curve. . . . .	96
7.7	Test Cases - milliAmpere - Model. . . . .	96
7.8	Test Cases - milliAmpere - Actuators layout. . . . .	97
7.9	Test Cases - milliAmpere - Combinator curve. . . . .	99
7.10	Test Cases - milliAmpere - Angles Allocations. . . . .	99
7.11	Test Cases - Minehunter - Layout configuration A. . . . .	100
7.12	Test Cases - Minehunter - Layout configuration B. . . . .	100
7.13	Test Cases - Minehunter - Loss due to interaction $\eta(\alpha)$ . . . . .	102
7.14	Test Cases - PSV - Model. . . . .	103
7.15	Test Cases - PSV - Layout. . . . .	103
7.16	Test Cases - PSV - Azimuthal combinator curve. . . . .	104
7.17	Test Cases - PSV - Bow Thruster combinator curve. . . . .	104
8.1	Results - Structure. . . . .	106
8.2	Results - Tito-Neri - Smart pilot layout. . . . .	107
8.3	Results - Tito-Neri - Smart pilot test desired time histories. . . . .	108
8.4	Results - Tito-Neri - Scenario A, Setpoints and states time histories. . . . .	109
8.5	Results - Tito-Neri - Scenario A, Trajectory. . . . .	110
8.6	Results - Tito-Neri - Scenario A, Propeller revolutions. . . . .	110
8.7	Results - Tito-Neri - Scenario A, Hull and Azimuthal Forces. . . . .	111
8.8	Results - Tito-Neri - Scenario B, Setpoints and states time histories. . . . .	112
8.9	Results - Tito-Neri - Scenario B, Trajectory. . . . .	112
8.10	Results - Tito-Neri - Scenario B, Propeller revolution. . . . .	113
8.11	Results - Tito-Neri - Scenario B, Hull and Azimuthal Forces. . . . .	113
8.12	Results - Tito-Neri - Scenario C, Setpoints and states time histories. . . . .	114
8.13	Results - Tito-Neri - Scenario C, Trajectory. . . . .	115
8.14	Results - Tito-Neri - Scenario C, Propeller revolutions. . . . .	115
8.15	Results - Tito-Neri - Scenario C, Hull and Azimuthal Forces. . . . .	116
8.16	Results - Tito-Neri - Target tracking layout. . . . .	117
8.17	Results - Tito-Neri - Operational Scenarios. . . . .	118
8.18	Results - Tito-Neri - Concept map of the simulation campaign. . . . .	118
8.19	Results - Tito-Neri - LOS tests. . . . .	120
8.20	Results - Tito-Neri - PP tests. . . . .	122
8.21	Results - Tito-Neri - Sketch of desired distances for CB tests. . . . .	123
8.22	Results - Tito-Neri - CB tests. . . . .	124
8.23	Results - Tito-Neri - Overall comparison. . . . .	126
8.24	Results - Tito-Neri - Slideshow. . . . .	127
8.25	Results - Tito-Neri - Simulation Loop Framework. . . . .	128
8.26	Results - Tito-Neri - HIL. . . . .	130
8.27	Results - milliAmpere - Low-speed layout. . . . .	130
8.28	Results - milliAmpere - Concept map of the simulation campaign. . . . .	131

8.29	Results - milliAmpere - 4 corner test. . . . .	132
8.30	Results - milliAmpere - Low-speed configurations tests: IAE. . . . .	134
8.31	Results - milliAmpere - Low-speed configurations tests: IAEW. . . . .	134
8.32	Results - milliAmpere - Low-speed configurations tests: IADC. . . . .	135
8.33	Results - milliAmpere - Low-speed configurations test: IATE. . . . .	135
8.34	Results - milliAmpere - Low-speed configurations. . . . .	136
8.35	Results - milliAmpere - Higher speed layout. . . . .	137
8.36	Results - milliAmpere - Higher-speed configurations. . . . .	138
8.37	Results - milliAmpere - Higher-speed configurations. . . . .	139
8.38	Results - Minehunter - Layout. . . . .	140
8.39	Results - Minehunter - Scatter diagram areas. . . . .	140
8.40	Results - Minehunter - Environmental disturbance. . . . .	141
8.41	Results - Minehunter - DPCP configuration A. . . . .	142
8.42	Results - Minehunter - DPCP configuration B. . . . .	143
8.43	Results - Minehunter - Operability analysis. . . . .	144
8.44	Results - Minehunter - Emission factor variables, Conf. B, North- East direction. . . . .	145
8.45	Results - Minehunter - Emission analysis. . . . .	146
8.46	Results - PSV - Layout. . . . .	147
8.47	Results - PSV - Static DPCP. . . . .	149
8.48	Results - PSV - Dynamic DPCP. . . . .	149
8.49	Results - PSV - Coming direction 0° to 45°. . . . .	150
8.50	Results - PSV - Coming direction 0° to 45°. . . . .	151
8.51	Results - PSV - Hardware in the loop Layout. . . . .	152
8.52	Results - PSV - RT HIL and SIM results. . . . .	153
8.53	Results - PSV - RT HIL and SIM results. . . . .	154





# List of Tables

1.1	Introduction - Autonomous levels - Sheridan. . . . .	26
1.2	Introduction - Autonomous levels - Lloyd's Register. . . . .	26
1.3	Introduction - Autonomous levels - SAE . . . . .	28
1.4	Introduction - Autonomous levels - NFAS . . . . .	29
1.5	Introduction - Autonomous levels - GALILEOnautic. . . . .	29
1.6	Introduction - Autonomous levels - Schiaretto. . . . .	30
1.7	Introduction - Autonomous levels - IMO. . . . .	31
1.8	Introduction - Autonomous levels - Proposed comparison. . . . .	33
2.1	Vessel mathematical model - Environmental - Beaufort wind scale. . . . .	54
6.1	KPIs - 3-DOF - SFC baseline . . . . .	89
6.2	KPIs - 3-DOF - Emission Factor . . . . .	89
7.1	Test Cases - Tito-Neri - Characteristics. . . . .	93
7.2	Test Cases - Tito-Neri - Adopted simulation model. . . . .	93
7.3	Test Cases - Tito-Neri - Hull resistance coefficient. . . . .	94
7.4	Test Cases - Tito-Neri - Parameters. . . . .	94
7.5	Test Cases - Tito-Neri - Thrust coefficient. . . . .	95
7.6	Test Cases - Tito-Neri - Azimuth first order function constants. . . . .	95
7.7	Test Cases - milliAmpere - Characteristics. . . . .	97
7.8	Test Cases - milliAmpere - Adopted simulation model. . . . .	97
7.9	Test Cases - milliAmpere - Parameters. . . . .	98
7.10	Test Cases - Minehunter- Characteristics. . . . .	100
7.11	Test Cases - Minehunter - Power distribution. . . . .	101
7.12	Test Cases - Minehunter - Engine Layout. . . . .	101
7.13	Test Cases - PSV - Characteristics. . . . .	102
7.14	Test Cases - PSV - Adopted simulation model. . . . .	103
8.1	Test Case - Tito-Neri - Smart pilot gains. . . . .	106
8.2	Results - Tito-Neri - Scenario A, Smart Pilot step-response characteristics. . . . .	109
8.3	Results - Tito-Neri - Scenario A, Smart Pilot input characteristics. . . . .	109
8.4	Results - Tito-Neri - Parameters of Target Tracking guidance law. . . . .	117
8.5	Results - Tito-Neri - Summary of LOS Tests. . . . .	119
8.6	Results - Tito-Neri - Line-Of-Sight KPI. . . . .	120
8.7	Results - Tito-Neri - Summary of PP Tests. . . . .	121
8.8	Results - Tito-Neri - Pure Pursuit KPI. . . . .	122

---

8.9	Results - Tito-Neri - Summary of CB Tests. . . . .	123
8.10	Results - Tito-Neri - Constant Bearing KPI. . . . .	123
8.11	Results - milliAmpere - IAE-RF. . . . .	133
8.12	Results - milliAmpere - Tests of low-speed controller configurations. . . . .	133
8.13	Results - milliAmpere - Higher-speed Scenario. . . . .	137
8.14	Results - Minehunter - Emission factor. . . . .	146

# Chapter 1

## Introduction

The etymology of automation comes from the English word *automaton* and was coined by Ford Executive Vice President Delmar S. Harder in the 1940s. It is the act or process of converting the control of a machine or device to a more automatic system, such as a computer or electronic control. The word *automaton* indeed comes from the Latinization of the ancient Greek word *automaton*, neuter of *automatos* that means *self-moving, self-willed*. Nowadays, it indicates a relatively self-operating machine or control mechanism designed to automatically follow a sequence of operations or respond to predetermined instructions. However, Homer first uses this word in the Iliad to describe machines moving on their own using internal energy, like the Trojan horse. During the centuries, interest in automation grew and started in the marine field. Several milestones can be defined like the Nikola Testa patent at the end of the 19<sup>th</sup> century [121] about the method for controlling from a distance the operation of the propellers, engines, steering apparatus and other mechanisms. Another milestone started with the invention of the gyroscope, leading to the first application of autopilot, named Metal Mike, by Elmer Sperry in 1910s [56]. From the last one, the motion control system starts to be designed as three independent modules: Guidance, Navigation, and Control (GNC) systems [45]. From that time, several milestones were set, like the introduction of a position feedback controller with a control law commonly named nowadays Proportional-Integrative-Derivative (PID) [85], or the introduction of the inertial navigation [37]. In recent years, the studies concerning autonomous vessels have multiplied. The growing attention is also underlined by the Global Marine Technology Trends 2030 (GMTT30) [108] and 2050 [62] reports publications. The Global Marine Technology Trends 2030 report was published in 2015 by Lloyd’s Register, Quintiq Group, and Southampton University. It defines eighteen key marine technologies in the future, putting the autonomous system and smart ship as two of the key points. Lloyd’s Register commissioned the Global Marine Technology Trends 2050 report to Economist Impact; it is a long-term vision of the GMTT30 themes. The growing attention is underlined also by the International Maritime Organization (IMO) sessions of the Marine Safety Control (MSC). Indeed, its 98<sup>th</sup> session [61] defines the concept of Maritime Autonomous Surface Ships (MASS).

The interest is due to the potential benefit in terms of safety, efficiency, and relieving humans from repetitive tasks. Due to the challenging and complex tasks, several disciplines are involved in this process, from the cyber-security perspective to risk assessment, the GNC system, and human perception. In this context, vari-

ous definitions and automation levels are identified to distinguish vessels and their capability before the general statement given by IMO during the 100<sup>th</sup> congress [60]. Several reviews and technical reports have appeared over the years. A literature review of the design and risk evaluation of MASS to support its safe operations is done in [69]. The first analysis conducted by the European Union Agency for Cybersecurity (ENISA) of the cyber threat landscape of the transport sector in Europe is reported in [39] with a focus on the marine environment. A review of the most relevant MASS project and the new trend is reported in [67] and another about the status up to 2022 of levels of automation in MASS is shown in [99]. A literature review about the evolution of the autonomy levels up to 2016 is reported in [125] with a focus on the differences between the different proposals. The state of the art up to 2019 on the motion control algorithms is elaborated in [130] with a final focus on the challenges given by autonomous surface vessels and a two-part literature review about path planning and collision avoidance methods is given in [124] and [123]; in the first part a highlight on the terminology, autonomous levels, regulatory framework, GNC components and advances in industry is given, while in the second part a comparative study on 45 selected algorithm is given. A comprehensive literature review of all the components of the GNC system is reported in [71] with a great focus on the existing USV and modelling methods up to 2016 and an overview of the components of global and local path planning for USV is shown in [111] with a focus on the compliance with COLREGs. A literature review with a focus on the path-following motion control scenario and on the control system is provided in [133] together with the statistical distribution of the most common practice; while one focused on the path planning algorithms and their collision regulation relevance is shown in [93]. A literature review of the recent advantages of the LOS guidance law and its variation is provided in [50] and one on collision avoidance algorithms that highlights the importance of the collaboration between the involved vessel is shown in [8]. Finally, a literature review of the progress up to 2022 in COLREGs-compliant navigation of ASVs from traditional to learning-based approach is reported in [54].

The research aim focuses on autonomous navigation for marine surface vehicles context. In this Chapter, the state of the art, the motivation, and the main contribution are stated, together with an overview of the GNC systems, the automation levels, and the adopted taxonomy.

In Chapter 2, the adopted mathematical model to describe the vessels is presented. In this work, four case studies are used through their detailed simulators representing the dynamics of the vessels and their components. The adopted reference frames in the thesis are described together with the motion equation and the dynamics model for the hull, propulsor, and environmental forces and moment array evaluation.

In Chapter 3, the adopted guidance algorithms are shown. The target tracking motion control scenario for a 2-DOF (Degree Of Freedom) controller structure is shown, together with the track keeping and the reference model used for the 3-DOF controlled structure.

In Chapter 4, the controller adopted for the 2-DOF motion control scenario is presented. The general structure comprises two PID controllers acting in parallel on the heading and speed setpoints. A synthesis approach is presented, and its application on a vessel with starboard-portside symmetry and propelled by two azimuthal thrusters is given.

In Chapter 5, the controller adopted for the 3-DOF motion control scenario is shown. The general structure adaptable to different propulsion plants is shown and comprises subsystems like control, force allocation, and thrust allocation. Several solutions are proposed for each subsystem, from optimised to simplified solutions.

In Chapter 6, the key performance indicators evaluating the selected performance of each scenario are presented. Integral metrics, operability and emission indices, dynamic polar capability plots, and defined errors are used in this case.

In Chapter 7, the vessels adopted as case studies and their main characteristics are presented. One model scale, a prototype, and two full-scale vessels are used.

In Chapter 8, the scenarios adopted in each test case are presented together with the results.

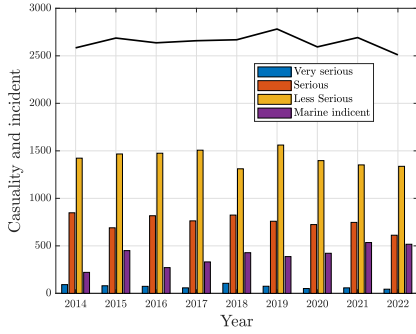
In the end, in Chapter 9 the conclusion are drawn.

## 1.1 Motivation

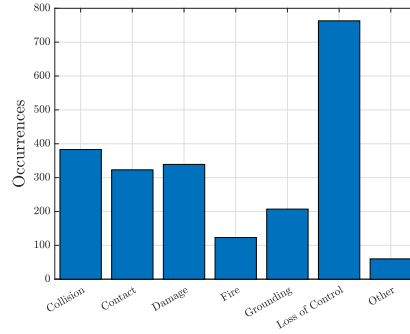
In recent years, robotic vehicles have become essential in many different applications and areas due to their ability to operate where people cannot, or the human risk is significant in everyday lives. In the maritime field, great progress is made with the growing development of autonomous surface vessels due to the promise to improve safety, increase efficiency, and relieve humans from repetitive tasks. Hence, there is a demand for an even greater level of complexity and autonomy in onboard systems that asks for greater computational power, leading to an ever higher level of automation. All ship systems need to be re-thought and modified according to the increased automation level, but a focus needs to be paid to the autonomous handling of the units. Hence, the motion control system becomes paramount. It is usually designed as three independent modules that interact with each other: Guidance, Navigation, and Control (GNC) systems [45]. The significant development of the IT sector has made possible the remarkable evolution in the field of automation and its possible applications in the maritime sector. Consequently, autonomous and smart ships are two of the eighteen themes identified by the Global Marine Technology Trends 2030 [108] and 2050 [62] as some of the main research topics of the following years.

Another motivation is the promise of improved life safety at sea for people and the environment. Indeed, accidents at sea inevitably occur, causing economic problems and risks for the crew and the environment. A report on accidents at sea is issued yearly by the European Maritime Safety Agency (EMSA) [38]. The total number of marine casualties and incidents reported from 2014 to 2022 was 23814, with an annual average of 2646. Its distribution and division according to the severity of the incidents is reported in the bars of Figure 1.1a, while the total number is reported with the black line. From the data it is possible to see that the number of casualties and incidents in 2022 is 5.1% under the annual average of 2670 occurrences before the pandemic. Also the severe marine casualties trend decreased at 44 in 2022 after registering 106 in 2018, 75 in 2019, 51 in 2020, and 58 in 2021. The report also stated that the navigational casualties constituted by collision and contact represent 32.1% of all casualty events as shown in Figure 1.1b; the 55.7% of the casualties occurred in internal waters like the port areas as shown in Figure 1.1c; and from 2014 to 2022, 59.1% of all occurrences were related to human action, either at accident event or contributing factor levels as shown in Figure 1.1d. The increasing development of autonomous navigation systems could

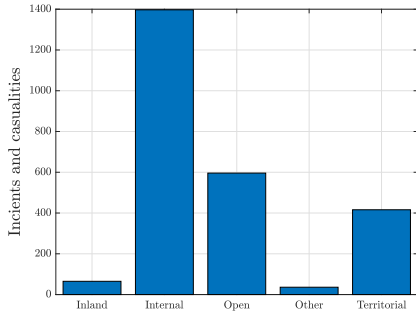
---



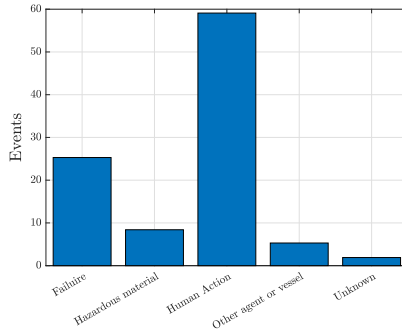
(a) Marine casualties and incidents.



(b) Occurrences with ship in 2022.



(c) Incidents navigation area in 2022.



(d) Accidents events percentage in 2022.

Figure 1.1: Introduction - EMSA report 2022.

lead to improved safety on the water, reduce the number of fatalities and save lives.

Other reasons can be found in the seventeen Sustainable Development Goals (SDGs) declared in the 2030 Agenda for Sustainable Development [87]. The evolution of the autonomous ship could contribute to several SDGs, such as SDG 7 "Ensure access to affordable, reliable, sustainable and modern energy for all", SDG 9 "Build resilient infrastructure, promote inclusive and sustainable industrialisation and foster innovation", SDG 11 "Make cities and human settlements inclusive, safe, resilient and sustainable", and SDG 13 "Take urgent action to combat climate change and its impacts". Indeed, autonomous technologies can contribute to reducing emissions thanks to more energy-efficient vessels. It is a direct consequence of autonomous route planning using one of the optimisation techniques available and the expected larger cargo capacity.

## 1.2 Level of Automation and Taxonomy

Studies on autonomous navigation are carried out over the years, leading to a vast literature and a need for more homogeneity regarding automation levels and the adopted definitions.

Hereinafter, a list of the most used terms adopted to define autonomous vessels is reported:

- **ASV** - Autonomous Surface Vehicle: a vessel that can take decisions and operate independently without human guidance, navigation, and control. ASVs are typically used in military operations, maritime surveillance cruises, marine environmental monitoring applications, and, in the near future, will likely also be used for the transportation of goods and people. Sometimes, the term is used to indicate model-scale vessels and separate them from the full-scale vessel MASS.
- **USV** - Unmanned Surface Vehicles : an unmanned vehicle that does not have a human on board to control its operations but is typically remotely controlled by a human operator. Crucially, an ASV may also be unmanned, but the critical distinction, when compared with a USV, is that it operates without direct intervention from a human operator during its mission, whatever that might be.
- **AMV** - Autonomous Marine Vehicles: all the vehicles used in the water (both underwater and surface).
- **ROV** - Remotely Operated Vehicle: underwater robots controlled by a human, typically on a surface vessel or in a proximate land, using a group of cables, or tether, that connects the ROV to the human interface.
- **AUV** - Autonomous Underwater Vehicles: Autonomous vessels that perform underwater missions without an operator.
- **ASC** - Autonomous Surface Craft: another name for ASV.
- **MASS** - Maritime Autonomous Surface Ships: acronyms defined during the 98<sup>th</sup> MSC session of IMO [61] to identify smart/autonomous ships and to unify the lots of named adopted. According to IMO, MASS is defined as a ship which, to a varying degree, can operate independently of human interaction.

In this thesis, the general acronym MASS is adopted for both full-scale vessels and models to maintain the generality of the treatment.

The process towards full automation goes through several steps, and over the years, several classifications with different Levels Of Automation (LOA) are proposed. Some reviews can be found in literature about this topic: in [125], a review about the evolution of the autonomy levels up to 2015 is done without a specific application together with a tentative cross-correlation between the different classifications; and in [99] and in [67] other small reviews are presented with a focus on the MASS. Hereinafter, some of the defined LOAs in the literature are presented.

Sheridan proposed the first classification in 1978 [109] and revise it with Parasuraman in 2000 [94]. He defines ten levels of interaction between humans and autonomous systems, as shown in Table 1.1, where the higher levels represent increased autonomy of the computers over human action.

Lloyd's Register [6] published a categorisation of vessels based on the level of autonomy. There are three main tasks: decision-making, actions taking, and exception handling. The characterisation is focused on the cyber safety of the vessel, where the hacking of the communication system is the worst risk. It assigns seven autonomy levels for ship design and operation according to Table 1.2.

SAE international [7] defines the levels of automation for on-road motor vehicles with six levels that go from level (0) 'No Automation' to level (5) 'Full automation'.

Level	Description
1	The computer offers no assistance: humans must take all decision and actions.
2	The computer offers a complete set of decision/action alternatives.
3	Computer narrows the selection down to a few.
4	Computer suggests one alternative.
5	The computer executes a suggestion if the human approves.
6	The computer allows human a restricted time to veto before automatic execution.
7	The computer executes automatically, then necessarily informs human.
8	The computer informs human only if asked.
9	The computer informs humans only if it (the computer) decides to.
10	The computer decides everything, acts autonomously, ignoring the human.

Table 1.1: Introduction - Autonomous levels - Sheridan.

Level	Name	Description
AL 0	Manual	All action and decision-making performed manually (n.b. systems may have level of autonomy, with Human in/ on the loop.), i.e. human controls all actions.
AL 1	Onboard Decision Support	All actions taken by human Operator, but decision support tool can present options or otherwise influence the actions chosen. Data is provided by systems on board.
AL 2	On & Off-board Decision Support	All actions taken by human Operator, but decision support tool can present options or otherwise influence the actions chosen. Data may be provided by systems on or off-board.
AL 3	'Active' Human in the loop	Decisions and actions are performed with human supervision. Data may be provided by systems on or off-board.
AL 4	Human on the loop, Operator/ Supervisory	Decisions and actions are performed autonomously with human supervision. High impact decisions are implemented in a way to give human Operators the opportunity to intercede and over-ride.
AL 5	Fully autonomous	Rarely supervised operation where decisions are entirely made and actioned by the system.
AL 6	Fully autonomous	Unsupervised operation where decisions are entirely made and actioned by the system during the mission.

Table 1.2: Introduction - Autonomous levels - Lloyd's Register.



The levels are developed for vehicles on wheels, but the solution can be easily compared with the marine environment. Four tasks characterise the six autonomy levels and each task is performed either by humans, a system, or by a collaboration of both. The summary of the SAE Levels is shown in Table 1.3. The following acronyms are used: Dynamic Driving Task (DDT), Object and Event Detection and Response (OEDR), Operational Design Domain (ODD), and Automated Driving System (ADS).

Norwegian Forum of Autonomous Ships proposes another classification level [5]. The approach is quite similar to the one proposed by SAE [7] for the automotive field and defined the following six categories of automation according to Table 1.4:

- *Direct control - NFAS 1*: The crew on the bridge is continuously in control of operations, although simple automation, e.g. autopilot, or advanced decision support functions may be in use. This is strictly speaking not an autonomy type, but is included in the taxonomy for completeness.
- *Automatic bridge - NFAS 2*: The bridge system controls the ship while crew on the bridge continuously monitors the situation and can intervene at any time. The level of automation may be arbitrarily high, but crew is always ready to intervene.
- *Remote control - NFAS 3*: Same as direct control, however here the Shore Control Centre is in control of the ship. One can also here argue that this is not really a type of autonomy. However, as communication links normally cannot be made 100% reliable, the ship will in most cases need fallback procedures that can be activated autonomously when communication fails.
- *Automatic ship - NFAS 4*: Same as Automatic bridge, but again being supervised from the Shore Control Centre.
- *Constrained autonomous - NFAS 5*: Supervised by Shore Control Centre.
- *Fully autonomous - NFAS 6*: Not supervised by Shore Control Centre. This type of autonomy is generally complicated to implement and will also mean that the owner of the ship has less control of its operation. Generally, approval of this type of ship will require major changes in regulations, mainly because there is no longer any equivalence to the master or other officers on board.

The NFAS classification was adopted inside the GALILEOnautic project [107] to define a different categorization. The classification is quite similar to the NFAS levels [5] except for the lower level Decision support, which is split in No manoeuvre automation (MAL 0) and Manoeuvr assistance (MAL 1) because the claimed autopilot is not available for manoeuvring in high safety areas. The levels are shown in Table 1.5.

The categorisations mentioned above do not consider all aspects subject to automation and the characteristics of vessels. However, vessels are not the only actors in the transport environment. The communication and cooperation between agents are essential functions that should be realised. Lloyd's Register only considers communications and data from the vessel or shared by a remote location, but no explicit reference exists. Schiaretti et al. [105] propose a new autonomy level categorisation that considers subsystems and overall systems. This new categorisation system considers four main subsystems:

Level	Name	Narrative Definition	DDT - Sustained lateral and longitudinal vehicle motion control	DDT-OEDR	DDT-Fallback	ODD
SAE 0	No driving Automation	The performance by the driver of the entire DDT, even when enhanced by active safety systems.	Human Driver	Human Driver	Human Driver	n/a
SAE 1	Driver Assistance	The sustained and ODD-specific execution by a driving automation system of either the lateral or the longitudinal vehicle motion control subtask of the DDT (but not both simultaneously) with the expectation that the driver performs the remainder of the DDT.	Human Driver and System	Human Driver	Human Driver	Limited
SAE 2	Partial Driving Automation	The sustained and ODD-specific execution by a driving automation system of both the lateral and longitudinal vehicle motion control subtasks of the DDT with the expectation that the driver completes the OEDR subtask and supervises the driving automation system.	System	Human Driver	Human Driver	Limited
SAE 3	Conditional Driving Automation	The sustained and ODD-specific performance by an ADS of the entire DDT with the expectation that the DDT fallback-ready user is receptive to ADS-issued requests to intervene, as well as to DDT performance-relevant system failures in other vehicle systems, and will respond appropriately.	System	System	Human Driver	Limited
SAE 4	High Driving Automation	The sustained and ODD-specific performance by an ADS of the entire DDT and DDT fallback without any expectation that a user will respond to a request to intervene.	System	System	System	Limited
SAE 5	Full Driving Automation	The sustained and unconditional (i.e., not ODD-specific) performance by an ADS of the entire DDT and DDT fallback without any expectation that a user will respond to a request to intervene.	System	System	System	Unlimited

Table 1.3: Introduction - Autonomous levels - SAE

	<b>Manned bridge</b>	<b>Unmanned bridge - crew on board</b>	<b>Unmanned bridge - no crew on board</b>
<b>Decision support</b>	Direct control No autonomy	Remote control	Remote control
<b>Automatic</b>	Automatic bridge	Automatic ship	Automatic ship
<b>Constrained autonomous</b>	<b>au-</b> -	Constrained au- tonomous	Constrained au- tonomous
<b>Fully autonomous</b>	-	-	Fully au- tonomous

Table 1.4: Introduction - Autonomous levels - NFAS

<b>Level Name</b>	<b>Description</b>
MAL 0 No Ma- noeuvre Automation	Equipment is depending on age and type of the vehicle (Sensors/ instruments), whether they have Auto- or Track pilot for transit mode on open seas
MAL 1 Manoeuvre Assistance	Additional sensors with higher precision to measure the distances to harbour facilities, complete dynamics. Motion model and harbour. Examples: for MAL 1 are visual manoeuvre Prediction or decision support
MAL 2 Partial Ma- noeuvre Au- tomation	It is defined as Single automated manoeuvres initialised by Watchkeeping Officer. It needs optimised trajectories for the actual situation (weather) and Adaptive control strategies. Watchkeeping Officer is always ready to intervene by safe fall-back solution. Examples: Automatic Berthing/ Docking, Collision avoidance
MAL 3 High Ma- noeuvre Automation	It is the last step before autonomy. This means that all functionalities of an autonomous vessel are realised already, but there is still a supervisor. Examples: An appropriate example is a ferry with defined ports, which can sail the complete route automatically
MAL 4 Autonomous Manoeu- vring	It presents autonomy, autonomous operation under all circumstances without a remote operation centre or a supervisor. There are numerous questions in case of an accident or already of lost communication.

Table 1.5: Introduction - Autonomous levels - GALILEOnautic.

Autonomy Level	Name
0	Human is alone
1	Human is helped by systems
2	Human is helped by the systems and other agents
3	Autonomous path following vessel
4	Autonomous trajectory tracking vessel
5	Human in the loop
6	Human supervise the decisions making system
7	Human supervise the actions making system
8	Human supervise the exceptions handling system
9	Human supervise actions, decision and exceptions
10	Fully autonomous

Table 1.6: Introduction - Autonomous levels - Schiaretta.

- Decision making: is the first and easiest to automate; routing and planning tasks can be autonomously optimised, together with the maintenance schedule. The levels scale from 1 to 10.
- Actions taking: is more complex since physically actuated mechanical components are involved in the control loop. The levels scale from 1 to 10.
- Exceptions handling: a key part of obtaining an overall high autonomy level, different solutions are being studied to detect and avoid obstacles. The levels scale from 1 to 10.
- Cooperation: considers the cooperation between the vessel and the surrounding environment. Information is exchanged with other vessels, infrastructures or remote-control locations. The levels are made by giving an increased level of cooperation based on the number of agents the system is able to communicate with. The level of cooperation ranges from 1 to 5.

The first three subsystems are based on Lloyd's Register and SAE International. The levels assessed in each subsystem go from a lack of interaction between humans and computers to full control of the computer that ignores human actions. Once autonomy levels of the subsystems are determined, the next move is to create the general autonomy level classification for the overall system of the ASVs of Table 1.6. The name of the levels describes each function. The autonomy levels of the subsystems determine the overall autonomy level according to relationships given in [105]. Based on this regulation, in [106], an analysis of 60 MASS characteristics and autonomy degrees is shown. From the data reported in the previous article, it is possible to see that the number of MASS projects has increased during the years and that, at the publication time, the trend is to develop a very high automation level MASS simultaneously with a low-level MASS, without the development of the intermediate grades. As the automation level increases, its integration into the ship system increases.

Other classifications are defined during years, like the one proposed by DNV [31] and the one proposed by Bureau Veritas [128]. However, a critical milestone was the definition of levels by the International Maritime Organization (IMO). Indeed, during the 99<sup>th</sup>, [58], and 100<sup>th</sup>, [60], sessions of the Marine Safety Committee

Level	Description
Degree one	Ship with automated processes and decision support: Seafarers are on board to operate and control shipboard systems and functions. Some operations may be automated and at times be unsupervised but with seafarers on board ready to take control.
Degree two	Remotely controlled ship with seafarers on board: The ship is controlled and operated from another location. Seafarers are available on board to take control and to operate the shipboard systems and functions.
Degree three	Remotely controlled ship without seafarers on board: The ship is controlled and operated from another location. There are no seafarers on board.
Degree four	Fully autonomous ship: The operating system of the ship is able to make decisions and determine actions by itself.

Table 1.7: Introduction - Autonomous levels - IMO.

(MSC) IMO proposed four levels of autonomy according to Table 1.7. The publication is the first tentative step toward the unification and homogeneity of the different classifications.

Different properties are underlined and grouped to summarise the classifications presented and find the common points. The proposed properties in this thesis adopted to compare the different autonomous levels classifications are the following:

- *No Assistance*, corresponds to the absence of automation and support systems;
- *Fully manual*, corresponds to the manual action, but there may be active alert systems;
- *Support system*, corresponds to the presence of decision support systems, but the action remains manual;
- *Remote control with seafarers*, corresponds to remote control with the presence of seafarers on board where there may or may not be automation systems;
- *Remote control without seafarers*, corresponds to remote control without the presence of seafarers on board where there may or may not be automation systems;
- *Single manoeuvre with active human*, corresponds to partial automation for specific operations and with active human supervision ;
- *Active human supervision*, corresponds to automation for all operations and with active human supervision;
- *Single manoeuvre with supervision*, corresponds to partial automation for specific operations;
- *Full autonomous with supervision*, corresponds to full automation with human supervision;

- *Full autonomous with rarely supervision*, corresponds to full automation with human supervision in exceptions;
- *Full autonomous with limited operability*, corresponds to full automation with limited operability;
- *Fully autonomous*, corresponds to full autonomous without human supervision.

The resulting outline is shown in the Table 1.8, where in the first column are reported the identified properties, while in the other columns, there are the corresponding autonomy levels of Sheridan, LLOYD's Register, SAE, adopted for the GalileoNautic, Schiaretto, NFAS, and IMO, respectively. Other properties and classifications can be found to define the comparison, but this is the one outlined in this thesis.

Multiple levels of automation are sometimes grouped since they are sub-cases of the identified properties. The overlapping happens in the following cases: Sheridan levels 2, 3, and 4 are all decision support levels but at different levels since level 2 provides a set of solutions, level 3 a selection of the set of solutions, and level 4 only the best solution; Lloyd levels 1 and 2 diverge in the origin of the information used in the support system which can be on-board or off-board; Levels 0 and 1 of the GalileoNautic classification differ in their application to open waters or shallow waters; levels 3 and 4 of the Schiaretto classification diverge in their cooperation component; Schiaretto levels 5, 6, 7, and 8 are all levels subject to active human supervision but differ in their decision-making, action, and exception management powers; finally, levels 6 and 7 of Sheridan diverge in the type of supervision given, as do levels 8 and 9.

Another important observation concerns the classification levels proposed by the IMO. These are seen and accepted as an attempt of unification, but from the analysis made in table 1.8 it can be seen that they leave a big gap in the gradual automation process. Indeed, the first three levels are all connectible to remote control levels and the next level refers to the fully autonomous vehicle without any intermediate step such as the presence or absence of supervision or the automation of only some scenarios. This then opens up a series of possible considerations about its applicability at this intermediate stage where the first prototypes begin to be put into operation together with the fully manual ships and which would not find their classification within the IMO scale.

	Sher.	Lloyd	SAE	Gal.Nau.	Schiar.	NFAS	IMO
No assistance	1	A0	0		0		
Fully manual	2,3,4	1, 2				1	
Support system				0, 1	1,2		One
Remote control with seafarers						3	Two
Remote control without seafar- ers							Three
Single manoeuvre with active human			1		3, 4		
Active human supervision	5	3			5, 6, 7, 8	2	
Single manoeuvre with super- vision			2	2		4	
Fully au- tonomous with supervision	6,7	4	3	3		5	
Fully au- tonomous with rarely supervi- sion	8,9	5			9		
Fully au- tonomous with limited operability			4				
Fully au- tonomous	10	6	5	4	10	6	Four

Table 1.8: Introduction - Autonomous levels - Proposed comparison.

## 1.3 Guidance, Navigation & Control

Generally, the architecture of a marine control system necessary for defining a MASS can be described with the Guidance, Navigation & Control (GNC) systems [45]. The architecture is shown in Figure 1.2.

The Navigation system receives inputs from the sensors onboard and provides the system state and information on the surrounding environment. It can be divided into two subsystems: Sensor Fusion and Situation Awareness. Sensor Fusion aims to condense and integrate information from heterogeneous sensors. It is based on a redundancy of measurements and sensors to compensate for the limitations of each. Situation Awareness makes it possible to perceive the surrounding environment based on the information obtained from the sensors and their integration into a model of the environment. In traditional vessels, the heart of Situation Awareness and Sensor fusion is the human being, who integrates and interprets the information from the different sensors, while the rest of the technologies play only a supporting role.

The Guidance system receives as input the information collected and elaborated from the navigation system and aims to answer the question: “When and where will the vessel arrive, and with what trajectory?”. The hierarchical structure of the guidance can be split into three subsystems. The first is a high-level path planner that defines a route based on geometrical parameters, the weather, maps or user-defined mission. The process output is a path defined, e.g. through waypoints or by employing a single point whether the requirement is following an object or station keeping. Once the path is defined in the first instance, it must be integrated with a collision-avoidance system composing the reactive path planning. Indeed, in collision risk, this system reprocesses the path to safely (w.r.t. international regulations [59]) accomplish the mission. At this stage, the Guidance system demands different motion control scenarios. Several scenarios can be defined to satisfy this aim, like path following, target tracking, and follow the leader.

The Control system determines the necessary input signal to satisfy the guidance aim. It collects the information about the desired setpoints from the guidance, the state information from the navigation system, and generates the inputs for each actuator. The desired output is the desired motion computed by the guidance; then the Control system generates the inputs to the actuators so that the ship motion is the desired one. Its most complete phase can be seen in three stages: a first phase with a high-level control algorithm that satisfies a generic control objective and provides a vector of virtual forces and moments; a second phase with control allocation algorithms that coordinate the different actuators to globally produce the virtual vector of forces and moments desired by each; finally, a third phase with low-level motion control algorithms, used to ensure that the actuator satisfies its single request given by the control allocation algorithm. The first two phases can be merged together, while the actuator producer sometimes develops the third phase.

The vessel needs to be taken into account together with the onboard sensors to close the loop of the GNC architecture. It can be physical or simulated according to the applications.

This thesis leads with the topics related to guidance and control systems. Hence, additional details are given about them.

Guidance becomes crucial for autonomous ships and a review of the ASVs focusing on the Guidance system is reported in [124]. The hierarchical structure



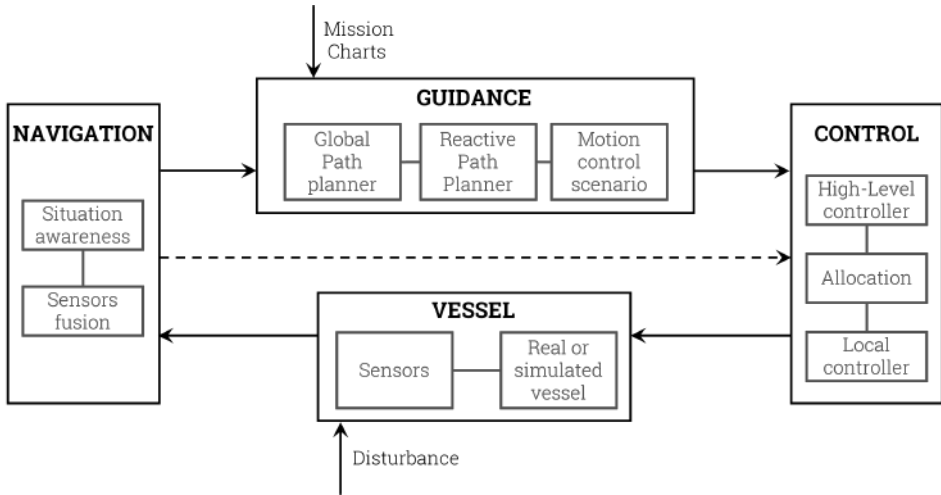


Figure 1.2: Introduction - GNC architecture.

of the guidance can be split into subsystems: the global path planner, the reactive planner, and the motion control scenario, as shown in Figure 1.3.

The global path planned computes a global and safe path from the initial state to the goal state, considering the fixed obstacles and the surrounding environment. The route is identified by defining a mission schedule, such as minimising fuel consumption, distance travelled, power output, time, and considering the constraints given by the static obstacles and the environment. Another possibility is the so-called weather routing, where the path is optimized according to the weather forecasts [137]. The method can be solved with optimisation methods and heuristic algorithms. Some examples are Genetic Algorithm [141], algorithms like the  $A^*$  and its variations [115], Rapidly-exploring random tree (RRT) [136], Ant Colony Optimization (ACO) [139], and Particle swarm optimisation (PSO) [51]. Sometimes, the optimisation and the heuristic approach can be combined, leading to hybrid scenarios. The output is a path defined through a list of waypoints. Review papers dealing with global path planning algorithms can be found in [111] and in [71].

Once the global path is defined, a reactive path planner is introduced with the role of collision avoidance. In this case, the risk of collision risk needs to be evaluated, and if the risk is present, a collision avoidance algorithm modifies the defined path to avoid the collision. It will find a collision-free path that can comply with COLREG rules [59]. The approach can adopt optimisation methods, heuristic algorithms, potential fields, and machine learning techniques to solve the collision problem, but in all cases, the output is the collision-free path defined through waypoints. In literature it is possible to find reviews of these methods, some example are: the literature review in [55] that offers a comprehensive overview of collision avoidance techniques based on the three basic processes of determining evasive solutions, namely, motion prediction, conflict detection, and conflict resolution; the literature review in [120] that reports a time-line of the study about collision avoidance up to 2009; the literature review in [24] that has a focus on the relevant weakness in obstacle detection and avoidance system found in literature up to 2012; the literature review done in [93] where there is a focus on the collision regulations;

the literature review in [8] with a focus on the importance of the collaboration between the involved vessel in collision; and the literature review in [54] that has a focus on the COLREGs compliant algorithms up to 2022.

Having the path defined, the guidance demands different motion control scenarios. One of the typical motion control scenarios is the path following, which regards following a user-defined time-invariant straight [46] or curved [68] path (waypoint navigation). A general review can be found in [133] and a review focusing on the Line-Of-Sight law and its variations for the path following can be found in [50]. Other scenarios add the time domain, as shown in [10], or the manoeuvrability constraints at the path following one. A different case is the dynamic positioning 3-DOF control scenario, where a vessel is required to maintain its position and heading via the exclusive use of its thrusters; in this case, reference models are used to compute a time trajectory that points to the final desired positions, [45]. Track keeping is a variation of this and required to follow a path at low speed, [10]. The follow-the-leader scenario regards following the leader path with the same speed at each point; some applications can be found in [97] and [16]. The extension of the follow-the-leader is the formation control, and some implementations are shown in [49] and [140]. Another is the target tracking scenario that regards following a target of which only the instantaneous position and velocity are known; hence, the motion evolution is unknown [21], [48]. Several common guidance laws can be adapted and used in these motion control scenarios, like the Line-Of-Sight, the Pure Pursuit, and the Constant Bearing laws. The outputs of the motion control scenarios subsystem are the control inputs, like a speed and a heading setpoint for the 2-DOF controller or a set of desired speeds and positions for the 3-DOF controller.

The control system takes as input the guidance setpoints and aims to set them, computing the proper input signal and the actuator setpoints. There are several types of approaches for the controller design that can be divided into Model-based control approaches (they are widely exploited over the years, exhibiting their ability to provide effective and reliable control laws in a large variety of control tasks [9]) and Data-driven control approaches (that are model-free control solutions in which the synthesis of controllers is entirely based on input-output data collections [17]). Both approaches can lead to different types of controllers like linear or non-linear control [44], model predictive control [80], fuzzy logic [127], and backstepping control [143]. A review of the control strategies adopted on autonomous vehicles can be found in [71] and [130]. Additionally, it is possible to divide the control system according to the degree of freedom the system wants to control (1-DOF, 2-DOF, and 3-DOF controllers for surface vessels). According to this, in this thesis, the controller layout is divided into 2-DOF and a 3-DOF. The 2-DOF controller layout is a smart pilot composed of an autopilot and a speed pilot for controlling the heading and the speed in the high-speed regime of the vessel with low drift angle is designed and modelled as two separate Proportional-Integral-Derivative (PID) controllers. It is synthesised to ensure the closed loop stability and performance thanks to Linear Matrix Inequality (LMI) techniques [19]. Some examples can be found in [104], [84], [81], [26], and [97]. The 3-DOF controllers are also known as dynamic position controllers and aim to control the pose and the speed of the vessels at high drift angle, computing the proper forces and moment array and allocating them to the actuators. A comprehensive review of dynamic position systems is shown in [116], in [65], in [52], and in [83]. In both cases, the outputs of

the control system are the actuator setpoints.

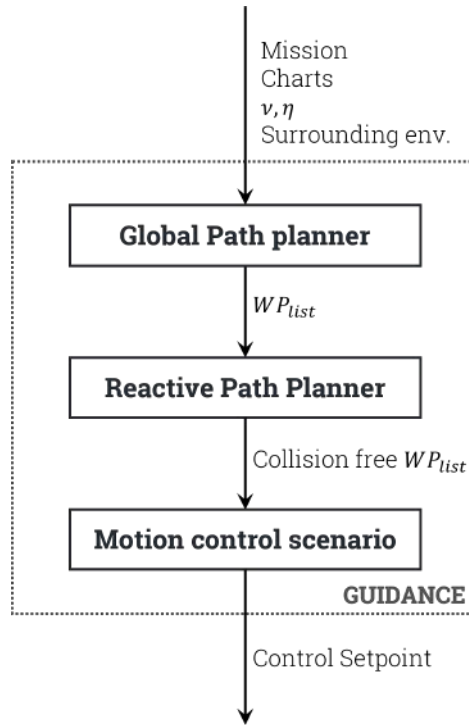


Figure 1.3: Introduction - Guidance architecture.

## 1.4 State of art

Studies concerning the world of autonomous navigation can be found in the literature, and they can be applied to both real and simulated models. Often, simulation is the intermediate step to experimental testing on the real model.

From the first developments of an ASV at the academic level in the last decades of the XX century, many institutes have started researching the field of autonomy onboard larger vessels, up to the more recent proposal of the industry to automate cargo and bulk carrier ships.

Several models are developed during the years, and review papers can be found in the literature. Some examples are the literature review in [95], where the authors systematically review 15 years of autonomous and unmanned surface vessels to determine the factors limiting technological diffusion into everyday maritime operations. In [13], the authors review the developments, types and applications of autonomous surface vessels up to 2022. In [70], the main projects are reported and analysed, focusing on human-machine cooperation. In [71], a summary of the autonomous surface model is reported and grouped according to nationality and purpose. In [106], an extensive overview of existing prototypes is shown with their categorisation according to the classification presented in [105]. In [41], a categorisation according to the adopted guidance system is reported. The reviews show

that models with different hulls, actuators, purposes, and sensors are present in industry and academia. An example is the MIT vessel ARTEMIS [126]. Its goal is to collect bathysphere data along a river. Another one is the SCOUT autonomous surface craft with a kayak hull shape [27] or the SWAMP catamaran developed by CNR [91] suitable for shallow waters. In recent years, the development has focused on the urban ferry and examples such as the milliAmpere one developed by NTNU [23] and the RoBoat [131] can be found together with their first trails.

From the industrial point of view, the three-year research project MUNIN (Maritime Unmanned Navigation through Intelligence in Networks) founded in 2012 by the European Commission [101] investigated the feasibility of autonomous ships within the following three years by developing technical solutions and suggestions for legal and contractual changes for the challenges that unmanned vessels represent. The developed concepts are validated in an integrated simulation prototype of an autonomous vessel. An explicit aim is to generate a solution that allows updating the current fleet and a gradual change from manned to unmanned fleets. It predicted savings of over \$7m over 25 years per autonomous vessel in fuel consumption, crew supplies, and salaries. On the other hand, there will be significant capital expenditures when initially investing in technology, especially in the early stages of its development, not only for the ship itself but also for the setting up of onshore operations to monitor fleet movements. There may also be incompatibilities between the current marine infrastructure and an unmanned vessel. Further, the lack of crew will make maintenance of moving parts challenging on long voyages, and breakdowns could result in significant delays.

Rolls-Royce conducted the research project Advanced Autonomous Waterborne Applications Initiative (AAWA) between 2015 and 2017 and the aim was to study the specification and preliminary designs for the next generation of ships [102]. The finding of the projects leads to the “the world’s first fully autonomous ferry” Falco [103].

Another important autonomous shipping project funded by the European Commission in 2019 is AUTOSHIP – Autonomous Shipping Initiative for European Waters [2]. It aims to speed up the transition towards the next generation of autonomous ships in the EU using increased coastal short-sea and inland waterways shipping to reduce road freight transport. The project has a consortium composed of several partners, including Bureau Veritas and Kongsberg (that acquired Rolls-Royce Commercial Marine in 2019) and build and operate two different autonomous vessels, demonstrating their operative capabilities in Short Sea Shipping and Inland Water Ways scenarios, with a focus on goods mobility. Other crucial European projects focusing on the harbour environment are the MOSES [4] and the Aegis [1].

In 2017, YARA and Kongsberg partnered to build the world first fully electric and autonomous container vessel, the YARA Birkeland [75]. The aim is to obtain a ship that can be manned from a remote position and is fully autonomous, equipped with electrical propulsion, battery and control systems for coastal navigation along the Norwegian coast. On November 18, 2021, Yara Birkeland took its first manned trip to Oslo before it was put into operation. Nowadays, it has started a two-year trial to become autonomous and certified as an autonomous, fully electric container vessel.

Several flagship projects in many countries already point in this direction; an example is the classification society DNV-GL that developed the 60 metres long

fully battery-powered autonomous vessel ReVolt [33]. The related topics are unmanned, zero-emission, and short-sea vessel navigation. To test the autonomous capabilities of ReVolt, a 1:20 scaled model is built thanks to a collaboration with the Norwegian University of Science and Technology (NTNU).

The Oceanalpha announcement in 2019 in Zhuhai (China) represents another critical event [90]. It is an unmanned surface vessel company managed by the Yunzhou Intelligent Technology Company in partnership with the Wuhan University of Technology, the China Classification Society (CCS), and the Zhuhai city government. Another significant and ambitious project based in the East is supported by The Nippon Foundation MEGURI, which aims to promote the development of entirely autonomous ships. On 2022 January 17, the world's first fully autonomous ship navigation system on the 222-meter SOLEIL car ferry was conducted on the Iyonada Sea from Shinmoji, Kitakyushu City. The ferry can have autonomous port berthing and unberthing and high-speed navigation of up to 26 knots. In addition, the advanced fully autonomous operation system includes sensors to detect other ships using infrared cameras, a remote engine monitoring system, and a sophisticated cyber security system [47].

In the end, the world first autonomous urban passenger ferry was launched in Stockholm in June 2023 [138]. It is the commercialisation of the idea born in 2017 regarding urban passenger ferries as integral parts of the city public transport network and which began with the development of the milliAmpere1 and milliAmpere2 models in the city of Trondheim by NTNU [23].

This extraordinary interest led to the creation of testing areas designated as official test beds for autonomous trials. Since Norway great interest, the first area was established in Trondheimsfjorden in 2016. However, other areas like the Marine Autonomy Research Site (MARS) was established in Great Lakes region in the USA [63]. In the East, the Wanshan Unmanned Test Site is established. The test site is located in the Wanshan Islands and covers an area of 771 square kilometres.

## 1.5 Contributions

The main purpose is to design control scenarios for the entire speed range of vessels. The analysis is carried out with a focus on the guidance and control systems with a distinction between control scenarios in 2 and 3 degrees of freedom. The general scenarios are applied to different case study spacings from model scale to full-scale vessels. All the scenarios and the proposed methodologies are evaluated using appropriate key performance indicators. The contribution can be summarised as follows:

- Line-Of-Sight, Pure Pursuit, and Constant Bearing guidance laws for Target Tracking motion control scenario are slightly modified with respect to the literature to make them suitable for a parametric analysis.
  - Dynamic positioning controller using time domain modelling is developed for a PSV and tested with the real hardware.
  - Synthesis of a smart pilot for a surface vessel is defined to ensure stability and performance regarding decay rate and limited overshoot of the closed loop.
-

- 
- Optimised force allocation logic accounts for non-linear hydrodynamic effects on the thrust generation is developed.
  - Operability and emission factor statistic indices for evaluating the station-keeping performance and the environmental footprint of a proposed propulsion plant during the early stage design are proposed for proper decisions in ship deployment.
  - Comparison study of different combinations of the subsystems defining the controller pipeline for the entire speed range of the milliAmpere test case is done through integral metrics.

# Chapter 2

## Vessel mathematical model

The test cases adopted for this work are surface vessels with different dimensions and propulsion systems. The guidance and control methods developed are tested and developed by means of modelling and simulation techniques in accordance with [77]. Through numerical simulation, it is indeed possible to model the physical ship model and study its dynamic behaviour also under the influence of the developed strategies without needing the physical model.

Considering the starboard-portside symmetries, the vessels are modelled through a detailed non-linear tree degree of freedom (DOF) simulator in the horizontal plane. The general simulator is shown in Figure 2.1. The general motion equation system is in Section 2.2 and has the aim of computing the positions, speed and acceleration starting from the forces acting on the vessel; the last one derives from the hull, see Section 2.3, from the propulsion plant and its actuators, see sections 2.4 and 2.5, and from the environmental disturbances, see Section 2.6. The inputs of all the vessel models are the actuator setpoints and depend on the actuator and the components of the propulsion plant system; examples are the voltage  $V_A$ , the engine revolutions  $n_E$ , the azimuth angle  $\alpha$ , and the rudder angle  $\delta$ .

### 2.1 Adopted reference frame

First, to support the definition of the vessel model, the reference frames adopted inside this work are defined according to Figure 2.2.

The n-frame  $\{\mathbf{\Omega}, \underline{n}_i\}$  is an Earth-fixed frame and it is inertial; it is the NED frame according to [45]. The origin  $\mathbf{\Omega}$  is located on the mean water-free surface at an appropriate location. The positive unit vector  $\underline{n}_1$  points towards the North,  $\underline{n}_2$  points towards the East, and  $\underline{n}_3$  points downwards.

The b-frame  $\{\mathbf{\Omega}_I, \underline{b}_i\}$  is fixed to the vessel hull; it is the BODY frame according to [45]. The origin,  $\mathbf{\Omega}_I = x_I \underline{n}_1 + y_I \underline{n}_2$ , is located in  $(\frac{L_{PP}}{2}, 0, z_{WL})$ , where  $L_{PP}$  is the vessel length between perpendiculars and  $z_{WL}$  is the quota of the waterline above the keel line; it corresponds to the vessel objective of the study, it will be the interceptor, i.e. the chasing ship, instantaneous position in the target tracking guidance. The positive unit vector  $\underline{b}_1$  points towards the bow,  $\underline{b}_2$  points towards starboard, and  $\underline{b}_3$  points downwards.

The e-frame  $\{\mathbf{\Omega}_R, \underline{e}_i\}$  is fixed with the vector between the reference  $\mathbf{\Omega}_R$  and the target  $\mathbf{\Omega}_T$  points. The origin  $\mathbf{\Omega}_R = x_{RN} \underline{n}_1 + y_{RN} \underline{n}_2$  corresponds to a stationary

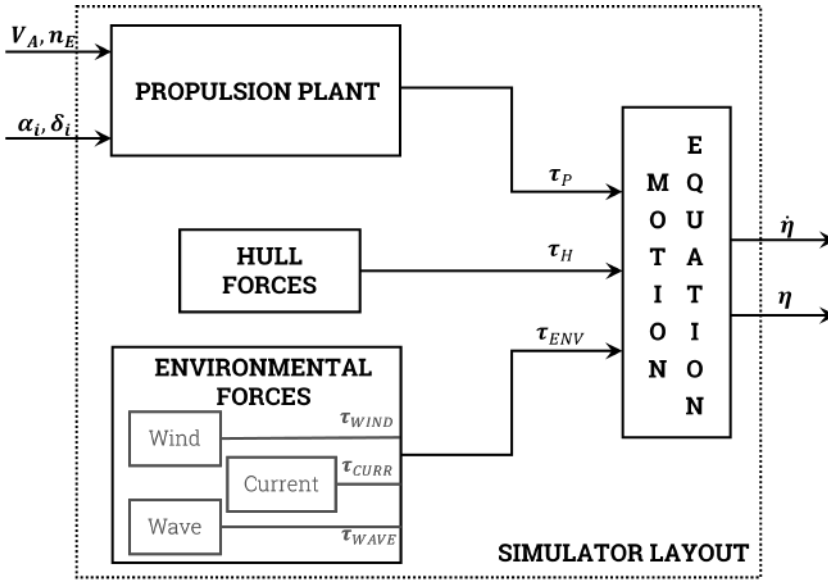


Figure 2.1: Vessel mathematical model - Layout.

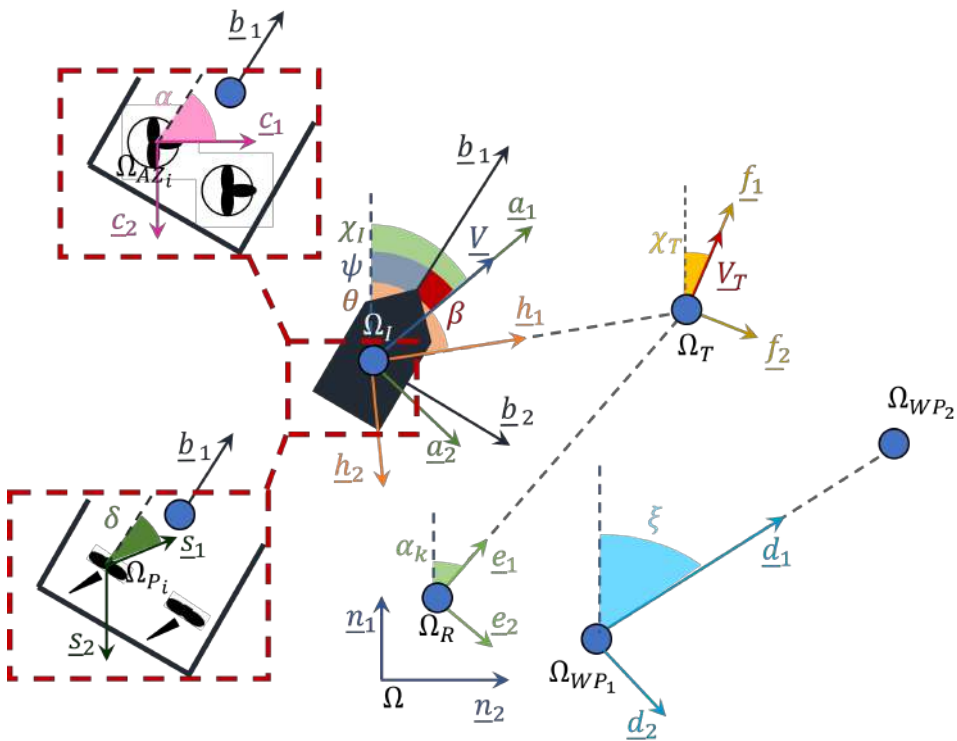


Figure 2.2: Vessel mathematical model - Reference frames.

reference point that supports the desired path definition in the target tracking guidance, its choice will be shown in Section 3.1.1. The positive unit vector  $e_1$



points towards the vector  $(\mathbf{\Omega}_T - \mathbf{\Omega}_R)$ ,  $\underline{e}_2$  points towards starboard, and  $\underline{e}_3$  points downwards.

The h-frame  $\{\mathbf{\Omega}_I, \underline{h}_i\}$  is fixed with the vector between the interceptor  $\mathbf{\Omega}_I$  and the target  $\mathbf{\Omega}_T$  points. The positive unit vector  $\underline{h}_1$  points towards the vector  $(\mathbf{\Omega}_T - \mathbf{\Omega}_I)$ ,  $\underline{h}_2$  points towards starboard, and  $\underline{h}_3$  points downwards. The origin  $\mathbf{\Omega}_I$  is already defined above.

The f-frame  $\{\mathbf{\Omega}_T, \underline{f}_i\}$  is fixed with the target velocity  $\underline{V}_T$ . The positive unit vector  $\underline{f}_1$  points towards the target velocity vector,  $\underline{f}_2$  points towards starboard, and  $\underline{f}_3$  points downwards. The origin,  $\mathbf{\Omega}_T = x_T \underline{n}_1 + y_T \underline{n}_2$ , corresponds to the instantaneous position of the target, i.e. the chased vessel in the target tracking guidance, it is located in the position  $(\frac{L_{EP}}{2}, 0, z_{WL})$  of the chased vessel.

The a-frame  $\{\mathbf{\Omega}_I, \underline{a}_i\}$  is fixed with the interceptor velocity  $\underline{V}$ . The positive unit vector  $\underline{a}_1$  points towards the interceptor velocity vector,  $\underline{a}_2$  points towards starboard, and  $\underline{a}_3$  points downwards. The origin,  $\mathbf{\Omega}_I$ , is already defined above.

The c-frame  $\{\mathbf{\Omega}_{AZ_i}, \underline{c}_i\}$  is fixed with the  $i$ - azimuthal thruster. The origin,  $\mathbf{\Omega}_{AZ_i} = x_{AZ_i} \underline{n}_1 + y_{AZ_i} \underline{n}_2$ , corresponds to the position of the  $i$ - azimuthal thruster and it is located in  $(x_{AZ_i}, y_{AZ_i}, z_{WL})$ . The positive vector  $\underline{c}_1$  points towards azimuth thrust,  $\underline{c}_2$  points towards starboard, and  $\underline{c}_3$  points downwards.

The d-frame  $\{\mathbf{\Omega}_{WP_1}, \underline{d}_i\}$  is fixed with the path defined by the two waypoints taken into consideration at each time step by the track-keeping guidance. The origin is in  $\mathbf{\Omega}_{WP_1} = x_{WP_1} \underline{n}_1 + y_{WP_1} \underline{n}_2$  and corresponds to the position of the first waypoint taken into consideration at each time step in the track keeping guidance. The second waypoint taken into consideration at each time step in the track keeping guidance is  $\mathbf{\Omega}_{WP_2} = x_{WP_2} \underline{n}_1 + y_{WP_2} \underline{n}_2$ . The positive vector  $\underline{d}_1$  points towards the vector  $(\mathbf{\Omega}_{WP_2} - \mathbf{\Omega}_{WP_1})$ ,  $\underline{d}_2$  points towards starboard, and  $\underline{d}_3$  points downwards.

The s-frame  $\{\mathbf{\Omega}_{P_i}, \underline{s}_i\}$  is fixed with the  $i$ - propeller plus rudder actuator. The origin,  $\mathbf{\Omega}_{P_i} = x_{P_i} \underline{s}_1 + y_{P_i} \underline{s}_2$ , corresponds to the position of the  $i$ - propeller and it is located in  $(x_{P_i}, y_{P_i}, z_{WL})$ . The positive vector  $\underline{s}_1$  points towards propeller plus rudder thrust,  $\underline{c}_2$  points towards starboard, and  $\underline{c}_3$  points downwards.

The introduced reference systems lie in the same plane and the unit vectors are related by the Euler angles and the rotation matrices in (2.1).

$$\begin{aligned}
 \underline{n} &= \mathbf{R}_{\underline{e}}^n(\alpha_k) \underline{e}, \\
 \underline{n} &= \mathbf{R}_{\underline{b}}^n(\psi) \underline{b}, \\
 \underline{n} &= \mathbf{R}_{\underline{h}}^n(\theta) \underline{h}, \\
 \underline{n} &= \mathbf{R}_{\underline{f}}^n(\chi_T) \underline{f}, \\
 \underline{n} &= \mathbf{R}_{\underline{a}}^n(\chi_I) \underline{a} \\
 \underline{n} &= \mathbf{R}_{\underline{d}}^n(\xi) \underline{d} \\
 \underline{b} &= \mathbf{R}_{\underline{c}}^b(\alpha) \underline{c} \\
 \underline{b} &= \mathbf{R}_{\underline{s}}^b(\delta) \underline{s}
 \end{aligned} \tag{2.1}$$

where  $\alpha_k$  is the angle between  $\underline{n}_1$  and  $\underline{e}_1$ ;  $\psi$  is the angle between  $\underline{n}_1$  and  $\underline{b}_1$ , it is the heading angle;  $\theta$  is the angle between  $\underline{n}_1$  and  $\underline{h}_1$ ;  $\chi_T$  is the angle between  $\underline{n}_1$  and  $\underline{f}_1$ , it is the target course angle; the interceptor course angle is identified as  $\chi_I$ , the angle between  $\underline{n}_1$  and  $\underline{a}_1$ ;  $\xi$  is the angle between  $\underline{n}_1$  and  $\underline{d}_1$ ;  $\alpha$  is the azimuth angle; and  $\delta$  is the rudder angle.

## 2.2 Kinetics

The motion equation in (2.2) expresses the vessel dynamic, deriving from Newton law. The motion model adopted for synthesising the controller is a 3-DOF model expressing the dynamics of a rigid body. The model takes into account the inertia  $\mathbf{M}_{RB}$  and Coriolis matrix  $\mathbf{C}_{RB}$  of the rigid body defined in (2.3) and (2.4) according to the well-known formulation in [45]. The general model is then simplified to consider the ship starboard-port side symmetry, i.e. when the centre of gravity is on the middle line.

$$\boldsymbol{\tau}_{RB} = \mathbf{M}_{RB}\dot{\boldsymbol{\nu}} + \mathbf{C}_{RB}\boldsymbol{\nu} \quad (2.2)$$

$$\mathbf{M}_{RB} = \begin{bmatrix} m & 0 & -y_G m \\ 0 & m & mx_G \\ -my_G & mx_G & I_Z \end{bmatrix} \quad (2.3)$$

$$\mathbf{C}_{RB} = \begin{bmatrix} 0 & 0 & -m(v + rx_G) \\ 0 & 0 & -m(u - ry_G) \\ mx_G r & my_G r & 0 \end{bmatrix} \quad (2.4)$$

where  $\boldsymbol{\tau}_{RB}$  is the array expressing the longitudinal and lateral forces and the moment acting on the vessel,  $\boldsymbol{\nu}$  is the ship speed array in  $\underline{b}$  frame,  $\dot{\boldsymbol{\nu}} = [\dot{u}, \dot{v}, \dot{r}]$  is the ship acceleration array in the  $\underline{b}$  frame,  $m$  is the mass of the ship,  $I_Z$  is the ship inertia, and the point  $G = [x_G, y_G]$  is the centre of gravity.

The forces acting on the vessel  $\boldsymbol{\tau}_{RB}$  can be expressed as the sum of the forces acting on the hull  $\boldsymbol{\tau}_H$ , the ones delivered by the propulsion plant  $\boldsymbol{\tau}_P$ , and the ones due to the surrounding environment  $\boldsymbol{\tau}_{ENV}$  as shown in (2.5).

$$\boldsymbol{\tau}_{RB} = \boldsymbol{\tau}_H + \boldsymbol{\tau}_P + \boldsymbol{\tau}_{ENV} \quad (2.5)$$

## 2.3 Hull Forces

The hull forces and moment are computed with two different approaches: the Oltmann & Sharma model and the MMG-like model.

### 2.3.1 Oltmann & Sharma model

The Oltmann & Sharma model proposed in [92] lets to compute the hydrodynamics forces acting on the vessels as functions of motion variables and hydrodynamics coefficients. This approach for evaluating the hull forces is comparable to the use of Computational Fluid Dynamics (CFD) techniques for control design purposes as shown in [79]. In [92], the total hydrodynamic forces are composed of three main contributions: the Ideal Fluid Force  $\boldsymbol{\tau}_I$ , which is assessed by using the potential theory, i.e. neglecting the effects of viscosity; the Lift Force  $\boldsymbol{\tau}_{HL}$ , which is assessed by comparing the hull with a low aspect ratio wing; and the Cross Flow Drag  $\boldsymbol{\tau}_{HC}$ , it represents the resistance due to the viscous forces generated by a moving body in a real fluid. Besides, hull resistance  $R_T$  is considered a separate term. In (2.6), the formulation of the hull forces according to the selected model is reported.

$$\boldsymbol{\tau}_H = \begin{cases} X_I + X_{HL} - R_T \\ Y_I + Y_{HL} + Y_{HC} \\ N_I + N_{HL} + N_{HC} \end{cases} \quad (2.6)$$

The Ideal Fluid Forces are modelled as in (2.7).

$$\boldsymbol{\tau}_I = \begin{cases} X_{vr}vr + X_{rr}r^2 + X_{vv}v^2 + X_{\dot{u}}\dot{u} \\ X_{\dot{u}}ur + Y_{\dot{v}}\dot{v} + Y_{\dot{r}}\dot{r} \\ N_{\dot{v}}ur + (Y_{\dot{v}} - X_{\dot{u}})uv + N_{\dot{v}}\dot{v} + N_{\dot{r}}\dot{r} \end{cases} \quad (2.7)$$

where  $X_{vr}$ ,  $X_{rr}$ ,  $X_{vv}$ ,  $X_{\dot{u}}$ ,  $Y_{\dot{v}}$ , and  $N_{\dot{v}}$  are parameters depends on the ship shape and identified by suitable experiment or numerical techniques.

The Hull Lifting forces and moment are modelled as in (2.8).

$$\boldsymbol{\tau}_{HL} = \begin{cases} \frac{\rho}{2} L_{PP} T \frac{u(c'kr \frac{L_{PP}}{2} \text{sign}(u) - cv)}{\sqrt{u^2 + (kr \frac{L_{PP}}{2} \text{sign}(u) - v)^2}} \left[ (kr \frac{L_{PP}}{2} \text{sign}(u) - v) - \frac{u^2 (d'kr \frac{L_{PP}}{2} \text{sign}(u) - dv)}{u^2 + (kr \frac{L_{PP}}{2} \text{sign}(u) - v)^2} \right] \\ \frac{\rho}{2} L_{PP} T \frac{u^2 (c'kr \frac{L_{PP}}{2} \text{sign}(u) - cv)}{\sqrt{u^2 + (kr \frac{L_{PP}}{2} \text{sign}(u) - v)^2}} \left[ 1 + \frac{(d'kr \frac{L_{PP}}{2} \text{sign}(u) - dv)(kr \frac{L_{PP}}{2} \text{sign}(u) - v)}{u^2 + (kr \frac{L_{PP}}{2} \text{sign}(u) - v)^2} \right] \\ -\frac{\rho}{2} L_{PP}^2 T \frac{u|u|(e'kr \frac{L_{PP}}{2} \text{sign}(u) - ev)}{\sqrt{u^2 + (kr \frac{L_{PP}}{2} \text{sign}(u) - v)^2}} \left[ 1 + \frac{(d'kr \frac{L_{PP}}{2} \text{sign}(u) - dv)(kr \frac{L_{PP}}{2} \text{sign}(u) - v)}{u^2 + (kr \frac{L_{PP}}{2} \text{sign}(u) - v)^2} \right] \end{cases} \quad (2.8)$$

where  $c'$ ,  $k$ ,  $c$ ,  $d$ ,  $d'$ ,  $e$ , and  $e'$  are parameters related to the ship. They depend on the vessel and are defined in [92] for a tanker and a container ship or in [64] for a tug.

The Cross-Flow drag forces and moment are defined in (2.9).

$$\boldsymbol{\tau}_{HC} = \begin{cases} 0 \\ -\frac{\rho}{2} \int T(x) C_{CFD}(x) (v + rx) |v + rx| dx \\ -\frac{\rho}{2} \int T(x) C_{CFD}(x) (v + rx) |v + rx| x dx \end{cases} \quad (2.9)$$

where  $T(x)$  is the local draft,  $x$  is the coordinate of the local section,  $C_{CFD}(x)$  is the local coefficient of cross-flow drag.

To complete the hull forces definition, the hull resistance coefficient is a curve tailored to the test case and function of the surge speed.

### 2.3.2 MMG-like model

Instead, the MMG-like model is the one defined by the Maneuvering Modeling Group [135] and used in [45] and [34]. The model can be considered a non-linear mass-damper-spring system with constant coefficients. It leads to writing the hull forces and moment array as in (2.10).

$$\boldsymbol{\tau}_H = \mathbf{M}_A \dot{\boldsymbol{\nu}} + \mathbf{C}_A(\boldsymbol{\nu}_R) \boldsymbol{\nu}_R + \mathbf{D}(\boldsymbol{\nu}_R) \boldsymbol{\nu}_R \quad (2.10)$$

where  $\mathbf{M}$  is the total inertia matrix given by the sum of the inertia and added mass matrix,  $\mathbf{C}_{RB}$  is the Coriolis matrix,  $\mathbf{C}_A$  is the hydrodynamics Coriolis and centripetal matrix,  $\mathbf{D}$  is the damping matrix, and  $\boldsymbol{\nu}_R = [u_R, v_R, r]^T$  is the relative speed between the ship and the current.

The inertia matrix  $\mathbf{M}$  is defined as  $\mathbf{M} = \mathbf{M}_{RB} + \mathbf{M}_A$ ; it is the sum of the rigid body mass matrix  $\mathbf{M}_{RB}$  (2.11) and the added mass matrix  $\mathbf{M}_A$  (2.12). The Coriolis matrices instead are the rigid body Coriolis matrix  $\mathbf{C}_{RB}$  (2.13) and the hydrodynamics Coriolis and centripetal matrix  $\mathbf{C}_A$  (2.14). In the end, the damping matrix  $\mathbf{D}$  is defined as  $\mathbf{D} = \mathbf{D}_L + \mathbf{D}_{NL}$ , therefore, as the sum of the linear viscous damping  $\mathbf{D}_L$  (2.15) and of the nonlinear damping  $\mathbf{D}_{NL}(\boldsymbol{\nu}_R)$  (2.16).

$$\mathbf{M}_{RB} = \begin{bmatrix} m & 0 & -my_G \\ 0 & m & mx_G \\ -my_G & mx_G & I_Z \end{bmatrix} \quad (2.11)$$

$$\mathbf{M}_A = \begin{bmatrix} -X_{\dot{u}} & -X_{\dot{v}} & -X_{\dot{r}} \\ -Y_{\dot{u}} & -Y_{\dot{v}} & -Y_{\dot{r}} \\ -N_{\dot{u}} & -N_{\dot{v}} & -N_{\dot{r}} \end{bmatrix} \quad (2.12)$$

$$\mathbf{C}_{RB}(\boldsymbol{\nu}) = \begin{bmatrix} 0 & 0 & -m(v + rx_G) \\ 0 & 0 & m(u - ry_G) \\ m(v + rx_G) & -m(u - ry_G) & 0 \end{bmatrix} \quad (2.13)$$

$$\mathbf{C}_A(\boldsymbol{\nu}_R) = \begin{bmatrix} 0 & 0 & Y_{\dot{u}}u_R + Y_{\dot{v}}v_R + Y_{\dot{r}}r \\ 0 & 0 & -X_{\dot{u}}u_R - X_{\dot{v}}v_R - X_{\dot{r}}r \\ -Y_{\dot{u}}u_R & X_{\dot{u}}u_R + & 0 \\ -Y_{\dot{v}}v_R - Y_{\dot{r}}r & X_{\dot{v}}v_R - X_{\dot{r}}r & 0 \end{bmatrix} \quad (2.14)$$

$$\mathbf{D}_L = \begin{bmatrix} -X_u & -X_v & -X_r \\ -Y_u & -Y_v & -Y_r \\ -N_u & -N_v & -N_r \end{bmatrix} \quad (2.15)$$

$$\mathbf{D}_{NL}(\boldsymbol{\nu}_R) = \begin{bmatrix} -X_{|u|u}|u_R| & 0 & 0 \\ -X_{uuu}u_R & -Y_{|v|v}|v_R| & -Y_{|v|r}|r| \\ 0 & -Y_{v|r}|r| & -Y_{|r|r}|r| \\ & -Y_{vvv}v_R & -N_{|v|r}|v_R| \\ 0 & -N_{|v|v}|v_R| & -N_{|r|r}|r| \\ & -N_{v|r}|r| & -N_{rrr}r \end{bmatrix} \quad (2.16)$$

where the elements of matrix  $M$  are the added mass coefficients and the adopted symbols in all matrices are according to the SNAME [114] notation.

The following simplification can be done on the matrices in the case of the symmetries:

- Fore-aft symmetry:  $y_G = 0$ ,  $Y_{\dot{r}} = N_{\dot{v}}$
- Port-starboard symmetry:  $x_G = 0$ ,  $X_{\dot{v}} = Y_{\dot{u}} = 0$ ,  $X_{\dot{r}} = N_{\dot{u}} = 0$ ,  $X_v = X_r = Y_u = N_u = 0$

## 2.4 Propulsion plant

The propulsion plant of the simulated models can be assumed to be composed of an electric motor, gearbox, shaft-line, and manoeuvring device or actuator, see Figure 2.3. The model can be represented with the physical model presented hereinafter.

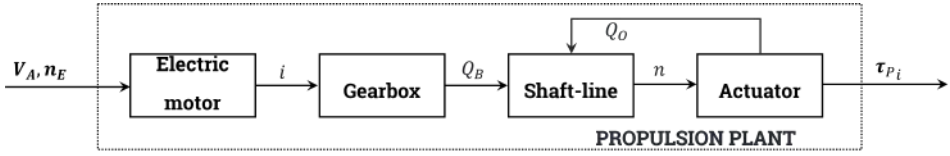


Figure 2.3: Vessel mathematical model - Propulsion Plant layout.

The behaviour of the DC engine is described using the differential equation in (2.17).

$$\frac{di}{dt} = -\frac{R}{L}i - \frac{1}{L}K_e\omega + \frac{1}{L}V_A \quad (2.17)$$

where  $R$  is the resistance,  $L$  is the inductance,  $i$  is the current,  $K_e$  is a constant of the electric engine,  $\omega$  is the shaft angular speed in ( $\frac{rad}{s}$ ), and  $V_A$  is the applied voltage.

The delivered engine torque  $Q_B$ , hence the output of the DC motor model, can be evaluated as in (2.18).

$$Q_B = K_m i \quad (2.18)$$

where  $K_m$  is the mechanical constant related to the construction characteristics of the electric motor and can be approximated equal to the electric constant; for more details, see [129].

The shaft line dynamic can be expressed with the shaft line equation of (2.19).

$$I_T \dot{n} = Q_B - Q_{fric} - \frac{Q_D}{i_{GB}} \quad (2.19)$$

where  $n$  is the motor angular speed in ( $RPS$ );  $i_{GB}$  is the gearbox ratio;  $Q_{fric}$  and  $Q_D$  are the friction and delivered torque, respectively; and  $I_T$  is the total moment of inertia.

The friction torque is described as in (2.20), while the delivered torque is described as in (2.21).

$$Q_{fric} = Q_B(1 - \eta_{TRP}) \quad (2.20)$$

$$Q_D = \frac{Q_O}{\eta_R} \quad (2.21)$$

where  $\eta_{TRP}$  is the transmission efficiency and it is a function of the motor speed, for more details see [78], and  $\eta_R$  is the relative rotative efficiency.

The dynamics of the shaft line can also be expressed with the non-physical model of (2.22).

$$\dot{\omega} = K_\omega(\omega_d - \omega) \quad (2.22)$$

where  $K_\omega$  is a constant representing the total inertia (the inertia of the shaft, electric motor and propeller and its added mass) and the shaft line dynamics, and  $\omega_d$  is the desired motor speed.

The adopted maneuvering device will be explained in the following section.

## 2.5 Manoeuvring device

Several manoeuvring devices are considered in the different test cases, for more details see Section 7. Based on the different propulsion plant schemes, the resulting forces and moment array  $\tau_P$  is the sum of the contribution of each actuator. Not all the manoeuvring devices adopted in the different test cases are modelled at the dynamic level, but some are adopted only the static approaches; hence, only the manoeuvring devices involved in the dynamics approach are modelled in time.

### 2.5.1 Azimuth propeller

The first device taken into consideration is the azimuth thruster. The array of forces and moment given by each thruster  $\tau_{AZ_i}$  is modelled as a function of both the azimuth angle  $\alpha$  and actuated thrust  $T_{AZ}$  according to (2.23).

$$\tau_{AZ_i} = \begin{cases} T_{AZ} \cos \alpha \\ T_{AZ} \sin \alpha \\ x_{AZ} T_{AZ} \sin \alpha - y_{AZ} T_{AZ} \cos \alpha \end{cases} \quad (2.23)$$

The azimuth angle  $\alpha$  can be modelled as in (2.24), i.e. putting a limitation on the maximum speed of the rotation of the azimuthal thruster  $\dot{\alpha}_{max}$ , or with the sigmoid function in (2.25) adopted in [96].

$$\dot{\alpha} \leq \dot{\alpha}_{max} \quad (2.24)$$

$$\dot{\alpha} = K_\alpha \frac{\alpha_d - \alpha}{\sqrt{(\alpha_d - \alpha)^2 + \epsilon^2}} \quad (2.25)$$

where  $\dot{\alpha}$  is the azimuth angle speed,  $\alpha_d$  is the desired azimuth angle,  $K_\alpha$  is a constant representing the rotational speed, and  $\epsilon$  is a tuning parameter to adjust the azimuth behaviour.

The thrust  $T_{AZ}$  is modelled with the open water diagram [25] as a function of the propeller revolution regime  $n_P$  found according to section 2.4. Another opportunity is considering an experimental combinator curve between  $T_{AZ}$  and  $n_P$ .

The propeller is described with a four quadrants model to takes into account all combination of the direction of the propeller and the inflow that can occur. The model provides the adimensional thrust and torque coefficients  $C_T$  (2.26) and  $C_Q$  (2.27) as function of the hydrodynamic pitch angle  $\beta_P$  (2.28). It defines the angle of the incoming velocity  $V_r$  (2.29). The coefficients behaviour of the Kaplan 19A ducted propeller [66] is shown in Figure 2.4.

$$C_T = \frac{T}{1/8\pi D^2 V_r^2 \rho} \quad (2.26)$$

$$C_Q = \frac{Q}{1/8\pi D^3 V_r^2 \rho} \quad (2.27)$$

$$\beta_P = \frac{V_a}{0.7\pi n_P D} \quad (2.28)$$

$$V_r = \sqrt{V_a^2 + (0.7\pi n_P D)^2} \quad (2.29)$$

where  $D$  is the propeller diameter.

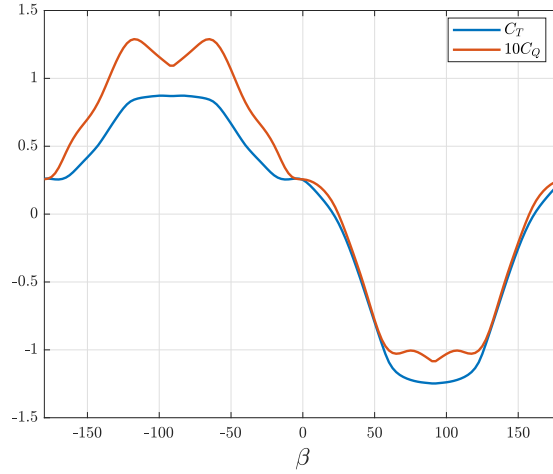


Figure 2.4: Vessel mathematical model - Propeller 4 quadrants coefficients.

## 2.5.2 Transversal Thruster

The transversal thrusters are used to improve manoeuvrability at low speeds. Thrusters can be installed at the stern and the bow. Only the bow thrusters are considered in the dynamic model in this thesis.

The bow thruster can be approximated as a ducted propeller with the addition of correction coefficients. Through this approximation, it is possible to evaluate the thrust delivered and the torque required through the Wageningen Ka series [66]. However, the adoption of transversal thrusters leads to the following hydrodynamics effects according to [14] that affect their performance: increasing of the ship resistance; the adjacent flow on each of the hull sides of the ship; different fields of pressure around the entrance and exit of the tunnel. All these effects decrease the thruster performance. An effectiveness coefficient is defined in [100] depending on the vessel speed, this coefficient takes into account the thrust loss due to the surge movement, the effective speed  $(v + rx)$  acting on the thruster, and the thrust loss due to the nozzle. Thanks to this, correcting the  $K_T$  coefficients deriving from the Wageningen diagram and finding the thrust  $T_{BT}$  is possible. The resulting forces and moment array  $\tau_{BT}$  can be defined as in (2.30).

$$\tau_{BT} = \begin{cases} 0 \\ T_{BT} \\ x_{BT}T_{BT} \end{cases} \quad (2.30)$$

where  $x_{BT}$  is the position of the bow thruster in the  $\underline{b}$  frame.

The propeller is described with the adimensional thrust and torque coefficients  $K_T$  (2.31) and  $K_Q$  (2.32) that are function of the advance coefficient  $J$  (2.33). The coefficients behaviour is shown in Figure 2.5.

$$K_T = \frac{T}{\pi n_p^2 D^2} \quad (2.31)$$

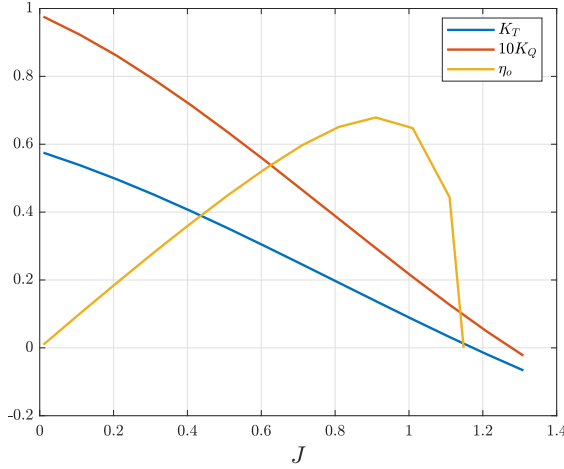


Figure 2.5: Vessel mathematical model - Propeller coefficients.

$$K_Q = \frac{Q}{\pi n_P^2 D^3} \quad (2.32)$$

$$J = \frac{v + rx}{n_P D} \quad (2.33)$$

## 2.6 Environmental forces

The environmental disturbances affect the performance of the surface vessel; hence wind, wave, and current disturbances are modelled and considered. Each disturbance leads to forces and moment array that can be summed since overlapping the effects can be considered a good approximation for marine application, leading to the array  $\boldsymbol{\tau}_{ENV}$ . Parametric functions are formulated to compute the environmental disturbance acting on a vessel like the DNV formulation [32], the Blenderman model for wind forces and moment [18], the OCIMF model for wind and current effects, cross-flow drag components for estimating the current [92] and [42], etc.

### 2.6.1 Wind

Wind is an environmental disturbances affecting the vessels. It is due to large-scale pressure variations affecting the Earth surface in its atmospheric boundary layer; in this area, the wind is affected by the friction force due to the roughness of the surface, resulting in a reduction in speed and a tapered speed profile, see [29] and [42] for more details. The wind disturbance, in this thesis, is defined through the wind speed  $V_{WIND}$  and the angle of attack  $\gamma_{WIND}$  as shown in Figure 2.6.

Different methods can be used to estimate the forces and moment vector due to the wind loads, like the parametric formulation of [32] or the model adopted by Blendermann [18]. Both models are adopted in this thesis and generally, these formulations lead to computing the loads as done in (2.34), as a function of the lateral and longitudinal projected areas ( $A_F$  and  $A_L$ ), of the wind speed  $V_{WIND}$ , of the angle of attack  $\gamma_{WIND}$ , and of the form coefficients  $C_{X_{AF}}$ ,  $C_Y$ , and  $C_N$ . These



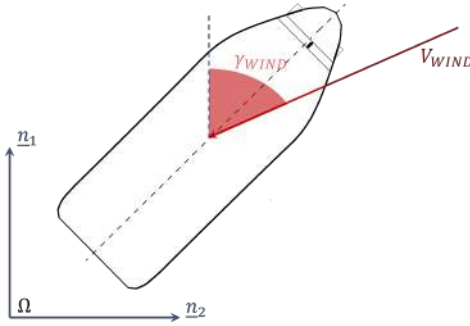


Figure 2.6: Vessel mathematical model - Environmental - Wind.

coefficients can be derived from regression based on wind tunnel tests like the one in [18] or [32], wind tunnel tests, or numerical methods. The average wind speed is considered in these formulations together with gust effects in the longitudinal components formulated with the simplified model in [35] of Davenport Spectrum of Horizontal Gustiness [29].

$$\tau_{WIND} = \frac{1}{2} \rho_{air} V_{rw}^2 \begin{bmatrix} C_{XAF}(\gamma_{WIND}) A_F \\ C_Y(\gamma_{WIND}) A_L \\ C_N(\gamma_{WIND}) A_L L_{OA} \end{bmatrix} \quad (2.34)$$

where  $L_{OA}$  is the overall length and  $\rho_{air}$  is the air density.

### 2.6.2 Current

Several effects influence the current disturbaner like gravity, wind friction, changes in salinity, variations in water density, the coast and landscape shape. This thesis considers a constant current with irrational motion and negligible acceleration. The current disturbance is defined as a function of the incoming direction  $\gamma_{CURR}$  and its intensity in terms of speed  $V_{CURR}$  according to [32] and to the sketch of Figure 2.7.

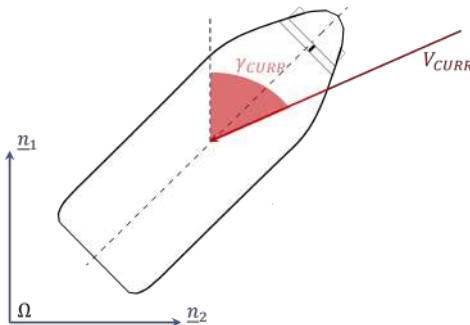


Figure 2.7: Vessel mathematical model - Environmental - Current.

The relative speed and coming direction are computed and used to estimate the additional loads on the ship. The current loads are also computed in this case with two methods: the first one is the adoption of the parametric model defined by [32] for application at zero speed, this method leads to a formulation like the one in (2.35); while the second one is the introduction of the relative speed components  $\nu_R$  in the hull forces computation; hence the Oltmann model of Section 2.3.1 is computed on the relative speed  $\nu_R$  components as the MMG-like model introduces the relative speed  $\nu_R$  as stated in Section 2.3.2.

$$\tau_{CURR} = \frac{1}{2}\rho V_{CURR}^2 \begin{bmatrix} BT(-0.07\cos(\gamma_{CURR})) \\ A_{L_{sub}}0.6\sin(\gamma_{CURR}) \\ A_{L_{sub}}0.6\sin(\gamma_{CURR})(x_{L_{sub}} + \max(\min(0.4(1 - \frac{2\gamma_{CURR}}{\pi}), 0.25), -0.2)L_{PP}) \end{bmatrix} \quad (2.35)$$

where  $A_{L_{sub}}$  is the submerged lateral area and  $x_{L_{sub}}$  is its center.

### 2.6.3 Wave

The wave loads are considered only in some of the test cases adopted in this thesis, while in others, they are neglected given their main dimensions, and the use is reduced to protected seas where the wave effect is neglectable. The wave disturbance is defined according to the peak wave period  $T_P$ , the zero-crossing period  $T_z$ , the main height  $H_S$ , and the coming direction  $\beta_{WAVE}$ , as shown in Figure 2.8. The relationship in (2.36) are adopted to correlate the different periods. The parametric model of [32] is adopted leading to the formulation in (2.37).

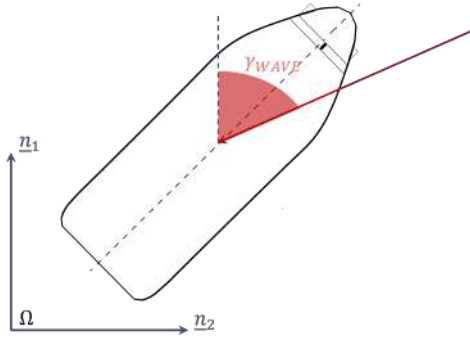


Figure 2.8: Vessel mathematical model - Environmental - Wave.

$$T_P = 1.4049T_Z \quad (2.36)$$

$$\tau_{WAVE} = \frac{1}{2}\rho g H_S^2 \begin{bmatrix} Bh(\gamma_{WAVE}, C_{WL_{aft}}, bow_{angle})f(T_z) \\ L_{OS}(0.09\sin(\gamma_{WAVE})f(T_z) \\ L_{OS}(0.09\sin(\gamma_{WAVE})f(T_z)(x_{L_{OS}} + (0.05 - 0.14\gamma_{WAVE}/\pi) * L_{OS})) \end{bmatrix} \quad (2.37)$$

where  $h$  and  $f$  are two function depending on the listed variable, for more details see [32];  $C_{WL_{aft}}$  is the water plane area coefficient of the water plane area behind midship;  $bow_{angle}$  is the angle between  $b_1$  and a line drawn from the foremost point in the water line to the point at  $B/4$  on the water line;  $L_{OS}$  is the longitudinal distance between the fore most and aft most point under water; and  $x_{L_{OS}}$  is its half point.

#### 2.6.4 Disturbances cross relationships

The environmental disturbances magnitude can be considered all linked since they influence each other. In this thesis the main relationship given by the Beaufort scale, the scatter diagram, and the Pierson relationship are taken into account.

The Beaufort scale born in the XIX century as a classification of wind forces at sea by commander Francis Beaufort. He identified 13 states of wind force on his vessel and ranked them 0 to 12. The scale, however, made no reference to the speed of the wind, and various attempts, particularly during the 20th century, have been made to correlate the two. In 1921 Simpson formulate the relationship between the wind speed and the Beaufort number, which were accepted in 1926 by the International Meteorological Committee. Later also the wave probable condition are added. In Table 2.1 the Beaufort scale defined in [132] is reported. The last two columns derive from the DNV standard [32], and the peak wave period is defined according to worldwide scatter diagram. A graphical representation of the Beaufort scale is in Figure 2.9.

Scatter diagram are used to define the environmental conditions of a specific geographic area. Thanks to these diagrams, for each incoming direction, it is possible to know all the combinations of significant wave height,  $H_{1/3}$ , and zero-crossing period,  $T_z$ , for the selected area, together with the percentage of occurrence. Several database contains this information, one is the BMT database [3] based on 130 years of observation. In this thesis, the BTM database is used since it left open access to the 25 geographical area, but the approach could be applicable with other database or areas. The data are available for incoming direction  $\gamma_i$  from  $0^\circ$  to  $360^\circ$  with step  $45^\circ$ , and the percentage of occurrence of each direction  $p_{\gamma_i}$  is available. An example of the data is shown in figures 2.10 and 2.11. Along the horizontal axis is reported the zero-crossing wave period, while the wave height is reported on the vertical axis, and the colour scale represents the percentage of occurrence of the couple  $H_{1/3}$ -  $T_z$ . Due to visualisation reasons, the vertical axis is cut, but the standard scatter diagram is extended for a wave height range up to values larger than  $14.5m$ .

In the end, Pierson lead several study trying to correlate the wind and wave disturbances. One of the output relationship is reported in [98] and leads to define a wind-wave correlation thanks to the relationship in (2.38).

$$H_{1/3} = 0.0214V_{WIND}^2 \quad (2.38)$$

Beaufort n	$V_w(\frac{m}{s})$	Description	$H_S(m)$	$T_P(s)$	$V_{CURR}(\frac{m}{s})$
0	0	Calm	0	-	0
1	1.5	Light air	0.1	3.5	0.25
2	3.4	Light breeze	0.4	4.5	0.5
3	5.4	Gentle breeze	0.8	5.5	0.75
4	7.9	Moderate breeze	1.3	6.5	0.75
5	10.7	Fresh breeze	2.1	7.5	0.75
6	13.7	Strong breeze	3.1	8.5	0.75
7	17.1	Moderate gale	4.2	9	0.75
8	20.7	Gale	5.7	10	0.75
9	24.4	Strong gale	7.4	10.5	0.75
10	28.4	Storm	9.5	11.5	0.75
11	32.6	Violent storm	12.1	12	0.75
12	>33	Hurricane force	-	-	-

Table 2.1: Vessel mathematical model - Environmental - Beaufort wind scale.

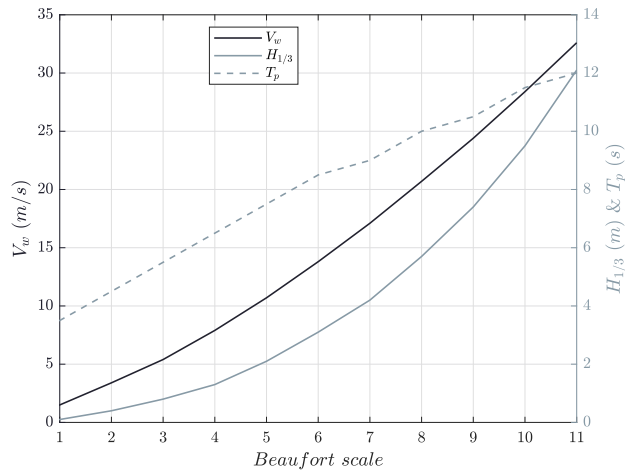


Figure 2.9: Vessel mathematical model - Environmental - Beaufort Wave-Wind relationship.

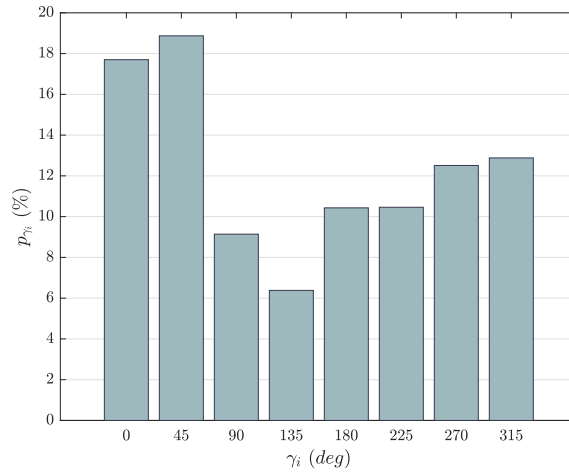


Figure 2.10: Vessel mathematical model - Environmental -  $p_{\gamma_i}$ .

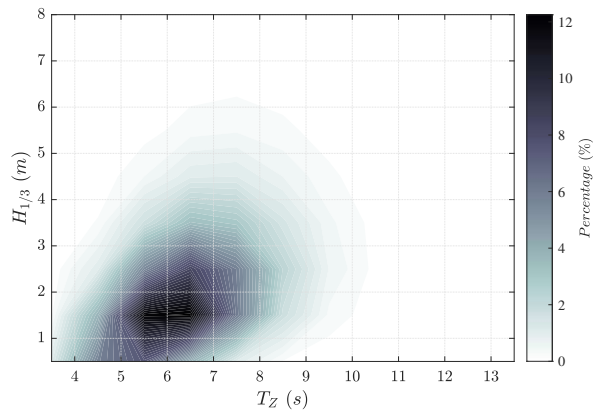


Figure 2.11: Vessel mathematical model - Environmental - Scatter diagram.



# Chapter 3

## Guidance

The Guidance system continuously processes the reference position, vessel velocity, and acceleration with the data collected from the Navigation system and other information to compute the path and the desired state to satisfy it.

In this thesis, the following guidance methods are developed for controlling both the three or two degrees of freedom scenarios:

- the target tracking motion control scenario of Section 3.1 is taken into account for the 2-DOF scenario, the outputs are the desired speed and heading to satisfy the tracking objective;
- the track keeping of Section 3.2 is taken into account for the 3-DOF scenario, the outputs are the desired velocity and pose array;
- the reference models of Section 3.3 are considered in the 3-DOF scenario for smoothly giving the desired setpoints.

### 3.1 Target Tracking

Target tracking is one of the most investigated motion control scenarios in the marine field since it allows several applications, from research to navy purposes. It regards following a target of which only the instantaneous position and velocity are known; hence, the motion evolution is unknown [21]. The target tracking motion control scenario is commonly adopted when information about the path is unknown in advance, and there is no fixed trajectory to track; otherwise, whenever the aim is tracking moving objects. The motion control scenario can be divided into two phases: the first one regards the approach phase, where the interceptor needs to reach the target, while the second one is the following phase, where the interceptor has reached the target and is required to follow it. The necessary condition to fulfil the mission goal is that the chasing vessel full speed is greater than the chased one. Fossen et al. in [45] and [20], propose three different guidance laws to satisfy the target tracking scenario: *(i)* the Line-Of-Sight (LOS) guidance, which tends to minimise the difference between the real trajectory and the desired path; *(ii)* the Pure Pursuit (PP) guidance, which points directly to the target; *(iii)* the Constant Bearing (CB) guidance, which tends to converge to a path parallel to the target one. Such laws belong to missile guidance studies. An overview of the guidance algorithms developed for missile purposes is shown in [22] and [110].

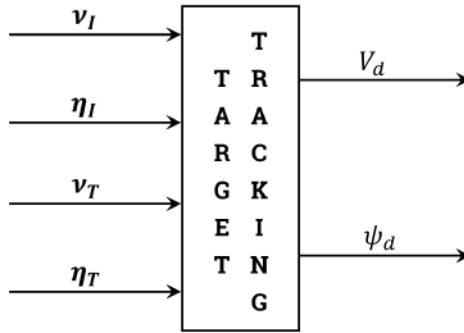


Figure 3.1: Guidance - Target Tracking - Layout.

The proposed guidance laws are slightly modified with respect to the literature to make them suitable for parametric analysis. Indeed, the aim is to assess all the parameters present inside the algorithms in the preliminary design phase since they strongly affect the overall performance of the guidance system. The proper parameter set selection is constrained by the system stability and required performance, widely discussed in the open literature.

The general inputs are the trajectory and the velocity vectors of both the target and interceptor. At the same time, the outcomes necessary at the control system are the desired speed  $V_d$  and heading  $\psi_d$  as shown in Figure 3.1.

### 3.1.1 Line Of Sight

The Line-Of-Sight (LOS) guidance minimises the difference between the real and desired trajectory. It is classified as a three-point guidance scheme since it involves a stationary reference point  $\Omega_R$  in addition to both the interceptor  $\Omega_I$  and the target  $\Omega_T$  positions, as shown in Figure 3.2. In this guidance law, the interceptor is forced to move along the vector between the reference point and the target, named the LOS vector, to achieve the desired path. In the Line-Of-Sight guidance, the interceptor can be guided to follow the target in a straight line, as in [10] and in this application, instead of curved trajectories path, as in [68].

Since the desired path depends instantaneously on the target kinematics, it is impossible to plan a series of static waypoints; hence, the reference point cannot be taken as the previous waypoints as doing in a traditional Line-Of-Sight guidance [10]. To the author's best knowledge, in literature, the choice of the reference point is not assessed; hence, the following approach is proposed. The candidate reference point is selected as a previous point of the target path, and it is updated over a user-defined time interval ( $\bar{\delta}t$  parameter). The reference point is updated whenever the interceptor has overtaken the new candidate reference point. The main idea is to consider the target trajectory curvature to evaluate a proper  $\bar{\delta}t$ . In this way, the reference point update frequency increases with the interceptor trajectory deviation from the straight path. Indeed, as the curvature crosses a fixed threshold,  $c_{limit}$ , a smaller time interval,  $\bar{\delta}t_{hc}$ , is needed to guarantee that the interceptor maintains its position as close to the target as possible. On the other hand, when the curvature is smaller, the updating procedure is relaxed with a more extended  $\bar{\delta}t_c$ . The curvature of the target trajectory is evaluated by using



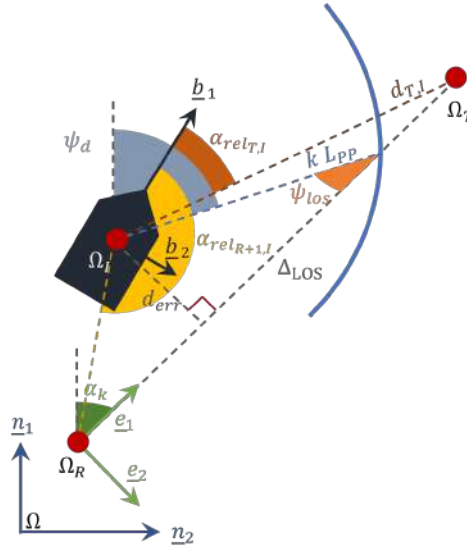


Figure 3.2: Guidance - Target Tracking - Geometrical Sketch of the LOS Guidance.

(3.1), and the  $\bar{\delta}t$  is selected according to (3.2). Hence, a new reference point on the target trajectory must be chosen at each  $\bar{\delta}t$  to keep the target at the desired distance from the interceptor. The projection of the distance between the target and the interceptor on  $\underline{e}_1$  is computed by  $(\Omega_I - \Omega_T) \cdot \underline{e}_1$ . The proposed reference point  $\Omega_{R+1} = (x_{R+1}, y_{R+1})$  is defined and it is required to check whether the interceptor has overstepped the proposed reference point. Then, the relative bearing angle between the interceptor and the proposed reference point is evaluated (3.3). If the relative bearing angle belongs to the interval  $\alpha_{rel_{R+1,I}} \in [\frac{\pi}{2}, \frac{3\pi}{2}]$ , the proposed reference point will be accepted.

$$c = \frac{1}{\rho} = \frac{|\dot{x}_T \ddot{y}_T - \dot{y}_T \ddot{x}_T|}{\sqrt{\dot{x}_T^2 + \dot{y}_T^2}} \quad (3.1)$$

$$\bar{\delta}t = \begin{cases} \bar{\delta}t_{hc}, & c > c_{limit} \\ \bar{\delta}t_{lc}, & 0 \leq c \leq c_{limit} \end{cases} \quad (3.2)$$

$$\alpha_{rel_{R+1,I}} = \arctan \frac{y_{R+1} - y_I}{x_{R+1} - x_I} - \psi \quad (3.3)$$

where  $\dot{\eta}_T = \dot{x}_T \underline{n}_1 + \dot{y}_T \underline{n}_2$  is the first derivative of the target position, and  $\ddot{\eta}_T = \ddot{x}_T \underline{n}_1 + \ddot{y}_T \underline{n}_2$  is the second derivative.

According to [10], it is possible to define the desired heading  $\psi_d \in [0, 2\pi]$  that allows the vessel to regain track, as reported by equations (3.4)-(3.8). The method is based on nullifying the lateral error,  $d_{err}$ , between the desired path and the trajectory within a circle of radius  $kL_{PP}$ . Hence, the equations in (3.4)-(3.8) are based on the idea of finding the intersection point between the circle of radius  $kL_{PP}$  around the interceptor and the line joining the reference point and the interceptor one, according to the geometrical sketch in Figure 3.2.

$$\psi_d = \alpha_k - \psi_{los} \quad (3.4)$$

$$\alpha_k = \arctan \frac{y_T - y_R}{x_T - x_R} \quad (3.5)$$

$$\psi_{los} = \arctan \frac{d_{err}}{\Delta_{LOS}} \quad (3.6)$$

$$d_{err} = (\boldsymbol{\Omega}_I - \boldsymbol{\Omega}_R) \cdot \underline{e}_2 \quad (3.7)$$

$$\Delta_{LOS} = \begin{cases} \sqrt{(kL_{PP})^2 - d_{err}^2}, & kL_{PP} \geq d_{err} \\ (\boldsymbol{\Omega}_T - \boldsymbol{\Omega}_I) \cdot \underline{e}_1, & kL_{PP} < d_{err} \end{cases} \quad (3.8)$$

where  $\psi_{los}$  is the angle between  $\underline{e}_1$  and the radius  $kL_{PP}$ , while  $\Delta_{LOS}$  is the projected distance of the target from the intercept point along  $\underline{e}_1$ .

Once the desired heading angle is defined, the desired velocity must be carried out. Based on the similar considerations above, the desired velocity depends on the distance  $d_{T,I}$  from the target, i.e., a law is implemented to guarantee that the required velocity increases as the target moves away. Moreover, it tends to the target velocity as the interceptor converges to the desired distance. In literature, the Line-Of-Sight law typically provides an algorithm to determine the desired angle but does not define a velocity law. For such a reason, in this application, the speed law is implemented with a ramp, following equation (3.9) and Figure 3.3, where the desired speed  $V_d$  is defined through the couple  $(n_{LOS}L_{pp}, V_T)$ . Indeed, as distance increases, then  $V_d$  smoothly increases, through the slope  $p$ , up to the interceptor maximum speed,  $V_{I_{max}}$ . Once the point and the slope are defined, for each time, it is possible to find the distance  $d^*$  at which the speed is set as the maximum value. The speed law is implemented as a function of the relative bearing angle (3.10) between them,  $\alpha_{rel_{T,I}}$ , to take into account the situation where the interceptor overtakes the target. In this condition, the algorithm requires the interceptor to slow down and wait until the target takes back the forward quadrants (3.11). On the other hand, the backward quadrant is identified through boundary tolerance (e.g.  $\frac{\pi}{18}$ ) to avoid critical behaviour when ships are alongside each other.

$$V_d = \begin{cases} \frac{V_T}{2}, & d_{T,I} < -d^* \\ V_T(1 + \frac{d_{T,I}}{2d^*}), & -d^* \leq d_{T,I} \leq 0 \\ V_T, & 0 < d_{T,I} < n_{LOS}L_{PP} \\ V_T + p(d_{T,I} - n_{LOS}L_{PP}), & n_{LOS}L_{PP} \leq d_{T,I} \leq d^* \\ V_{max}, & d_{T,I} > d^* \end{cases} \quad (3.9)$$

$$\alpha_{rel_{T,I}} = \arctan \frac{y_T - y_I}{x_T - x_I} - \psi \quad (3.10)$$

$$d_{T,I} = \begin{cases} -(\boldsymbol{\Omega}_T - \boldsymbol{\Omega}_I) \cdot \underline{h}_1, & \frac{5\pi}{9} \leq \alpha_{rel_{T,I}} \leq \frac{13\pi}{9} \\ (\boldsymbol{\Omega}_T - \boldsymbol{\Omega}_I) \cdot \underline{h}_1, & \alpha_{rel_{T,I}} < \frac{5\pi}{9} \vee \alpha_{rel_{T,I}} > \frac{13\pi}{9} \end{cases} \quad (3.11)$$

where  $V_T$  and  $V_{max}$  are the target and the maximum speeds admitted by the vessel, respectively.

The law in (3.9) means that since the interceptor is ahead of the target and the distance is lower than  $n_{LOS}L_{PP}$ , the speed setpoint coincides with the target speed. On the other hand, when the distance is larger than  $n_{LOS}L_{PP}$ , speed increases with a ramp with a slope equal to  $p$  until it reaches its maximum speed. Knowing the instantaneous target speed allows us to assess the maximum speed value to reach the target as fast as possible. Moreover, when the interceptor overtakes the target,

the bearing angle is in either the second or third quadrant. Then, the distance projection is negative and the speed decreases with a smooth slope until it reaches half of the target one at a distance equal to  $-d^*$ .

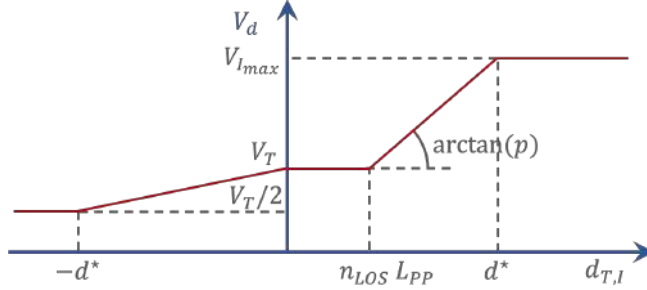


Figure 3.3: Guidance - Target Tracking - Speed law for LOS Guidance.

In summary, the parameters of the proposed Line-Of-Sight guidance are six:  $n_{LOS}$ ,  $p$ ,  $k$ ,  $\bar{\delta}t_{hc}$ ,  $\bar{\delta}t_{lc}$ , and  $c_{limit}$ .

### 3.1.2 Pure Pursuit

The Pure Pursuit (PP) guidance points directly to the target, as shown in Figure 3.4. Hence, this guidance law tends to reach the target as soon as possible without focusing on forcing the movement along the covered target trajectory or following the target with a given lateral offset. This guidance is classified as a two-point guidance scheme; indeed, only the interceptor and the target are considered in the engagement geometry. The control variable is the drift angle  $\beta$  defined as the angle between  $\underline{b}_1$  and  $\underline{a}_1$  as shown in Figure 3.4, and the proposed law aims to nullify it. In this application, the angle  $\psi_d \in [0, 2\pi]$  coincides with the angle  $\theta$  shown in Figure 2.2.

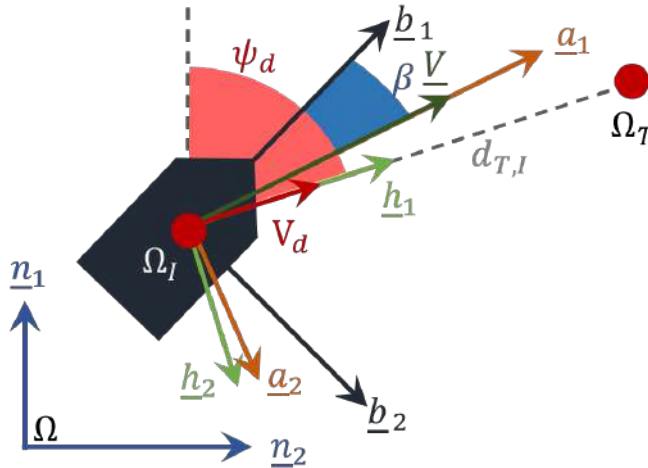


Figure 3.4: Guidance - Target Tracking - Geometrical Sketch of the PP Guidance.

The Pure Pursuit guidance law is based on the main idea of suiting the speed setpoint with respect to the distance between the objects. Indeed, the speed will be higher as the distance between the ships increases. As it can be seen in (3.12)-(3.14), the distance is normalised through its modulus plus a positive quantity  $\xi_{PP}^2$  and it is proportional to a coefficient  $K_{PP}$ . Such parameters must be computed to guarantee algorithm convergence and allow the required speed to avoid the interceptor overtaking the target.

$$V_d = K_{PP} \frac{d_{T,I}}{\sqrt{d_{T,I}^2 + \xi_{PP}^2}} \quad (3.12)$$

$$d_{T,I} = (\mathbf{\Omega}_T - \mathbf{\Omega}_I) \cdot \mathbf{h}_1 \quad (3.13)$$

$$K_{PP} = V_{I_{max}} \quad (3.14)$$

where  $K_{PP}$  is a speed gain and it is equal to the maximum allowable speed  $V_{I_{max}}$ ,  $d_{T,I}$  is the distance between the target and the interceptor, and  $\xi_{PP}$  is a parameter that affects the chasing phase and the distance at which is possible to have a stable following phase.

This thesis proposes an adaptive relationship that allows tailoring the parameter to the desired distance (user-defined) from the target. By substituting in (3.12) such desired distance  $d_D$  and the measured target speed  $V_T$  during the previous time step, it is possible to evaluate  $\xi_{PP}$  as shown in (3.15).

$$V_T = K_{PP} \frac{d_D}{\sqrt{d_D^2 + \xi_{PP}^2}} \implies \xi_{PP} = d_D \sqrt{\frac{K_{PP}^2}{V_T^2} - 1} \quad (3.15)$$

While the heading law is taken from the geometrical sketch and shown in (3.16).

$$\psi_d = \arctan \frac{y_T - y_I}{x_T - x_I} \quad (3.16)$$

In summary, the input parameters of the Pure Pursuit guidance law are  $d_D$  and  $K_{PP}$ .

### 3.1.3 Constant Bearing

The Constant Bearing (CB) guidance law is based on parallel navigation. Indeed, the interceptor is required to keep a path parallel to the target one and the required distance vector is a user-defined input. Distance vector components can be chosen with all possible combinations. Constant Bearing, like the Pure Pursuit, is a two-point guidance scheme that only requires the target and interceptor positions and velocities. In the CB law, the interceptor corrects the path as long as the distance between the target and the interceptor exceeds the desired one. In this case, the relative interceptor-target velocity is the key control variable, and it is on the vector between the target and the interceptor, named the LOS vector. Hence, in the following part, the interceptor perceives the target at a constant bearing and a constant distance; this means that the LOS vector drifts without rotating at each instant. For this reason, the Constant Bearing guidance is often referred to as parallel navigation, as known in the missile guidance, and shown in [110]. The guidance geometrical scheme is shown in Figure 3.5.

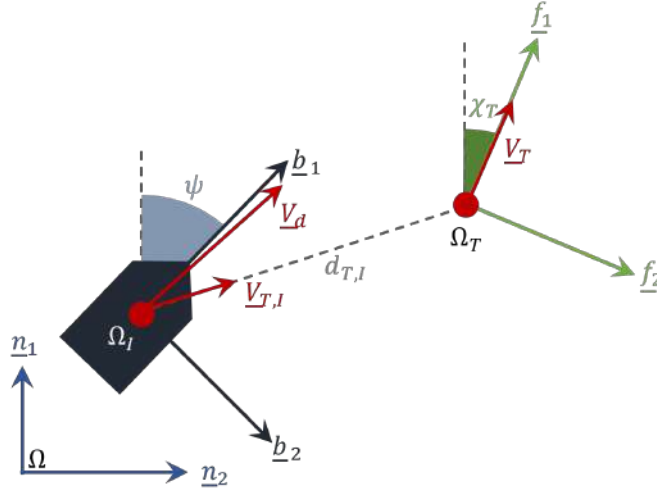


Figure 3.5: Guidance - Target Tracking - Geometrical Sketch of the CB Guidance.

A possible strategy to implement the missile parallel navigation is according to [21]. In this thesis, the heading and speed law is developed to give as input the desired lateral  $e_{des}$  and longitudinal  $s_{des}$  offsets on  $f_2$  and  $f_1$  directions respectively, as shown in Figure 3.6. Introducing the desired distance is the main difference concerning the missile guidance, where the objective is to catch the target by nullifying the distance. The signs of the desired lengths are taken according to the  $f$  basis, in other words, a positive  $e_{des}$  means that the desired position of the interceptor is on starboard, a negative  $e_{des}$  means that the desired position is on portside; a positive  $s_{des}$  means that the desired position is ahead of the target, and a negative  $s_{des}$  means that the desired position is astern the target. Hence, it is possible to define the speed law as the module of the velocity thanks to Equation (3.17)-(3.19).

$$\begin{aligned} \underline{V}_d &= \underline{V}_T + \underline{V}_{T,I} \\ &= \underline{V}_T + K_{CB} \frac{\underline{d}_{T,I}}{\sqrt{\underline{d}_{T,I}^2 + \xi_{CB}^2}} \end{aligned} \quad (3.17)$$

$$\underline{d}_{T,I} = (x_T - x_I)\underline{n}_1 + (y_T - y_I)\underline{n}_2 + e_{des}\underline{f}_2 + s_{des}\underline{f}_1 \quad (3.18)$$

$$K_{CB} = V_{I_{max}} - V_T^* \quad (3.19)$$

where  $\underline{V}_T$  is the target velocity;  $\underline{V}_{T,I}$  is the velocity aligned with the LOS vector, as described in the previous paragraph;  $\underline{d}_{T,I}$  is the vector between the interceptor and the target;  $K_{CB}$  is a speed gain and is set equal to the maximum speed minus the maximum target speed in a previous time interval ( $V_T^*$ ); and  $\xi_{CB}$  is the main parameter that affects the chasing phase.

This law computes the velocity commands needed to track the target: in addition to the target velocity  $\underline{V}_T$ , which nullifies the relative velocity between the interceptor and the target, also an approach velocity  $\underline{V}_{T,I}$  is assigned along the LOS vector to reach the desired distances with a smooth behaviour thanks to the  $\xi_{CB}$  parameter. From the laws in (3.17), it is possible to note that when the interceptor reaches the desired distances from the target, the approach velocity  $\underline{V}_{T,I}$  is



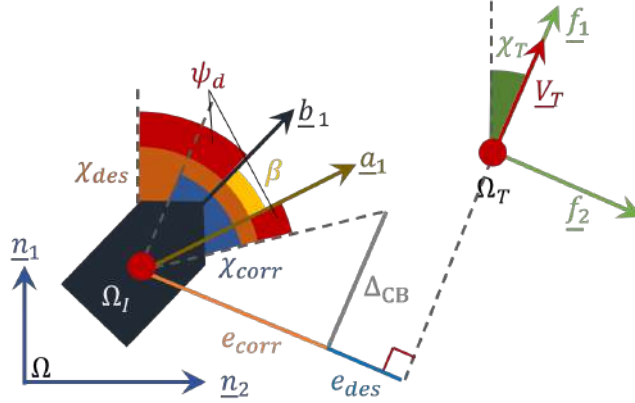


Figure 3.7: Guidance - Target Tracking - Constant Bearing heading law.

## 3.2 Track keeping

The track keeping guidance scenario regards following a path at low speed controlling 3-DOF. The inputs of the scenario are the waypoints list  $WP_{list}$  together with the pose feedback  $\eta$ , while the outputs are the time history of the trajectory  $\eta_{TR}$  and the relative desire velocity  $\nu_{TR}$ , as shown in Figure 3.8.

At each time step two waypoints are selected ( $\Omega_{WP_1}$  and  $\Omega_{WP_2}$ ) from the waypoint list given as input and the  $\underline{d}$  reference frame is defined leading to the draft in Figure 3.9. As described in Section 2.1, it has the origin on  $\Omega_{WP_1}$  and points to  $\Omega_{WP_2}$  outlining the angle  $\xi$  between the positive unit vector  $\underline{n}_1$  of the inertial frame and  $\underline{d}_1$ . The angle  $\xi$  is computed as in (3.27).

$$\xi = \text{atan2}(y_{WP_2} - y_{WP_1}, x_{WP_2} - x_{WP_1}) \quad (3.27)$$

The switch at the following waypoints couple occurs when the along-track distance respect to  $\Omega_{WP_2}$ ,  $d_{sw}$ , is lower than a given distance  $nL_{PP}$  according to (3.28).

$$d_{sw} = (\Omega_{WP_2} - \eta)\underline{d}_1 < nL_{PP} \quad (3.28)$$

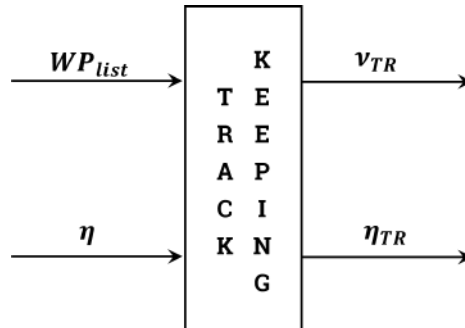


Figure 3.8: Guidance - Track Keeping - Layout.

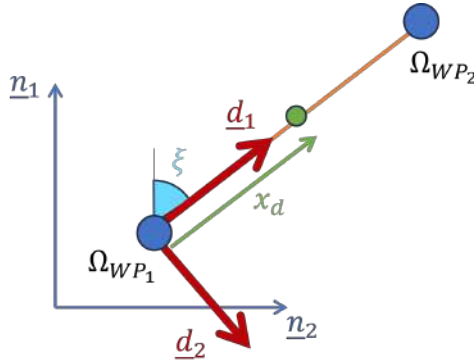


Figure 3.9: Guidance - Track Keeping - Reference frame.



Figure 3.10: Guidance - Track Keeping - Trapezium speed law.

The speed law is defined according to the trapezium speed law in Figure 3.10. As it is possible to see from the figure, the speed law is composed of four phases: the first phase starts at  $t_0$  when switching to the next waypoint and has an acceleration from the chosen minimum speed  $V_{min}$  to the chosen maximum value  $V_{max}$ , and ending at  $t_1$ ; the second phase keeps  $V_{max}$  constant up to time  $t_2$ ; the third phase has a deceleration up to  $t_3$  when it reaches  $V_{min}$ ; and the fourth phase when it reaches  $\Omega_{WP_2}$  with the minimum speed. The time steps are defined in (3.29).

$$\begin{aligned}
 t_1 &= t_0 + \frac{2d_{TK}^*}{V_{max} + V_{min}} \\
 t_2 &= t_1 + \frac{d_{WP} - 2d_{TK}^* - nL_{pp}}{V_{max}} \\
 t_3 &= t_2 + \frac{2d_{TK}^*}{V_{max} + V_{min}}
 \end{aligned} \tag{3.29}$$

where  $d_{WP} = \sqrt{(y_{WP_2} - y_{WP_1})^2 + (x_{WP_2} - x_{WP_1})^2}$  is the distance between the selected waypoints and  $d_{TK}^*$  is the distance in which the acceleration phase is designed.

The inputs of the trapezium speed law are three of the following:  $V_{max}$ ,  $V_{min}$ ,  $d_{TK}^*$ , and  $a_{set}$ . The relationship in (3.30) exists between the four variables.

$$a_{set} = \frac{V_{max}^2 - V_{min}^2}{2d_{TK}^*} \tag{3.30}$$



The desired speed array trajectory is:

$$\boldsymbol{\nu}_{TR} = [V \ 0 \ 0]^T \quad (3.31)$$

The desired instantaneous position  $x_d$  along  $\underline{f}_1$  is defined following the kinematics outlined by the speed (3.32) and then rotated in the  $\underline{n}$  frame to have the desired position trajectory  $\boldsymbol{\eta}_D^*$  (3.33). It is the green point in Figure 3.8.

$$x_d = \begin{cases} \frac{1}{2}a_{set}(t-t_0)^2 + V_{min}(t-t_0), & \text{if phase 1} \\ V_{max}(t-t_1) + d_{TK}^*, & \text{if phase 2} \\ -\frac{1}{2}a_{set}(t-t_2)^2 + V_{max}(t-t_2) + d_{WP} - d_{TK}^* - d_{sw}, & \text{if phase 3} \\ V_{min}(t-t_3) + d_{WP} - d_{sw}, & \text{if phase 4} \end{cases} \quad (3.32)$$

$$\boldsymbol{\eta}_D^* = R^{-1}(\xi)[x_d \ 0 \ 0]^T + \boldsymbol{\Omega}_{WP_1} \quad (3.33)$$

To avoid giving a too different desired angle after the switch between the waypoints, the desired angle  $\xi$  is given with a ramp between  $t_0$  and  $t_1$ , see Figure 3.11. In the figure,  $\xi_{old}$  is the angle defined by the previous couple of waypoints and  $\phi$  is the desired angle setpoint at each time step to send to the controller.

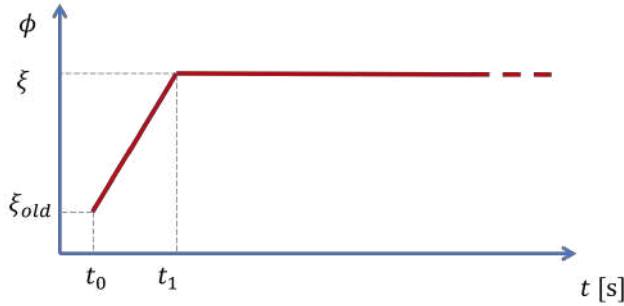


Figure 3.11: Guidance - Track Keeping - Desired heading angle.

The desired pose array trajectory is:

$$\boldsymbol{\eta}_{TR} = [\boldsymbol{\eta}_D^*(1:2) \ \phi]^T \quad (3.34)$$

### 3.3 Reference models

Reference models compute a smooth time-varying reference trajectory starting from the desired final waypoint position. Several options can be used to fulfil this aim, but this thesis considers three options for a 3-DOF scenario structure. In all cases, the input is the final desired waypoint position  $\boldsymbol{\Omega}_{WP}$  or the list of waypoints  $WP_{list}$ , while the outputs are the trajectory in terms of pose  $\boldsymbol{\eta}_{TR}$  in  $\underline{n}$  frame and of speed  $\boldsymbol{\nu}_{TR}$  in the  $\underline{b}$  frame. The layout is shown in Figure 3.12.

One solution is physically-based and uses the vessel model as the reference model. The formulation is done in (3.35).

$$\mathbf{M}\dot{\boldsymbol{\nu}}_{TR} + (\mathbf{D} + \mathbf{C})\boldsymbol{\nu}_{TR} = -\mathbf{K}_P\mathbf{e}^* + \mathbf{K}_I \int \mathbf{e}^* dt + \mathbf{K}_D\boldsymbol{\nu}_{TR} \quad (3.35)$$

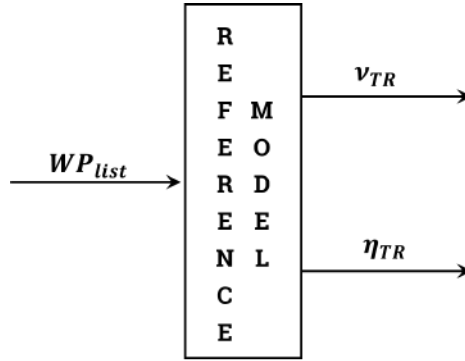


Figure 3.12: Guidance - Reference Model - Layout.

where  $\mathbf{e}^* = \mathbf{R}^T(\psi)(\boldsymbol{\eta}_{TR} - \boldsymbol{\eta}_{WP})$  is the error between the computed trajectory and the selected waypoint.

The second solution uses the first-order lowpass filter in (3.36). It is the simplest form for a reference model and, if adequately tailored, can compute a feasible trajectory.

$$\dot{\boldsymbol{\eta}}_{TR} = \frac{1}{\tau_1}(\boldsymbol{\eta}_{TR} - \boldsymbol{\eta}_d) \quad (3.36)$$

where  $\tau_1 \in \mathbb{R}$  is a constant.

The last solution adopted is a trapezoidal speed law between the two selected waypoints according to the one described in Section 3.2. With respect to the formulation in (3.31),  $V_{min}$  is selected equal to zero, and a total time  $t^*$  is assigned to cover the segment between the selected waypoints.

# Chapter 4

## Control: 2-DOF

The control systems can be studied within this framework: controllers account for the three-plane motion of the ship (surge, sway, yaw), named 3-DOF, used for scenarios at zero or low speed, however for scenario with high drift angle; and controllers account only with speed and heading, named 2-DOF, used for scenarios at higher speed, however with low drift angle.

In this chapter, the adopted 2-DOF controller and its synthesis are shown. The control action is provided by a smart pilot composed of two PID controllers: an autopilot for setting the desired heading and a speed pilot for setting the desired speed. The smart pilot structure is shown in Figure 4.1 and its synthesis is done considering all the motions in the horizontal plane and the desired speed. The inputs are the desired speed  $V_d$  and heading  $\psi_d$  and the feedback values  $v$  and  $\psi$ . The output are the desired voltage  $V_{A_{set}}$  and azimuth angle  $\alpha_{set}$  since these are the setpoints required from the selected test case, the Tito-Neri one of Section 7.1, but can be extended to different test case with the same propulsion plant.

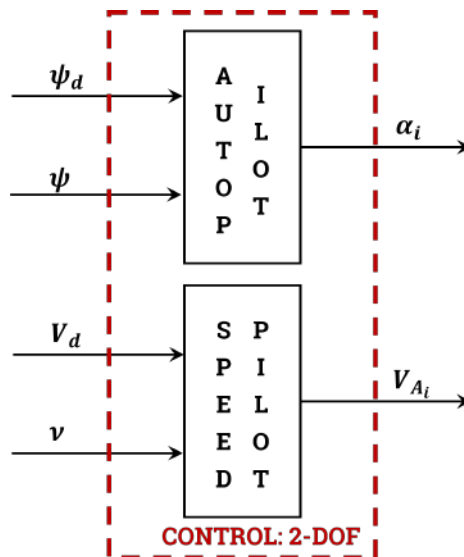


Figure 4.1: Control: 2-DOF - Controller layout.

## 4.1 Autopilot

Autopilot is responsible for maintaining the desired heading  $\psi_d$ . The PID controller of (4.1) is used and the input is the heading error  $e_\psi = \psi_d - \psi$  as shown in Figure 4.1. At the same time, the output is the desired azimuth angle since the case study adopted in this case is equipped with two azimuthal thrusters that are coupled as shown in Section 7.1. The same structure can be applied to actuators like propeller plus rudder and cycloidal propeller. It means that the output can be adapted to the different cases, for example, the rudder angle or the generic required moment that can be allocated to the propulsion configuration in a second phase.

$$\alpha_{set} = K_P^\psi(\bar{u})e_\psi + K_I^\psi(\bar{u}) \int_0^t e_\psi(\tau)d\tau + K_D^\psi(\bar{u}) \frac{de_\psi}{dt} \quad (4.1)$$

where  $K_P^\psi(\bar{u})$ ,  $K_I^\psi(\bar{u})$ , and  $K_D^\psi(\bar{u})$  are the proportional, integrative, and derivative gains, respectively.

## 4.2 Speed pilot

The speed pilot is responsible for maintaining the desired ship speed  $\bar{u}$  and correcting deviations from that value. The PID controller of (4.2) fulfils this aim. As shown in Figure 4.1, the input of the speed pilot is the speed error  $e_u = u_d - u$ , while the output is the desired voltage  $V_{A_{set}}$ . Also in this case the general layout can be tailored to different test case and the output can be the required propeller revolutions or the required force.

$$V_{a_{set}} = K_P^u(\bar{u})e_u + K_I^u(\bar{u}) \int_0^t e_u(\tau)d\tau + K_D^u(\bar{u}) \frac{de_u}{dt} \quad (4.2)$$

where  $K_P^u(\bar{u})$ ,  $K_I^u(\bar{u})$ , and  $K_D^u(\bar{u})$  are the proportional, integrative, and derivative gains, respectively.

## 4.3 Linearised model for synthesis purpose

The non-linear ship model of sections 2.2 and 2.3.1 is used to describe the ship dynamics and is then linearised for the synthesis of the controller. The linearisation is computed on the design speed  $\bar{u}$  with zero drift and zero yaw.

The motion equation of (2.2) is then linearised as in (4.3).

$$\tau_{RB} = \begin{cases} m\dot{u} \\ m\dot{v} + mx_G\dot{r} + m\bar{u}r \\ mx_G\dot{v} + I_Z\dot{r} + mx_Gr\bar{u} \end{cases} \quad (4.3)$$

The hull forces computed with the Oltmann & Sharma model of (2.6) are linearised as in (4.4).

$$\tau_H = \begin{cases} X_{\dot{u}}\dot{u} + \zeta_{R_T}(\bar{u})u \\ Y_{\dot{v}}\dot{v} + Y_{\dot{r}}\dot{r} + X_{\dot{u}}\bar{u}r + \frac{\rho}{2}L_{PP}T\bar{u}(e'kr\frac{L_{PP}}{2} - cv) \\ N_{\dot{v}}\dot{v} + N_{\dot{r}}\dot{r} + N_{\dot{u}}\bar{u}r + (Y_{\dot{v}} - X_{\dot{u}})\bar{u}v - \frac{\rho}{2}L_{PP}^2T\bar{u}(e'kr\frac{L_{PP}}{2} - ev) \end{cases} \quad (4.4)$$

where  $\zeta_{R_T}$  is the hull resistance coefficient function of the surge.

The synthesis is done on the test case described in 7.1 but the same approach can be extended to other vessels; hence, two azimuthal thrusters are the only actuators involved and are coupled; it leads to a factor 2 in the equation (2.24). The linear model is the one in (4.5).

$$\tau_{AZ} = \begin{cases} 2\zeta_{az}(\bar{n})n \\ 2\zeta_{az}(\bar{n})\bar{n}m_{sin}\alpha \\ x_{az}2\zeta_{az}(\bar{n})\bar{n}m_{sin}\alpha \end{cases} \quad (4.5)$$

where  $\zeta_{az}$  is the thrust coefficient function of the shaft-line revolutions,  $\bar{n}$  is the desired shaft-line revolution that is linked to the desired speed, and  $m_{sin}$  is the tangent that approximates the sinus around  $\alpha = 0$ .

The dynamic of the azimuthal angle and the shaft-line revolution are modelled as two first-order equations, (4.6) and (4.7). The two time-constants,  $\tau_n^{AZ}$  for the shaft line and  $\tau_\alpha^{AZ}$  for the azimuth angle, are found through an identification procedure based on a pseudo-random binary sequences approach.

$$\dot{\alpha} = \frac{1}{\tau_\alpha^{AZ}}(\alpha_{set} - \alpha) \quad (4.6)$$

$$\dot{n} = \frac{1}{\tau_n^{AZ}}\left(\frac{V_{A_{set}}}{K_e} - n\right) \quad (4.7)$$

In summary, the dynamic model of the vessel can be obtained by merging equations (4.3), (4.4), and (4.5), since, as reported before,  $\tau_{RB} = \tau_H + \tau_{AZ}$ . The resulting equations combined with (4.6) and (4.7), with the relationship between the heading angle  $\psi$  and the rate of turn  $r$  (4.8), and with the defined two augmented state variables (4.9) necessary to define the state equation of the closed loop, leads to have to linearised model of the selected vessel of (4.10).

$$\dot{\psi} = r \quad (4.8)$$

$$\dot{e}_u = e_u \quad (4.9)$$

$$\dot{e}_\psi = e_\psi$$

$$\begin{cases} (m - X_{\dot{u}})\dot{u} \\ (m - Y_{\dot{v}})\dot{v} + (m x_G - Y_{\dot{r}})\dot{r} \\ (m x_G - N_{\dot{v}})\dot{v} + (I_Z - N_{\dot{r}})\dot{r} \\ \dot{\psi} \\ \dot{\alpha} \\ \dot{n} \\ \dot{e}_u \\ \dot{e}_\psi \end{cases} = \begin{cases} -\zeta_{R_T}(u)u + 2\zeta_{az}(n)n \\ X_{\dot{u}}\bar{u}r + \frac{\rho}{2}L_{PP}T\bar{u}(e'kr\frac{L_{PP}}{2} - cv) \\ + 2\zeta_{az}(\bar{n})\bar{n}m_{sin}\alpha \\ N_{\dot{v}}\bar{u}r + (Y_{\dot{v}} - X_{\dot{u}})\bar{u}v - \frac{\rho}{2}L_{PP}^2T\bar{u} \\ (e'kr\frac{L_{PP}}{2} - ev) + 2x_{az}\zeta_{az}(\bar{n})\bar{n}m_{sin}\alpha \\ r \\ \frac{1}{\tau_\alpha^{AZ}}(\alpha_{set} - \alpha) \\ \frac{1}{\tau_n^{AZ}}\left(\frac{V_{A_{set}}}{K_e} - n\right) \\ e_u \\ e_\psi \end{cases} \quad (4.10)$$

The state equations of the open and closed loops are defined starting from the linearised model.

The state equation of the open loop takes into consideration the first six equations of (4.10) and is shown in Figure 4.2 and defined as in (4.11).

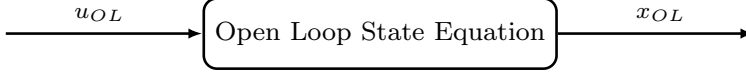


Figure 4.2: Control: 2-DOF - Open Loop Layout.

$$\dot{\mathbf{x}}_{OL} = \mathbf{A}_{OL}\mathbf{x}_{OL} + \mathbf{B}_{OL}\mathbf{u}_{OL} \quad (4.11)$$

where  $\mathbf{u}_{OL} = [V_{A_{set}}, \alpha_{set}]^T$  is the input vector of the overall system,  $\mathbf{x}_{OL} = [u, v, r, \psi, n, \alpha]^T$  is the state vector,  $\mathbf{A}_{OL}$  and  $\mathbf{B}_{OL}$  are the system and the input matrices of the open loop, respectively, they are defined in (4.12) and (4.13).

$$\mathbf{A}_{OL} = \begin{bmatrix} A_{11} & 0 & 0 & 0 & A_{15} & 0 \\ 0 & A_{22} & A_{23} & 0 & 0 & A_{26} \\ 0 & A_{32} & A_{33} & 0 & 0 & A_{36} \\ 0 & 0 & 1 & 0 & 0 & 0 \\ 0 & 0 & 0 & 0 & -\frac{1}{\tau_n^{AZ}} & 0 \\ 0 & 0 & 0 & 0 & 0 & -\frac{1}{\tau_\alpha^{AZ}} \end{bmatrix} \quad (4.12)$$

$$\mathbf{B}_{OL} = \begin{bmatrix} 0 & 0 \\ 0 & 0 \\ 0 & 0 \\ 0 & 0 \\ \frac{1}{\tau_n^{AZ} K_e} & 0 \\ 0 & \frac{1}{\tau_\alpha^{AZ}} \end{bmatrix} \quad (4.13)$$

where:

$$\begin{aligned} \bar{A} &= (I_Z - N_{\dot{r}})(m - Y_{\dot{v}}) - (Y_{\dot{r}} - mx_G)(N_{\dot{v}} - mx_G) \\ A_{11} &= -\frac{\zeta_{RT}(u)}{m - X_{\dot{u}}} \\ A_{15} &= \frac{\zeta_{az}(n)}{m - X_{\dot{u}}} \\ A_{22} &= \frac{(I_Z - N_{\dot{r}})\frac{\rho}{2}L_{PP}Tc + (mx_G - Y_{\dot{r}})(Y_{\dot{v}} - X_{\dot{u}} + \frac{\rho}{2}L_{PP}^2Te)\bar{u}}{\bar{A}} \\ A_{23} &= \frac{(mx_G - Y_{\dot{r}})(-N_{\dot{v}} + mx_G + \frac{\rho}{4}L_{PP}^3Te'k) + (I_Z - N_{\dot{r}})(X_{\dot{u}} - m + \frac{\rho}{4}L_{PP}^2Tc'k)\bar{u}}{\bar{A}} \\ A_{26} &= \frac{2m_{sin}\zeta_{az}(\bar{n})\bar{n}(I_Z - N_{\dot{r}} + x_{az}(Y_{\dot{r}} - mx_G))}{\bar{A}} \\ A_{32} &= \frac{\frac{\rho}{2}L_{PP}Tc(mx_G - N_{\dot{v}}) + (m - Y_{\dot{v}})(Y_{\dot{v}} - X_{\dot{u}} + \frac{\rho}{2}L_{PP}^2Te)\bar{u}}{\bar{A}} \\ A_{33} &= \frac{(N_{\dot{v}} - mx_G)(X_{\dot{u}} - Y_{\dot{v}} + \frac{\rho}{4}L_{PP}^2Tc'k) + (Y_{\dot{v}} - m)\frac{\rho}{4}L_{PP}^3Te'k\bar{u}}{\bar{A}} \\ A_{36} &= \frac{N_{\dot{v}} - mx_G - x_{az}(Y_{\dot{v}} - m)}{\bar{A}} 2m_{sin}\zeta_{az}(\bar{n})\bar{n} \end{aligned}$$

The controller layout is shown in Figure 4.3 and it is a summary of the speed pilot and autopilot described in sections 4.1 and 4.2. The input is the error array  $e = [e_u, e_\psi]^T$ ; while the output is the array  $u_{OL}$  expressing the desired voltage  $V_{a_{set}}$  and azimuth angle  $\alpha_{set}$ .

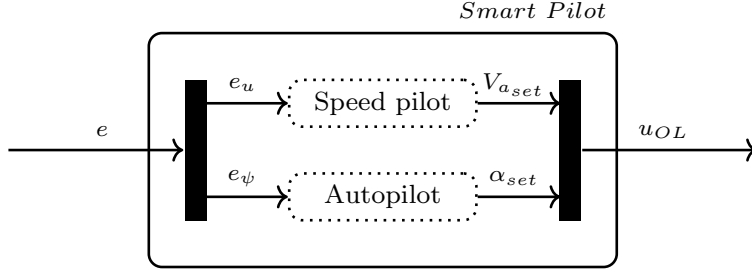


Figure 4.3: Control: 2-DOF - Smart pilot layout.

The scheme representing the adopted closed-loop is shown indeed in Figure 4.4 where  $\mathbf{x}_e = [u, v, r, \psi, n, \alpha, \epsilon_u, \epsilon_\psi]^T$  is the extended state vector.

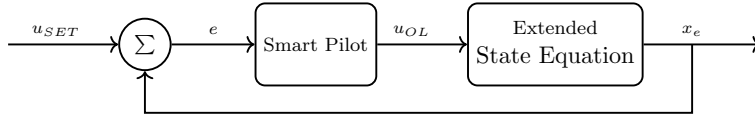


Figure 4.4: Control: 2-DOF - Closed Loop Layout.

The new extended state equation is the one in (4.14) and can be combined with the feedback control action (4.15) resulting in the closed loop dynamics of (4.16).

$$\dot{\mathbf{x}}_e = \mathbf{A}_e \mathbf{x}_e + \mathbf{B}_e \mathbf{u}_{OL} + \mathbf{F}_e \mathbf{u}_{set} \quad (4.14)$$

$$\mathbf{u}_{OL} = -\mathbf{K}_{CL} \mathbf{x}_e + \mathbf{G}_e \mathbf{u}_{set} \quad (4.15)$$

$$\dot{\mathbf{x}}_e = (\mathbf{A}_e - \mathbf{B}_e \mathbf{K}_{CL}) \mathbf{x}_e + (\mathbf{B}_e \mathbf{G}_e + \mathbf{F}_e) \mathbf{u}_{set} \quad (4.16)$$

where  $\mathbf{A}_e$ ,  $\mathbf{B}_e$ , and  $\mathbf{F}_e$  are the augmented system matrices defined in (4.17) and (4.18), and  $\mathbf{K}_{CL}$  and  $\mathbf{G}_e$  are two matrices that include the PID gains defined as (4.19) and (4.20).

$$\mathbf{A}_e = \begin{bmatrix} & & & & & & 0 & 0 \\ & & & & & & 0 & 0 \\ & & & & & & 0 & 0 \\ & & & & & & 0 & 0 \\ & & & & & & 0 & 0 \\ & & & & & & 0 & 0 \\ & & & & & & 0 & 0 \\ -1 & 0 & 0 & 0 & 0 & 0 & 0 & 0 \\ 0 & 0 & 0 & -1 & 0 & 0 & 0 & 0 \end{bmatrix} \quad (4.17)$$

$$\mathbf{B}_e = \begin{bmatrix} B_{OL} \\ \\ \\ 0 & 0 \\ 0 & 0 \end{bmatrix} \quad \mathbf{F}_e = \begin{bmatrix} 0 & 0 \\ 0 & 0 \\ 0 & 0 \\ 0 & 0 \\ 0 & 0 \\ 1 & 0 \\ 0 & 1 \end{bmatrix} \quad (4.18)$$

$$\mathbf{K}_{CL} = \begin{bmatrix} K_P^u + K_D^u A_{11} & 0 & 0 & 0 & K_D^u A_{15} & 0 & -K_I^u & 0 \\ 0 & 0 & K_D^\psi & K_P^\psi & 0 & 0 & 0 & -K_I^\psi \end{bmatrix} \quad (4.19)$$

$$\mathbf{G}_e = \begin{bmatrix} K_P^u & 0 \\ 0 & K_P^\psi \end{bmatrix} \quad (4.20)$$

## 4.4 Synthesis

The PID gains  $(K_P^{\psi/u}(\bar{u}), K_I^{\psi/u}(\bar{u}), K_D^{\psi/u}(\bar{u}))$  selection for the smart pilot controller is accomplished by using Linear Matrix Inequalities (LMIs) as a design tool to ensure closed-loop stability as introduced in [9]. The problem is solved numerically thanks to the Sedumi solver [119] and the Matlab toolbox Yalmip [72]. The aim of the control design is firstly to guarantee the stability of the closed loop, verifying the Lyapunov theorem, as the common practice wants, but also some properties related to the convergences of the state variable. Indeed, the first property added to the common practice method is related to the convergence speed and is named the decay rate. The second and last property added in this work wants to limit the overshoot of the state variables, it is named peak limits. These two properties want to improve the dynamics of the closed loop.

The properties ensured with this synthesis are given in detail, together with the related LMI problems.

### 4.4.1 Closed Loop Stability

The gains selection of the two controllers is accomplished by verifying the stability of the closed loop through the Lyapunov theorem [73]. According to this, the system (4.16) is quadratically stabilisable if there exists a state-feedback gain  $\mathbf{K}_{CL}$  such that (4.16) is quadratically stable or, equivalently, if there exists a Lyapunov function  $\mathbf{V}(\mathbf{x})$  such that the function is positive or equal to zero and its time derivative is strictly negative for all  $\mathbf{x}$  out of origin. Following a well-known strategy, it is possible to define the Lyapunov function as  $\mathbf{V}(\mathbf{x}) = \mathbf{x}^T \mathbf{P} \mathbf{x}$  with  $\mathbf{P}$  assumed symmetric and positive matrix, and, as a consequence, the theorem corresponds to finding a matrix gain  $\mathbf{K}_{CL}$  such that the condition in (4.21) is fulfilled.

$$\begin{cases} \mathbf{P} > 0 \\ (\mathbf{A}_e - \mathbf{B}_e \mathbf{K}_{CL})^T \mathbf{P} + \mathbf{P} (\mathbf{A}_e - \mathbf{B}_e \mathbf{K}_{CL}) < 0 \end{cases} \quad (4.21)$$

As shown in [19], (4.21) can be expressed equivalently by multiplying both sides for  $\mathbf{P}^{-1}$  and defining  $\mathbf{Q} = \mathbf{P}^{-1}$  and  $\mathbf{Y} = \mathbf{K} \mathbf{Q}$ . In this way, it is possible to write the Lyapunov stability theorem as the LMIs (4.22) in the unknowns  $\mathbf{Y}$  and  $\mathbf{Q}$ .



$$\begin{cases} \mathbf{Q} > 0 \\ \mathbf{Q}\mathbf{A}_e^T - \mathbf{Y}^T\mathbf{B}_e^T + \mathbf{A}_e\mathbf{Q} - \mathbf{B}_e\mathbf{Y} < 0 \end{cases} \quad (4.22)$$

Solving (4.22), it is possible to find the matrix gain  $\mathbf{K}_{CL} = \mathbf{Y}\mathbf{Q}^{-1}$  and, as a consequence, the values of the PIDs gains of the speed pilot and autopilot of (4.2) and (4.1) that guarantee the stability of the closed loop according to [73].

#### 4.4.2 Decay Rate

In case fast dynamics characterise the controlled system, it appears necessary to introduce a further constraint in addition to stability requirements. The decay rate constraint aims to guarantee the achievement of the set point as quickly as possible to have a responsive system. Indeed, it describes how fast the function decays (or grows) with time, and the problem of maximising it is discussed in deep detail in [134] where starting from its definition it arrives to compute an upper bound on the minimum decay rate as an optimisation problem. As stated in [19], the problem of searching the decay rate  $\alpha$  can be written using the quadratic Lyapunov function  $\mathbf{V}(\mathbf{x})$ , defined before in section 4.4.1, and as the optimisation problem of (4.23).

$$\begin{aligned} & \text{maximize } v \\ & \text{subject to } \mathbf{P} > \mathbf{O} \\ & \quad \dot{\mathbf{V}}(x) \leq -2v\mathbf{V}(x) \end{aligned} \quad (4.23)$$

The problem in (4.23) is a Generalised Eigenvalue Problem (GEVP) in the unknowns  $\mathbf{P}$  and  $v$  where the optimal value is the decay rate of the system and can be written as the Linear Matrix Inequality in (4.24).

$$\begin{cases} \mathbf{P} \geq 0 \\ \mathbf{A}^T\mathbf{P} + \mathbf{P}\mathbf{A} \leq -2v\mathbf{P} \end{cases} \quad (4.24)$$

Applying the condition in (4.24) at the system (4.16), adding the resulting LMI to the conditions deriving from the Lyapunov stability theorem stated in (4.22), and applying the  $S$ -Procedure which leads to considering the more conservative inequalities, it is possible to write the Bilinear Matrix Inequality (BMI) (4.25) in the unknowns  $v$ ,  $\mathbf{Y}$ , and  $\mathbf{Q}$  that ensure the stability of the closed-loop and that would maximise the decay rate.

$$\begin{cases} \mathbf{Q} > 0 \\ \mathbf{Q}\mathbf{A}_e^T - \mathbf{Y}^T\mathbf{B}_e^T + \mathbf{A}_e\mathbf{Q} - \mathbf{B}_e\mathbf{Y} \leq -2v\mathbf{Q} \end{cases} \quad (4.25)$$

Solving (4.25), it is possible to find the matrix gain  $\mathbf{K}_{CL} = \mathbf{Y}\mathbf{Q}^{-1}$  and, as a consequence, the values of the PIDs gains of the speed pilot and autopilot of (4.2) and (4.1) that guarantee the stability and the fast convergence of the closed loop.

#### 4.4.3 Peak Limit

An overshoot on the control setpoint can be dangerous for the real model and lead to controllability problems due to the strong action that saturations will have.

For this reason, a condition that limits the peak is introduced. As stated in [19] and [26], the problem of limiting the peak can be described with the inequalities in (4.26).

$$\begin{bmatrix} \mathbf{Q} & \mathbf{Y}^T \\ \mathbf{Y} & \mu^2 \mathbf{I} \end{bmatrix} \geq 0 \quad \text{or} \quad \begin{cases} \mathbf{Q} - \mathbf{Y}^T (\mu^2 \mathbf{I})^{-1} \mathbf{Y} \geq 0 \\ \mathbf{Q} > 0 \end{cases} \quad (4.26)$$

The new condition (4.26) can be applied to the system (4.16), resulting in an LMI. The last need to be included in the BMI problem reported in (4.25) which summarises the Lyapunov stability theorem (4.22) and the decay rate condition (4.24). The resulting problem is a system (4.27) in the unknowns  $v$ ,  $\mathbf{Y}$ ,  $\mu$ , and  $\mathbf{Q}$ . Finding a solution for (4.27) ensures the stability of the closed-loop where the control action is also intended to maximise the decay rate and limit the overshoot.

$$\begin{cases} \mathbf{Q} > 0 \\ \mathbf{Q} \mathbf{A}_e^T - \mathbf{Y}^T \mathbf{B}_e^T + \mathbf{A}_e \mathbf{Q} - \mathbf{B}_e \mathbf{Y} \leq -2v \mathbf{Q} \\ \mathbf{Q} - \mathbf{Y}^T (\mu^2 \mathbf{I})^{-1} \mathbf{Y} \geq 0 \end{cases} \quad (4.27)$$

Solving (4.27), it is possible to find the matrix gain  $\mathbf{K}_{CL} = \mathbf{Y} \mathbf{Q}^{-1}$  and, as a consequence, the values of the PIDs gains of the speed pilot and autopilot of (4.2) and (4.1) that guarantee the stability, rapid convergence to the setpoint and a limitation on the overshoot. The resulting numerical problem can be solved with a global optimisation approach and the use of a bisection algorithm for different values of  $\mu$ . Briefly, it consists initially of defining a lower and an upper bound of the decay rate  $v$  for which the problem is feasible and after applying the bisection, i.e. in checking the value between the lower and upper bound and in updating the lower or the upper bound if the problem is feasible or infeasible until bounds are sufficiently close. A solution for each value of  $\mu$  is found, and the set made with all the feasible solutions is considered. The linear system step-response under each feasible solution is evaluated, and the solution with the lower rise time is selected.

# Chapter 5

## Control: 3 DOF

The pipeline of the 3-DOF controller is proposed in Figure 5.1 and different solutions for each controller subsystem can be identified and combined. The pipeline starts taking as input the following value: the feedback velocity and pose array  $\eta$  and  $\nu$  and the desired path in terms of velocity  $\nu_{TR}$  and pose  $\eta_{TR}$  computed by the reference models starting from the desired waypoint list as shown in Section 3.3. After the error between the desired and the feedback state values are evaluated and the proper thrust loads and moment needed to compensate them are computed by the controller; in the end the allocation system allocates the control signal to the actuators. The allocation module is divided into two parts: the Force Allocation Logic (FAL), which computes the required thrust for each actuator, and the Thrust Allocation Logic (TAL), which computes the right setpoints for each actuator.

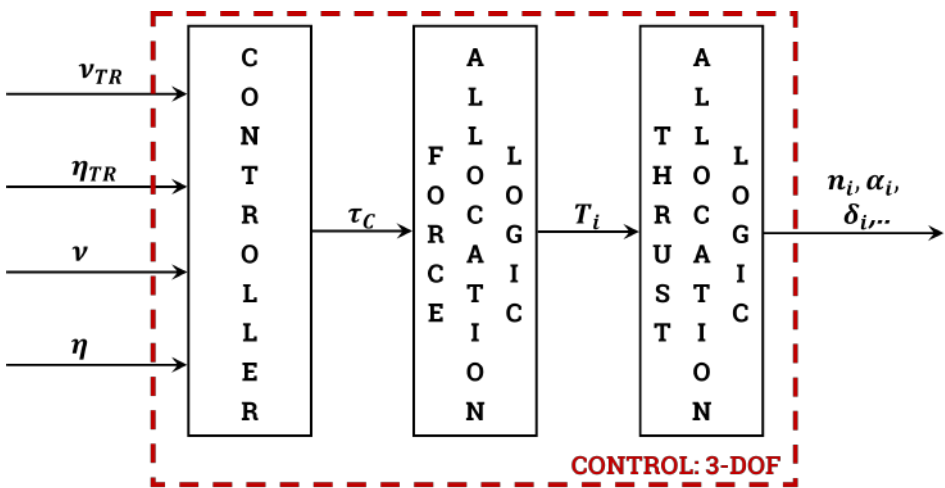


Figure 5.1: Control: 3-DOF - Controller layout.

### 5.1 Controller

Several control methodologies, such as linear/nonlinear control, fuzzy control, (numerical) optimal control, and machine learning-based approaches can be used to ful-

fil the aim. Some examples of control methodologies can be found in [36], [80], [116], and [122]. The input of this system are the filtered position and velocity components  $(\boldsymbol{\eta}, \boldsymbol{\nu})$  and the desired values  $(\boldsymbol{\eta}_{TR}, \boldsymbol{\nu}_{TR})$ . At the same time, the output is the array of forces and moment necessary to nullify the errors  $\boldsymbol{\tau}_C$ .

### 5.1.1 Model-Base PID

The controller is chosen as a model-based PID in (5.1). The control action  $\boldsymbol{\tau}_C$  is the sum of two contributions: a model-based feedforward  $\boldsymbol{\tau}_{FF}$  and a feedback term  $\boldsymbol{\tau}_{FB}$ .

$$\boldsymbol{\tau}_C = \boldsymbol{\tau}_{FF} + \boldsymbol{\tau}_{FB} \quad (5.1)$$

The feedforward term is computed through the vessel model calculated on desired setpoints as shown in (5.2). This term will compute the necessary loads to obtain the desired changes in the setpoint, leaving the feedback controller to deal only with external disturbances.

$$\boldsymbol{\tau}_{FF} = \mathbf{M}\dot{\boldsymbol{\nu}}_{TR} + \mathbf{D}(\boldsymbol{\nu}_{TR})\boldsymbol{\nu}_{TR} + \mathbf{C}(\boldsymbol{\nu}_{TR})\boldsymbol{\nu}_{TR} \quad (5.2)$$

where  $\boldsymbol{\eta}_{TR}$  is the desired trajectory in the  $\underline{n}$  frame and  $\boldsymbol{\nu}_{TR}$  is the desired speed in the  $\underline{b}$  frame.

The feedback term is chosen as the Proportional Integrative and Derivative (PID) controller stated in (5.3). The PID terms are functions of the pose error  $\mathbf{e}$  and the velocity error  $\boldsymbol{\nu}_e$  defined in (5.4) and (5.5).

$$\boldsymbol{\tau}_{FB} = \mathbf{K}_P\mathbf{e} + \mathbf{K}_I \int_0^t \mathbf{e}(\tau)d\tau + \mathbf{K}_D\boldsymbol{\nu}_e \quad (5.3)$$

$$\mathbf{e} = \mathbf{R}^T(\psi)(\boldsymbol{\eta}_{TR} - \boldsymbol{\eta}) \quad (5.4)$$

$$\boldsymbol{\nu}_e = \boldsymbol{\nu}_{TR} - \boldsymbol{\nu} \quad (5.5)$$

where  $\mathbf{K}_P$ ,  $\mathbf{K}_I$ , and  $\mathbf{K}_D$  are positive diagonal matrices containing the proportional, integral, and derivative gains, respectively.

### 5.1.2 Environmental Feedforward

The controller is modelled as in [36] and consists of three independent PDs, one per each DOF. The integrative term needed to correct the mean offset error is replaced with the reconstruction of the compensated environmental forces. The current and the wave are estimated through an average of the forces and moment required by the PD controller in a previous fixed time interval  $\bar{\boldsymbol{\tau}}_{PD}$ , while the wind action  $\boldsymbol{\tau}_{WIND}$  is reconstructed as a feedforward through a wind force model, see Section 2.6.1. In this case, the relative wind speed  $V_{WIND}$  and the relative wind coming direction  $\gamma_{WIND}$  are also needed.

The control law that gives as output the required forces and moment  $\boldsymbol{\tau}_C$  in the  $\underline{b}$  base can be written as in (5.6).

$$\boldsymbol{\tau}_C = \mathbf{R}(\psi)[\mathbf{K}_P\bar{\boldsymbol{\eta}} + \mathbf{K}_D\dot{\bar{\boldsymbol{\eta}}}] + \bar{\boldsymbol{\tau}}_{PD} + \boldsymbol{\tau}_W \quad (5.6)$$

where the speed and pose error  $\bar{\boldsymbol{\eta}}$  and  $\dot{\bar{\boldsymbol{\eta}}}$  are computed according to (5.7) and (5.8)

$$\bar{\boldsymbol{\eta}} = \boldsymbol{\eta} - \boldsymbol{\eta}_{TR} \quad (5.7)$$

$$\dot{\bar{\boldsymbol{\eta}}} = \mathbf{R}(\psi)^{-1}(\boldsymbol{\nu} - \boldsymbol{\nu}_{TR}) \quad (5.8)$$

## 5.2 Force Allocation Logic

The kernel of the 3-DOF controller is the force allocation algorithm (FAL). Usually, the number of unknowns is greater than the available equations, i.e. the equilibrium equations in the horizontal plane. The result is an over-actuated system with infinite solutions to the force allocation problem. Several techniques are proposed in the literature as reported in [30] and [65] to solve the problem. Possible solutions lead to simplifying the approach with equivalent systems and fixed angles or using optimal thrust allocation methods.

### 5.2.1 Simplified approach

Simplification and reduction of each actuator unknowns can be done to obtain an analytical formulation of the allocation problem. These depend on the test case propulsion plant and the problem aim. Hereinafter, the application done on the PSV test case (Section 7.4) is reported as an example but it can be extended to all the propulsion configuration with two azimuth angle and one or two bow thrusters.

The PSV test propulsion configuration, as shown in Section 7.4, consists of two azimuthal thrusters and two bow thrusters. Each azimuthal thruster has two degrees of freedom, the thrust  $T_{AZ_i}$  and the angle  $\alpha_i$ , while the bow thruster has only one degree of freedom, the thrust  $T_{BT_i}$ . In summary, the total amount of unknowns in the equilibrium equations in the horizontal plane is six; indeed, the vessel is over-actuated. The choice is to reduce the order of the problem working on constant azimuthal angles and considering the two bow thrusters as one with an equivalent thrust  $\underline{T}_{BT_{eq}} = Y_{BT_{eq}}$  and position  $x_{BT_{eq}}$ . The resulting system is in (5.9) and is function of the allocation matrix  $\mathbf{A}$  in 5.10 and 5.11.

$$\boldsymbol{\tau}_{ALL} = \mathbf{A}^{-1} \boldsymbol{\tau}_C \quad (5.9)$$

$$\mathbf{A} = [\mathbf{t}_{PT}, \mathbf{t}_{SB}, \mathbf{t}_{BT_{eq}}]^T \quad (5.10)$$

$$\mathbf{t}_{PT} = \underbrace{\begin{bmatrix} -1 & 0 \\ 0 & -1 \\ y_{PT} & -x_{PT} \end{bmatrix}}_{\text{portside}}, \quad \mathbf{t}_{SB} = \underbrace{\begin{bmatrix} -1 & 0 \\ 0 & -1 \\ y_{SB} & -x_{SB} \end{bmatrix}}_{\text{starboard}}, \quad \mathbf{t}_{BT_{eq}} = \underbrace{\begin{bmatrix} 0 \\ -1 \\ -x_{BT_{eq}} \end{bmatrix}}_{\text{bow thruster}} \quad (5.11)$$

where  $\boldsymbol{\tau}_{ALL} = [X_{PT}, Y_{PT}, X_{SB}, Y_{SB}, T_{BT_{eq}}]^T$  is the unknown vector.

The second step involves the definition of time dependence of  $\mathbf{A}$ . The selected relationship is  $\mathbf{A} := \mathbf{A}(\boldsymbol{\tau}_C)$  and is governed by (5.12). The main idea is to assign two states at each time step by nullifying one of the two components of the thrust force of each main azimuthal thruster. In this way, the allocation matrix is always n-by-n invertible, and the reduced order allocation problem is pointwise solvable. Three main configurations are identified following the sketch in Figure 5.2 (b-d). Such configurations are toggled depending on the prevailing components of the forces and moments required by the controller according to the switch logic of Figure 5.3, where  $N_{LOC} = x_{BT_{eq}} \boldsymbol{\tau}_C(2) - \boldsymbol{\tau}_C(3)$ . Three main cases are identified: (i) bow or stern seas, Figure 5.2 (b), where  $Y_{PT} := Y_{SB} := 0$ ; (ii) portside seas, Figure 5.2 (c), where  $Y_{PT} := X_{SB} := 0$ ; (iii) starboard seas, Figure 5.2 (d), where  $X_{PT} := Y_{SB} := 0$ .

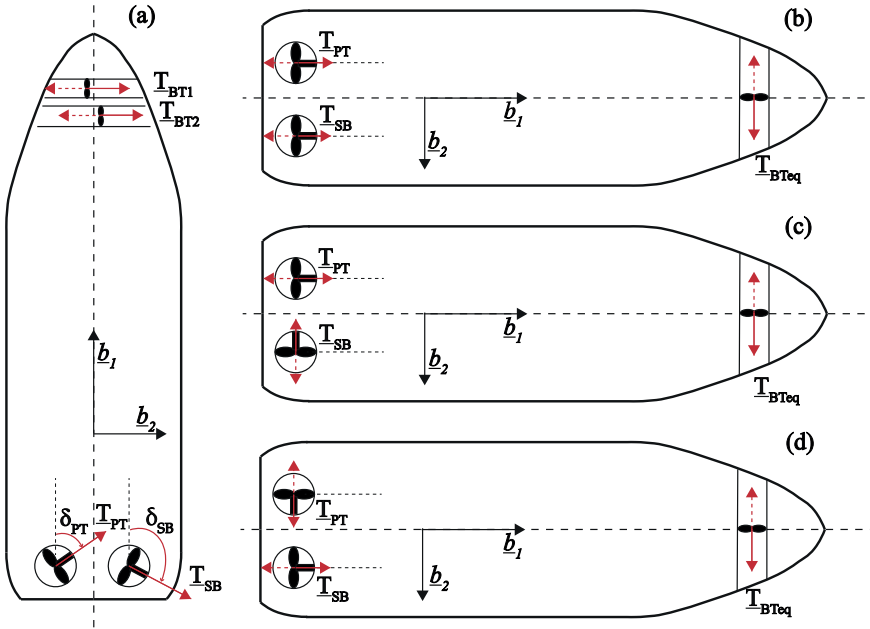


Figure 5.2: Control: 3-DOF - (a) Actuators layout (b-d) Fixed Angles Allocations.

$$t_{PT} = \begin{bmatrix} -1 \\ 0 \\ y_{PT} \end{bmatrix} \text{ and } t_{SB} = \begin{bmatrix} 0 \\ -1 \\ -x_{SB} \end{bmatrix} \quad \text{if } \begin{cases} |y_{PT} X_R| \leq |x_{BT_{eq}} \tau_C(2) - \tau_C(3)| \\ x_{BT_{eq}} \tau_C(2) - \tau_C(3) < -a \end{cases} \quad (5.12a)$$

$$t_{PT} = \begin{bmatrix} 0 \\ -1 \\ -x_{PT} \end{bmatrix} \text{ and } t_{SB} = \begin{bmatrix} -1 \\ 0 \\ y_{SB} \end{bmatrix} \quad \text{if } \begin{cases} |y_{PT} \tau_C(1)| \leq |x_{BT_{eq}} \tau_C(2) - \tau_C(3)| \\ x_{BT_{eq}} \tau_C(2) - \tau_C(3) \geq a \end{cases} \quad (5.12b)$$

$$t_{PT} = \begin{bmatrix} -1 \\ 0 \\ y_{PT} \end{bmatrix} \text{ and } t_{SB} = \begin{bmatrix} -1 \\ 0 \\ y_{SB} \end{bmatrix} \quad \text{otherwise} \quad (5.12c)$$

where  $a > 0$  is a coefficient introduced to avoid fast transitions when the required forces are limited in magnitude. In this way, reducing the machinery wear and preventing the fast change of the azimuth angle is possible. Moreover, the switching law described in (5.12) guarantees that propellers are never flushing on other working propellers.

Ultimately, the thrust required at the equivalent bow thruster must be split into the thrust requirements for each thruster. In this case, the two bow thrusters are of the single-propeller type, with the propellers symmetrically placed with respect to the middle-line. When the thrust is required in the opposite direction to the propeller position, a thrust loss coefficient of 70% determines the thrust requirement of the individual bow thruster. Hence, the thrust required at each bow thruster

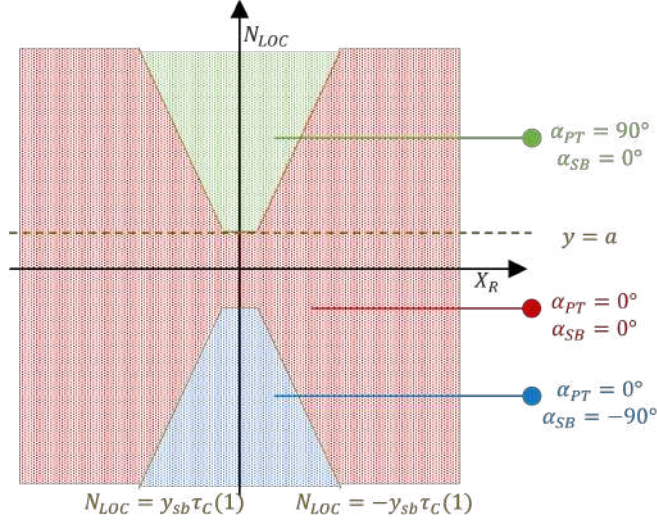


Figure 5.3: Control: 3-DOF - Allocation Switch condition.

can be found according to (5.13).

$$\begin{cases} \text{if } Y_{BT_{eq}} \geq 0 & \text{then } \begin{cases} Y_{BT_{aft}} = \frac{100}{170} Y_{BT_{eq}} \\ Y_{BT_{fore}} = \frac{70}{170} Y_{BT_{eq}} \end{cases} \\ \text{if } Y_{BT_{eq}} < 0 & \text{then } \begin{cases} Y_{BT_{aft}} = \frac{70}{170} Y_{BT_{eq}} \\ Y_{BT_{fore}} = \frac{100}{170} Y_{BT_{eq}} \end{cases} \end{cases} \quad (5.13)$$

## 5.2.2 Optimized methods

Optimisation methods can be used to solve the allocation problem. The optimisation methods can be solved through nonlinear programming techniques or mathematics techniques like Lagrange Multiplier.

### 5.2.2.1 Nonlinear programming

The general allocation problem is formulated as the general constrained optimisation problem of (5.14) where the aim is to minimise an objective function  $f(\mathbf{x})$  in the variables  $\mathbf{x}$  under the equality  $h(\mathbf{x})$  and inequality constraints  $g(\mathbf{x})$  with the lower bounds  $\mathbf{lb}$  and upper bounds  $\mathbf{ub}$ . One of the methods for solving this problem is the use of nonlinear programming techniques.

$$\begin{aligned} & \underset{\mathbf{x}}{\text{minimize}} && f(\mathbf{x}) \\ & \text{subject to} && h(\mathbf{x}) = \mathbf{0}, \\ & && \mathbf{x}(0) = \mathbf{x}_0, \\ & && \mathbf{lb} \leq \mathbf{x} \leq \mathbf{ub}, \\ & && g(\mathbf{x}) \leq \mathbf{0} \end{aligned} \quad (5.14)$$

The unknowns of the problem are the thruster load, the direction, and the corresponding rectangular force components defined for the  $n_{ac}$  thruster:  $\mathbf{x} =$

$[X_i, Y_i, T_i, \alpha_i]^T$ ,  $i = 1, \dots, n_{ac}$ . The four unknowns of each thruster can be modified and reduced according to the actuator type; for example, the tunnel thrusters have only the thrust as unknown.

The general equality constraints are given by the horizontal plane static equilibrium and the relationships between the unknowns, as shown in (5.15).

$$h(\mathbf{x}) = \begin{cases} \sum_{i=1}^4 X_i \eta(\alpha_i) - \tau_C(1) \\ \sum_{i=1}^4 Y_i \eta(\alpha_i) - \tau_C(2) \\ \sum_{i=1}^4 (x_{az_i}, y_{az_i}) \times (X_i, Y_i) \eta(\alpha_i) - \tau_C(3) \\ T_i^2 - X_i^2 - Y_i^2 \\ \alpha_i - \text{atan2}(Y_i, X_i) \\ X_i - T_i(1 - c_x \delta_i) \\ Y_i - T_i c_y \delta_i \end{cases} \quad (5.15)$$

where  $c_x$  and  $c_y$  are parameters to rotate the thrust given by the rudder and the propeller and  $\eta(\alpha_i)$  represents the thruster efficiency and considers the thruster-thruster and the thruster-hull interactions depending on the actuator angle. The nonlinear effects can be considered with the parametric formulations of [32] without requiring time-consuming and resource-intensive calculations. The thruster efficiency  $\eta(\alpha_i)$  is one of the possibilities for considering the thruster-thruster interactions; this interaction can affect the thruster performance sensibly according to the actuator diameters and the distance between them. An experimental evaluation of the interaction is shown in [12] together with applications in [11] and [142]. Since there are interference effects, it is not simple to evaluate these efficiency curves; hence, another possibility is to consider a sector for each couple of actuators in which it can not operate due to the interactions; these sectors are commonly known as forbidden zones, and the amplitude of the sector can be considered thanks with some parametric formulation like the one proposed in [32]. In this case, the forbidden zones can be integrated into the optimum problem by setting the bounds on the variables or can be added after the optimisation problem checking if the found solution is inside the forbidden sector and if it is, solving the optimisation problem fixing the azimuthal angles inside the forbidden range at the boundaries of them.

The bounds  $\mathbf{lb}$  and  $\mathbf{ub}$ , for example, set the limits on the azimuth angles  $\alpha_i$ , on the magnitude of the thrust  $T_i$ , or on the rudder angles  $\delta_i$ .

A set of inequality constraints  $g(\mathbf{x})$  can be defined, for example, to put a limit on the derivative of the azimuth angles  $\dot{\alpha}_i$  to limit their movements according to:

$$g(\mathbf{x}) = \dot{\alpha}_i - \dot{\alpha}_{max_i} \leq 0 \quad i = 1, \dots, n_{ac} \quad (5.16)$$

where  $\dot{\alpha}_{max_i}$  is the maximum value of the derivative given by the actuator limits.

The objective function is the function to minimise. It can be defined in several ways according to the study objective. In the applications analysed in this thesis, the aim is always to minimise the total actuator thrust. For such a reason, the resulting objective functions are like the one in (5.17) that tends to minimise the thrust or the one of (5.18) where penalties in the changes of the angle  $\alpha$  and of the thrust  $T_{AZ}$  are taken into account.

$$f(\mathbf{x}) = \sum_{i=1}^4 \mathbf{t}_i^T \mathbf{W}_i \mathbf{t}_i \quad (5.17)$$



$$f(\mathbf{x}) = \sum_{i=1}^4 \mathbf{t}_i^T \mathbf{W}_i \mathbf{t}_i + (\alpha - \alpha_{t-1})' \mathbf{T} (\alpha - \alpha_{t-1}) + (\mathbf{T} - \mathbf{T}_{t-1})' \mathbf{S} (\mathbf{T} - \mathbf{T}_{t-1}) \quad (5.18)$$

where  $\mathbf{t}_i = [X_{AZ_i}, Y_{AZ_i}]$  are the thrust components,  $\mathbf{W}_i$  is a weight diagonal matrix penalising the square of the maximum allowable thrust  $T_{max_i}$  of each actuator,  $\mathbf{T}$  is a diagonal matrix penalising the square of the maximum  $\Delta\alpha$  considered,  $\alpha_{t-1}$  is the vector of the actuator angles at the previous time step,  $\mathbf{S}$  is a diagonal matrix penalising the maximum thrust, and  $\mathbf{T}_{t-1}$  is the vector of thrust magnitudes at the previous time step.

### 5.2.2.2 Lagrange Multiplier

The optimum allocation problem can also be solved analytically using the method of Lagrange Multipliers [15], [76]. The method lets to have an analytical solution of the optimum problem (5.19) subject to equality constraints. The problem is formulated as in Theorem 1.

$$\begin{aligned} & \underset{\mathbf{x}}{\text{minimize}} && f(\mathbf{x}) \\ & \text{subject to} && h(\mathbf{x}) = \mathbf{0} \end{aligned} \quad (5.19)$$

**Theorem 1** (Lagrange Multiplier). *Let  $x^*$  a minimum for the problem (5.19) and let  $\nabla h_1(x^*), \dots, \nabla h_m(x^*)$  linear independent. Then  $\exists!$   $\lambda^*$  named Lagrange Multipliers such that*

$$\nabla f(x^*) + \sum_{i=1}^m \lambda_i^* \nabla h_i(x^*) = \mathbf{0}$$

The geometric interpretation is that this method is going to search the minimum of the function  $f(x)$  subject to the constraints  $h(x)$  when the function  $f(x)$  is tangent to the function  $h(x)$ , in other words when the gradient of  $f(x)$  is parallel to the gradient of  $h(x)$ , see Figure 5.4. This method adds the same numbers of  $\lambda$  of the constraints and the same number of relationships of the unknown. The result is a system with the same number of unknowns and equations that can be solved analytically.

Inequalities constraints can be added in the Lagrange Multiplier problem, transforming the nonlinear programming problem of (5.20) to the equality problem (5.21) adding the additional variables  $z_i$ .

$$\begin{aligned} & \underset{\mathbf{x}}{\text{minimize}} && f(\mathbf{x}) \\ & \text{subject to} && h(\mathbf{x}) = \mathbf{0}, \\ & && g(\mathbf{x}) < \mathbf{0} \end{aligned} \quad (5.20)$$

$$\begin{aligned} & \underset{\mathbf{x}}{\text{minimize}} && f(\mathbf{x}) \\ & \text{subject to} && h(\mathbf{x}) = \mathbf{0}, \\ & && g(\mathbf{x}) + z_i^2 = \mathbf{0} \end{aligned} \quad (5.21)$$

The method is applied to two of the case studies: the milliAmpere of Section 7.2 and the PSV of Section 7.4.

In the PSV application, the optimum problem of (5.14) with no bounds and inequalities constraints, the objective function of (5.17), and the equality constraints given by the equilibrium in the horizontal plane are taken into account.

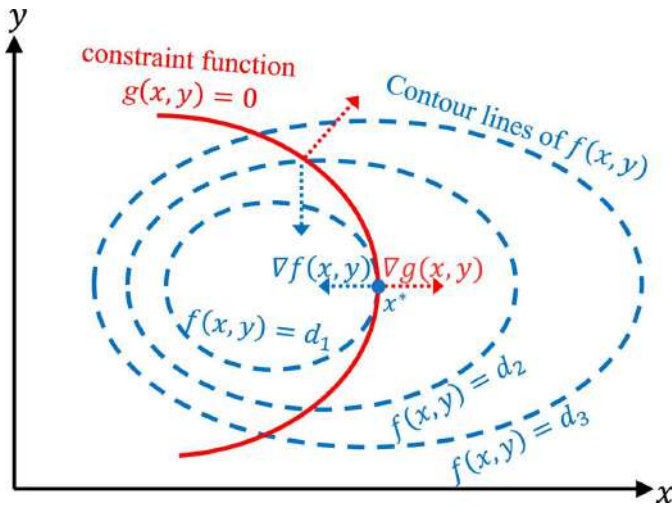


Figure 5.4: Control: 3-DOF - Lagrange Multiplier.

In the milliAmpere application, the actuator angles are kept fixed, reducing the unknown to the only actuator thrust. In this case, the limits on the maximum and the minimum actuator thrust are considered, transforming the inequalities constraints in equalities and adding a number of unknowns that are double with respect to the actuators. The optimum problem is the one of (5.14) with bounds, equality constraints and the objective function of (5.17).

### 5.3 Thrust Allocation Logic

The Thrust Allocation Logic (TAL) module takes as input the thrust request of each actuator computed by the FAL and translate it into an actuator setpoint. The setpoint can be a rate number, a pitch request, a voltage, and an angle setpoint depending on the actuator type or the propulsion plant.

The required thrusts and the actuator setpoints are linked with combinator curves depending on the actuator and the vessel itself. The adopted combinator curves are shown in Section 7 for each test case.

# Chapter 6

## Key Performance Indicators

A set of suitable Key Performance Indicators (KPIs) are proposed for a quantitative comparison among the different scenarios developed. The aim is to exploit and adapt methods already present in the literature in order to better compare the results obtained. In this chapter, the KPI identified for the 2-DOF scenario with the target tracking guidance law of Section 3.1 are selected and shown in Section 6.1, while the different KPI adopted for the different 3-DOF scenarios are presented in Sections 6.2-6.5. In the last case, KPIs for static and dynamic evaluations are considered.

Key Performance Indicators (KPIs) are identified to evaluate mission performances for all the scenarios adopted.

### 6.1 Target Tracking KPIs

The 2-DOF scenario studied in this thesis considers the target tracking guidance law. As shown in Section 3.1, different parameter sets are inside the three guidance laws. They affect the performance of the control scenario and some proper KPIs are needed to quantify the performance.

The first KPI is the distance  $e$  that is equal to the projection of the vector  $(\Omega_T - \Omega_I)$  on  $\underline{f}_2$ . It is possible to evaluate the target trajectory overshoot through  $e$ , because the  $\underline{f}$  basis is fixed with the target velocity. The distance  $e$  is linked to the heading angle  $\psi$ . The maximum and the minimum values during the simulation time ( $e_{max}$  and  $e_{min}$  respectively) are analysed together with the general behaviour.

The second KPI identified is the distance  $s$  that is equal to the projection of the vector  $(\Omega_T - \Omega_I)$  along  $\underline{f}_1$ . Such quantity influences the following manoeuvring stability. The mean value during the following phase,  $s_{mean}$ , is evaluated with the general behaviour.

The third KPI is the interceptor path convergence time  $t_R$ . The latter can be evaluated in a straight path manoeuvre, and it depends on the distance  $s$  and the speed. Indeed, when the speed setpoint converges to the target one, and the distance  $s$  remains constant, the following phase begins, and it is possible to get  $t_R$ .

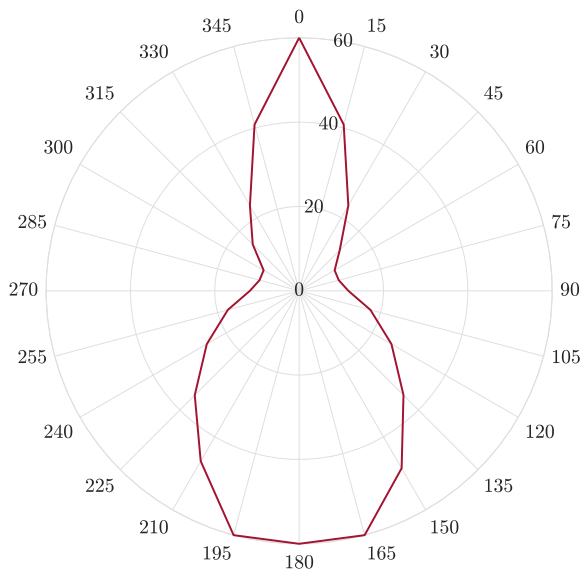


Figure 6.1: KPI - DPCP - Example.

## 6.2 Dynamic Positioning Capability Plot (DPCP)

The station-keeping performance of the proposed vessel and relative propulsion configuration is strictly linked with the environmental disturbances in which the vessel can operate. An indicator of the station-keeping capability is the Dynamic Positioning Capability Plot evaluated at a static and a dynamic level; in this case, it is possible to evaluate the limiting environmental disturbance. The environmental disturbance considered in this analysis are wave, wind, and current as stated in Section 2.6 and can be considered as independent or linked. The representation of the station-keeping capability is standardised in [74]. It leads to having the polar plot where, for each angle, the maximum wind speed that the vessel can support is defined. This analysis considers wind, wave, and current, and their contributions are summed. The coming direction can be considered coincident or not, and the disturbances can be linked or not; for more details see Section 2.6. The analysis can be done at static and dynamic levels. One method for linking the environmental disturbances is, for example, the use of the Beaufort scale of Figure 2.9 or of the Pierson relationship (2.38). An example of DPCP is shown in Figure 6.1.

### 6.2.1 Static analysis

The analysis conducted at the static level wants to evaluate if the selected propulsion plant, together with the selected force allocation algorithms, is able to support the selected environmental disturbance. Hence, only the force allocation problem is solved starting from the environmental disturbance forces and moment array, and the thrust required at each actuator is defined. These values are compared with the maximum available thrust for each actuator; if the required values are lower than the maximum ones, the environmental condition analysed is considered satisfied; otherwise, the analysis is stopped for the selected coming direction, and the maximum allowable value is selected. Usually, a dynamic allowance coefficient

is introduced to consider the dynamic effects in the case of a static analysis. This coefficient increases the environmental forces, and a reasonable value can be 1.25 as suggested by [32] and [113]. It is a rapid and helpful way for comparing different allocation and propulsion plant since only the main vessel dimension are required together with the definition of the allocation logic; hence also the computational time and effort is low.

### 6.2.2 Dynamic analysis

To consider all the dynamic effects that occur during low-speed operations, the DPCP can also be evaluated at the dynamic level. In this case, several dynamic simulations are done to evaluate the maximum environmental condition the vessel can support. In this case, the environmental disturbances are increased until the position and speed errors after the end of the transient phase necessary to initialise the controller are inside the defined limits. When the limits are not respected, the maximum environmental condition the system can support is found. Examples can be found in [113] and [76]. In this case, a fully detailed simulator representing the vessel with the controller and the TAL system is required, hence it results in a huge computational time.

## 6.3 Yearly operability

To better define the operability of the vessel, it is possible to conduct an analysis that considers the environmental condition of a selected geographic area, considering all the probabilistic combinations of environmental and heading conditions. The proposed calculation for each combination of wave height and period present in a geographic area allows the evaluation of an operability index of the vessel in the selected area, [113] and [82]. It is valuable information in the design phase, even more during the vessel operability, since the mission planner can properly select the most appropriate unit to operate in a specific sea area. The scatter diagram allows the knowledge of the wave environmental magnitude; hence, it is necessary to associate a wind condition in terms of speed  $V_w$ . Indeed, thanks to the Pierson wind-wave correlation (2.38), the triplets  $H_{1/3}$ - $T_z$ - $V_w$  are available.

The current speed can be linked or fixed, while the incoming direction is considered the same.

Based on the previous assumptions, it is possible to evaluate the station-keeping capability of the two propulsive configurations for each cell (triplet  $H_{1/3}$ - $T_z$ - $V_w$ ) of the scatter diagram. It means verifying where the static equilibrium between the external and the delivered forces is satisfied. Taking into account if the equilibrium is verified and the probability of occurrence of the cell, it is possible to define an operability index  $\chi$  for each incoming direction analysed  $\gamma_i$  following the formulation in (6.1).

$$\chi_{\gamma_i} = \sum_{j=1}^{n_H} \sum_{k=1}^{n_T} \zeta_{jk} p_{jk} \quad (6.1)$$

where  $n_H$  is the number of the wave height values on the scatter diagram involved in the analysis,  $n_T$  is the number of the wave period values on the scatter diagram involved in the analysis,  $p_{jk}$  is the probability of occurrence of the cell  $jk$ , and  $\zeta_{jk}$

is the function that states if the equilibrium in the cell  $jk$  is satisfied ( $\zeta_n = 1$ ) or not ( $\zeta_n = 0$ ).

In the end, taking into account the analysis done for each incoming direction  $\gamma_i$  and its percentage of occurrence, it is possible to find a global index  $\chi_{tot}$  defined as in (6.2). This index defines the operability of the propulsion configuration in the selected geographic area.

$$\chi_{tot} = \sum_{i=1}^{n_\gamma} p_{\gamma_i} \chi_{\gamma_i} \quad (6.2)$$

where  $p_{\gamma_i}$  is the probability of occurrence of the environmental incoming direction  $\gamma_i$  (see Figure 2.10) and  $\chi_{\gamma_i}$  is defined in equation (6.1).

## 6.4 Emission factor

Besides the operability index  $\chi_{tot}$  that leads to defining the operability of the selected propulsion configuration in the selected geographic area, attention is also on the impact, in terms of greenhouse gas emissions, of the configuration in the selected geographic area as a function of its operability. Indeed, in recent years, studies are done to estimate atmospheric emissions, and in [88] and [86], a review of the methods to perform the global emissions of the marine field is done. The two main methods for performing the ship emission can be divided into top-down and bottom-up methods. The top-down method is also called fuel-based since it estimates the emission in a specific geographic area starting from the fuel usage statistic. The bottom-up method, instead, is also called activity-based since it uses the ship specification plus the operational data to compute the pollutants emitted by a single ship in a specific position. The single data are aggregated over the fleet and time, and the total emissions of an area are computed. The approach is quite similar to a bottom-up method since the starting point is the operational data of the ship.

The analysis wants to estimate the emission of each cell of the scatter diagram where the static equilibrium is verified (i.e. for each triplet  $H_{1/3}$ -  $T_z$ - $V_w$  where  $\zeta_n = 1$ ) starting from the total power required by the actuators  $P_{B_{tot_{jk}}}$ . The first step is to share the load on the available engine. In this case, the load sharing is done by searching the minimum number of motors  $\zeta_{e_{jk}}$  required to meet the demand, and if more than one motor is switched on, the load is divided equally. Hence, the number of the engine turned on  $\zeta_{e_{jk}}$  and the power required for each engine  $P_{B_{jk}}$  is defined for each cell.

After, the Specific Fuel Consumption (*SFC*) of each engine is computed with the formulation proposed in [57] and shown in equation (6.3).

$$SFC_{e_{ik}} = SFC_b(0.455P_{B_{\%_{jk}}}^2 - 0.71P_{B_{\%_{jk}}} + 1.28) \quad (6.3)$$

where  $SFC_b$  is the lowest SFC for a given engine and is reported in Table 6.1 (at 80% of the load) and provided by [57],  $P_{B_{\%_{jk}}}$  is the percentage of the engine load of each cell (i.e. is the value of power required for each engine  $P_{B_{jk}}$  over the maximum value reported in Table 6.1), and  $SFC_{e_{ik}}$  is the SFC of the single-engine for each cell.

The total hourly consumption  $HC_{jk}$  is computed as in equation (6.4).

	<b>HSD</b>	<b>LBSI</b>
	$(\frac{g}{kWh})$	$(\frac{g}{kWh})$
$SFC_b$	185	156

Table 6.1: KPIs - 3-DOF - SFC baseline

$$HC_{jk} = SFC_{e_{ik}} \zeta_{e_{jk}} P_{B_{jk}} \quad (6.4)$$

The pollutant emissions are evaluated based on statistical data. For each pollutant  $P$  an emission factor is defined; this indicates the percentage of each pollutant emitted with respect to the hourly consumption. Hence, each pollutant emission factor  $EF_P$  for each engine is defined according to [57]. The data adopted are reported in Table 6.2. The emission given by each pollutant for each cell  $EM_{P_{jk}}$  in terms of  $[g_p/h]$  are found according to equation (6.5).

$$EM_{P_{jk}} = EF_P HC_{jk} \quad (6.5)$$

<b>EF<sub>P</sub></b>	<b>HSD</b>	<b>LBSI</b>
	$\frac{kg_{poll}}{t_{fuel}}$	$\frac{kg_{poll}}{t_{fuel}}$
$CO_2$	3206	2755
$CH_4$	0.05	11.96
$N_2O$	0.18	0.1
$NO_X$	56.71	13.44
$CO$	2.59	3.97
$NMVOC$	2.4	1.59
$SO_X$	1.37	0.03
$PM$	0.9	0.11
$PM_{2.5}$	0.83	0.1
$BC$	0.38	0.019

Table 6.2: KPIs - 3-DOF - Emission Factor

An approach similar to the one adopted for the operability index described above is found to find an emission index for each pollutant. Taking into account the  $EM_{P_{jk}}$  of each cell of the scatter diagram, the function  $\zeta_{jk}$  that states if the equilibrium is verified, and the probability of occurrence of the cell  $p_{jk}$ , it is possible to define an emission index  $\epsilon$  for each incoming direction analysed  $\gamma_i$  and for each pollutant  $P$  following the formulation in (6.6).

$$\epsilon_{P_{\gamma_i}} = \sum_{j=1}^{n_H} \sum_{k=1}^{n_T} \zeta_{jk} p_{jk} EM_{P_{jk}} \quad (6.6)$$

In the end, taking into account the analysis done for each incoming direction  $\gamma_i$  and its percentage of occurrence, it is possible to find a global index  $\epsilon_{P_{tot}}$  defined as in equation (6.7). This index defines an emission index of each pollutant of the propulsion configuration in the selected geographic area.

$$\epsilon_{P_{tot}} = \sum_{i=1}^{n_\gamma} p_{\gamma_i} \epsilon_{P_{\gamma_i}} \quad (6.7)$$

## 6.5 Integral metrics

Integral metrics can also be used to evaluate the full desired performance. The first formulation dates back to 1942 when the method of the derivative area to measure the control error was proposed for the first time [89]. Metrics are proposed from this first formulation, leading to the well-known formulation defined in [117]. Five different integral metrics are adopted in this thesis.

The Integral of Absolute Error (*IAE*) is introduced in [43] as a measure of the system error and it is defined as in (6.8) with the error of (6.9).

$$IAE = \int_0^t |e_{IAE}(\epsilon)| d\epsilon \quad (6.8)$$

$$e_{IAE} = \sqrt{\mathbf{e}^T \mathbf{W}_{IAE} \mathbf{e}} \quad (6.9)$$

where  $\mathbf{W}_{IAE}$  is a diagonal matrix penalising the pose error.

The absolute value of the error multiplied by the energy consumption (*IAEW*) is proposed in [118] to take into account also the energy consumption, and is defined as in (6.10) with the power consumption of (6.11). It penalises the error linearly with the magnitude and is a measure of control precision.

$$IAEW = \int_0^t |e_{IAE}(\epsilon)| d\epsilon \int_0^t P(\epsilon) d\epsilon \quad (6.10)$$

$$P(t) = |\boldsymbol{\nu}^T \mathbf{W}_\tau \boldsymbol{\tau}_C| \quad (6.11)$$

where  $\mathbf{W}_\tau$  is the diagonal matrix penalising the thrust vector

To take into account the actuator wear and tear and to penalise actuator changes, the Integral of Absolute Differentiated Control (*IADC*) is suggested in [40] and is defined as in (6.12) with the normalised thrust vector of (6.13).

$$IADC = \int_0^t |\dot{\tau}^*(\epsilon)| d\epsilon \quad (6.12)$$

$$\dot{\tau}^* = \sqrt{\dot{\boldsymbol{\tau}}_C^T \mathbf{W}_\tau \dot{\boldsymbol{\tau}}_C} \quad (6.13)$$

The Integral of Absolute Thrust Error (*IATE*) is defined as in (6.14) with the error in (6.15) to take into account the actuation error.

$$IATE = \int_0^t |e_{IATE}(\epsilon)| d\epsilon \quad (6.14)$$

$$e_{IATE} = \sqrt{(\mathbf{T} - \mathbf{T}_{act})^T \mathbf{W}_{IATE} (\mathbf{T} - \mathbf{T}_{act})} \quad (6.15)$$

where  $\mathbf{T}_{act}$  is the actuated thrust and  $\mathbf{W}_{IATE}$  is the diagonal matrix penalising the thrust error.

A variation of the *IAE* index is also added for an initial evaluation of the different reference models for the low-speed range, which is called *IAE - RF*. It is formulated as in (6.16) and it is a function of the error  $e_{IAE-RF}$  between the trajectories computed by each reference model and the straight line trajectory defined between the waypoints.

$$IAE - RF = \int_0^t e_{IAE-RF}(\epsilon) d\epsilon \quad (6.16)$$



# Chapter 7

## Vessel test cases

The above-mentioned guidance, control, and modelling techniques can be applied to different vessels and different case studies can be selected to test and validate it. In this thesis, four test cases are considered, spacing from model scale to prototype and then to full-scale vessel. The Tito-Neri model described in section 7.1 is a model scale vessel physically available in the UniGe laboratory for trial tests together with a detailed simulator. The milliAmpere test case of Section 7.2 is a ferry prototype physically available in the NTNU infrastructures with a detailed simulator. In the end, the last two test cases, the Platform Supply Vessel of Section 7.4 and the Minehunter of Section 7.3, are the vessels in full scale; the Platform Supply Vessel is a real ocean-going vessel and a detailed simulator is available and used, while the Minehunter test case is approached during the early design stage, hence only the main dimension are known. Different actuators, propulsion plants, and hull shapes characterise each test case; further details are shown in the following sections. All the adopted simulators are implemented in Matlab and Simulink.

### 7.1 Tito-Neri tug model

The first test case is a model-scale tugboat (1:33) named “Tito-Neri” and developed by Delft University of Technology for teaching and research activities [53]. It has an overall length ( $L_{OA}$ ) equal to  $0.97\text{ m}$  and is shown in Figure 7.1. The model is available physically in the UniGe laboratory and via an in-house-developed and fully validated simulator. The construction plan is shown in Figure 7.2 together with the main characteristics of Table 7.1. The construction plan is defined starting from the hull shape obtained employing a 3D scanner developed by Shining 3D. The scan results is the elaborated through the Rhinoceros software and the results are shown in Figure 7.3.

A starboard-portside symmetry characterises the model, while the propulsion plant comprises two azimuthal thrusters and a bow thruster to ensure manoeuvrability at low speed, as shown in Figure 7.4. A dedicated DC motor drives each actuator, and a Z-drive shaft is present in each azimuthal shaft line. Two RPM encoders, one on each shaft line, are mounted between the DC motor and the azimuthal component to provide information of the revolutions of the main propellers. Three current sensors were installed downstream of the DC drives for feedback logic application since they let the DC motors know the current absorbed. The electric



Figure 7.1: Test Case - Tito-Neri - Model.

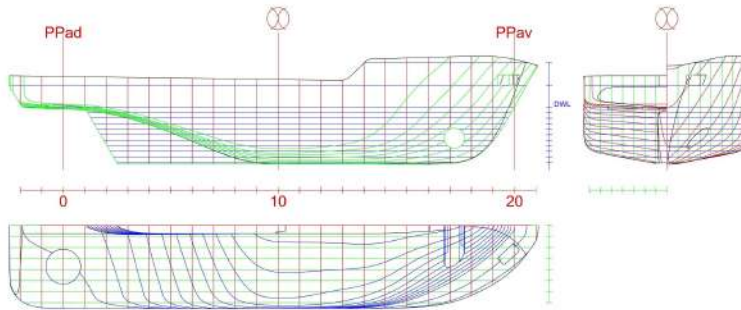


Figure 7.2: Test Cases - Tito-Neri - Construction plan.

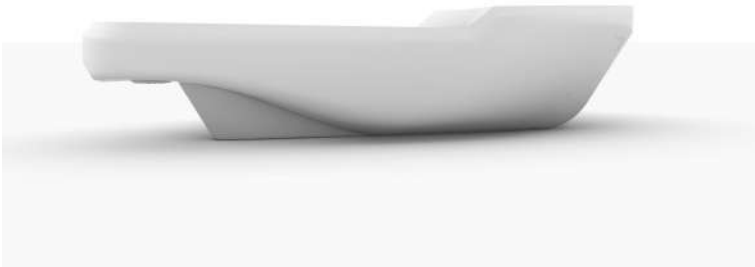


Figure 7.3: Test Cases - Tito-Neri - Hull.

energy is provided by a battery pack that supplies direct current at 12 *Volt*. The model can be equipped with ultrasonic sensors to measure small distances in an acceptably accurate manner, one humidity and temperature sensor to use the sound speed in air to evaluate the obstacle distance, a LiDAR sensor for detection and tracking, and an IMU coupled with a GPS for having the information about the

Name	UoM	Value
$L_{OA}$	(m)	0.97
$L_{PP}$	(m)	0.82
$B$	(m)	0.3
$T$	(m)	0.103
$\nabla$	(kg)	13.275
$(x_{AZ}, y_{AZ})$	(m)	$(-0.41, \pm 0.075)$
$(x_{BT}, y_{BT})$	(m)	$(0.325, 0)$
$V_{max}$	(kn)	2.5

Table 7.1: Test Cases - Tito-Neri - Characteristics.

vessel motion and position. Wireless communication is done via the Xbee module mounted on the onboard microprocessor (Arduino). The communication could also be via cable directly connected to the Arduino board.

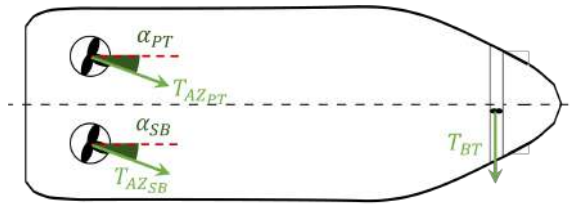


Figure 7.4: Test Cases - Tito-Neri - Actuators layout.

The components of the non-linear simulation model adopted for the Tito-Neri test case are summarised in Table 7.2.

In the 2-DOF scenarios, where the tug is supposed to work in its high-speed regime, only the two azimuthal thrusters are taken into consideration; indeed, the controllable inputs are the voltage  $V_A$  and the azimuth angle  $\alpha$  for each shaft-line. A saturation level is present in the model: the voltage  $V_A$  is saturated with the maximum value of 8 Volt to protect the electric motors. At the same time, the desired heading derivative is limited to a maximum of  $1^\circ/s$  for safety reasons. All the actuators are used in the 3-DOF scenarios, and the azimuthal thrusters can operate in the  $360^\circ$  range.

	Adopted simulated model
<i>Hull symmetry</i>	Portside-Starboard
<i>Hull forces</i>	Oltmann & Sharma, Section 2.3.1
<i>Propulsion Plant</i>	DC, Z-drive with gearbox, according to (2.17)-(2.21)
<i>Manoeuvring Device</i>	2 Az. thruster: model of 2.5.1 with dynamic eq (2.24) 1 Bow Thruster: Section 2.5.2
<i>Env. Disturbances</i>	DNV model [32], Blenderman, and relative currents 2.6
<i>Control variables</i>	Azimuthal and bow thruster voltages ( $V_{A_i}$ , $V_{A_{BT}}$ ), Azimuth angles $\alpha_i$

Table 7.2: Test Cases - Tito-Neri - Adopted simulation model.

The coefficients necessary to describe the hull forces according to the model in 2.3.1 are listed in Table 7.4 while the hull resistance coefficient  $\zeta_{R_T}$  introduced in Section 4.3 is defined by the curve in Table 7.3.

$\mathbf{u}$	$\zeta_{R_T}$
(m/s)	(kg/s)
0	0
0.28	-0.63
0.37	-0.68
0.45	-0.74
0.52	-0.93
0.66	-1.28
0.8	-1.57

Table 7.3: Test Cases - Tito-Neri - Hull resistance coefficient.

Name	UoM	Adopted value
$I_z$	(kg m <sup>2</sup> )	0.8
$(x_G, y_G)$	(m)	(-0.02, 0)
$X_{\dot{u}}$	(kg)	-1.86
$Y_{\dot{v}}$	(kg)	-13.07
$Y_{\dot{r}}$	(kg m)	0.888
$N_{\dot{v}}$	(kg)	0.888
$N_{\dot{r}}$	(kg m)	-0.162
$X_{vr}$	(kg)	13.0706
$X_{rr}$	(kg m)	-0.8876
$X_{vv}$	(kg/m)	0
$c$	-	0.741
$c'$	-	1.039
$d$	-	1
$d'$	-	1
$e$	-	0.204
$e'$	-	0.433
$k$	-	0.4
$K_e$	( $\frac{Nm}{A}$ )	0.0183
$i$	-	3
$R$	( $\Omega$ )	1.51
$L$	(H)	$6.03 \cdot 10^{-4}$
$I_T$	(kg m <sup>2</sup> )	$3.18 \cdot 10^{-5}$
$m_{cos}$	-	-0.296
$m_{sin}$	-	0.939

Table 7.4: Test Cases - Tito-Neri - Parameters.

The thrust coefficient  $\zeta_{AZ}$  defined in 4.3 is defined according to the curve in Table 7.5. The desired speed is reported in the first column, the related shaft-line revolution in the second column, and the thrust coefficient in the last.

The constants of the two first-order equations of (4.5) and (4.7) are defined as

<b>u</b> (m/s)	<b>n</b> (RPS)	$\zeta_{AZ}$ (kg m/s)
0.076	8.58	0.0088
0.19	17	0.0112
0.31	25.37	0.0123
0.42	33.57	0.0146
0.52	41.82	0.0187
0.61	50.07	0.0245
0.71	58.18	0.0283
0.8	66.2	0.0318

Table 7.5: Test Cases - Tito-Neri - Thrust coefficient.

in Table 7.6.

<b>Name</b>	<b>Value</b>
$\tau_n^{AZ}$	0.14
$\tau_\delta^{AZ}$	0.16

Table 7.6: Test Cases - Tito-Neri - Azimuth first order function constants.

The adopted combinator curves for the azimuthal thruster and the bow thruster are in figures 7.5 and 7.6, respectively. Both are a function of the voltage setpoints and link the correspondent thrust.

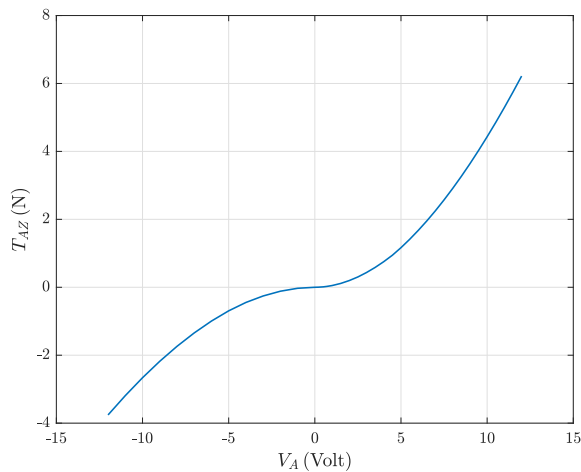


Figure 7.5: Test Cases - Tito-Neri - Azimuthal combinator curve.

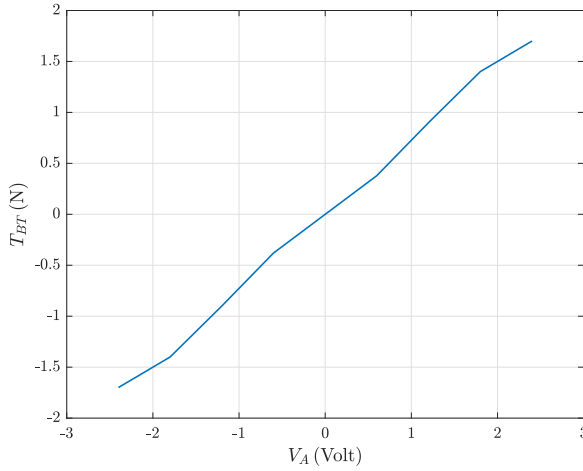


Figure 7.6: Test Cases - Tito-Neri - Bow thruster combinator curve.

## 7.2 milliAmpere ferry prototype vessel

milliAmpere1 (MA1) is an autonomous passenger ferry development prototype, which is used as a test platform in numerous research projects at the Norwegian University of Science and Technology since 2017 [23]. The ferry is shown in Figure 7.7 and is equipped with sensors like GNSS, IMU, Cameras, Radar, and Lidar to fulfil the Navigation system aim. The main characteristics are reported in Table 7.7.



Figure 7.7: Test Cases - milliAmpere - Model.

Name	UoM	Value
$L_{OA}$	( $m$ )	5
$L_{PP}$	( $m$ )	4.8
$B$	( $m$ )	2.8
$T$	( $m$ )	0.2
$\nabla$	( $kg$ )	1800
$(x_{AZ}, y_{AZ})$	( $m$ )	$(\pm 1.45, \pm 0.6)$
$V_{max}$	( $kn$ )	3

Table 7.7: Test Cases - milliAmpere - Characteristics.

The model is physically available and modelled through a non-linear simulator. A post-starboard and fore-aft symmetries characterise the ferry. The details about the model adopted in the milliAmpere simulator are summarised in Table 7.8.

	Adopted simulated model
<i>Hull symmetry</i>	Portside-Starboard, Fore-Aft
<i>Hull forces</i>	MMG-like model, Section 2.3.2
<i>Propulsion Plant</i>	Non-physical model of (2.22)
<i>Manoeuvring Device</i>	4 Az. thruster: Non-physical model of (2.25)
<i>Env. Disturbances</i>	Blenderman and relative current, t Sec. 2.6
<i>Control variables</i>	Actuator revolutions $n_i$ , Azimuth angles $\alpha_i$

Table 7.8: Test Cases - milliAmpere - Adopted simulation model.

The propulsion plant comprises four azimuthal thrusters, an electric motor, and batteries. The four azimuthal thrusters are placed at the four corners, as shown in Figure 7.8. Each thruster can be used within a  $90^\circ$  angle sector, where the working ranges are defined by an interval of  $\pm 45^\circ$  from the reference angle  $\alpha_i^*$ . Two options are identified for choosing the  $\alpha_i^*$  angle: the first is to select the reference angle along the bisectors of the vessel reference frame  $\underline{b}$ , this configuration is named  $\alpha_A^*$  and is shown in the starboard part of Figure 7.8; the second is to choose the reference angle along the diagonals of the rectangular defined by the four actuators, this configuration is named  $\alpha_B^*$  and is shown in the portside part of Figure 7.8.

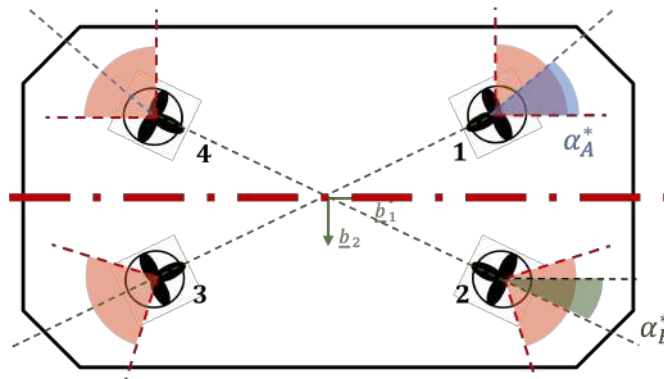


Figure 7.8: Test Cases - milliAmpere - Actuators layout.

The parameters necessary to define the non-linear simulator are reported in

Table 7.9. The parameters came from an identification procedure based on some experimental tests. The system identification problem can be formulated as an Optimal Control Problem where an optimisation problem is solved by simulating the dynamics of the candidate models. Using multiple shooting, it is possible to write the general problem as a Non-linear programming problem, considering the key idea of multiple shooting, for which the integration function can be made arbitrarily linear by reducing the integration time. For more details, see [96].

Variables	UoM	Data
$m$	(kg)	1800
$I_Z$	(kg m <sup>2</sup> )	3280
$X_{\dot{u}}$	(kg)	-589.6570
$Y_{\dot{v}}$	(kg)	-733.911
$Y_{\dot{r}}$	(kg m)	-62.386
$N_{\dot{r}}$	(kg m)	-3069
$X_u$	(kg/s)	-27.632
$Y_v$	(kg/s)	-52.947
$Y_r$	(kg m/s)	24.732
$N_v$	(kg m/s)	3.524
$N_r$	(kg m <sup>2</sup> /s)	-122.860
$X_{ u u}$	(kg/m)	-110.064
$X_{uuu}$	(kg/m)	-13.965
$Y_{ v v}$	(kg/m)	-116.486
$Y_{v r }$	(kg)	-1540.383
$Y_{vvv}$	(kg/m)	-24.313
$Y_{v r}$	(kg)	572.141
$Y_{r r}$	(kg m)	-115.457
$N_{ v v}$	(kg)	-0.832
$N_{v r }$	(kg m)	336.827
$N_{ v r}$	(kg m)	-121.957
$N_{r r}$	(kg m <sup>2</sup> )	-874.428
$N_{rrr}$	(kg m <sup>2</sup> )	0
$K_\alpha$	(deg/s)	37.5
$\epsilon$	(deg)	7
$K_\omega$	(1/s)	0.56

Table 7.9: Test Cases - milliAmpere - Parameters.

The thrust-shaftline revolutions combinator curve is shown in Figure 7.9.

This test case is used in 3-DOF scenarios and also in some cases where the angles are kept fixed with the Lagrange multiplier method, see Section 5.2.2.2. The 3-DOF motion scenario wants to cover the entire speed range of the ferry with two different controllers with the same layout and will be referred to henceforth as low- and higher-speed. These definitions are related to the speed range in which the ferry can operate. The low-speed speed range considers speeds from zero to 0.2 m/s, while the higher-speed range considers speeds up to the supposed maximum speed 1.2 m/s. The selected azimuth angle quadruplets are the following:

- Low-speed with configuration  $\alpha_B^*$ :  $[0^\circ, 0^\circ, 135^\circ - \alpha_B^*, 270^\circ - \alpha_B^*]$  &  $[-\alpha_B^*, 90^\circ - \alpha_B^*, 180^\circ + \alpha_B^*, 270^\circ - \alpha_B^*]$ ; it is shown in Figure 7.10a.



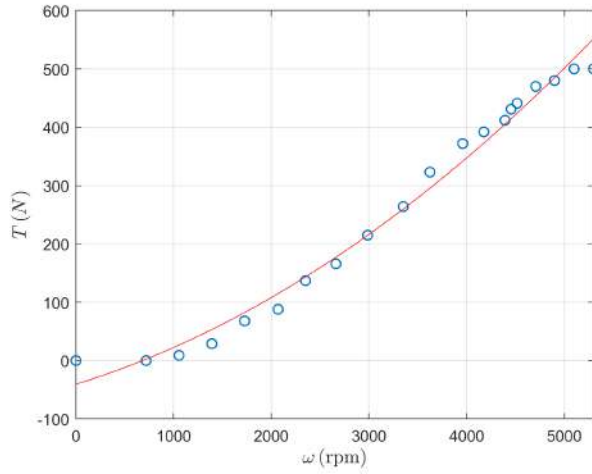


Figure 7.9: Test Cases - milliAmpere - Combinator curve.

- Low-speed with configuration  $\alpha_A^*$ :  $[0^\circ, 0^\circ, 90^\circ, 270^\circ]$  &  $[0^\circ, 90^\circ, 90^\circ, 180^\circ]$ ; it is shown in Figure 7.10b.
- Higher-speed:  $[5^\circ, -5^\circ, 225^\circ - \alpha_B^*, 135^\circ + \alpha_B^*]$  it is shown in Figure 7.10c.

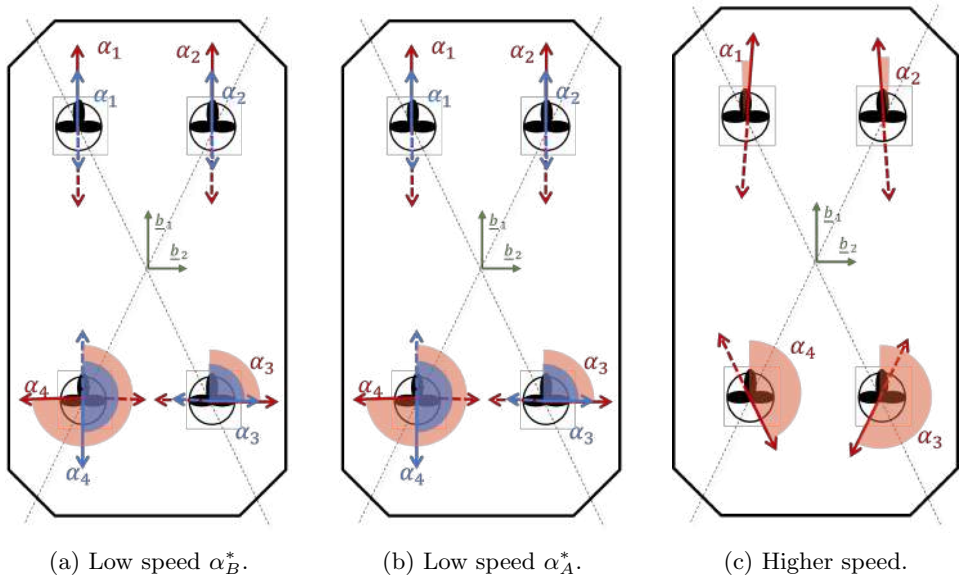


Figure 7.10: Test Cases - milliAmpere - Angles Allocations.

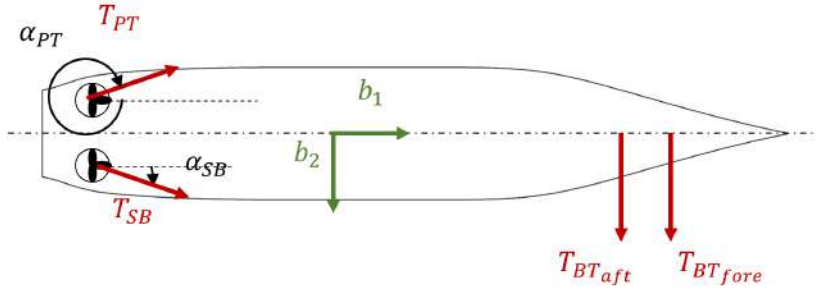


Figure 7.11: Test Cases - Minehunter - Layout configuration A.

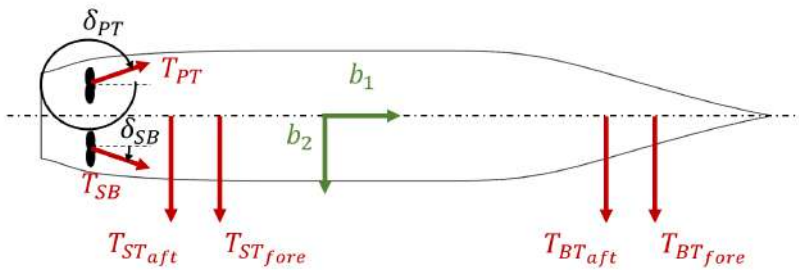


Figure 7.12: Test Cases - Minehunter - Layout configuration B.

## 7.3 Minehunter

The third test case used in this thesis is a Minehunter prototype with the main dimension of Table 7.10. The test case is considered in the early stage design phase; hence, only the main dimensions are defined together with the main data of the proposed propulsion plant. Hence, a fully detailed simulation is not developed, and the approach is done at a static level.

Name	UoM	Value
$L_{PP}$	(m)	60
$B$	(m)	27.3
$T$	(m)	3.18
$\nabla$	(kg)	1200

Table 7.10: Test Cases - Minehunter- Characteristics.

Two propulsion configurations are considered. The layout of the first configuration, named “Configuration A”, is shown in Figure 7.12. It comprises two azimuthal thrusters at the stern and two bow thrusters.

The layout of the second propulsion configuration, named “Configuration B”, is shown in Figure 7.12. It comprises two propeller-plus-rudder actuators, two bow thrusters, and two stern thrusters.

In both configurations, the prime movers and the tunnel thrusters are electric and diesel generators provide the energy. The available power onboard is the same for the two configurations, and the power available at each thruster is reported in Table 7.11. The thrusts available for each actuator are derived using the parametric formulations defined in [32], to maintain the generality of the comparison.

	<b>Configuration A</b>	<b>Configuration B</b>
	(kW)	(kW)
<i>Total Power</i>	2600	2600
<i>Azimuthal Thruster</i>	1000	–
<i>Shaft-line propeller</i>	–	700
<i>Bow Thruster</i>	300	300
<i>Stern Thruster</i>	–	300

Table 7.11: Test Cases - Minehunter - Power distribution.

In both the layout configurations, two different kinds of internal combustion engines for the energy supply are taken into account:

- High-speed diesel engine (HSD). The fuel used in this case is Marine Diesel Oil (MDO).
- Lean Burn Spark-Ignited (LBSI). The engine is mono-fuel and the adopted fuel is Liquefied natural gas (LNG).

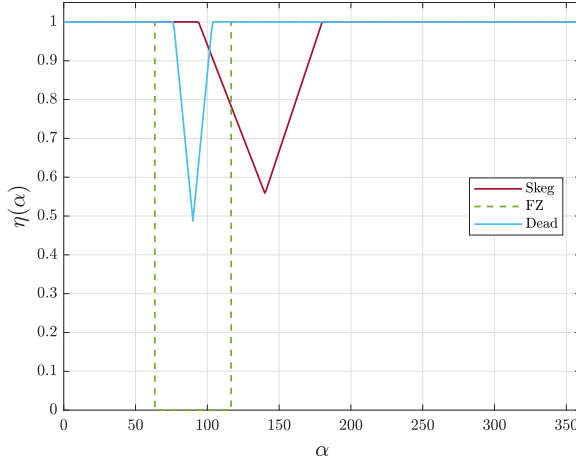
The characteristics of the two types of engines are reported in Table 7.12.

	<b>HSD</b>	<b>LBSI</b>
<i>Engine Power</i>	1300 kW	1300 kW
<i>Engine Number</i>	2	2
<i>Engine Power</i>	MDO	LNG

Table 7.12: Test Cases - Minehunter - Engine Layout.

The environmental disturbances action on the vessel are modelled with the parametric formulation of [32], with the Blenderman wind model [18], and the Faltinsen current model [42].

The interaction between thrusters, with the skeg, and with a dead actuator are considered through parametric formulation like the one proposed in [32]. These formulations are functions of the actuator thrust direction and lead to adding non-linearities to the motion control problem. An example of the loss deduction coefficient  $\eta$  for Configuration A is shown in Figure 7.13. In the figure, the loss due to the skeg is marked in red, the forbidden zones angle is marked with the dashed green line, and the loss due to a dead thruster is marked in light blue. All are function of the azimuth angle.

Figure 7.13: Test Cases - Minehunter - Loss due to interaction  $\eta(\alpha)$ .

## 7.4 Platform Supply Vessel

The last test case adopted in this thesis is the Platform Supply Vessel (PSV) of Figure 7.14; it is an off-shore vessel and its main dimensions are reported in Table 7.13.

Name	UoM	Value
$L_{OA}$	(m)	83.83
$L_{PP}$	(m)	81.5
$B$	(m)	16.8
$T$	(m)	5
$\nabla$	(kg)	2953586
$(x_{AZ}, y_{AZ})$	(m)	$(-38, \pm 3.8)$
$(x_{BT}, y_{BT})$	(m)	$(31.7 - 34.2, 0)$
$V_{max}$	(kn)	14

Table 7.13: Test Cases - PSV - Characteristics.

The vessel is characterised by a starboard-portside symmetry and is modelled through a non-linear simulator. The details about the model adopted for the PSV simulator are summarised in Table 7.14.

The propulsion system comprises two azimuthal and two bow thrusters, each powered by an electric motor. The propulsion plant layout is shown in Figure 7.15. Each azimuthal thruster can rotate of  $360^\circ$  and is modelled through a four-quadrant propeller model function of the effective angle of attack of the actuator  $\alpha_{eff} = \alpha - \beta$  and the advance angle  $\epsilon = \arctan(\frac{J}{0.7\pi})$ . The propeller is a fixed-pitch propeller where the setpoint is the shaft rate of turn. Interactions between thrusters are taken into account in the simulator through an efficiency coefficient that is a function of the azimuthal angle; the function is going to reduce the effectiveness of the actuator when the flush direction is in the direction each of the other actuators, see [28] for more details. A single controllable propeller characterises the two bow



Figure 7.14: Test Cases - PSV - Model.

	<b>Adopted simulated model</b>
<i>Hull symmetry</i>	Portside-Starboard
<i>Hull forces</i>	Oltmann & Sharma model, Section 2.3.1
<i>Propulsion Plant</i>	Non-physical model of (2.22)
<i>Manoeuvring Device</i>	2 Az. thruster: model of 2.5.1 with dynamic eq (2.24) 2 Bow Thruster: Section 2.5.2
<i>Env. Disturbances</i>	Wind, Wave, and Current - DNV model & Parametric formulation with experimental coefficients, Section 2.6
<i>Control variables</i>	Propeller revolutions $n_{AZ_i}$ , Azimuth angles $\alpha_i$ , Bow thruster Pitches $P/D_{BT_i}$

Table 7.14: Test Cases - PSV - Adopted simulation model.

thrusters. They are designed to operate at constant revolution speed and change the pitch to meet various thrust requirements; hence, the pitch is the setpoint. The two bow thrusters are of the single-propeller type, with the propellers symmetrically placed with respect to the middle line. When the thrust is required in the opposite direction to the propeller position, a thrust loss coefficient of 70% determines the thrust requirement of the individual bow thruster.

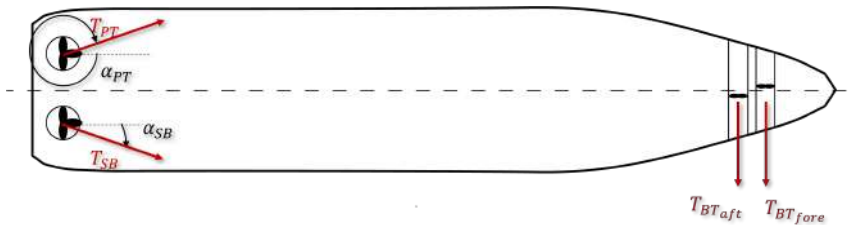


Figure 7.15: Test Cases - PSV - Layout.

The azimuthal and bow thruster combinator curves are shown in figures 7.16 and 7.17, respectively. Propellers with fixed blades characterise the azimuthal thrusters,

and the combinator curve links the thrust  $T_{AZ}$  and the number of revolutions  $n_{AZ}$ . Hence, knowing the required thrust, the setpoint in terms of the number of revolutions is found. The bow thrusters, indeed, are designed to operate at constant revolution speed and to change the pitch to meet various thrust requirements; to be able to assume a setpoint as close as possible to the real one, a corrected setpoint is generated based on the prediction of the sway  $v$  and yaw  $r$  speeds at low speed according to (2.31) and (2.33) where the advance speed  $V_a$  is equal to  $v + rx_{BT}$ . At this point, it is possible to find the pitch request to be sent to the thrusters to satisfy the request given by the allocation as function of the required adimensional thrust and the advance angle.

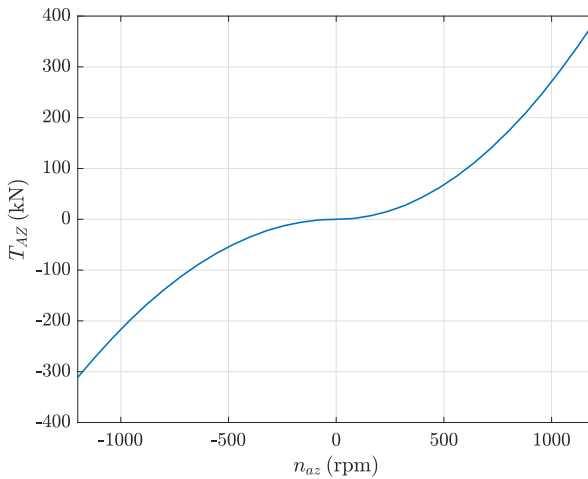


Figure 7.16: Test Cases - PSV - Azimuthal combinator curve.

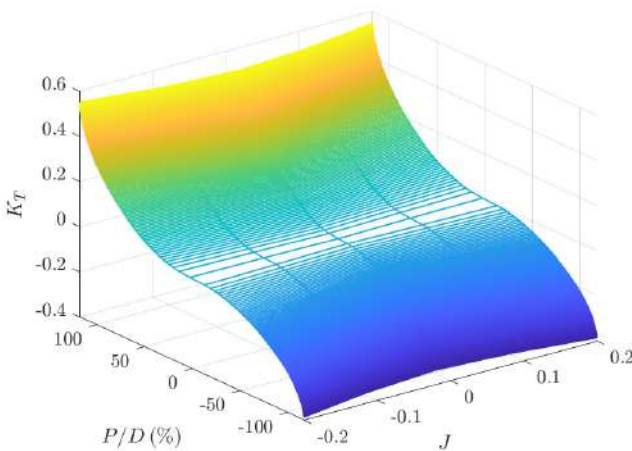


Figure 7.17: Test Cases - PSV - Bow Thruster combinator curve.

# Chapter 8

## Results

The control and guidance logic described in chapters 3, 4, and 5 are tested in the case study described in Chapter 7 and evaluated through the KPIs of Chapter 6. Figure 8.1 summarises the structure of the applications done on the various test cases. In the figure the guidance and control logic adopted for each test case are summarised together with the relative KPIs and the results reported in the following sections.

The Tito-Neri model is a test case for a 2-DOF scenario and the applications done are developed and tested through its simulator. The smart pilot structure and its synthesis approach described in Chapter 4 are applied to this case study together with the Target Tracking guidance logic of Section 3.1. The performances are evaluated through the well-known step response characteristics and the metrics described in Section 6.1. The results reported concern the synthesis of the smart pilot, the results of the target tracking guidance logic, and the introduction of the human inside the simulation loop.

Thanks to its simulator, the milliAmpere ferry prototype vessel is a test case for 3-DOF scenarios. A 3-DOF controller according to Chapter 5 is adopted with optimised allocation logic, and two different guidance logic are used to cover the full speed range, the track keeping guidance of Section 3.2 and the reference models of Section 3.3. Different controller pipeline are adopted and the resulting pipeline results are compared through the integral metrics defined in Section 6.5. The results concern both the defined low and higher-speed scenarios.

The Minehunter case study is approached during its early design stage, where only the main dimensions are known and the propulsion system needs to be defined. The station-keeping capabilities in a 3-DOF scenario are evaluated thanks to a static analysis. Only the force allocation system is developed, and optimisation logic are taken into account according to Section 5.2.2. The adopted KPIs are the DPCP of Section 6.2.1, the operability index of Section 6.3, and the emission factor of Section 6.4. The results are reported in terms of DPCP, operability index, and emission factor for a specific geographical area.

Ultimately, the simulator of the PSV case study is a test case for a 3-DOF scenario. A 3-DOF controller according to Chapter 5 is adopted with optimised and simplified allocation logic, and the evaluations are done with the static and dynamic DPCP of Section 6.2. The results include the static and dynamic analysis in the simulation environment and the dynamic analysis done after introducing the real controller hardware inside the simulation loop.





Tito-Neri		milliAmpere		Minehunter		PSV	
							
Non-linear simulator		Non-linear simulator		Static model		Non-linear simulator	
2-DOF Controller		3-DOF Controller		FAL		3-DOF Controller	
TT		TK RM					
Step-response, TT metrics		Integral metrics		Static DPCP, $\chi_{tot}$ , $\epsilon_{P_{tot}}$		Static and dynamic DPCP	
Smart Pilot synthesis TT results Human in the loop		Low speed range results Higher speed range results		Static DPCP Operability analysis Emission factor analysis		Static Analysis Dynamic Analysis Hardware in the loop	

Figure 8.1: Results - Structure.

## 8.1 Tito-Neri tug model

The Tito-Neri model described in Section 7.1 is used as a test case for the 2-DOF scenario, with the control structure of Section 4 and with the target tracking guidance law of Section 3.1, as shown in Figure 8.1. In this case, the first problem is to validate the synthesised control system, see Section 8.1.1; after a simulation campaign is carried out to validate the proposed layout and to understand the parameter influence assessment, see Section 8.1.2; in the end, an additional test phase leading with the introduction of the human inside the simulation loop, see Section 8.1.3.

### 8.1.1 Smart pilot synthesis results

The smart pilot composed of a speed pilot and an autopilot proposed for the Tito-Neri test case in Chapter 4 is synthesised according to the method proposed in Section 4.4. The resulting controller coefficients are reported in Table 8.1.

Coefficient	Synthesised value
$K_P^u$	15.2855
$K_I^u$	1.1955
$K_D^u$	2.16
$K_P^\psi$	-4.4
$K_I^\psi$	-0.2431
$K_D^\psi$	-0.8039

Table 8.1: Test Case - Tito-Neri - Smart pilot gains.



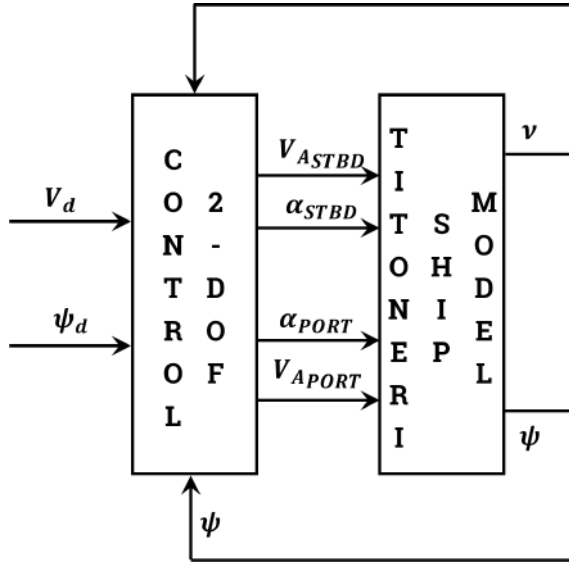


Figure 8.2: Results - Tito-Neri - Smart pilot layout.

The resulting pipeline is shown in Figure 8.2. Here the resulting smart pilot is tested together with the non-linear model of Chapter 2 tailored on the characteristics of the test case described in Section 7.1. The inputs are the desired heading and speed time history. They are defined a priori and three test scenarios are selected for this study.

The three test scenarios used in this case are:

- Scenario A: slam start starting from rest with a concurrent heading change. The desired speed is a step signal from  $0 \text{ m/s}$  to  $0.5 \text{ m/s}$  at the initial simulation time, while the desired heading is a step signal from  $0^\circ$  to  $10^\circ$  always at the initial simulation time, see Figure 8.3a. The initial conditions consider the tug at rest ( $\nu_0 = [0, 0, 0]$ ) and with the heading pointing toward the North ( $\eta_0 = [0, 0, 0]$ ).
- Scenario B: staircase for both velocity and heading changes. A series of ramps and constant setpoints characterise it. The desired speed time history comprises an initial value of  $0.1 \text{ m/s}$  and several ramps leading to  $0.2 \text{ m/s}$  increments in the speed setpoint. The ramps start at  $0 \text{ s}$ ,  $200 \text{ s}$ , and  $400 \text{ s}$  with a length of  $50 \text{ s}$ ,  $30 \text{ s}$ , and  $70 \text{ s}$ , respectively. The ramps on the heading setpoints have the same initial time and the same lengths, but they lead to an increment in the desired heading value of  $5^\circ$  with an initial value of zero. See Figure 8.3b. The initial conditions consider the tug with initial surge ( $\nu_0 = [0.1, 0, 0]$ ) and with the heading pointing toward the North ( $\eta_0 = [0, 0, 0]$ ).
- Scenario C: encompasses several step signals repeated over time for the velocity. The desired speed time history is characterised by an initial value of  $0.1 \text{ m/s}$  and by several steps of  $0.2 \text{ m/s}$  each at the time step  $300 \text{ s}$ ,  $700 \text{ s}$ , and  $1400 \text{ s}$ . The desired heading time history is characterised by an initial value of  $5^\circ$  and by several steps of  $5^\circ$  at time step  $200 \text{ s}$ ,  $500 \text{ s}$ ,  $800 \text{ s}$ ,  $1300 \text{ s}$ , and  $1500 \text{ s}$ . In addition, a sinusoidal signal with amplitude  $10^\circ$ , phase  $0$ ,

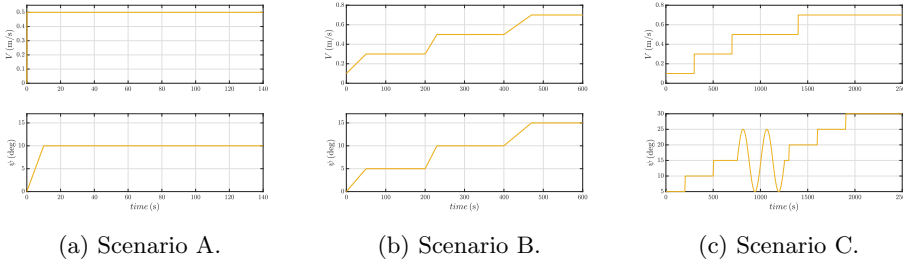


Figure 8.3: Results - Tito-Neri - Smart pilot test desired time histories.

and frequency  $\omega_0 = 1/40 \text{ rad/s}$  starting at 750 s and ending at 1250 s is added. See Figure 8.3c. The initial conditions consider the tug with initial surge ( $\nu_0 = [0.1, 0, 0]$ ) and with the heading pointing at  $5^\circ$  respect the North ( $\eta_0 = [0, 0, 005^\circ]$ ).

For all the figures reported from now on: the voltage and azimuth angle setpoints are marked with the blue continuous line; the speed and heading state are marked with the dashed blue line; the speed and heading setpoints are marked with the red lines; the Ideal Fluid components  $\tau_I$  are marked with the light blue continuous line with circle markers; the Hull Lift components  $\tau_{HL}$  are marked with the dash-dot green line with asterisk markers; the hull resistance component  $R_T$  is marked with the dotted orange line with cross markers; the Hull Cross-Flow components  $\tau_{HC}$  are marked with the dotted purple line with square markers; the total hull forces components  $\tau_H$  are marked with the blue continuous line with pentagram markers; and the azimuthal components  $\tau_{AZ}$  are marked with the dashed red line with triangle marker.

### 8.1.1.1 Scenario A

Firstly, the results coming from the controller synthesis are implemented in scenario A of Figure 8.3a. The well-known step-response characteristics in terms of rise time, peak time, settling time and peak are evaluated to verify the effectiveness of the synthesised controller. Additional information regarding the output value  $V_A$  and  $\alpha$  are computed as the maximum, minimum, and steady-state values and the settling time. The result are reported in Figure 8.4, Table 8.2, and Table 8.3.

In the upper part of Figure 8.4a, the time histories of the voltage computed by the defined speed controller are displayed, while in the bottom part, the results in terms of speed time history are shown. The related speed step-response and input characteristics are reported in the first column of Table 8.2 and 8.3, respectively. As it is possible to see from the results, the synthesised controller reaches the desired speed without overshooting, and the dual behaviour of the speed time history in its initial phase is a consequence of the non-linear contributions of the model.

In the upper part of Figure 8.4b, the time history of the desired actuator angle computed by the defined autopilot is displayed, while in the bottom part, the result in terms of heading time history is shown. The related heading step-response and input characteristics are reported in the second column of Table 8.2 and 8.3, respectively. The results show that the defined controller lets reach the desired heading with a convergent oscillatory behaviour with a maximum overshoot of

about  $2^\circ$ .

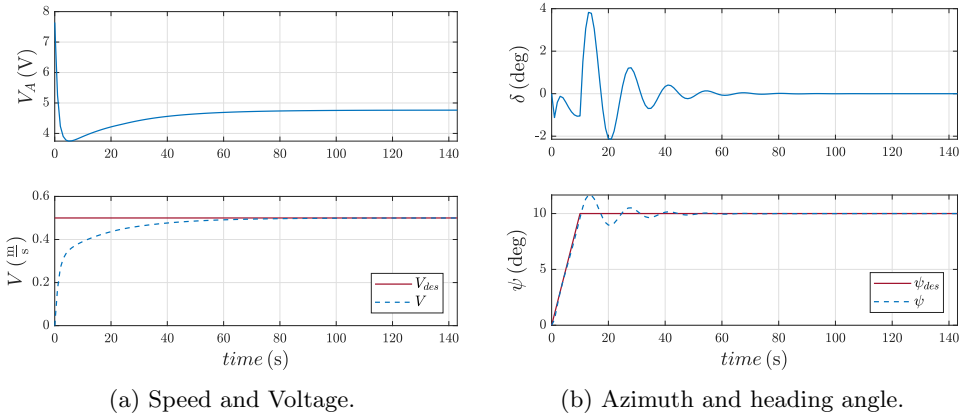


Figure 8.4: Results - Tito-Neri - Scenario A, Setpoints and states time histories.

	$V$	$\psi$
<i>Rise time</i>	29 s	8 s
<i>Settling time</i>	57 s	37 s
<i>Peak time</i>	/	13 s
<i>Peak</i>	/	$12^\circ$

Table 8.2: Results - Tito-Neri - Scenario A, Smart Pilot step-response characteristics.

	$V_a$	$\alpha$
<i>Maximum value</i>	7.6 V	$3.82^\circ$
<i>Minimum value</i>	3.8 V	$-2.14^\circ$
<i>Steady-state value</i>	4.7 V	$0^\circ$
<i>Settling time</i>	64 s	61 s

Table 8.3: Results - Tito-Neri - Scenario A, Smart Pilot input characteristics.

The resultant trajectory is reported in Figure 8.5 and, as expected, is a straight line with a constant heading equal to  $10^\circ$ . In the zoom, it is possible to see the initial transient phase when the tug starts with the heading pointing to the north and is moving to the heading equal to  $10^\circ$ .

The resultant propeller revolution is reported in Figure 8.6 and, as expected, has the same behaviour as the voltage setpoint due to the linear relationship between the two. The stabilised regime speed is of 13 *RPS*.

The hull and azimuthal forces and moment computed with the defined non-linear model of Section 2.3.1 are reported in Figure 8.7. The ideal fluid, lift, resistance, hull, and azimuthal longitudinal components are reported in Figure 8.7a; the ideal fluid, lift, cross flow, hull, and azimuthal lateral forces and moments are reported respectively in Figure 8.7b and 8.7c. The results show that the cross-flow contributions can be considered equal to zero; hence, the hypothesis of neglecting its

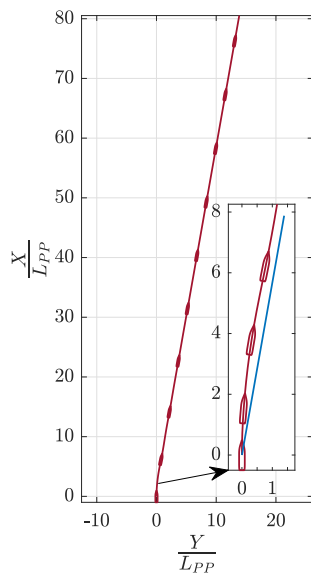


Figure 8.5: Results - Tito-Neri - Scenario A, Trajectory.

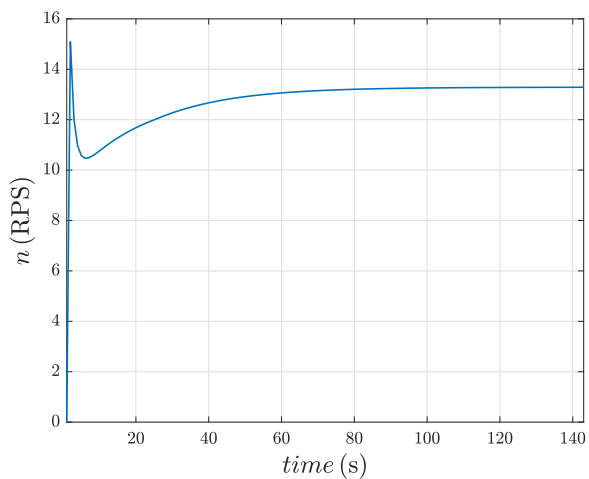


Figure 8.6: Results - Tito-Neri - Scenario A, Propeller revolutions.

contribution in the linearised model is verified. The hull lateral force and moment have an oscillatory behaviour following the same trend and phase as the yaw rate.

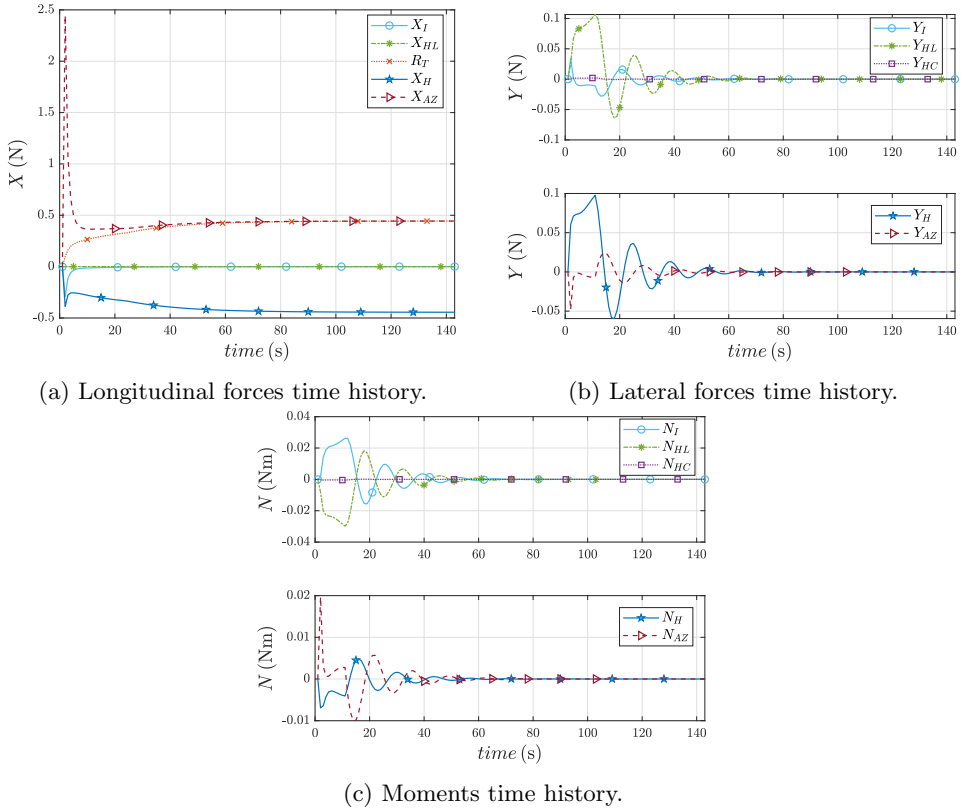


Figure 8.7: Results - Tito-Neri - Scenario A, Hull and Azimuthal Forces.

### 8.1.1.2 Scenario B

The synthesised smart pilot is also tested with scenario B of Figure 8.3b.

In Figure 8.8a, the time history of the voltage computed by the speed controller in the upper part, together with the resulting speed time history in the bottom part are reported. Also in this case, the synthesised controller let to reach the desired speed without overshooting.

In Figure 8.8b, the azimuth angle computed by the heading controller, in the upper part, is reported together with the real heading time history in the bottom. The controller allows it to reach the desired heading with a convergent oscillatory behaviour. Neglecting the initial phase, where the error is considerable, the amplitude of the oscillations is related to the ramp slope; indeed, the second ramp starting at 200 s has a more significant slope with respect to the third one starting at 400 s and the corresponding azimuthal angle maximum values are more considerable.

As expected, the resultant trajectory is reported in Figure 8.9 and is a series of straight lines with constant headings. A zoomed picture reports the initial phase and it is possible to see the tug initial heading pointing to the north and rotating gradually to the desired value.

The resultant propeller revolution is reported in Figure 8.10 and, as expected, has the same behaviour as the voltage setpoint (overdamped). It reaches a steady

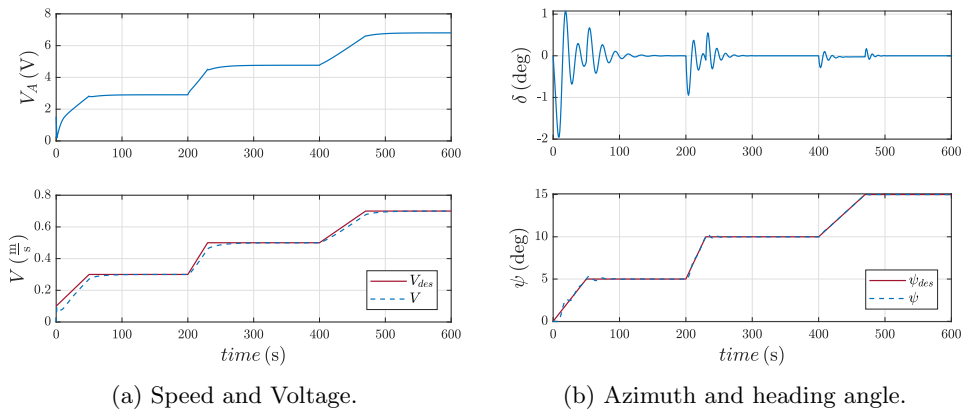


Figure 8.8: Results - Tito-Neri - Scenario B, Setpoints and states time histories.

state value after a transient due to each ramp.

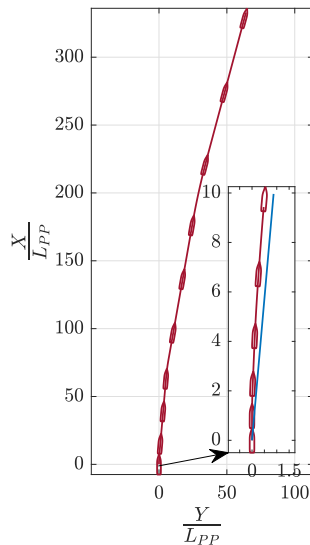


Figure 8.9: Results - Tito-Neri - Scenario B, Trajectory.

The hull and azimuthal forces and moment computed with the defined non-linear model of Section 2.3.1 are reported in Figure 8.11 with the same format of section 8.1.1.1. Hence, the longitudinal components are shown in Figure 8.11a, the lateral one in Figure 8.11b, and the moments in Figure 8.11c. The longitudinal components increase according to the surge speeds, while the lateral and the moment components have a convergent oscillation phase due to the yaw rate behaviour at each ramp set. The cross-flow drag components can be considered neglectable, validating the hypothesis in the linearised model.

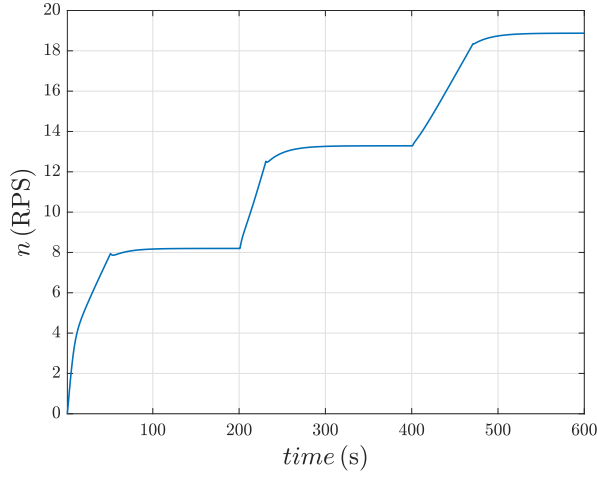
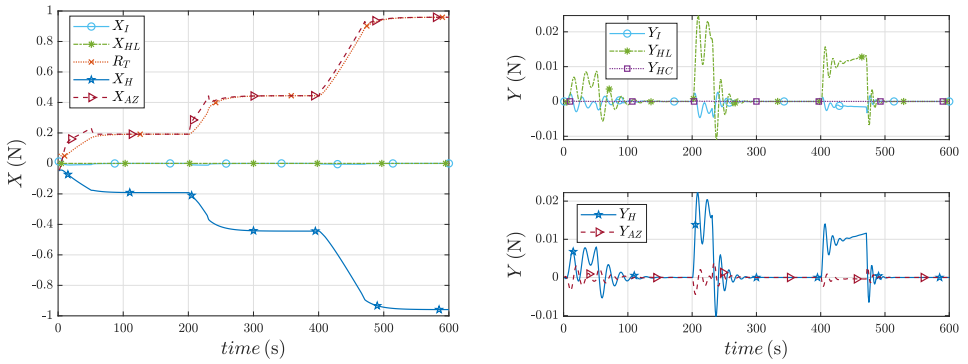
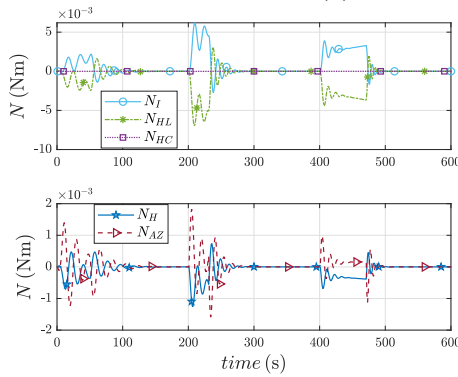


Figure 8.10: Results - Tito-Neri - Scenario B, Propeller revolution.



(a) Longitudinal forces time history.

(b) Lateral forces time history.



(c) Moments time history.

Figure 8.11: Results - Tito-Neri - Scenario B, Hull and Azimuthal Forces.

### 8.1.1.3 Scenario C

The synthesised smart pilot is also tested with the more complex scenario C of Figure 8.3c.

In Figure 8.12a, the speed controller-related variables are reported as done before. The peaks present at each step are a typical behaviour in the DC engines and are not present in the state variable, i.e. the speed, where they are damped, as desired. Instead, in Figure 8.12b, the heading controller-related variables are reported as before. The controller lets reach the desired value besides a small transient phase after each step; the behaviour is oscillatory convergence. All the steps have the same amplitude, but the oscillation amplitude will decrease, increasing time due to the controller integral effect.

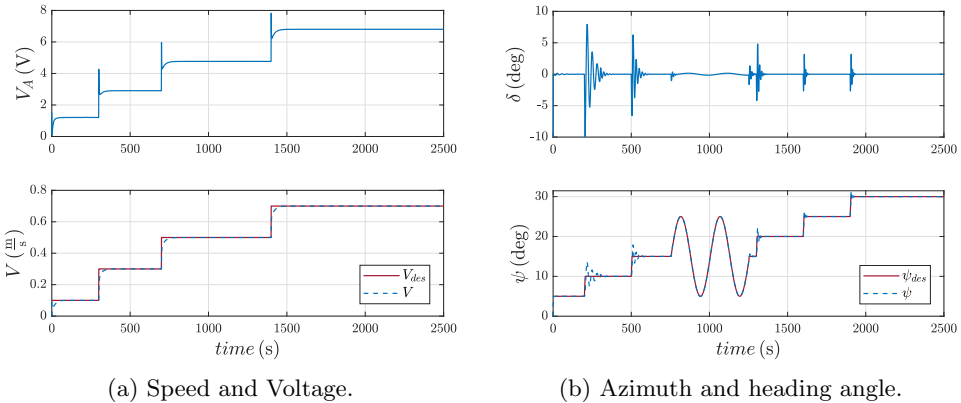


Figure 8.12: Results - Tito-Neri - Scenario C, Setpoints and states time histories.

The obtained trajectory is reported in Figure 8.13 and, as expected, is a series of straight lines with constant headings and with a zig-zag part in the middle. In this case, the initial heading is equal to the desired one.

The resultant propeller revolution is reported in Figure 8.14 and, as expected, has the same behaviour as the voltage setpoint. The peaks linked with the voltage need to be considered for the shafting components design.

The hull and azimuthal forces and moment computed with the defined non-linear model of Section 2.3.1 are reported in Figure 8.15 with the same format of section 8.1.1.1. Hence, the longitudinal components are shown in Figure 8.15a, the lateral one in Figure 8.15b, and the moments in Figure 8.15c. The lateral forces and moments components are equal to zero besides the transient phases that follow each step and the time steps from 750 s to 1200 s where the desired speed is sinusoidal. In this case, the lateral forces and moments components have a sinusoidal behaviour too, since they are linked with the kinematics of the vessel, while the peaks are linked with the behaviour of the azimuth angle. The peaks in the longitudinal forces are also relevant for designing propulsion plant parts like the thrust bearing.



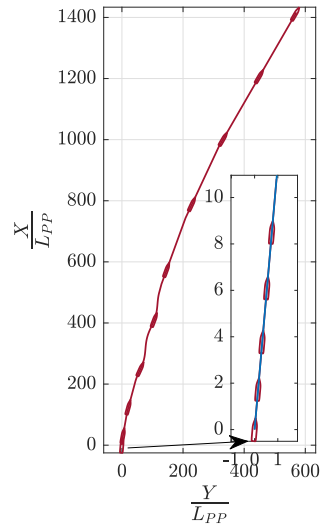


Figure 8.13: Results - Tito-Neri - Scenario C, Trajectory.

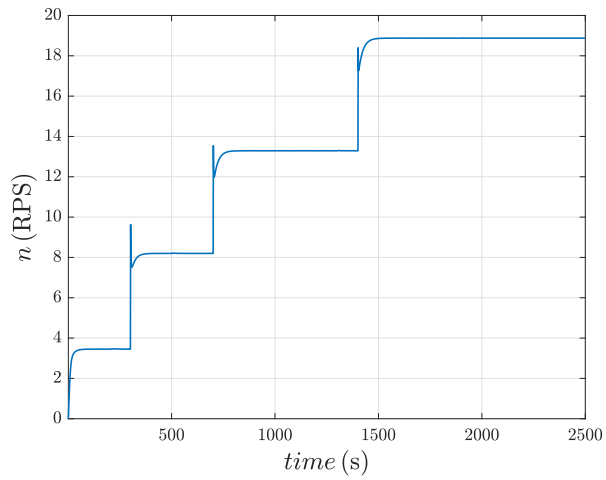
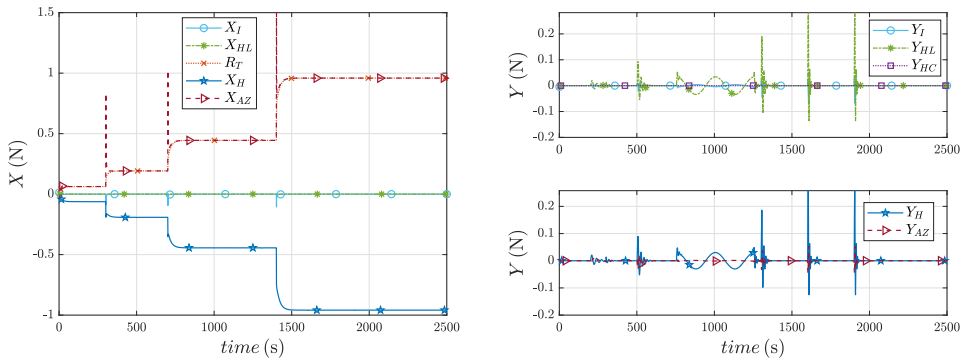
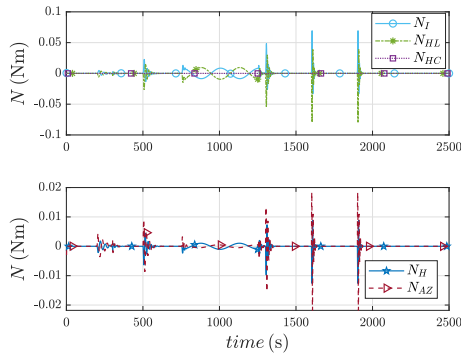


Figure 8.14: Results - Tito-Neri - Scenario C, Propeller revolutions.



(a) Longitudinal forces time history.

(b) Lateral forces time history.



(c) Moments time history.

Figure 8.15: Results - Tito-Neri - Scenario C, Hull and Azimuthal Forces.

### 8.1.2 Target Tracking parameters sensitivity analysis

Thanks to the developed simulation platform and controller, the three guidance law of Section 3.1 are tested with different combinations of parameters. The adopted pipeline is shown in Figure 8.16. Here the three target tracking guidance laws are tested together with the the non-linear model of Chapter 2 tailored on the characteristics of the test case described in Section 7.1 and the smart pilot of Section 4.

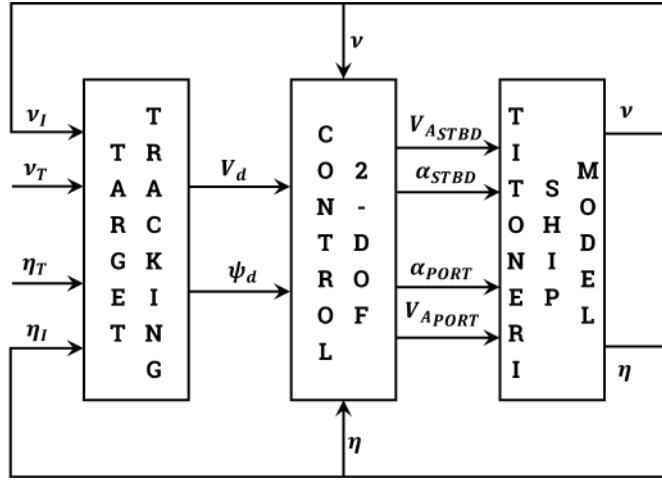


Figure 8.16: Results - Tito-Neri - Target tracking layout.

Each parameter of the guidance laws influences the ship behaviour in the approach and following phases. Table 8.4 summarises the target tracking guidance laws parameters defined according to Section 3.1. This section studies the effect and physical meaning of each input parameter.

Line-Of-Sight	Pure Pursuit	Constant Bearing
$n_{LOS}$		
$p$		$\xi_{CB}$
$k$	$d_D$	$\Delta_{CB}$
$\bar{\delta}t_{hc}$	$K_{PP}$	$K_{CB}$
$\bar{\delta}t_{lc}$		
$Climit$		

Table 8.4: Results - Tito-Neri - Parameters of Target Tracking guidance law.

Three scenarios are adopted and defined through three target paths with different kinematics. The first path is a straight manoeuvre, as shown in Figure 8.17a and named A. The second one is a manoeuvre with two direction changes, i.e. zig-zag manoeuvre; this is reported in Figure 8.17b and is named B. The last is a manoeuvre with significant heading variations and evolutions representing two consecutive Williamson turns, as in Figure 8.17c and it is named C.

The simulation campaign done to evaluate the parameter influence assessment is summarised in the concept map of Figure 8.18. The simulations are done at

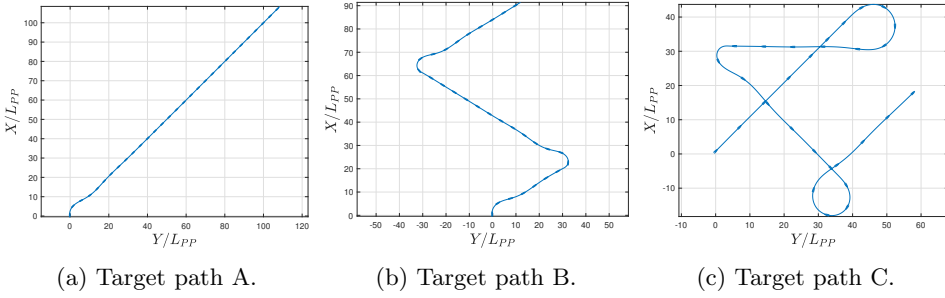


Figure 8.17: Results - Tito-Neri - Operational Scenarios.

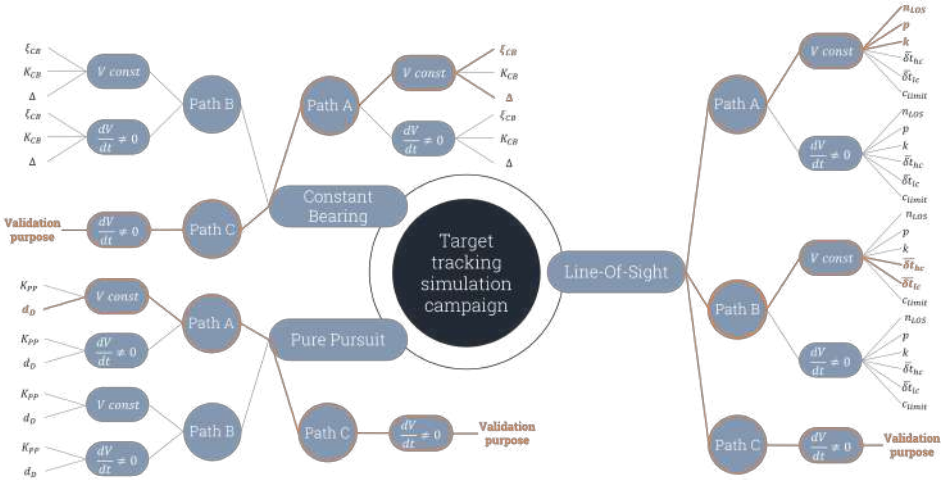


Figure 8.18: Results - Tito-Neri - Concept map of the simulation campaign.

constant and variable speed with different combinations of parameters to investigate the Guidance system response. The parameters were assumed to vary in the following ranges:

- Line-Of-Sight guidance law:  $\frac{n_{LOS}}{L_{PP}} \in [2, 10]$ ,  $\frac{k}{L_{PP}} \in [3, 10]$ ,  $p \in [0.02, 0.1]$ ,  $\bar{\delta}t_{hc} \in [5, 50]$ ,  $\bar{\delta}t_{lc} \in [20, 50]$ , and  $c_{limit}$  is kept fixed;
- Pure Pursuit guidance law:  $d_D \in [2, 15]$  and  $K_{PP} \in [V_T^*, V_{I_{max}}]$ ;
- Constant Bearing guidance law:  $\xi_{CB} \in [1, 10]$ ,  $\Delta_{CB} \in [5, 30]$ , and  $K_{CB} \in [0, V_{I_{max}} - V_T^*]$ .

The most significant tests that help the reader to understand the influence of the input parameters are highlighted in orange in Figure 8.18 and reported hereinafter. The target path A is used for the parameter assessment for the Constant Bearing and Pure Pursuit, and the analysis of  $n_{LOS}$ ,  $p$ , and  $k$  Line-Of-Sight parameters. The target path B is used for the study of the Line-Of-Sight parameters  $\bar{\delta}t_{hc}$  and  $\bar{\delta}t_{lc}$ , while the target path C is used for the validation of the proposed laws and the overall comparison.

Each parameter and KPI is reported in a non-dimensional form. The simulations were all conducted with the same delay between the interceptor and the

target at the initial time step using the initial distance between the two objects of  $17L_{PP}$ .

### 8.1.2.1 Line-Of-Sight analysis

Few trials are performed to evaluate the curvature value,  $c_{limit}$ , corresponding to the target course variation threshold for the updating time interval switch. A value that allows small fluctuations in the path is chosen. The value of  $c_{limit}$  is kept constant for all the tests and it is set equal to  $0.1L_{PP}$ . Table 8.4 summarises the input parameters of the LOS guidance.

The parameters assessment for LOS guidance law is done in two steps. The first one is needed to evaluate the influence of  $n_{LOS}$ ,  $p$ , and  $k$ ; for such parameters, the target path A of Figure 8.17a with a constant speed equal to  $V_T/V_{I_{max}} = 0.6$  is used. The second step concerns the evaluation of the influence of  $\bar{\delta}t_{lc}$  and  $\bar{\delta}t_{hc}$  parameters. Path B of Figure 8.17b is used to appreciate the change of target curvature. In all the cases, the target speed is kept constant with the previous value.

Only the summary of the more significant test is reported in Table 8.5; for the sake of shortness, a summary of the KPI results is given in Table 8.6.

The first three tests (LOS-1, LOS-2, and LOS-3) help understand the influence of the radius of the return circle  $kL_{PP}$ . Indeed, by keeping all the parameters constant, the stabilising radius is evaluated. As expected, results show that  $k$  needs to be large enough to guarantee algorithm stability. Figure 8.19a reports  $e$  fluctuation time histories, i.e. by increasing  $k$  up to the one in test LOS-3, it is possible to avoid the fluctuation, but the distance  $s$  during the steady-state is approximately equal to the largest value assigned to  $n_{LOS}$ , as shown in Figure 8.19b.

Hence, the value of  $n_{LOS}$  is decreased in test LOS-4, and a stable following phase remains at a smaller distance ( $s \equiv n$ ) concerning LOS-1, LOS-2, and LOS-3. Of course, in this case, the KPI referred to the time needed to reach the target ( $t_R$ ) increases since the distance to be covered is larger than the one in the previous tests.

As the next step in the test LOS-5 and LOS-6, the speed low slope  $p$  impact is evaluated. Converging time is not affected by  $p$  increases, but when the target path has significant variations, the speed setpoint changes too fast. On the other hand, with smaller values of  $p$ , converging time increases, as it is possible to see from the KPI in Table 8.6 that increase by 75% approximately.

Simulations LOS-7 and LOS-8 are necessary to evaluate the influence of the

Test	Target path	k	$n_{LOS}$	p	$\bar{\delta}t_{lc}$	$\bar{\delta}t_{hc}$
LOS-1	A	3	7	0.04	25	25
LOS-2	A	5	7	0.04	25	25
LOS-3	A	7	7	0.04	25	25
LOS-4	A	7	2	0.04	25	25
LOS-5	A	7	2	0.06	25	25
LOS-6	A	7	2	0.02	25	25
LOS-7	B	7	2	0.04	25	25
LOS-8	B	7	2	0.04	5	25

Table 8.5: Results - Tito-Neri - Summary of LOS Tests.

Test	$\frac{e_{max}}{L_{PP}}$	$\frac{e_{min}}{L_{PP}}$	Steady-state behaviour of $e$	$\frac{s_{mean}}{L_{PP}}$ at steady-state	Steady-state behaviour of $s$	$\frac{t_R V_T}{L_{PP}}$
LOS-1	3.7	-3.3	Oscillatory	9	Oscillatory	19
LOS-2	1	-1.2	Oscillatory	7	Oscillatory	37
LOS-3	0.5	-1.2	Convergent	7	Stable	37
LOS-4	0.5	-1.2	Convergent	2	Stable	46
LOS-5	0.5	-1.2	Convergent	2	Stable	34
LOS-6	0.5	-1.2	Convergent	2	Stable	80
LOS-7	3.2	-2.5	Convergent	2	Stable	/
LOS-8	2.9	-2.1	Convergent	2	Stable	/

Table 8.6: Results - Tito-Neri - Line-Of-Sight KPI.

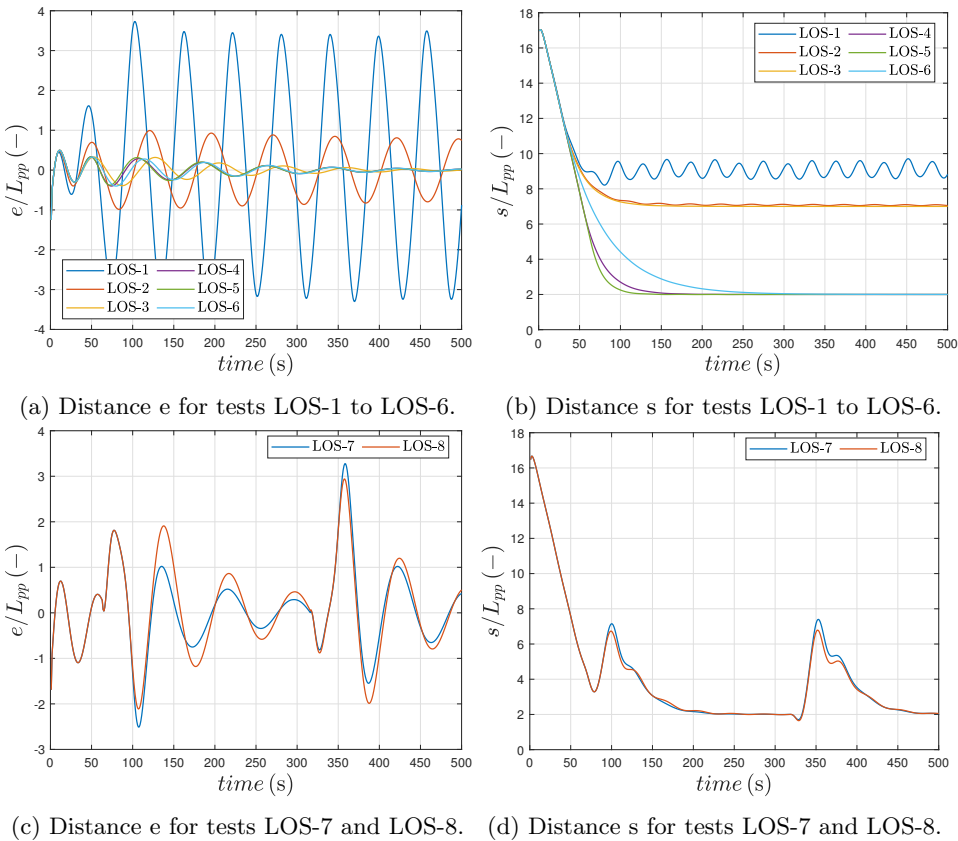


Figure 8.19: Results - Tito-Neri - LOS tests.

time step,  $\bar{\delta t}$ , for the reference update. As it is possible to see from Table 8.5, test LOS-7 has the same parameters as test LOS-4 but with the target path B, while test LOS-8 has a different  $\delta t_{hc}$ . In these cases, two direction changes are present, and it is possible to evaluate the effect of a different  $\delta t_{hc}$  on the overshoot of the distances  $e$ . The comparison is shown in Figure 8.19c and Figure 8.19d, and the KPIs are summarised in Table 8.6. Hence, it is possible to see that a lower

$\bar{\delta}t_{hc}$  reduces the maximum and minimum value of distance  $e$ . This means that, as expected, a lower  $\bar{\delta}t$  is suitable for reducing overshooting after each change of direction.

In tests LOS-7 and LOS-8,  $t_R$  cannot be evaluated since the parameter is defined only for straight manoeuvre. However, the trend observed in the straight manoeuvre could be expected for manoeuvres in which the curvature is relevant.

It is possible to summarise that the radius  $kL_{PP}$  of the return circle defines whether the following phase is stable or not. The parameter  $n_{LOS}$  describes the distance at which the following phase is done, and it can be set as desired. The slope  $p$  of the speed law influences the approach phase. If slope  $p$  decreases,  $t_R$  increases. Instead,  $\bar{\delta}t_{hc}$  and  $\bar{\delta}t_{lc}$  parameters change the reference updating and they become relevant when a relevant curvature is present. When the curvature is greater than  $c_{limit}$ , the  $\bar{\delta}t_{hc}$  needs to be small to follow the target path better.

### 8.1.2.2 Pure Pursuit analysis

The Pure Pursuit input parameters are  $K_{PP}$  and  $\xi_{PP}$ . As shown in section 3.1.2,  $K_{PP}$  is chosen equal to the maximum interceptor speed, allowing the ship to reach the target as fast as possible and exploit the maximum performance. However, as a general remark,  $K_{PP}$  can be set as desired with the only condition that it should be greater than the target speed. Indeed,  $K_{PP}$  is multiplied for a quantity smaller than 1 and if it is lower than the target speed, the interceptor will not be able to reach the target, i.e. the distance between the two ships tends to increase in time.

Hence, the only parameter considered in this analysis is  $d_D$ . All the tests reported are carried out through the target path A of Figure 8.17a with a constant speed equal to  $V_T/V_{I_{max}} = 0.6$  and a summary of the more significant tests is reported in Table 8.7. A summary of the KPI results is given in Table 8.8.

The simulations are done by increasing the value of  $d_D$ . As it is possible to see in Figure 8.20a, with the increase of  $d_D$ , the distance  $e$  tends to avoid fluctuation, from test PP-4 to test PP-6, it is possible to note that the oscillatory and divergent behaviour disappears. On the other side, the distance  $s$ , shown in Figure 8.20b, is linked with the value of  $d_D$ , hence the distance at which the following phase is done increases. The behaviour of  $s$  is stable from test PP-3. Another consequence of increasing  $d_D$  is the growth of  $t_R$  despite the distance to cover to reach the target decrease. It is due to the formulation of the speed law and the presence of  $d_D$  under the square root at the denominator. In this case, it is possible to summarise that the distance  $d_D$  defines the following phase distance and stability. The value of  $d_D$  can be set as desired considering the minimum value ( $d_D = 7.5L_{PP}$ ) that let to avoid the oscillations in the following phase.

Test	Target path	$\frac{d_D}{L_{PP}}$
PP-1	A	2
PP-2	A	4
PP-3	A	5
PP-4	A	7.5
PP-5	A	10
PP-6	A	12

Table 8.7: Results - Tito-Neri - Summary of PP Tests.

Test	$\frac{e_{max}}{L_{PP}}$	$\frac{e_{min}}{L_{PP}}$	Steady-state behaviour of $e$	$\frac{s_{mean}}{L_{PP}}$ at steady-state	Steady-state behaviour of $s$	$\frac{t_R V_T}{L_{PP}}$
PP-1	4	-3.8	Oscillatory	3	Oscillatory	31
PP-2	0.8	-1.2	Divergent	4	Divergent	43
PP-3	0.6	-1.2	Divergent	5	Stable	48
PP-4	0.7	-1.2	Convergent	7.5	Stable	62
PP-5	0.9	-1.2	Convergent	10	Stable	73
PP-6	1	-1.2	Convergent	12	Stable	77

Table 8.8: Results - Tito-Neri - Pure Pursuit KPI.

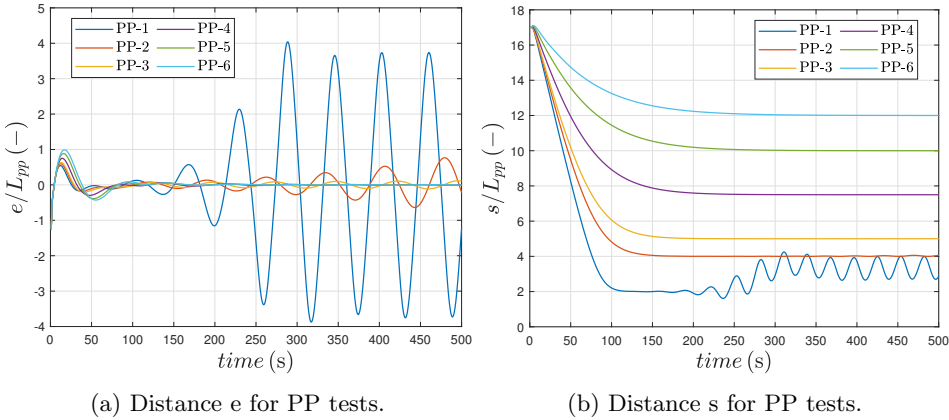


Figure 8.20: Results - Tito-Neri - PP tests.

### 8.1.2.3 Constant Bearing analysis

The Constant Bearing guidance input parameters are three:  $K_{CB}$ ,  $\Delta_{CB}$ , and  $\xi_{CB}$ . As in the previous case, all parameters are included within the sensitivity analysis, except  $K_{CB}$ . Indeed, it is set equal to the difference between the maximum interceptor speed and the target speed in a previous time interval. In this way, as for the Pure Pursuit case, the interceptor can reach the target as fast as possible and compensate for the lack of knowledge about the maximum target speed. All the tests are carried out through the target path A of Figure 8.17a, with a constant speed equal to  $V_T/V_{I_{max}} = 0.6$  and with the distances  $s_{des}$  and  $e_{des}$  set to  $-2L_{PP}$  and  $2L_{PP}$ , respectively. With this setpoint, the interceptor follows the target in a point  $\Omega_T^*$  set ahead and on the starboard side with respect to the target, as shown in Figure 3.5. Among all the simulations conducted, only the more significant are reported in Table 8.9 with the relative KPIs shown in Table 8.10.

The first three tests (CB-1, CB-2, and CB-3) are shown for understanding the effect of  $\xi_{CB}$ . Unlike the detected effect on PP laws, in CB, such quantities only affect  $t_R$ , i.e.  $t_R$  increases together with  $\xi_{CB}$ . The value used in test CB-2 is considered a good trade-off.

The last three simulation results (CB-4, CB-5, and CB-6) show the influence of  $\Delta_{CB}$ . In CB-4, the value of  $\Delta_{CB}$  is increasing with respect to test CB-2 and, as reported in Table 8.10 and Figure 8.22a, the oscillation around  $e_{des}$  value dis-



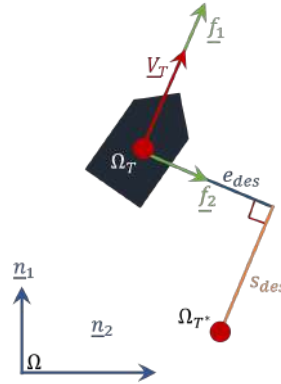


Figure 8.21: Results - Tito-Neri - Sketch of desired distances for CB tests.

Test	Target path	$\frac{d_{gain,CB}}{L_{PP}}$	$\frac{\Delta_{CB}}{L_{PP}}$
CB-1	A	1	10
CB-2	A	5	10
CB-3	A	10	10
CB-4	A	5	20
CB-5	A	5	5
CB-6	A	5	30

Table 8.9: Results - Tito-Neri - Summary of CB Tests.

appears. With a smaller value, like in test CB-5, oscillatory behaviour begins, as shown in Figure 8.22a and Figure 8.22b. Instead, with a larger one, like in test CB-6, there are no benefits with respect to test CB-4.

It is possible to summarise that the parameter  $\xi_{CB}$  influences the time necessary to reach the target ( $t_R$ ), while the parameter  $\Delta_{CB}$  affects the following phase stability.

Test	$\frac{\epsilon_{max}}{L_{PP}}$	$\frac{\epsilon_{min}}{L_{PP}}$	Steady-state behaviour of e	$\frac{s_{mean}}{L_{PP}}$ at steady-state	Steady-state behaviour of s	$\frac{t_R V_T}{L_{PP}}$
CB-1	0.4	-2.6	Convergent	2	Stable	26
CB-2	0.4	-2.6	Convergent	2	Stable	46
CB-3	0.5	-2.6	Convergent	2	Stable	80
CB-4	0.45	-2	Stable	2	Stable	46
CB-5	0.45	-4	Oscillatory	2.5	Oscillatory	77
CB-6	0.4	-2	Stable	2	Stable	46

Table 8.10: Results - Tito-Neri - Constant Bearing KPI.

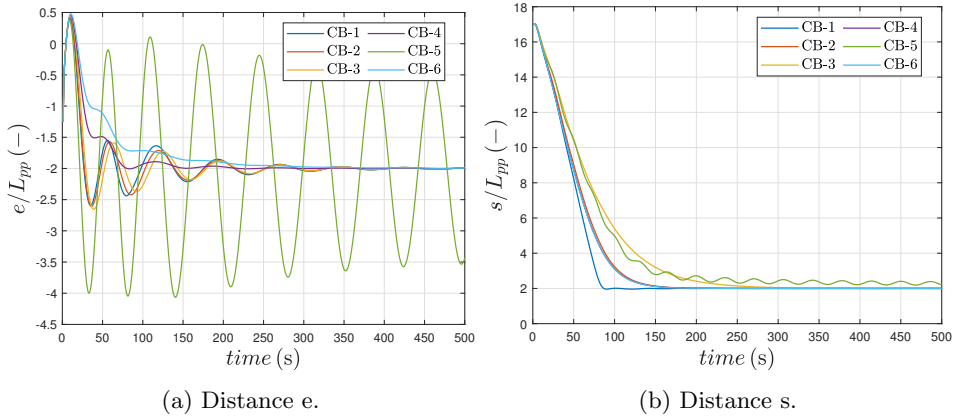


Figure 8.22: Results - Tito-Neri - CB tests.

#### 8.1.2.4 Parameters selection and validation

The influence of each parameter is investigated in sections 8.1.2.1, 8.1.2.2, and 8.1.2.3 with a sensitivity analysis. Hence, selecting a proper set of parameters for each mission is possible based on the mission requirements. Here, the hypothesised mission is that the interceptor must reach the target as soon as possible, with a stable following phase at the shortest distance allowed. Based on that, a set of parameters that accomplish the requirements is selected.

For the Line-Of-Sight guidance, the set used for the test LOS-8 of Table 8.5 is selected. The reason is related to the values of KPIs; indeed, the distance  $s$  is the shortest allowed (i.e. the following phase is the nearest), and the distance  $e$  is lower than  $3L_{PP}$  with the target path B of Figure 8.17b, this set lets to reach the target quickly.

For the Pure Pursuit guidance, the set used for the tests PP-4 of Table 8.7 is selected because it is the simulation with the smallest distance  $s$ , as shown in Table 8.8, without unstable responses during the following phase.

The set used for the test CB-4 of Table 8.9 is selected for the Constant Bearing guidance. In this law, the distance at which the following phase is done does not affect the behaviour and can be chosen as desired. This set of parameters allows reaching the target quickly, as it is possible to see from the  $t_R$  KPI in Table 8.10 and to have stable behaviour, as it is possible to see from the behaviour of  $e$  and  $s$ .

The three laws are tested with the set of parameters defined above, with the target trajectory shown in Figure 8.17c, where the target navigates with a variable speed, as shown in black in Figure 8.23c. The interceptor starts with an initial delay, that assumes the same value for all the guidance methods. All the trajectories are reported together at different time steps better to understand the differences among the three guidance laws, as shown in Figure 8.24. Here, the three guidance laws outcomes, Line-Of-Sight, Pure Pursuit, and Constant Bearing are reported in red, blue, and green, respectively, while the target trajectory is reported in black. The time history of distance  $e$ , distance  $s$ , speed  $V$ , distance  $d_{T,I}$ , and heading angle  $\psi$  is reported from Figure 8.23a to Figure 8.23e.

The Line-Of-Sight guidance is the fastest to reach the target, as shown in Figure 8.23d, since the speed is set equal to the maximum value for long-distance, see

Figure 8.23c. However, it has a relevant overshoot after each change of direction, as shown in the slideshow in Figure 8.24, in the time history of the heading angle in Figure 8.23e, and in the time history of the distance  $e$  and  $s$  in Figure 8.23a and Figure 8.23b. With this law and thanks to the  $n_{LOS}$  parameters, is it possible to set the distance along the vector  $\underline{f}_1$  for the following phase. Hence, the interceptor follows the target trajectory with a given distance.

The Pure Pursuit model has a speed law proportional to the distance between the target and interceptor, and after each change of direction, it tends to converge, as shown in Figure 8.23e. However, in this law, the distance  $s$  is larger during the following phase than in the LOS and CB laws, as shown in Figure 8.23b. Also, in this case, it is possible to set the distance at which the following phase ( $d_D$ ) is done, but in Section 8.1.2.2 is shown that this value needs to be larger than  $7.5L_{PP}$  to obtain a stable following phase.

The Constant Bearing model, like the Pure Pursuit one, has a speed law proportional to the distance between the target and the interceptor, but in this case, the speed law depends on the target speed. Indeed, it is possible to give as input the desired distances for the following phase along the vector  $\underline{f}_1$  and  $\underline{f}_2$  ( $e_{des}$  and  $s_{des}$ ). This law is the fastest to stabilise after each direction change, as it is possible to see from Figure 8.23e. Hence, the model with this law tends to converge to a parallel path with respect to the target one.

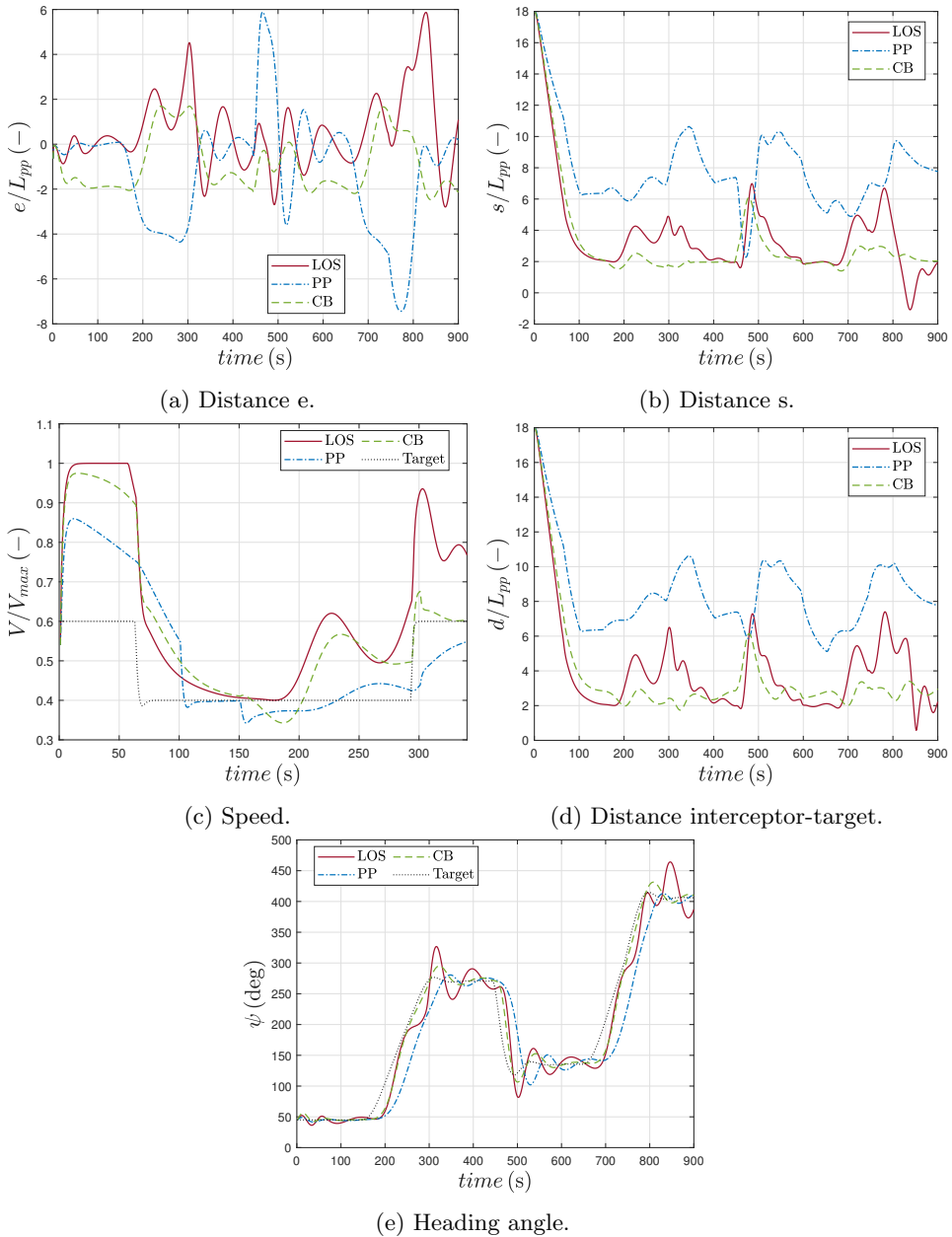


Figure 8.23: Results - Tito-Neri - Overall comparison.

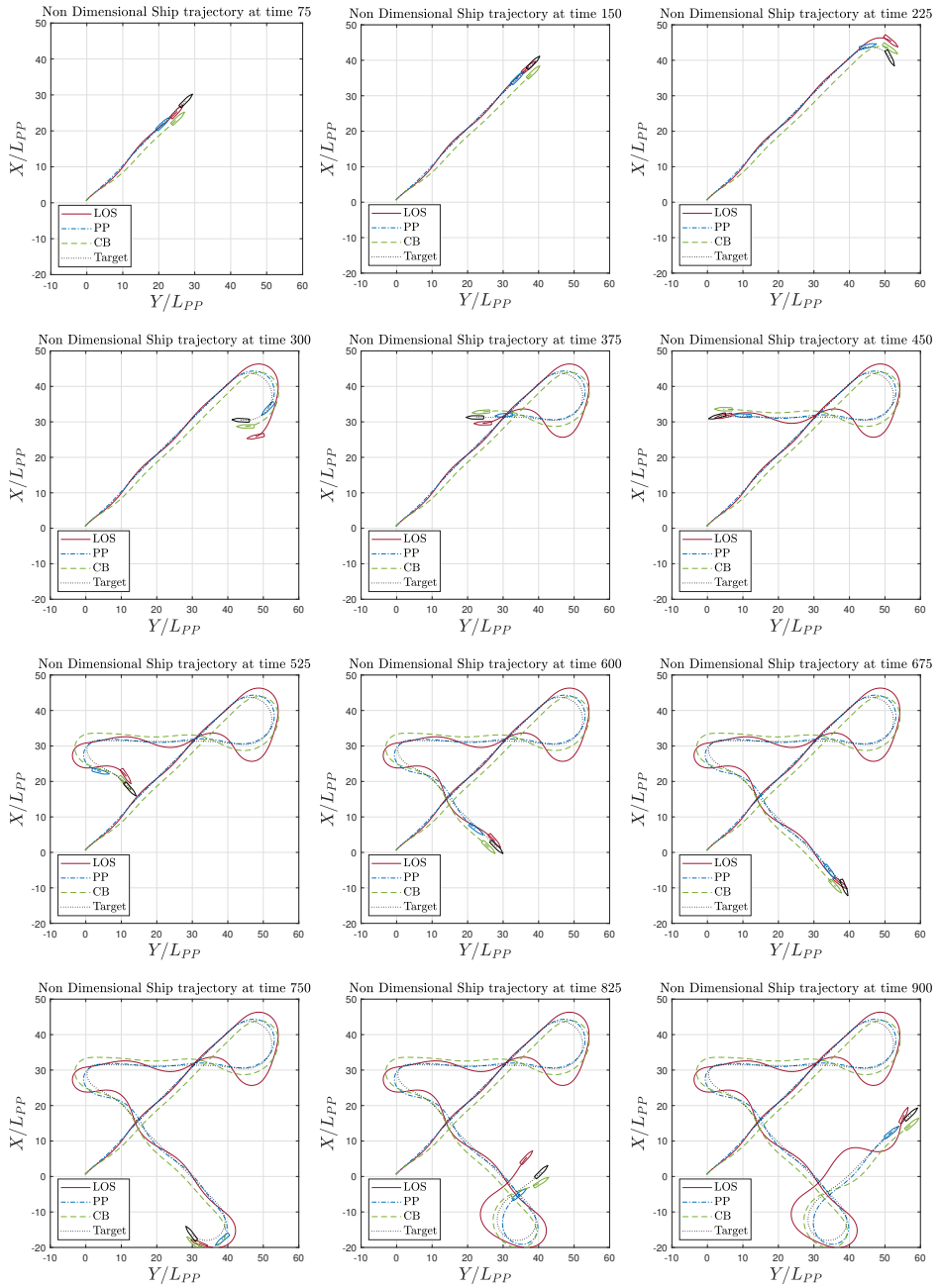


Figure 8.24: Results - Tito-Neri - Slideshow.

### 8.1.3 Human in the loop

The 2-DOF scenario of the Tito-Neri test case is also tested introducing the human inside the simulation loop. He interacts with the simulator, and the reaction of the autonomous system can be tested. The ultimate aim of this approach is to further test the developed tracking algorithm. Indeed, the target trajectories adopted in Section 8.1.2 are defined a priori, while here the additional evasive action resulting from human thinking is introduced for further testing. In addition, IMO 2-3 levels involve humans within the control loop, so it may be a first step to test the systems from this perspective.

The architecture adopted is drawn in Figure 8.25. The target setpoints are given manually by an operator via a human-machine interface. Since the target has two azimuthal thrusters, the manual setpoints are each azimuthal voltage and azimuthal angle. The signals are processed through the ship model of Chapter 2 that computes the target trajectory and sends it to the interceptor. The interceptor, instead, is an autonomous ship model with the 2-DOF controller of Chapter 4 and the Constant Bearing target tracking law of Section 3.1.3. It automatically computes the course through the guidance module. It computes a speed and heading setpoints to be sent to the control module and after to the ship model that computes the interceptor trajectory that follows the target.

The test is done setting the distances  $e_{des}$  and  $s_{des}$  along the  $f$  basis equal to  $2L_{PP}$  and  $-2L_{PP}$ , respectively and the total time is of 1000 s. The trajectory covered during the simulation is shown in Figure 8.26a: the target is marked in red, the interceptor in blue, and the yellow lines are used to connect the target and interceptor positions at the same time step.

The inputs in terms of azimuth angle and voltage given manually to the target are shown in Figure 8.26b and 8.26c. The inputs are required for the starboard and portside azimuth thrusters, but in this case, the choice was to couple the starboard and portside signals and mimic a navigation situation.

In Figure 8.26d, the speeds of the target and the interceptor are shown. In red is shown the target speed as the result of the manual inputs, in green is shown the maximum speed available for the interceptor, in orange, the desired value found by the guidance law, and in blue is the speed assumed by the interceptor in reaction to the setpoint given by the guidance.

In Figure 8.26e, the heading setpoint given by the guidance law, in orange, and

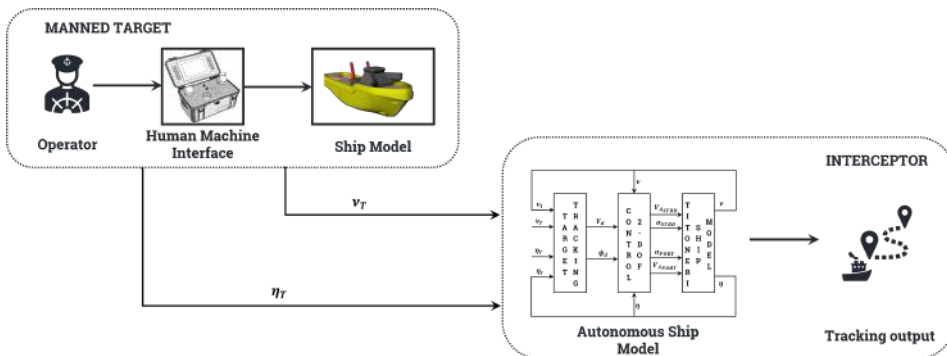
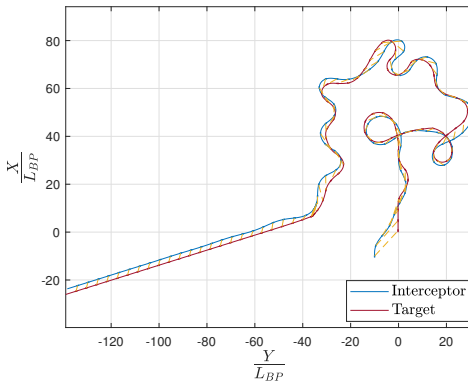


Figure 8.25: Results - Tito-Neri - Simulation Loop Framework.

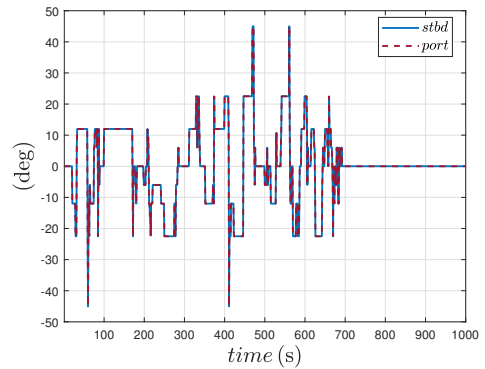
the real value, in blue, are shown.

In Figure 8.26f, the distances between the interceptor and the target are shown, the distance  $e$  is shown in yellow, while the distance  $s$  is shown in purple.

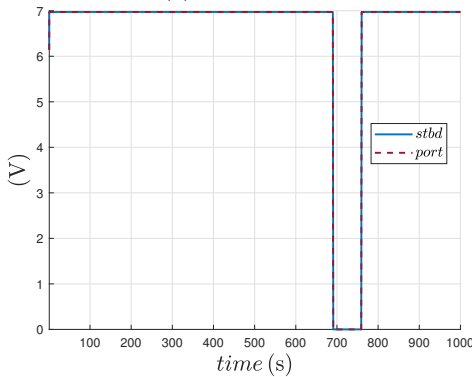
As it is possible to see in Figure 8.26c, it is tried to keep the maximum speed available for the target to leave behind the interceptor, and to stop the voltage inputs of the target, around 700 s, to see how the guidance law reacts when the target stops. As it is possible to see from the target path in Figure 8.26a, the trajectory given as input through the azimuth angles in Figure 8.26b has several changes of direction and ends with a straight path to see the following part. Indeed, in the final part, the interceptor speed is set equal to the target one, as shown in Figure 8.26d, and the distances are set equal to the desired values, as shown in Figure 8.26f. From the results, it is also possible to note that when the speed target goes to zero, the interceptor stops to wait for the target, as highlighted in Figure 8.26d, and that the interceptor, thanks to the guidance law, reacts at each change of direction properly.



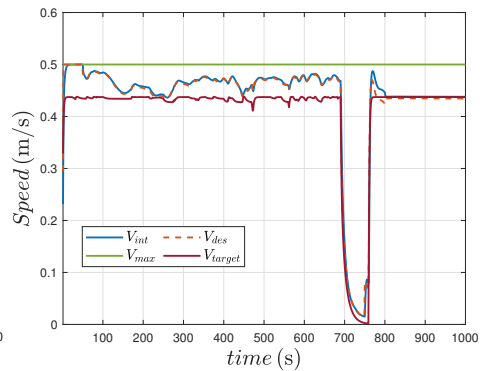
(a) Trajectory.



(b) Target manual input - Azimuth angles.



(c) Target manual input - Voltages.



(d) Interceptor and Target speed.

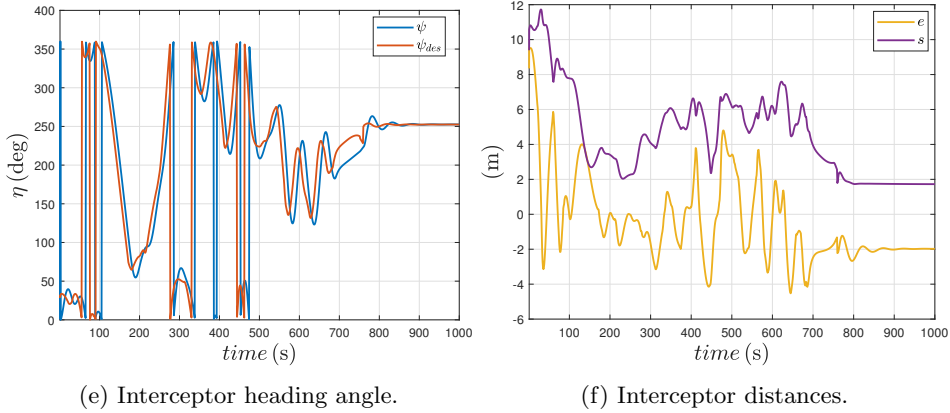


Figure 8.26: Results - Tito-Neri - HIL.

## 8.2 milliAmpere ferry prototype vessel

The milliAmpere test case described in Section 7.2 is used to test and develop 3-DOF scenarios. All the wall speed range is considered and controlled with two controllers, the so-called low speed and higher speed, as defined in Section 7.2.

### 8.2.1 Low Speed range scenario

Different solutions are considered for defining the low-speed range scenarios. All the controllers have the structure of Figure 8.27, and the test summary is shown in Figure 8.28.

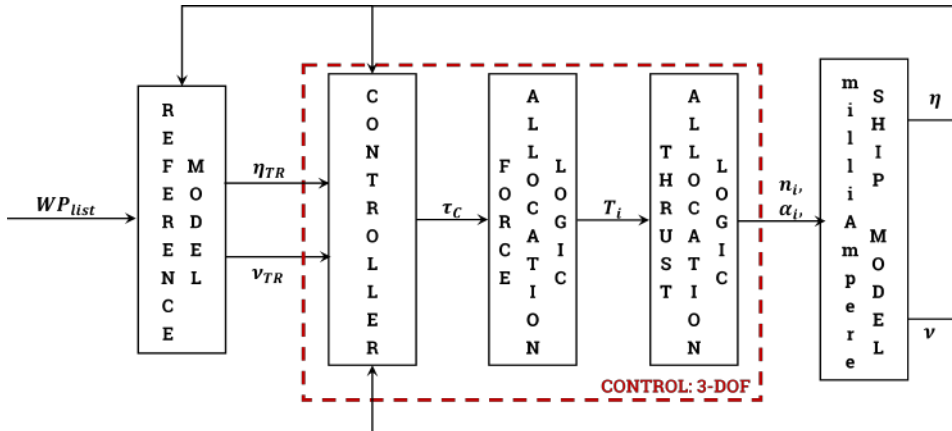


Figure 8.27: Results - milliAmpere - Low-speed layout.

The three reference model of Section 3.3 are taken into consideration together with the two solutions proposed for the reference angle  $\alpha_i^*$  shown in Section 7.2 and Figure 7.8, the controller of Section 5.1.1, the thrust allocation composed by the combinator curve of Figure 7.9, and the three different force allocations. The three allocations are the following:



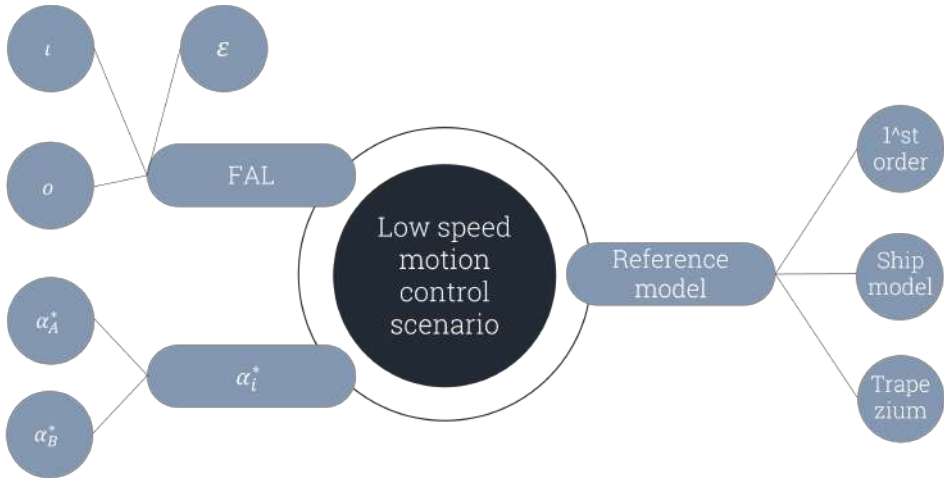


Figure 8.28: Results - milliAmpere - Concept map of the simulation campaign.

- $\kappa$ : optimal allocation solved with non-linear programming techniques of section 5.2.2.1. The problem is the one in (5.14) with no inequality constraints, the equality constraints of (8.1), the objective function of (5.17), the unknowns are  $\mathbf{x} = [X_i, Y_i, T_i, \alpha_i]^T$ ,  $i = 1, \dots, 4$ , and the lower and upper bound comes from the minimum and maximum thrust and from the azimuth angle limits coming from the selected reference angle  $\alpha_i^*$  mode.

$$h(\mathbf{x}) = \begin{cases} \sum_{i=1}^4 X_i - \tau_C(1) \\ \sum_{i=1}^4 Y_i - \tau_C(2) \\ \sum_{i=1}^4 (x_{azi}, y_{azi}) \times (X_i, Y_i) - \tau_C(3) \\ T_i^2 - X_i^2 - Y_i^2 \\ \alpha_i - atan2(Y_i, X_i) \end{cases} \quad (8.1)$$

- $\Xi$ : optimal allocation solved with non-linear programming techniques of Section 5.2.2.1. The problem is the one in (5.14) with the inequality constraints of (5.16), the equality constraints of (8.1), and the objective function of (5.18).
- $\Pi$ : semi-optimal allocation solved with Lagrange multiplier method of Section 5.2.2.2. The optimum problem is the one of (5.20) where the equality constraints are the one in (8.2) together with the bounds on the minimum and maximum thrusts. The bounds were transformed into equalities by introducing a variable for each inequality as explained in Section 5.2.2.2. The number of unknowns is reduced since the angle are kept fixed ( $\mathbf{x} = [T_i]^T$ ,  $i = 1, \dots, 4$ ), the selected angle allocations are shown in Section 7.2 and figures 7.10b and 7.10a.

$$h(\mathbf{x}) = \begin{cases} \sum_{i=1}^4 T_i \cos \alpha_i - \tau_C(1) \\ \sum_{i=1}^4 T_i \sin \alpha_i - \tau_C(2) \\ \sum_{i=1}^4 (x_{azi}, y_{azi}) \times (T_i \cos \alpha_i, T_i \sin \alpha_i) - \tau_C(3) \end{cases} \quad (8.2)$$

All the combinations are tested through simulations with a four-corner test scenario shown in [112]. The four-corner test allows the evaluation of the trajectory tracking capabilities of the ferry for each degree of freedom and with the coupled motions. During the test, the following waypoints are reached: the starting point is the position  $[0, 0, 0^\circ]^T$ , then the ferry moves to  $[l, 0, 0^\circ]^T$  with a pure surge motion, then it moves in  $[l, l, 0^\circ]^T$  with a pure sway motion, then it rotates up to  $[l, l, 45^\circ]^T$  with a pure rotation motion, then it moves in  $[0, l, 45^\circ]^T$  coupling the surge and sway movements, and at the end, it comes back to  $[0, 0, 0^\circ]^T$ , thus coupling all the motions. The side of the square  $l$  is assumed to be equal to 10 m in these tests and the time assumed to cover one side is assumed to be  $t^* = 100$  s. The scheme is shown in Figure 8.29.

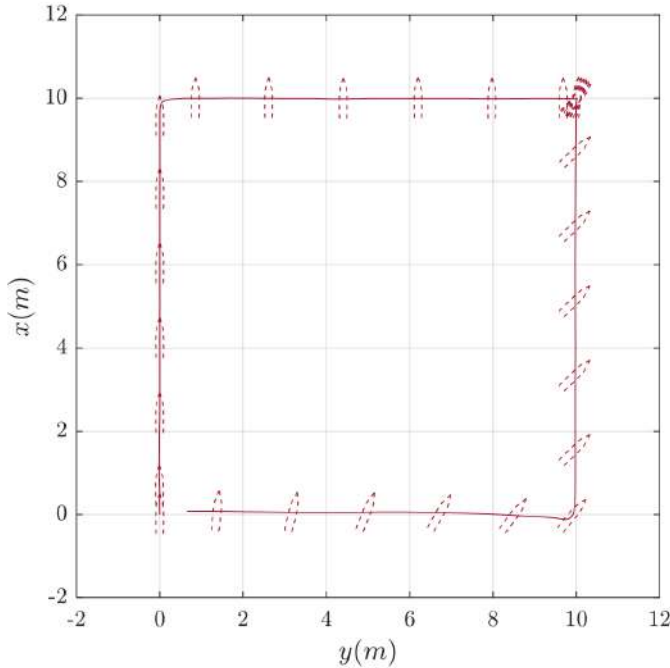


Figure 8.29: Results - milliAmpere - 4 corner test.

The first evaluation is done on the proposed reference models of section 3.3 on the four-corner trajectory with the IAE-RF metrics. The adopted reference models are the first-order transfer function, the trapezium speed law, and the ship model. The results in terms of  $IAE - RF$  are reported in Table 8.11. From these, it is possible to see that the trapezium and the 1<sup>st</sup> order model have small values of  $IAE - RF$ , while the vessel model has the biggest value due to some delays that arise when there is a change of the corner. Hence, only the trapezium and the 1<sup>st</sup> order reference model are taken into consideration in the following tests.

Since there are two options for the reference angle  $\alpha_i^*$  (see section 7.2), two for the remaining reference model (RM), and three for the force allocation logic (FAL), hence different tests are proposed and summarised in the first four columns of Table 8.12.

The results, in terms of the KPI highlighted in section 6.5, are shown in the

Reference Model	IAE – RF
1 <sup>st</sup> order	2.48
vessel model	12.48
Trapezium	0

Table 8.11: Results - milliAmpere - IAE-RF.

last three columns of Table 8.12 and in figures 8.30, 8.31, 8.32, and 8.33. The table values correspond to the metrics values at the last simulation time step, i.e. at the end of the four-corner test, while the total time histories are reported in the figures. All simulations have the same total and partial time extension to make them comparable. Lower metrics mean better performance in terms of precision, energy consumption, actuator wear and tear, and actuation error. As it is possible to see from the results, in general, the cases with the 1<sup>st</sup> order reference model have lower (better) values of  $IAE$  and  $IAEW$ , which means higher precision, while the cases with the allocation  $\Xi$  and  $\Pi$  have, as expected, the smallest values of  $IADC$ , which means they move the actuators less. Allocation  $\kappa$  is generally the best in terms of  $IATE$ . The best value of each metric is highlighted in bold in Table 8.12.

Case	$\alpha_i^*$	RM	FAL	IAE	IAEW	IADC	IATE
1	$\alpha_A^*$	1 <sup>st</sup> order	$\kappa$	4,55	1,39	1,32	6,23
2	$\alpha_A^*$	1 <sup>st</sup> order	$\Xi$	3,30	1,08	1,49	11,88
3	$\alpha_A^*$	1 <sup>st</sup> order	$\Pi$	2,17	0,67	<b>0,72</b>	7,36
4	$\alpha_A^*$	Trapez.	$\kappa$	11,42	6,04	2,36	9,03
5	$\alpha_A^*$	Trapez.	$\Xi$	6,51	3,64	2,55	15,78
6	$\alpha_A^*$	Trapez.	$\Pi$	3,11	1,58	1,40	14,21
7	$\alpha_B^*$	1 <sup>st</sup> order	$\kappa$	2,98	0,91	1,02	<b>3,91</b>
8	$\alpha_B^*$	1 <sup>st</sup> order	$\Xi$	<b>1,43</b>	<b>0,40</b>	0,94	5,11
9	$\alpha_B^*$	1 <sup>st</sup> order	$\Pi$	2,66	0,84	0,74	8,5
10	$\alpha_B^*$	Trapez.	$\kappa$	6,04	3,43	1,96	5,77
11	$\alpha_B^*$	Trapez.	$\Xi$	9,84	6,46	2,73	16,65
12	$\alpha_B^*$	Trapez.	$\Pi$	5,09	2,51	1,40	11,12

Table 8.12: Results - milliAmpere - Tests of low-speed controller configurations.

In the end, the results concerning cases 3, 7, 8, and 10 are reported in terms of trajectory, pose errors in the  $\underline{n}$  frame, and speed errors in the  $\underline{b}$  reference frame in figures 8.34c, 8.34a, and 8.34b, respectively. In all the figures, in blue are marked the time histories related to test case 3, with the red dash-dotted line the data related to test case 5, with the green dashed line the data related to test case 7, and with the dotted light blue line the data related to test case 10. From the trajectories time histories, it is possible to see the difference between the two reference models that leads to the different values of the  $IAE - RF$  values of Table 8.11; while from the others, it is possible to see that errors are born when the corners are switched (every 100 s). Since this application aims to have high precision and reduced azimuth movements, case 8 can be considered a good trade-off for this case, together with the reference angle  $\alpha_B^*$  selection.

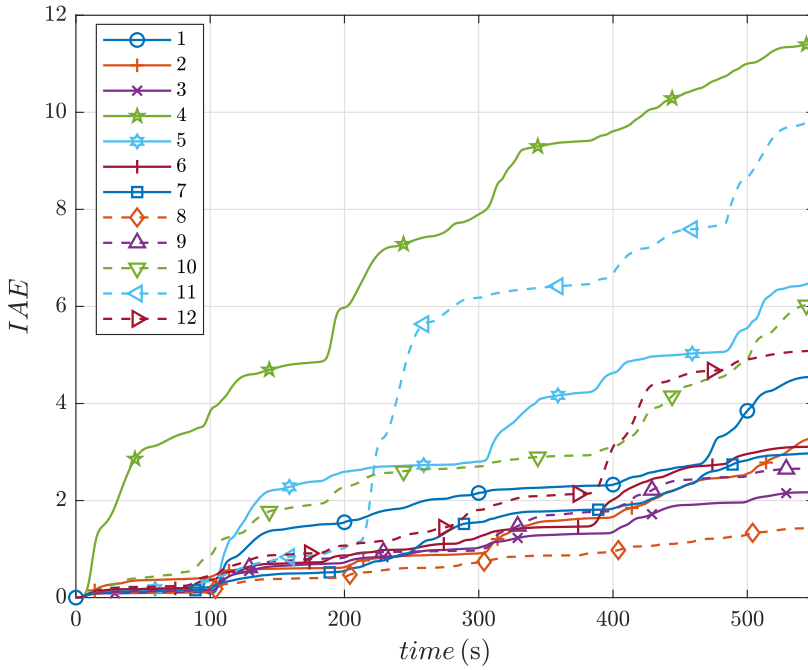


Figure 8.30: Results - milliAmpere - Low-speed configurations tests: IAE.

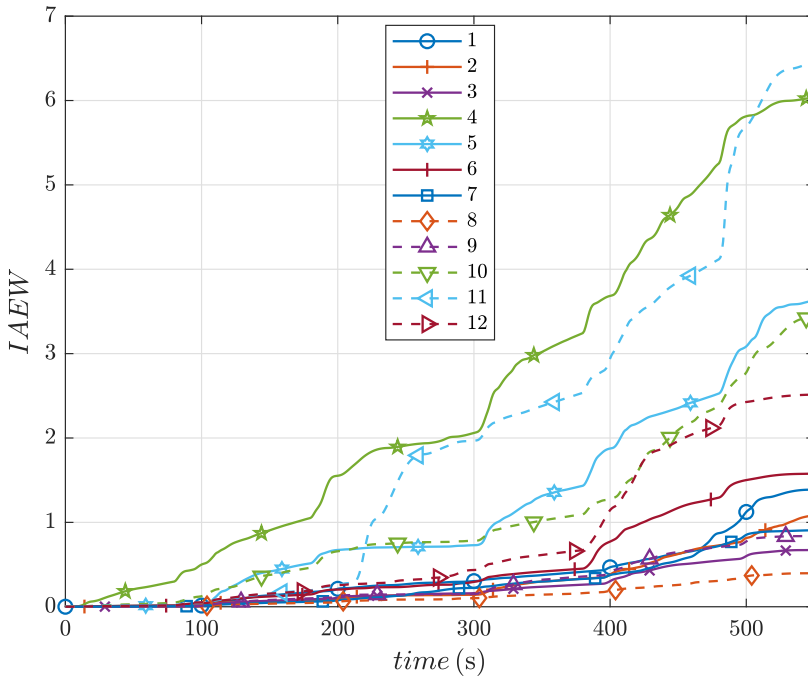


Figure 8.31: Results - milliAmpere - Low-speed configurations tests: IAEW.

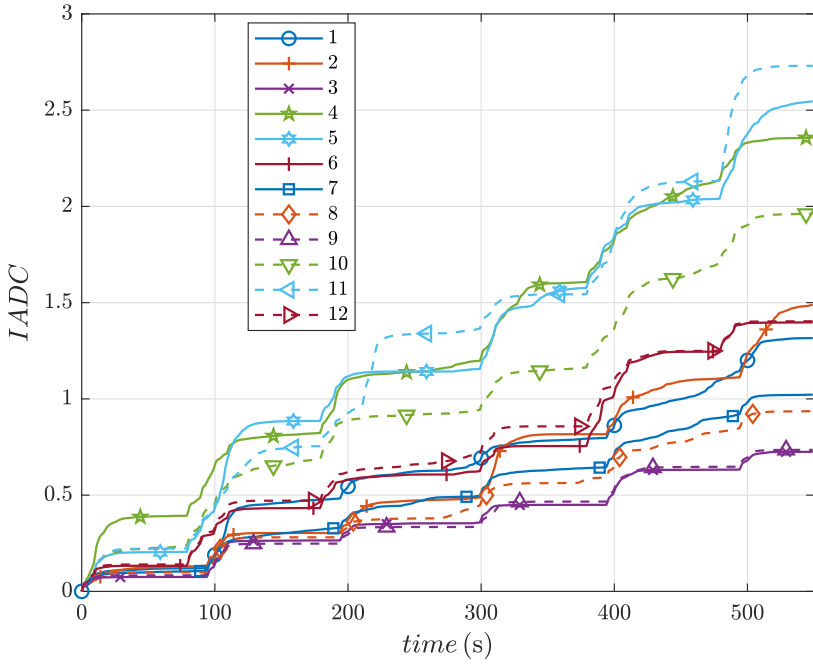


Figure 8.32: Results - milliAmpere - Low-speed configurations tests: IADC.

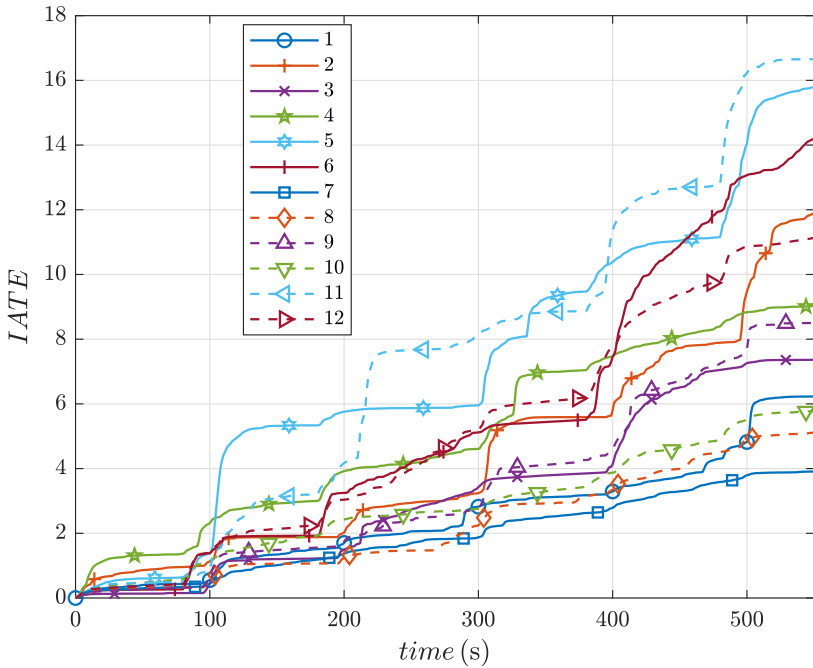
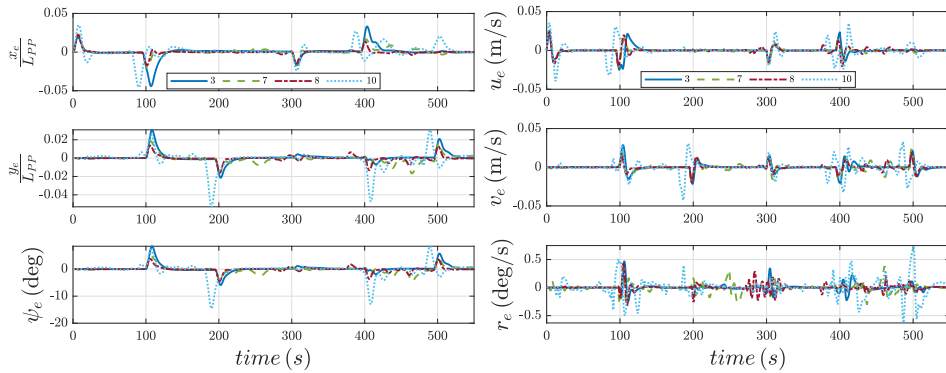
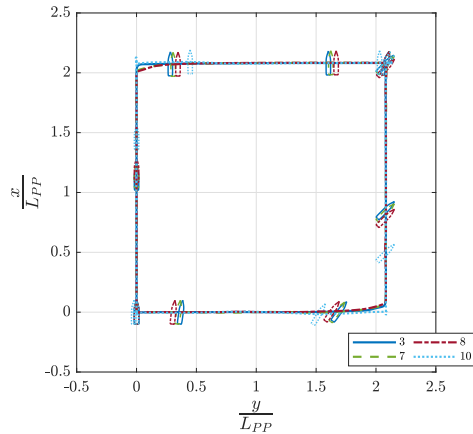


Figure 8.33: Results - milliAmpere - Low-speed configurations test: IATE.

(a) Pose errors  $n$  frame.(b) Speed errors  $b$  frame.

(c) Trajectories.

Figure 8.34: Results - milliAmpere - Low-speed configurations.

### 8.2.2 Higher Speed range scenario

The layout of the controller adopted for the higher speed range of milliAmpere, see Section 7.2, is the one in Figure 8.35.

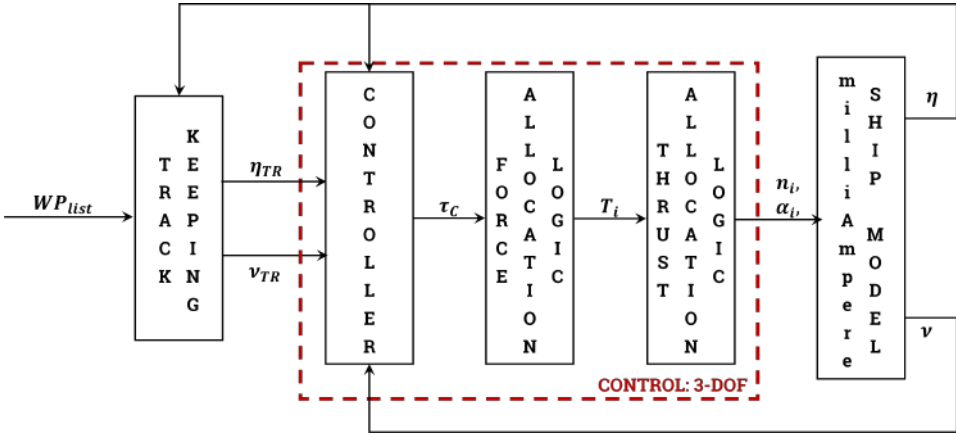


Figure 8.35: Results - milliAmpere - Higher speed layout.

The reference model adopted in this case is substituted by the track keeping guidance laws of Section 3.2. The controller is the one of Section 5.1.1 with integral gains equal to zero, the thrust allocation is composed by the combinator curve of Figure 7.9, and the force allocation is the semi-optimal allocation solved with Lagrange multiplier method of Section 5.2.2.2. The optimum problem is the one of (5.20) where the equality constraints are the one in (8.2) together with the bounds on the minimum and maximum thrusts. The number of unknowns is reduced since the angles are kept fixed, the selected angle allocations are shown in Section 7.2 and Figure 7.10c.

To define the track keeping guidance law, the following parameters are assumed:  $V_{max} = 1.2 \frac{m}{s}$ ,  $V_{min} = 0.2 \frac{m}{s}$ ,  $d_{TK}^* = 8.3 L_{PP}$ , and  $n = 3$ .

The proposed higher-speed controller is tested with a series of waypoints that lead to several heading changes. The desired path is highlighted in blue in Figure 8.36c and defined according to the waypoint list of Table 8.13. Here, in the first column, there is the waypoint number; in the second and third columns, the position of the waypoints in the  $\underline{n}$  frame is defined, while in the last two columns, the angle  $\gamma$  and the distances between each couple of waypoints made of the one in the same line and the one in the line before are computed. The adopted initial conditions are:  $\eta_0 = [0, 0, 0]$  and  $\nu_0 = [0.1, 0, 0]$

$\mathbf{n}$	$\mathbf{x}_{WP}$	$\mathbf{y}_{WP}$	$\gamma$	$d_{wp}$
1	0	0		
2	$20 L_{PP}$	$50 L_{PP}$	69	$53 L_{PP}$
3	$30 L_{PP}$	$100 L_{PP}$	79	$51 L_{PP}$
4	$15 L_{PP}$	$150 L_{PP}$	106	$52 L_{PP}$
5	$15 L_{PP}$	$200 L_{PP}$	90	$50 L_{PP}$
5	$80 L_{PP}$	$300 L_{PP}$	56	$120 L_{PP}$

Table 8.13: Results - milliAmpere - Higher-speed Scenario.

In terms of resultant trajectory, the results are highlighted with the red line in Figure 8.36c. The pose errors time history in the  $\underline{f}$  reference frame are reported in Figure 8.36d, while the corresponding pose in the  $\underline{n}$  frame is reported in Figure 8.37b. The velocity errors in the  $\underline{b}$  frame are reported in Figure 8.37a, while the corresponding speeds are reported in Figure 8.37c. As it is possible to see from the results, errors in terms of speed and pose arise, as expected, after each switch, while the long error  $f_1$  converges on the selected value for the switch  $nL_{PP}$ . In the end, the computed controller forces and moment are reported in figures 8.36a and 8.36b, while the motor speed setpoints are in Figure 8.37d.

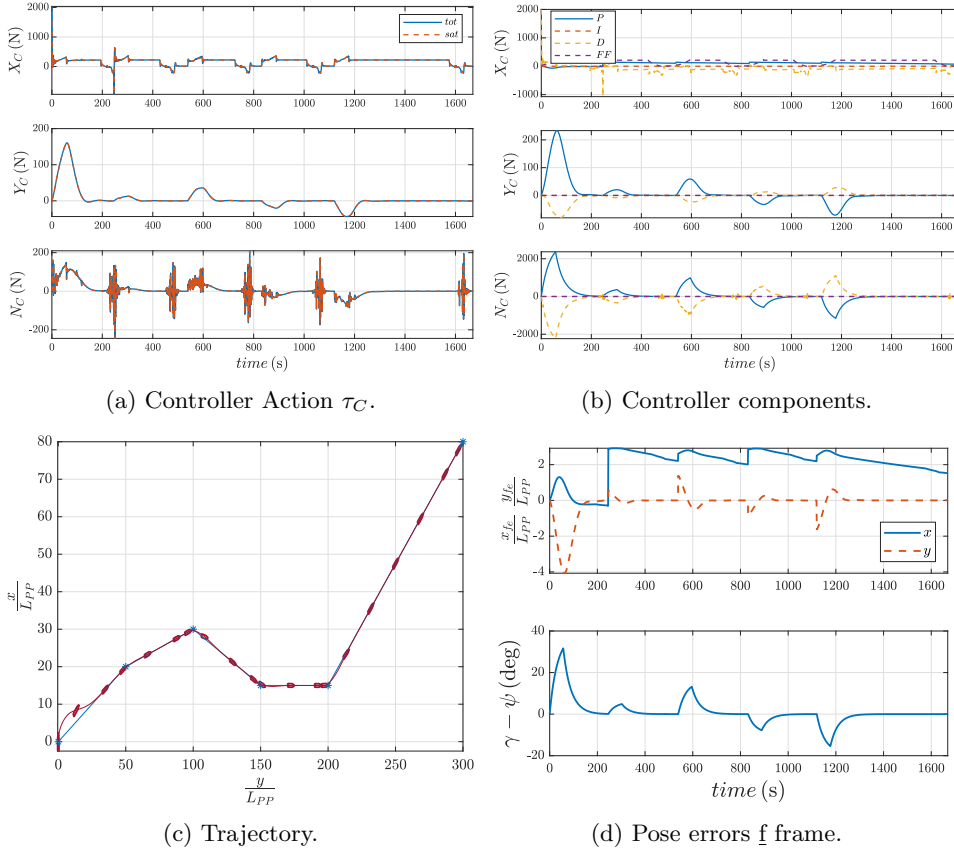


Figure 8.36: Results - milliAmpere - Higher-speed configurations.



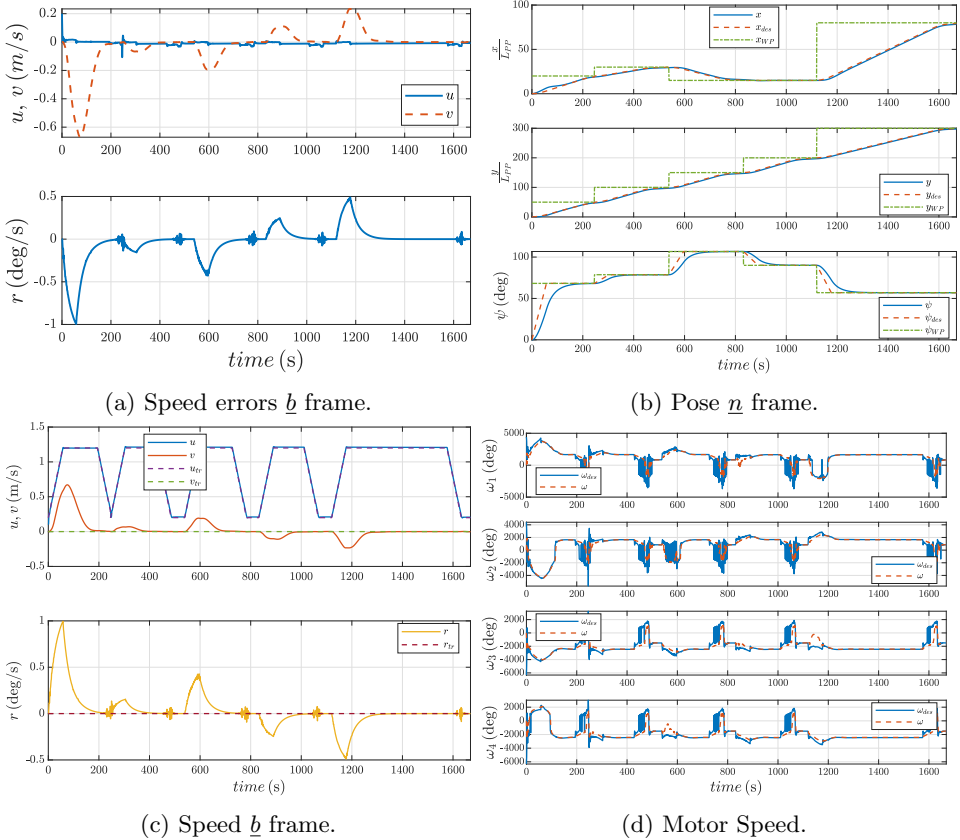


Figure 8.37: Results - milliAmpere - Higher-speed configurations.

## 8.3 Minehunter

The activities done on the Minehunter test case of Section 7.3 evaluates its station-keeping capability. The analysis is done at the static level during the early stage of design and different propulsion plants are evaluated to define the performance of each one. The environmental forces acting on the vessel are computed according to Section 2.6, and optimum allocation law are defined and solved to verify the forces and moment equilibrium in the horizontal plane. The adopted layout is shown in Figure 8.38.

The station-keeping capabilities are evaluated with three key performance indicators: the static Dynamic Positioning Capability Plot of Section 6.2, the operability indexes of Section 6.3, and the emission factor of Section 6.4.

The environmental conditions adopted for the DPCP analysis consider the wind, wave, and current disturbances coming from the same direction. The current speed is considered fixed with a value of 0.5 *kn*, while the wind and wave conditions are linked following the Beaufort scale as in Figure 2.9.

The environmental condition adopted for the operability and emission analysis considers always the wind, wave, and current disturbances coming from the same direction with the same fixed current speed. The wind and wave conditions of the selected geographic area are defined through a scatter diagram; for more details, see

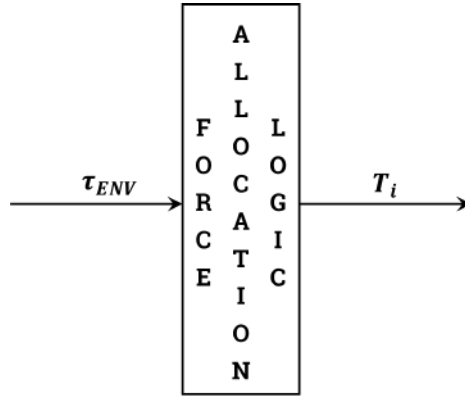


Figure 8.38: Results - Minehunter - Layout.

Section 2.6.4. Thanks to these diagrams, for each incoming direction, it is possible to know all the combinations of significant wave height,  $H_{1/3}$ , and zero-crossing period,  $T_z$ , for the selected area, together with the percentage of occurrence. The data come from the database [3] and refers to the sea area 25, i.e. the area of the Atlantic Ocean off the Canary Islands as shown in Figure 8.39. For each area, a scatter diagram is available for incoming direction  $\gamma_i$  from  $0^\circ$  to  $360^\circ$  with step  $45^\circ$ , together with the percentage of occurrence of each direction  $p_{\gamma_i}$  shown in Figure 8.40a. For example, a representation of the scatter diagram for a North-East, most probable, incoming direction is reported in Figure 8.40b. Each cell of the scatter diagram is linked with a wind speed magnitude through the Pierson relationship (2.38); to validate the chosen procedure, the statistical distribution of the wind speeds found is compared with the statistical data always provided in [3]. The two cumulative distributions are compared in Figure 8.40c. As it is possible to see from the Figure, the probability distribution coming from the adopted wind-wave correlation (in blue) provides results comparable to the one based on the statics observation (in leaf); hence, for this purpose, the adopted correlation is considered a good approximation of the real conditions.

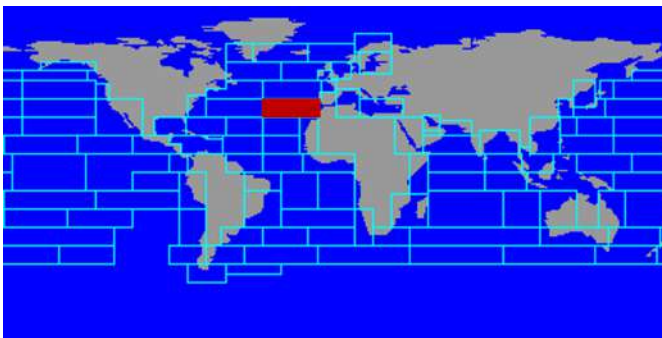
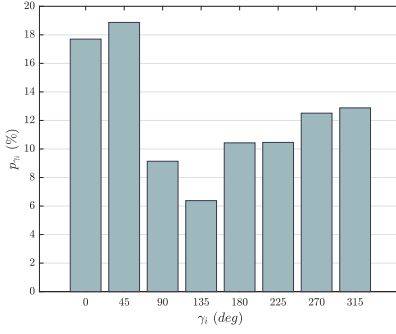
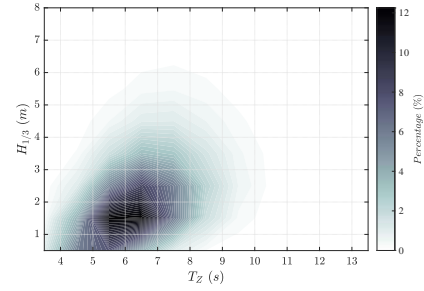


Figure 8.39: Results - Minehunter - Scatter diagram areas.

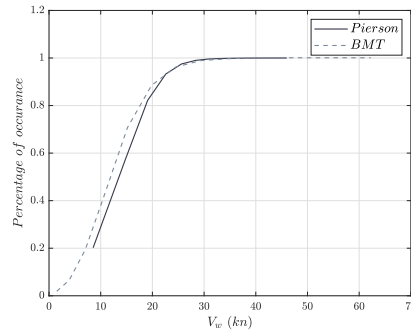
The allocation logic is the same for the three key performance indicators. It is an optimized allocation logic solved with a nonlinear programming method, as shown in Section 5.2.2.1. Hence, the problem is a constrained optimization problem



(a) Incoming direction percentage of occurrence.



(b) Scatter diagram - North-East direction.



(c) Cumulative distribution of wind speed.

Figure 8.40: Results - Minehunter - Environmental disturbance.

as the one in (5.14) where the aim is to minimize the total thrust according to (5.17) under equality and inequality constraints. The unknown  $x$  for the configuration A and B described in Section 7.3 are reported in (8.3) and (8.4), respectively. The equality constraints are defined according to (8.7) and (8.8), the inequality according to (8.5) and (8.6), in both cases for configuration A and B respectively.

$$\mathbf{x} = [T_{AZ_i}, X_{AZ_i}, Y_{AZ_i}, \alpha_{AZ_i}, T_{BT_i}] \quad (8.3)$$

$$\mathbf{x} = [T_{P_i}, X_{P_i}, Y_{P_i}, \delta_i, T_{BT_i}, T_{ST_i}] \quad (8.4)$$

$$g(\mathbf{x}) = -T_{AZ_i} \quad (8.5)$$

$$g(\mathbf{x}) = |\delta_i| - 30 \quad (8.6)$$

$$h(\mathbf{x}) = \begin{cases} \sum_{i=1}^2 X_{AZ_i} \eta(\alpha_i) - \tau_C(1) \\ \sum_{i=1}^2 Y_{AZ_i} \eta(\alpha_i) + \sum_{i=1}^2 T_{BT_i} - \tau_C(2) \\ \sum_{i=1}^2 (x_{AZ_i}, y_{AZ_i}) \times (X_{AZ_i}, Y_{AZ_i}) \eta(\alpha_i) - \sum_{i=1}^2 x_{BT_i} T_{BT_i} - \tau_C(3) \\ T_{AZ_i}^2 - X_{AZ_i}^2 - Y_{AZ_i}^2 \\ \alpha_i - \text{atan2}(Y_{AZ_i}, X_{AZ_i}) \end{cases} \quad (8.7)$$

$$h(\mathbf{x}) = \begin{cases} \sum_{i=1}^2 X_{P_i} \eta(\delta_i) - \tau_C(1) \\ \sum_{i=1}^2 Y_{P_i} \eta(\delta_i) + \sum_{i=1}^2 T_{BT_i} + \sum_{i=1}^2 T_{ST_i} - \tau_C(2) \\ \sum_{i=1}^2 (x_{P_i}, y_{P_i}) \times (X_{P_i}, Y_{P_i}) \eta(\delta_i) - \sum_{i=1}^2 x_{BT_i} T_{BT_i} - \sum_{i=1}^2 x_{ST_i} T_{ST_i} - \tau_C(3) \\ X_{P_i} - T_{P_i}(1 - c_x \delta_i) \\ Y_{P_i} - T_{P_i} c_y \delta_i \\ \delta_i, \text{ if } T_{P_i} \leq (\text{reverse}) \end{cases} \quad (8.8)$$

### 8.3.1 DPCP

The resulting DPCPs are reported in Figure 8.41 and Figure 8.42 for configurations A and B, respectively. The black lines represent the maximum wind speed that the vessel can support for each angle, while the colour scale represents the wave height.

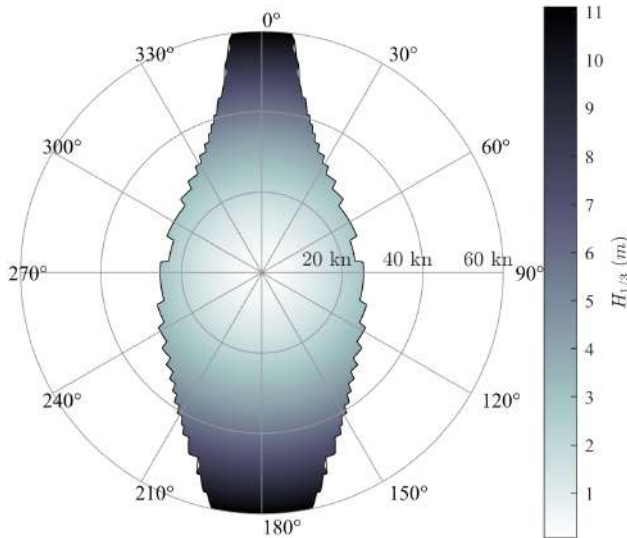


Figure 8.41: Results - Minehunter - DPCP configuration A.

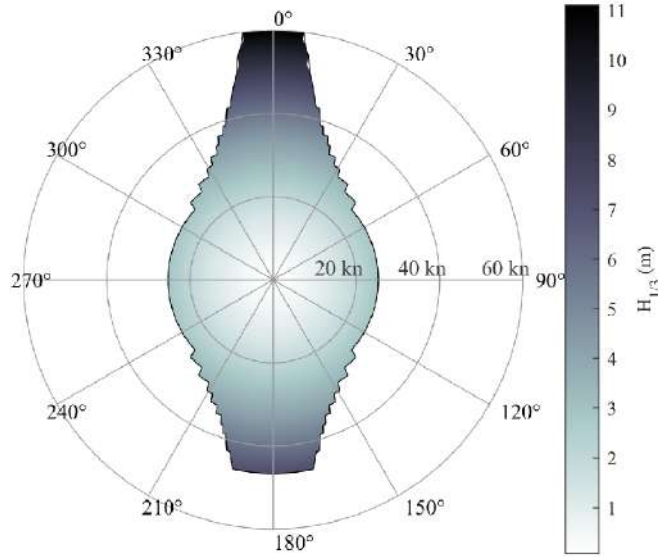
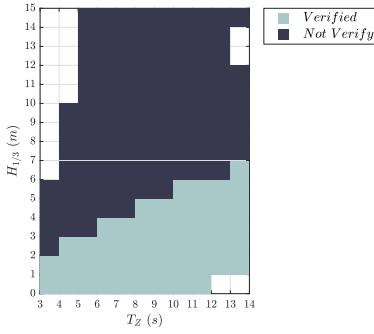


Figure 8.42: Results - Minehunter - DPCP configuration B.

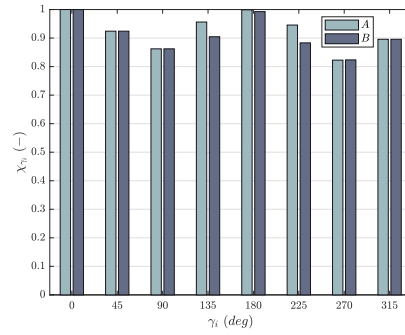
### 8.3.2 Operability index

The resulting operability index analysis starts from solving the allocation problem and verifying the equilibrium with the index  $\zeta_{jk}$ . In Figure 8.43a, as an example, the function  $\zeta_{jk}$  for the North-East incoming direction for the propulsion configuration B is reported. If the equilibrium is verified, the cell is teal, on the contrary, it is blue. Combining the data of Figure 8.43a with the probability of occurrence of each cell  $p_{jk}$  (data shown in Figure 8.40a), the operability indexes  $\chi_{\gamma_i}$  of (6.1) for each incoming direction and for configuration is found. The results for the two configurations are reported in Figure 8.43b, in blue are reported the data concerning configuration B and in leaf are the ones corresponding to configuration A. At this point, it is possible to assess the overall operability index  $\chi_{tot}$  for each configuration as shown in equation (6.2) taking into account the percentage of occurrence of each incoming direction shown in Figure 8.40a. The results are reported in Figure 8.43c, in blue is marked the index concerning configuration B and in leaf is marked the one for configuration A.

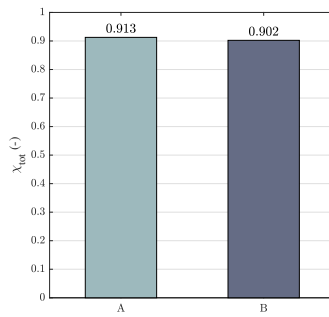
The comparison between the propulsive configurations shows a difference in term operability of about 1%, demonstrating that they are equivalent for such a purpose in terms of station-keeping capability. The analysis of the absolute number shows an interesting aspect in probabilistic terms of the days out of services (i.e. 32 days per year for Configuration A and 36 days per year for Configuration B). It is essential to underline that the calculation does not include additional effects (e.g. vertical acceleration limits, stability, structural constraints, heeling angle, etc.) that certainly will reduce the yearly index. As stated before, the operability index expresses, from a statistical point of view, the probability that the proposed propulsion configuration can operate in a specific geographic area during the year according to the statistical environmental conditions given by the scatter diagram of the area. The results obtained for the two analysed configuration demonstrate that they are both able to keep the position for more than 90% of the year but does



(a) Function  $\zeta_{jk}$ , Configuration B, North-East direction.



(b) Operability index for each  $\gamma_i$ .



(c) Operability index.

Figure 8.43: Results - Minehunter - Operability analysis.

not give any information on the power required to do it; hence, from the point of view of the station keeping capability the two configurations are equivalent.

### 8.3.3 Emission Factor

The resulting emission factor analysis starts from the definition of the total power  $P_{B_{jk}}$  required by the actuators after the load sharing, of the SFC according to (6.3), of the hourly consumption according to (6.4), and of the hourly emission  $EM_{P_{jk}}$  according to (6.5). As an example, the resultant concerning Configuration B with the engine type LBSI, coming direction North-East and for the of  $CO_2$  pollutant are reported respectively in figure 8.44a, 8.44b, 8.44c, and 8.44d. On the other side, combining the probability of occurrence of each cell  $p_{jk}$  (data shown in Figure 8.40a) with the emission  $EM_{P_{jk}}$ , the emission indexes  $\epsilon_{P_{\gamma_i}}$  of (6.6) for each incoming direction, for each propulsion configuration, for each engine kind, and each pollutant is found. Figure 8.45a shows the result for the  $CO_2$  pollutant for both the propulsion configuration and the engine type as a function of the coming direction. The same representation can also be found for all the pollutants, and the one related to the  $CO_2$  is reported only as an example. In light leaf is reported the propulsion configuration A with the HSD engine, in leaf is the configuration A with the LBSI engine, in blue is the configuration B with the HSD engine, and in

dark blue is the configuration B with the LBSI engine.

At this stage, it is possible to assess the overall emission index  $\epsilon_{P_{TOT}}$  for each configuration as shown in (6.7) taking into account the percentage of occurrence of each incoming direction. The data are reported in Table 8.14 and in Figure 8.45b. In the table the data are reported as proportion respect to the reference value of configuration A with HSD engine. In the Figure, in light leaf is reported the propulsion configuration A with the HSD engine, in leaf is the configuration A with the LBSI engine, in blue is the configuration B with the HSD engine, and in dark blue is the configuration B with the LBSI engine. For the display of results, the values for  $CO_2$  are scaled by 1000, the one of  $CH_4$  by 3, and the one of  $NO_X$  by 100.

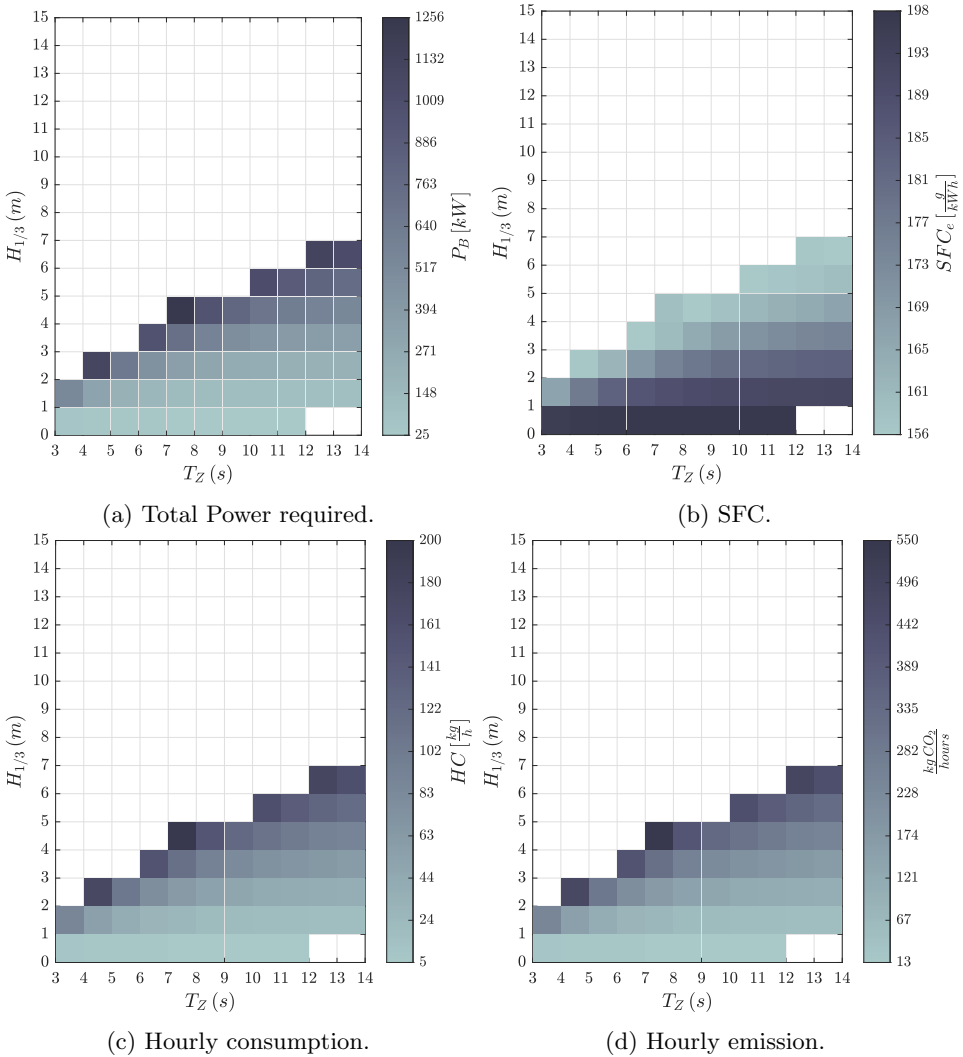


Figure 8.44: Results - Minehunter - Emission factor variables, Conf. B, North-East direction.

From these results, it is possible to see the average hourly inputs in the operating

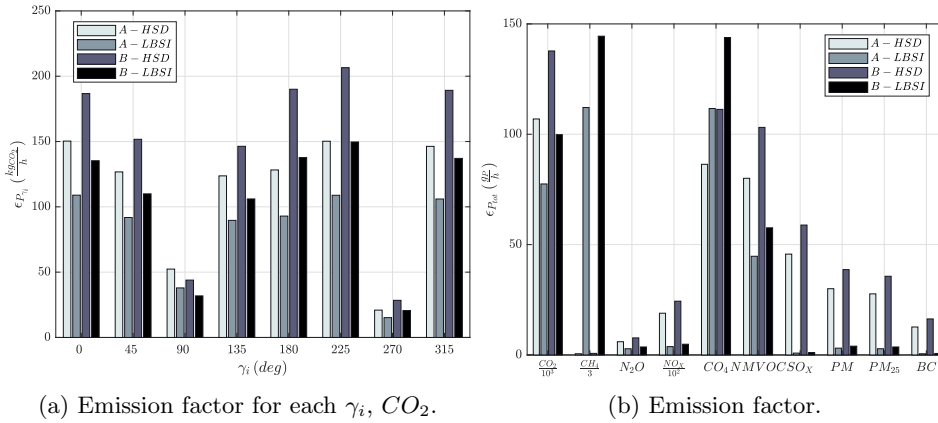


Figure 8.45: Results - Minehunter - Emission analysis.

	Configuration A		Configuration B	
	HSD	LBSI	HSD	LBSI
	$\frac{gP}{H}$	$\frac{gP}{H}$	$\frac{gP}{H}$	$\frac{gP}{H}$
$CO_2$	1	0,725	1,289	0,933
$CH_4$	1	201	1,289	259
$N_2O$	1	0,468	1,289	0,603
$NO_X$	1	0,120	1,289	0,257
$CO$	1	1,29	1,289	1,66
$NMVOCSO_X$	1	0,559	1,289	0,719
$SO_X$	1	0,0185	1,289	0,0238
$PM$	1	0,103	1,289	0,133
$PM_{2.5}$	1	0,102	1,289	0,131
$BC$	1	0,0422	1,289	0,0543

Table 8.14: Results - Minehunter - Emission factor.

area for each propulsion configuration for the two different engines. Of course, the primary pollutants for the two engines follow the emission factor values given in Table 8.14; it is possible to see that for the engine type HSD, the main pollutants are the  $CO_2$ ,  $NO_X$ ,  $NMVOCSO_X$ , and the  $CO_4$  but other pollutants are also present with non-negligible values. For the engine type LBSI, the main pollutants are always the same with the  $CH_4$ , but the others almost always have negligible values. This reflects the main problem of the LBSI engine, the methane-slip problem; it is the reason for which the  $CH_4$  index in Table 8.14 for the LBSI engine is so high. An interesting result is obtained when comparing configurations A and B with the same engine. It is possible to see that the emissions of configuration B are generally higher due to the higher hourly consumption together with a slightly lower operability index (see Figure 8.43c). Indeed, the operability indexes were almost equivalent, but the real difference was in the total thrust and, consequently, in the total power required to achieve the same performance. It turns out that configuration A has a lower energy deployment than configuration B, leading to a lower emission index. Instead, by comparing the same layout configuration with the two different engines, it is possible to see how pollutants differ and to assess



with which configuration the possible given limits are met.

## 8.4 Platform Supply Vessel

After the static analysis, necessary for the initial design, in this case study the subsequent analysis approach considering the chosen propulsion system is seen to define the dynamic capabilities. Indeed, the activities done on the PSV case study of Section 7.4 are linked to the evaluation of the station-keeping capability with both static and dynamic approaches and the design of a dynamic positioning controller.

The environmental forces acting on the vessel are computed according to Section 2.6 and a 3-DOF controller is developed to ensure the station-keeping capability. The 3-DOF controller, as shown in Figure 5.1, comprises a controller, a force allocation logic, and a thrust allocation logic. The pipeline is shown in Figure 8.46.

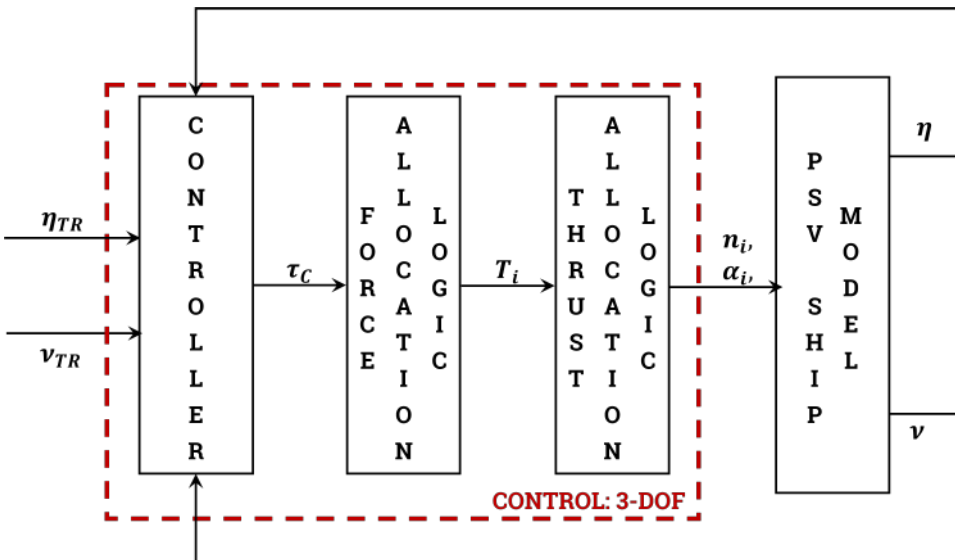


Figure 8.46: Results - PSV - Layout.

The controller is composed of the environmental feedforward controller described in Section 5.1.2; indeed in the vessel, an anemometer is present, and it is possible to estimate the wind speed and coming direction. The thrust allocation logic is indeed defined through the azimuthal and bow thruster combinator curves of figures 7.16 and 7.17. The allocation logic is solved in two different ways. Indeed, six unknowns (two for each azimuthal angle and one for each bow thruster) lead to an over-actuated propulsion plant and infinite solutions.

The first approach simplifies the problem by reducing the unknowns; this is done by fixing the azimuthal angles and is the approach described in Section 5.2.1.

The second solution consists of solving an optimum problem through the Lagrange multiplier method of Section 5.2.2.2. The optimum problem has the unknowns of (8.9) where the two bow thrusters are considered as an equivalent one as done for the simplified approach. The objective function tends to minimize the

total thrust and is the one stated in (5.17), and equality constraints are the one defined in (8.10) ensuring the equilibrium in the horizontal plane and the relationship between the unknowns.

$$\mathbf{x} = [T_{AZ_i}, X_{AZ_i}, Y_{AZ_i}, T_{BT_{eq}}], \quad i = 1, 2 \quad (8.9)$$

$$h(\mathbf{x}) = \begin{cases} \sum_{i=1}^2 X_{AZ_i} - \tau_C(1) \\ \sum_{i=1}^2 Y_{AZ_i} + T_{BT_{eq}} - \tau_C(2) \\ \sum_{i=1}^2 (x_{AZ_i}, y_{AZ_i}) \times (X_{AZ_i}, Y_{AZ_i}) - x_{BT_{eq}} T_{BT_{eq}} - \tau_C(3) \\ T_{AZ_i}^2 - X_{AZ_i}^2 - Y_{AZ_i}^2 \end{cases} \quad (8.10)$$

### 8.4.1 Static Analysis

The first step evaluates the station-keeping capability through the DPCP static analysis of Section 6.2.1. The capability of both the optimised and the simplified allocation are evaluated in this case. The selected environmental disturbances for the analysis considered those coming from the same direction and a constant current and wave magnitude, hence, only the wind speed is increased. The current speed is considered equal to  $1.5 \text{ kn}$ , while the wave height and zero crossing period are considered equal to  $6.2 \text{ m}$  and  $10.4 \text{ s}$ , respectively. The dynamic allowance coefficient is not considered in this analysis. The resulting DPCP is shown in Figure 8.47. The results concerning the simplified allocation are marked in blue, while those concerning the optimized allocation are marked with the dashed orange line. In this case, the optimized allocation does not provide many benefits in terms of station-keeping capability for two reasons: firstly, the available degrees are limited compared to typical dynamic positioning applications where the optimization method is essential; secondly, by using azimuthal thrusters and bow thrusters, the first object to be saturated is the bow thruster, which limits the performance of the system. However, using an optimized system adds the security of having the best possible solution at the implementation level, which is not guaranteed by the simplified logic.

### 8.4.2 Dynamic Analysis

The second step was the introduction of the time domain in the station-keeping capability evaluation. The developed controller is implemented in the time domain simulator representing the PSV and a simulation campaign is done to find the maximum environmental disturbance that the ship can support without having position and heading errors after the transient phase larger than defined offsets. The final result is the dynamic DPCP of Section 6.2.2. The selected environmental conditions are the same used for the static analysis, hence only the wind speed magnitude is increased. The offsets adopted for verifying the selected environmental condition are the following: the position error offset is  $\frac{1}{4} L_{PP}$ , while the heading offset is  $15^\circ$ . The adopted allocation is simplified since there are no sensible differences, as shown from the static analysis. Two hundred and fifty simulations of  $4000 \text{ s}$  are carried out to define the dynamic DPCP shown in Figure 8.48.

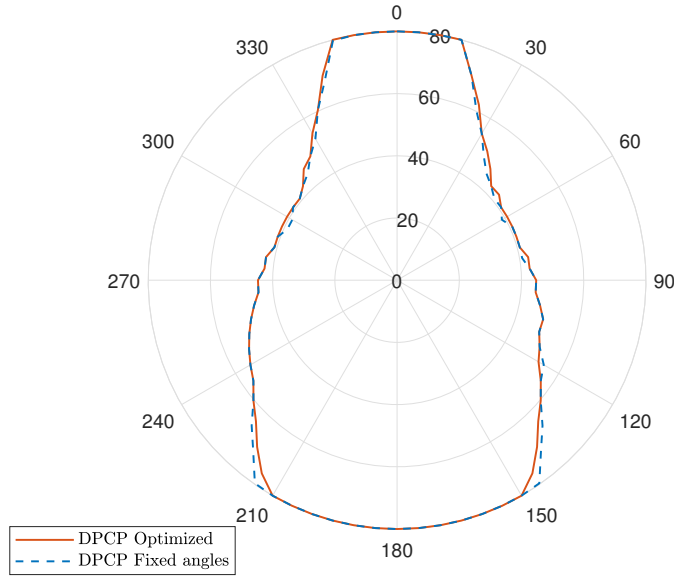


Figure 8.47: Results - PSV - Static DPCP.

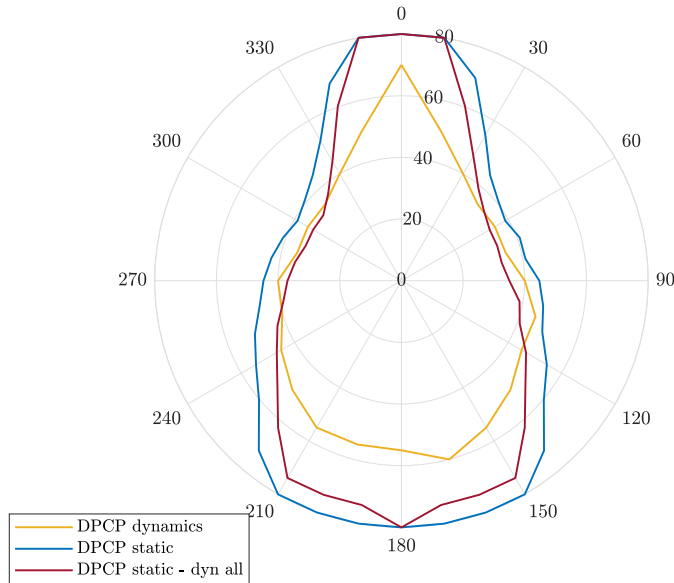


Figure 8.48: Results - PSV - Dynamic DPCP.

The dynamic positioning capability plot found at the dynamic level, marked in yellow, is now compared with the one found at the static level, marked in blue. Considering the dynamic effects of the whole ship system, the maximum environmental disturbances that the ship can support are lower. This is the reason for taking into account the dynamic allowance coefficient in the static analysis; indeed, in the end, the static DPCP with a dynamic allowance coefficient equal to 1.25 is marked in red.

The dynamic analysis also embraces a detailed review of the simulation results for several environmental conditions. Here, the result of a simulation in the time domain is shown as an example. The simulation is done with all the disturbances coming from the same direction but with a change of direction at 1500 s, otherwise than in the simulations used for the dynamic DPCP where the disturbances always maintain the same direction. The coming direction change from  $0^\circ$  to  $45^\circ$ , the current speed is always  $1.5\text{ kn}$ , the wave height and zero crossing period are considered equal to  $6.2\text{ m}$  and  $10.4\text{ s}$  respectively, and the wind speed is assumed equal to  $38\text{ kn}$ . The simulation is carried out for  $5000\text{ s}$  to test the stability of the system, and the results are reported in figures 8.49 and 8.50. The trajectory is shown in Figure 8.49a with respect to the circle that defines the limiting position. The pose and the speed errors are shown respectively in figures 8.49b and 8.49c, in the pose error are reported in orange the defined offset. The outputs of the allocation are: the azimuthal angles of Figure 8.49d, here it is possible to see that the fixed angle allocation changes at 1500 s when the coming direction of the disturbances changes; the shaft revolutions of Figure 8.50b; and the pitch of the bow thruster of Figure 8.50a, here it is possible to see that when the lateral thrust is required they are near to the saturation limits. In the end, relative speeds, the wave height, and the coming directions are reported in figures 8.50c, 8.50d, and 8.50e.

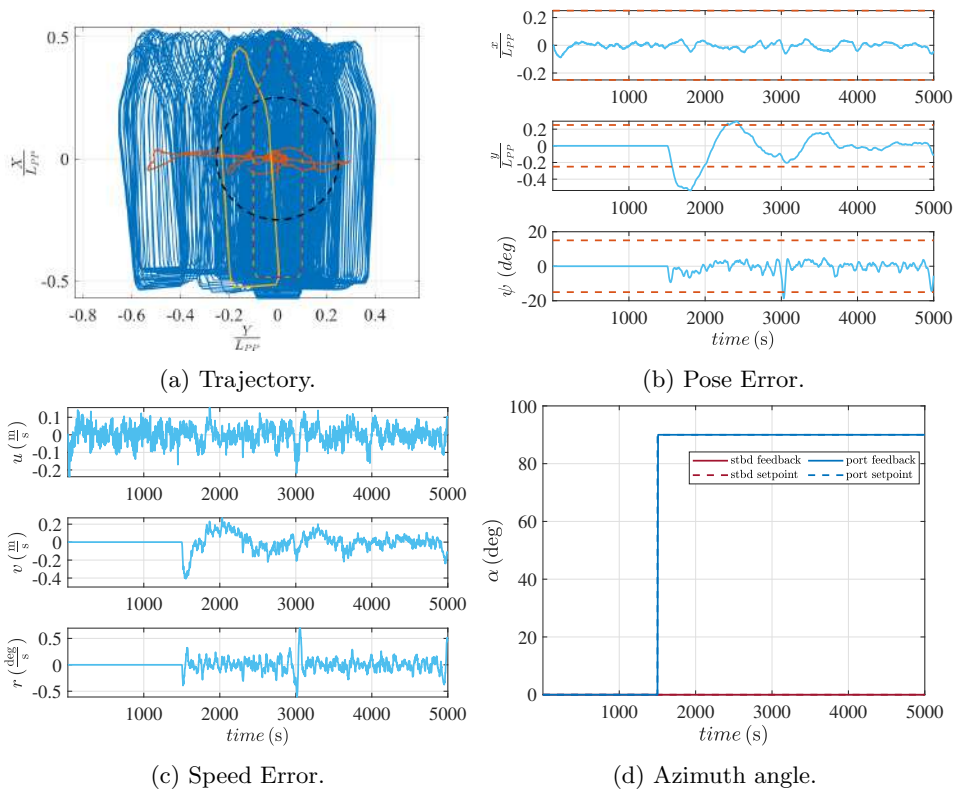


Figure 8.49: Results - PSV - Coming direction  $0^\circ$  to  $45^\circ$ .

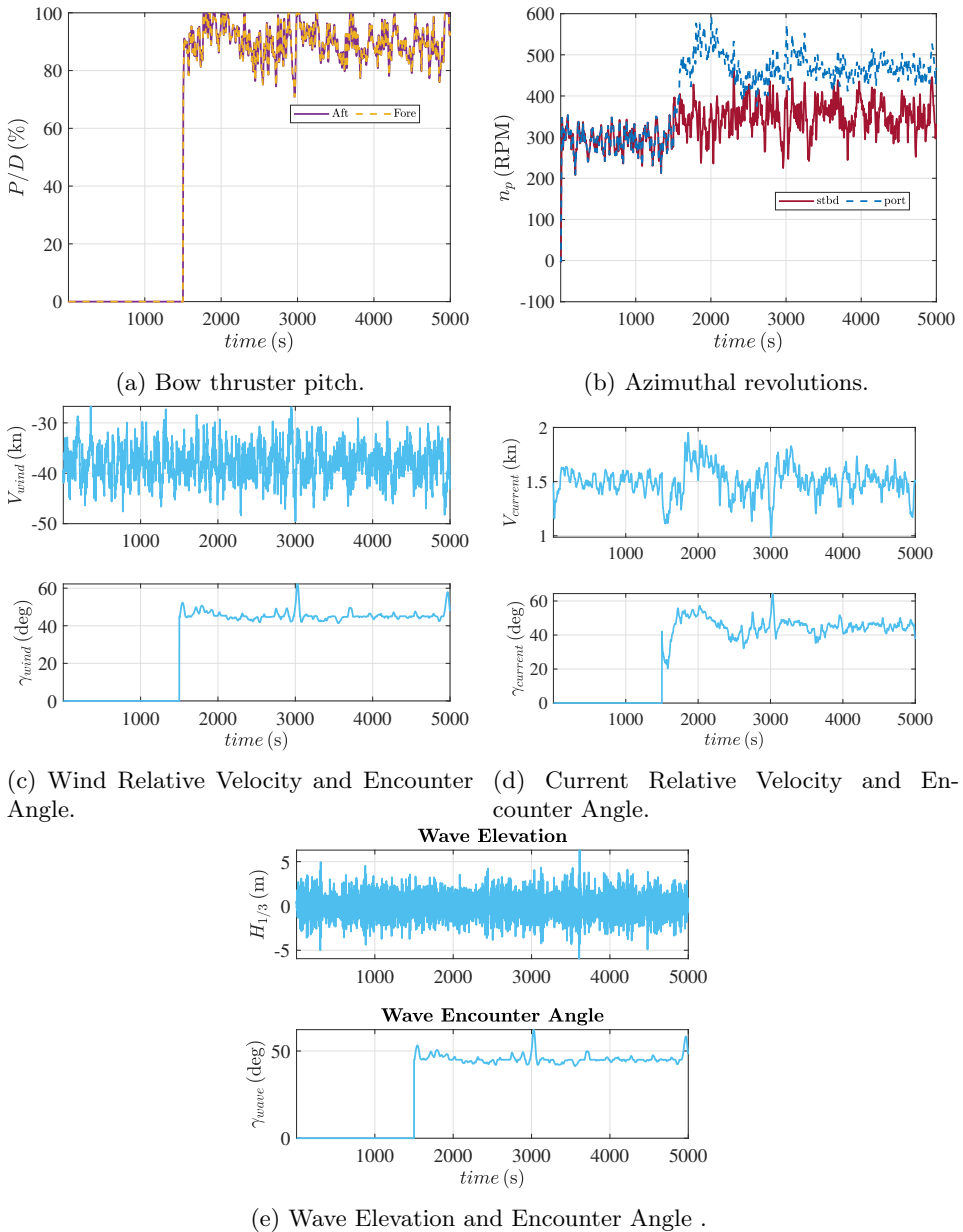


Figure 8.50: Results - PSV - Coming direction  $0^\circ$  to  $45^\circ$ .

### 8.4.3 Real-Time Hardware in the loop

In a real system, the whole control system has to work in real-time, and the automation designer must ensure that the performance foreseen by simulation will also be maintained in a real environment. To this end, it is necessary to limit most of the differences between the two worlds. This could be made possible by adopting the Real-Time Hardware In the Loop (RT HIL) method. Several CPUs are usually used to control different components of the propulsion system, trying to

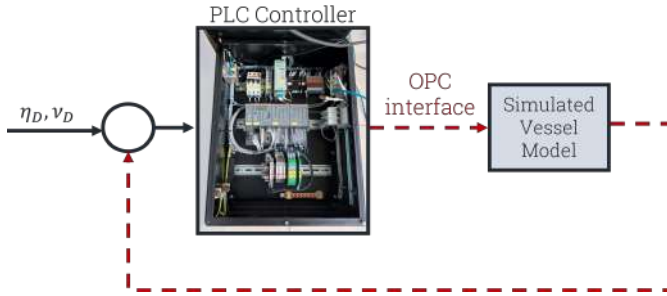


Figure 8.51: Results - PSV - Hardware in the loop Layout.

limit the loss of functionalities in case of failure of one of them. Unfortunately, the behaviour of the real hardware on board could differ from the simulated one during the preliminary design phase. The main differences could be due to the cyclic time of the CPUs, the time delay in exchanging data among controllers and the native functions that can be implemented; further differences can be represented by the presence of many functionalities usually not implemented in the ship numerical model (but that interact with the propulsion control) and the thousands of signals that the automation has to monitor on the real system.

Figure 8.51 shows a general sketch of the RT HIL methodology. The simulated vessel model is the one also used for the dynamic analysis of Section 8.4.2 and is implemented in a Matlab & Simulink environment, while the controller is implemented in the real Programmable Logic Controller (PLC). In this way, the physical availability of the ship is not required. Generally, the test of the real controller is made onboard, partially during the delivery period and completely during ship full-scale trials. These trials are time-consuming and very expensive, requiring ship availability. By using RT HIL simulation, the physical availability of the ship is not required and the controller testing can be done even before the ship is built. The controller is the AC500 CPU family produced by ABB. The CPU model used for RT HIL test is the PM591 with the following processor module characteristics related to cycle time for one instruction: (i) Binary min.  $0.002\mu s$ ; (ii) Word min.  $0.004\mu s$ ; (iii) Floating point  $0.004\mu s$ . A real-time application executes the ship model; an Open Platform Communications (OPC) client reads the command parameters on the controllers through OPC servers and returns the feedback. OPC servers and the application are on the same PC, and each OPC Server exchanges data with the controllers through Ethernet LAN.

Hereinafter, the results concerning the RT HIL (named HIL) are reported together with the simulated results that are named SIM. The controller parameters are modified to allow the RT HIL controller to converge. The environmental disturbances are aligned and coming from  $90^\circ$ , with a wind speed magnitude equal to  $20 kn$ , a current speed equal to  $1.5 kn$ , a wave height equal to  $6.2 m$ , and a wave period equal to  $10.4 s$ . In all the figures, the continuous orange line refers to the RT HIL test, while the blue dotted line refers to the SIM.

In Figure 8.52a reports the trajectories of the ships, and it is worth of notice that all the design requirements are satisfied (black dotted line equal to  $L_{PP}/4$ ). In Figure 8.52b, the position and heading errors are reported, the green dotted lines refer to the maximum allowed errors, these are set equal to  $L_{PP}/4$  for the position errors, and equal to  $15^\circ$  for the heading error. The figure shows a more significant

fluctuation in the case of RT HIL due to previously mentioned motivations. In Figure 8.52d both setpoint and feedback of the propeller revolutions are reported. Thanks to the fast dynamic of the electric prime mover, it is possible to note that no delays in actuation are experienced. Figure 8.53a shows the azimuth angle setpoints. Figure 8.53b shows required bow propeller pitch time histories. It is possible to notice that the mean values of commands are similar for RT HIL and SIM results. In Figures 8.53c and 8.53d, the time histories of azimuthal and tunnel thrusters are reported. In both cases, the actuation strictly follows the commands by remaining within their design limits.

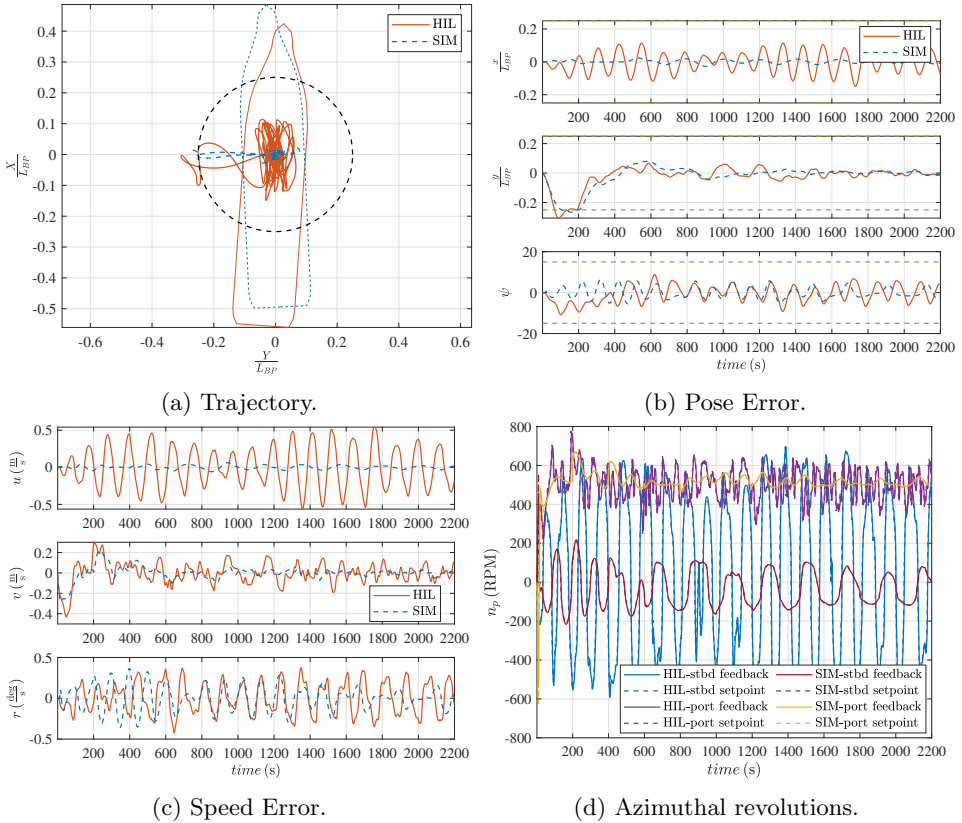


Figure 8.52: Results - PSV - RT HIL and SIM results.

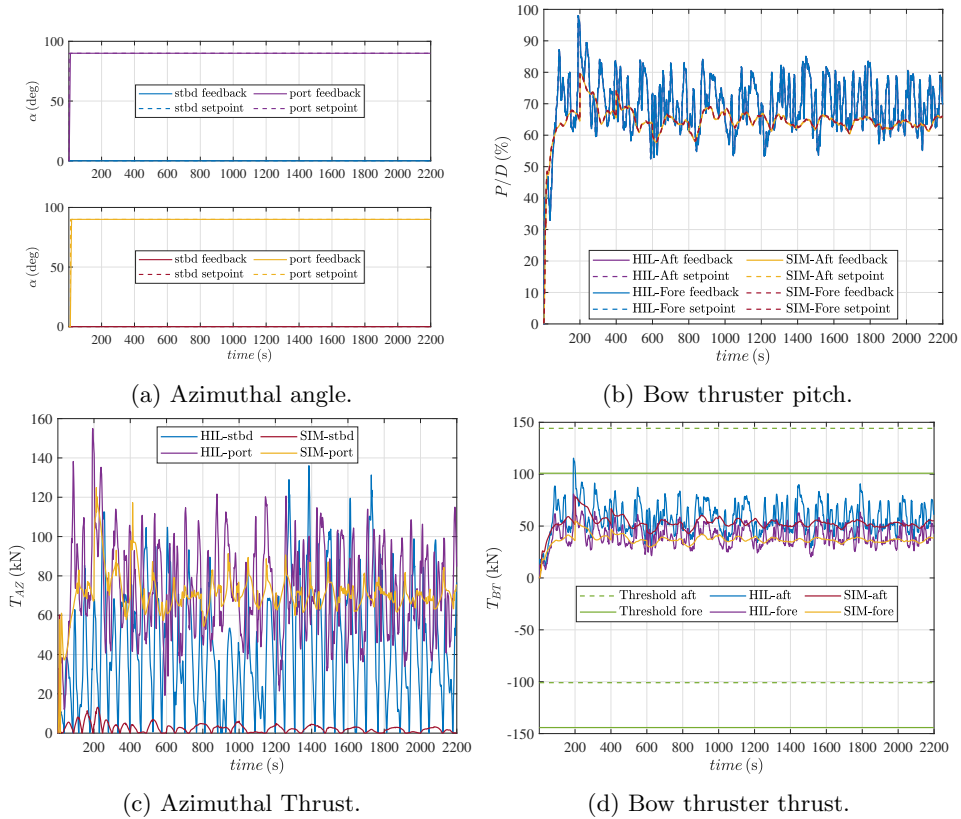


Figure 8.53: Results - PSV - RT HIL and SIM results.



## Chapter 9

# Conclusion and future developments

The proposed guidance and control methods for 2-DOF and 3-DOF scenarios are applied to four case studies leading to models to full scale vessels, and the performances are evaluated through proper key performance indicators. An approach design for a 2-DOF controller synthesis is presented and applied to the Tito-Neri model, together with the target tracking guidance laws and the relative sensitivity analysis. The last one highlights that the choice of parameters is strongly influenced by the operational condition and how each parameter affects the behaviour. The controller is designed to guarantee the stability of the closed loop, together with some performance like the rapid convergence to the setpoint and the overshoot limitation. The human factor is also introduced inside the simulation loop to stress the proposed architecture. A 3-DOF control pipeline is defined and applied at the milliAmpere prototype. Two separate controllers for the low- and higher-speed ranges are defined with the same controller layout and different strategies for each subsystem. The results are compared through integral metrics. A focus on evaluating station-keeping capabilities during the early stages design is made in the Minehunter case study; in addition to the DPCP, an index for emissions and one for operability are defined. Lastly, a 3-DOF control controller is also applied to a PSV, and its performances are evaluated using static and dynamic DPCP; finally, the developed controller is also tested on real hardware.

The layouts investigated and developed for the 3-DOF and 2-DOF scenarios represent the foundation for the following integration with the navigation, global path planning, and collision avoidance systems. Given the generalized nature of the developed layouts, these can be applied to different scale models, mainly those available in the UniGe infrastructures, to conduct experimental tests and lead the subsequent integrations. Indeed, the development of both scenario pipelines allows future developments over the entire operating range of the models, and the effectiveness of the higher-level logic implemented later also depends on them.

Naturally, the scenarios developed need subsequent improvements to increase their performance; indeed, motion prediction is not taken into account in both the 2-DOF and 3-DOF layouts, and if integrated, it could lead to significant benefits. It is an essential addition, mainly in the target tracking motion control scenario where predicting the future motion of the target could be helpful in the approach phase.

Additional aspect that should be investigated in the target tracking scenario is the constraints that the regulations represent regarding relative positions between the two moving objects. A limitation is due to the types of controllers used for both scenarios, which need to be tailored to the case study employed. Another critical improvement is introducing the bumpless function to link the 2-DOF and 3-DOF scenarios. The parametric formulations adopted to take into account the hydrodynamic interactions between the thrusters and the hull and between the thrusters themselves is another limitation; a more precise formulation of these coefficients for the 3-DOF scenarios could lead to significant improvements in force allocation. Moreover, only one controlled element is considered, and cooperation between several vessels is not taken into account. Finally, object of further studies is failure management, which must be integrated into the defined scenarios.

In addition to those mentioned above, further improvements may include introducing MPC control systems and the stability and bifurcation analysis of closed cycles with guidance for both scenarios.

Of future interest could be an investigation into how the developed procedures can be incorporated into current regulations to move on to the next level from experimental to actual implementation. The cooperative vision must be increasingly considered, and the individual strategies must be integrated with the general pipeline defined in the previous chapters. Indeed, keeping the overall vision into account and integrating it with the various pieces of the final system will serve to achieve the final objective of complete autonomy. At the same time, the individual focus is defined and structured in such a way as not to talk to the general structure, which will only lead to slowing down the process. At a more general level, however, studies on the subject will have to address the evaluation of cybersecurity aspects, moral implications, and economic and regulatory aspects that need to be implemented. Of further interest could also be the definition of the benefits and needs associated with autonomous navigation at the local level in order to focus on the territory and respond promptly to its demands; this could be accompanied by a detailed analysis of the impact and confidence placed in these technologies at the local level by humans.

Numerous overarching inquiries still need to be solved in the international and legislative spheres and are anticipated to find resolution in the years ahead. Primarily, these queries are oriented toward establishing a regulatory structure. The trajectory adopted by the International Maritime Organization (IMO) in formulating definitions for its four levels of automation indicates a trend toward inclusive and less detailed regulations governing various autonomy levels, potentially necessitating adherence to uniform regulations. A pivotal concern also revolves around the approach to handling collisions, prompting contemplation on the continuity of COLREG or the development of novel standards tailored to this evolving navigation paradigm.

# List of publications

## Journal papers:

1. Fruzzetti, C., Donnarumma, S., Martelli, M. *Dynamic target chasing: parameters and performance indicators assessment*. Journal of Marine Science and Technology 27, 712–729 (2022).  
<https://doi.org/10.1007/s00773-021-00865-3>
2. Fruzzetti C., Donnarumma S., Martelli M., Maggiani F. *Probabilistic operability and greenhouse gas assessment during dynamic positioning operations*. Proceedings of the Institution of Mechanical Engineers, Part M: Journal of Engineering for the Maritime Environment. 2023;0(0). 10.1177/14750902231203441
3. Fruzzetti C., Donnarumma S., Martelli M., *LMI-based Smart Pilot Controller Synthesis for a Maritime Autonomous Surface Ship* **Under review - Journal of Ocean Engineering and Science**

## Conference papers:

1. Donnarumma S., Fruzzetti C., Martelli M., Chiti R., Pecoraro A., Sebastiani L. (2022) *Rapid prototyping for enhanced dynamic positioning systems*. Progress in Marine Science and Technology - Volume 6, Pages 641 – 649 - 20th International Conference on Ship and Maritime Research, NAV 2022 -La Spezia, 15-17 June 2022 10.3233/PMST220075
2. Fruzzetti C., Donnarumma S., Martelli M., Maggiani F. (2023) *Dynamic positioning operability assessment by using thrust allocation optimization*. Sustainable Development and Innovations in Marine Technologies (pp. 25-32). CRC Press. IMAM 2022 – 19th International Congress of the International Maritime Association of Mediterranean – Istanbul, 26-29 September 2022. 10.1201/9781003358961-5
3. Fruzzetti, C., Martelli, M. (2023). *Unmanned Surface Vehicle Chase a Moving Target Remotely Controlled*. In: Mazal, J., et al. Modelling and Simulation for Autonomous Systems. MESAS 2022. Lecture Notes in Computer Science, vol 13866. Springer, Cham. [https://doi.org/10.1007/978-3-031-31268-7\\_14](https://doi.org/10.1007/978-3-031-31268-7_14)

4. Fruzzetti C., Martelli M., Lekkas A., Skjetne R., Breivik M. *Model-based motion control design for the milliAmpere1 prototype ferry* **Under review - ECC**

# Nomenclature

$\mathbf{A} \in \mathbb{R}^{3 \times 3}$  Allocation matrix

$a \in \mathbb{R}$  Coefficient of the simplified FAL (-)

$\{\underline{a}_i\} \in \mathbb{R}^3$  Vessel/Interceptor velocity fixed frame

$\mathbf{A}_e \in \mathbb{R}^{8 \times 8}$  Augmented state matrices

$A_F \in \mathbb{R}$  Projected frontal area exposed to the wind ( $m^2$ )

$A_L \in \mathbb{R}$  Projected lateral area exposed to the wind ( $m^2$ )

$A_{L_{sub}} \in \mathbb{R}$  Submerged lateral area ( $m^2$ )

$\mathbf{A}_{OL} \in \mathbb{R}^{6 \times 6}$  A matrix of the open loop state equation

$a_{set} \in \mathbb{R}$  Desired acceleration for the track keeping guidance ( $\frac{m}{s^2}$ )

$\{\underline{b}_i\} \in \mathbb{R}^3$  Vessel-fixed frame, BODY frame

$\mathbf{B}_e \in \mathbb{R}^{8 \times 2}$  Augmented state matrices

$\mathbf{B}_{OL} \in \mathbb{R}^{6 \times 2}$  B matrix of the open loop state equation

$bow_{angle} \in \mathbb{R}$  Angle between  $\underline{b}_1$  and a line drawn from the foremost point in the water line to the point at  $B/4$  on the water line ( $rad$ )

$\{\underline{c}_i\} \in \mathbb{R}^3$  Azimuthal thrust fixed frame

$c \in \mathbb{R}$  Curvature ( $\frac{m}{s^2}$ )

$c', k, c, d, d', e, e' \in \mathbb{R}$  Oltman model parameters (-)

$\mathbf{C}_A \in \mathbb{R}^{3 \times 3}$  Hydrodynamics Coriolis and centripetal matrix

$C_{CFD} \in \mathbb{R}$  Cross-flow drag coefficient (-)

$c_{limit} \in \mathbb{R}$  Curvature threshold ( $\frac{m}{s^2}$ )

$C_N \in \mathbb{R}$  Moment wind resistance coefficient (-)

$C_Q \in \mathbb{R}$  Adimensional propeller torque(-)

$\mathbf{C}_{RB} \in \mathbb{R}^{3 \times 3}$  Coriolis rigid body matrix

$C_T, C_Q \in \mathbb{R}$  Open water characteristics (-)

$C_{WL_{aft}} \in \mathbb{R}$  Water plane area coefficient of the water plane area behind midship  
(-)

$c_x \in \mathbb{R}$  Rudder thrust parameter (-)

$C_{X_{AF}} \in \mathbb{R}$  Longitudinal force wind resistance coefficient (-)

$C_Y \in \mathbb{R}$  Lateral force wind resistance coefficient (-)

$c_y \in \mathbb{R}$  Rudder thrust parameter (-)

$\mathbf{D} \in \mathbb{R}^{3 \times 3}$  Damping matrix

$D \in \mathbb{R}$  Propeller diameter ( $m$ )

$\{\underline{d}_i\} \in \mathbb{R}^3$  Waypoints fixed frame

$d_D \in \mathbb{R}$  Desired distance for PP speed law in the following phase ( $m$ )

$\bar{\delta}t \in \mathbb{R}$  Time interval ( $s$ )

$\bar{\delta}t_{hc} \in \mathbb{R}$  Time interval for high curvature in LOS guidance ( $s$ )

$\bar{\delta}t_{lc} \in \mathbb{R}$  Time Interval for low curvature in LOS guidance ( $s$ )

$d_{err} \in \mathbb{R}$  Distance between the desired path and the interceptor ( $m$ )

$\mathbf{D}_L \in \mathbb{R}^{3 \times 3}$  Linear viscous damping matrix

$\mathbf{D}_{NL} \in \mathbb{R}^{3 \times 3}$  Non linear damping matrix

$d_{TK}^* \in \mathbb{R}^+$  Distance at which the acceleration phase is designed in track keeping guidance ( $m$ )

$d^* \in \mathbb{R}$  Distance corresponding to the LOS speed law maximum speed ( $m$ )

$d_{sw} \in \mathbb{R}$  Along-track distance respect to  $\Omega_{WP_2}$  ( $m$ )

$d_{T,I} \in \mathbb{R}$  Interceptor-Target distance ( $m$ )

$d_{WP} \in \mathbb{R}$  Distance between waypoints ( $m$ )

$\{\underline{e}_i\} \in \mathbb{R}^3$  ( $\Omega_T - \Omega_R$ ) fixed frame

$e \in \mathbb{R}$  Component on  $\underline{f}_2$  of the distance vector between the interceptor and the target ( $m$ )

$e_{corr} \in \mathbb{R}$  Residual error distance between the target and  $e_{des}$

$e_{des} \in \mathbb{R}$  Desired distance on  $\underline{f}_2$  in the CB guidance law ( $m$ )

$EF_P \in \mathbb{R}$  Pollutant emission factor ( $\frac{kg_P}{t_{fuel}}$ )

$e_{IAE} \in \mathbb{R}$  IAE error (-)

$e_{IAE-RF} \in \mathbb{R}$  IAE-RF error (-)

$e_{IATE} \in \mathbb{R}$  IATE error (-)

- $EM_{P_{jk}} \in \mathbb{R}$  Emission given by each pollutant for each cell ( $\frac{gP}{h}$ )
- $e_\psi \in \mathbb{R}$  Heading error in the smart pilot controller ( $rad$ )
- $\mathbf{e}^*$  Error between the computed trajectory and the selected waypoint ( $m$ )
- $e_u \in \mathbb{R}$  Speed error in the smart pilot controller ( $\frac{m}{s}$ )
- $\{\underline{f}_i\} \in \mathbb{R}^3$  Target velocity fixed frame
- $\mathbf{F}_e \in \mathbb{R}^{8 \times 2}$  Augmented state matrices
- $G = [x_G, y_G] \in \mathbb{R}^2$  centre of gravity ( $m, m$ )
- $\mathbf{G}_e \in \mathbb{R}^{2 \times 2}$  Matrix with PID gains
- $\{\underline{h}_i\} \in \mathbb{R}^3$  ( $\mathbf{\Omega}_I - \mathbf{\Omega}_T$ ) fixed frame
- $HC_{jk} \in \mathbb{R}$  Total hourly consumption for each scatter diagram cell ( $\frac{gP}{h}$ )
- $H_S \in \mathbb{R}$  Main wave height ( $m$ )
- $i \in \mathbb{R}$  Current of the DC motor ( $A$ )
- $IADC \in \mathbb{R}$  Integral of Absolute Differentiated Control ( $-$ )
- $IAE \in \mathbb{R}$  Integral of Absolute Error ( $-$ )
- $IAE - RF \in \mathbb{R}$  IAE for the reference model ( $-$ )
- $IAEW \in \mathbb{R}$  Integral of the absolute value of the error multiplied by the energy consumption ( $-$ )
- $IATE \in \mathbb{R}$  Integral of Absolute Thrust Error ( $-$ )
- $i_{GB} \in \mathbb{R}$  Gearbox ratio ( $-$ )
- $I_T \in \mathbb{R}$  Moment of inertia of the shaftline ( $kg\ m^2$ )
- $I_Z \in \mathbb{R}$  Vessel inertia ( $kg\ m$ )
- $J \in \mathbb{R}$  Advance angle ( $-$ )
- $k \in \mathbb{R}$  Fraction of the LOS circle ( $-$ )
- $K_\alpha \in \mathbb{R}$  Constant representing the rotational speed ( $Hz$ )
- $K_{CB} \in \mathbb{R}$  Speed gain of the CB speed law ( $\frac{m}{s}$ )
- $\mathbf{K}_{CL} \in \mathbb{R}^{2 \times 8}$  Matrix with PID gains
- $\mathbf{K}_D \in \mathbb{R}^{3 \times 3}$  3-DOF controller derivative coefficient matrix
- $K_D^{\psi,u} \in \mathbb{R}$  Smart pilot derivative coefficients
- $K_e \in \mathbb{R}$  Constant of the DC motor ( $\frac{Nm}{A}$ )
- $\mathbf{K}_I \in \mathbb{R}^{3 \times 3}$  3-DOF controller integral coefficient matrix
- $K_I^{\psi,u} \in \mathbb{R}$  Smart pilot integral coefficients
-

$K_m \in \mathbb{R}$  Mechanical constant of the DC motor ( $\frac{Nm}{A}$ )

$\mathbf{K}_P \in \mathbb{R}^{3 \times 3}$  3-DOF controller proportional coefficient matrix

$K_\omega \in \mathbb{R}$  Constant representing the total inertia ( $Hz$ )

$K_{PP} \in \mathbb{R}$  Speed gain of the PP speed law ( $\frac{m}{s}$ )

$K_P^{\psi,u} \in \mathbb{R}$  Smart pilot proportional coefficients

$K_T, K_Q \in \mathbb{R}$  Open water characteristics ( $-$ )

$L \in \mathbb{R}$  Inductance of the DC motor ( $H$ )

$L_{OA} \in \mathbb{R}$  Overall length ( $m$ )

$L_{OS} \in \mathbb{R}$  Longitudinal distance between the fore most and aft most point under water ( $m$ )

$L_{PP} \in \mathbb{R}$  Length between perpendiculars ( $m$ )

$m \in \mathbb{R}$  Mass of the ship ( $kg$ )

$\mathbf{M}_A \in \mathbb{R}^{3 \times 3}$  Added mass matrix

$\mathbf{M}_{RB} \in \mathbb{R}^{3 \times 3}$  Inertia matrix

$m_{sin} \in \mathbb{R}$  Tangent that approximates the sinus around  $\alpha = 0$  ( $-$ )

$n \in \mathbb{R}$  Fraction of the distance for waypoint switch ( $-$ )

$\bar{n} \in \mathbb{R}$  Desired shaft-line revolution ( $RPS$ )

$\{\underline{n}_i\} \in \mathbb{R}^3$  Earth-fixed frame, NED frame

$n_{ac} \in \mathbb{R}$  Number of actuators ( $-$ )

$n_E \in \mathbb{R}$  Engine revolution ( $RPS$ )

$n_H \in \mathbb{R}$  Number of the wave height values on the scatter diagram ( $-$ )

$n_{LOS} \in \mathbb{R}$  Fraction of the LOS speed law minimum distance ( $-$ )

$n_P \in \mathbb{R}$  Propeller revolution ( $RPS$ )

$n_T \in \mathbb{R}$  Number of the wave period values on the scatter diagram ( $-$ )

$N_u, N_v, N_r \in \mathbb{R}$  Ship model parameters

$\mathbf{P} \in \mathbb{R}^{8 \times 8}$  Lyapunov LMI matrix

$p \in \mathbb{R}$  Slope of the LOS speed law ( $-$ )

$P_{B_{jk}} \in \mathbb{R}$  Power required for each engine ( $kW$ )

$P_{B_{\%jk}} \in \mathbb{R}$  Percentage of the engine load of each cell ( $-$ )

$P_{B_{tot_{jk}}} \in \mathbb{R}$  Total power required by the actuators in each scatter diagram cell ( $kW$ )



- $p_{\gamma_i} \in \mathbb{R}$  Percentage of occurrence of each environmental direction (*deg*)  
 $p_{jk} \in \mathbb{R}$  Probability of occurrence of the cell of the scatter diagram (–)  
 $P(t) \in \mathbb{R}$  Power consumption IAEW (–)  
 $\mathbf{Q} \in \mathbb{R}^{8 \times 8}$  Lyapunov LMI matrix  
 $Q_B \in \mathbb{R}$  Engine torque (*Nm*)  
 $Q_D \in \mathbb{R}$  Delivered torque (*Nm*)  
 $Q_{fric} \in \mathbb{R}$  Friction torque (*Nm*)  
 $Q_O \in \mathbb{R}$  Propeller torque (*Nm*)  
 $R \in \mathbb{R}$  Resistance of the DC motor ( $\Omega$ )  
 $R_{from}^{to} (*) \in \mathbb{R}^{3 \times 3}$  Rotation matrix  
 $R_T \in \mathbb{R}$  Resistance (*N*)  
 $\mathbf{S} \in \mathbb{R}^{n_{ac} \times n_{ac}}$  Weight diagonal matrix FAL ( $\frac{1}{N^2}$ )  
 $\{\underline{s}_i\} \in \mathbb{R}^3$  Propeller plus rudder fixed frame  
 $s \in \mathbb{R}$  ( $\Omega_T - \Omega_I$ ) on  $\underline{f}_1$  (*m*)  
 $s_{des} \in \mathbb{R}$  Desired distance on  $\underline{f}_1$  in the CB guidance law (*m*)  
 $SFC \in \mathbb{R}$  Specific Fuel Consumption ( $\frac{g}{kWh}$ )  
 $SFC_b \in \mathbb{R}$  Lowest SFC for a given engine ( $\frac{g}{kWh}$ )  
 $SFC_{e_{ik}} \in \mathbb{R}$  SFC of the single-engine for each scatter diagram cell ( $\frac{g}{kWh}$ )  
 $s_{mean} \in \mathbb{R}$  Mean value of  $s$  during the following phase (*deg*)  
 $t_0, t_1, t_2, t_3 \in \mathbb{R}$  Time steps in the trapezium speed law (*s*)  
 $T \in \mathbb{R}$  Vessel draft (*m*)  
 $T_{act} \in \mathbb{R}_{ac}^n$  Actuated thrust (*N*)  
 $T_{AZ} \in \mathbb{R}$  Azimuth thrust (*N*)  
 $T_{BT} \in \mathbb{R}$  Bow thruster thrust (*N*)  
 $\mathbf{t}_i = [X_i, Y_i] \in \mathbb{R}^2$  Thrust component (*N, N*)  
 $T_P \in \mathbb{R}$  Peak wave period (*s*)  
 $t_R \in \mathbb{R}$  Interceptor path convergence time in a straight path manoeuvre (*s*)  
 $t^* \in \mathbb{R}$  Time for covering the segment between waypoints (*s*)  
 $\mathbf{T}_{t-1} \in \mathbb{R}_{ac}^n$  Vector of thrust magnitudes at the previous time step (*N*)  
 $T_z \in \mathbb{R}$  Zero-crossing wave period (*s*)
-

- $\bar{u} \in \mathbb{R}$  Smart pilot design speed ( $\frac{m}{s}$ )
- $\mathbf{u}_{OL} \in \mathbb{R}^2$  Input sector of the linearised model ( $V, rad$ )
- $V \in \mathbb{R}$  Desired angle setpoint at each time step ( $\frac{m}{s}$ )
- $\underline{V} \in \mathbb{R}$  Interceptor velocity ( $\frac{m}{s}$ )
- $V_A \in \mathbb{R}$  Voltage ( $V$ )
- $V_a \in \mathbb{R}$  Advance speed ( $\frac{m}{s}$ )
- $V_{A_{set}} \in \mathbb{R}$  Voltage setpoint ( $Volt$ )
- $V_{CURR} \in \mathbb{R}$  Current speed magnitude ( $\frac{m}{s}$ )
- $V_d \in \mathbb{R}$  Desired speed ( $\frac{m}{s}$ )
- $V_{I_{max}} \in \mathbb{R}$  Interceptor maximum speed ( $\frac{m}{s}$ )
- $V_{max} \in \mathbb{R}$  Maximum admitted speed ( $\frac{m}{s}$ )
- $V_{min} \in \mathbb{R}$  Selected minimum speed in the track keeping guidance law ( $\frac{m}{s}$ )
- $V_r \in \mathbb{R}$  Incoming propeller velocity ( $-$ )
- $\underline{V}_T \in \mathbb{R}$  Target velocity ( $\frac{m}{s}$ )
- $\underline{V}_{T,I} \in \mathbb{R}$  Velocity vector of the CB speed law ( $\frac{m}{s}$ )
- $V_T^* \in \mathbb{R}$  Maximum target speed in the a defined time interval ( $\frac{m}{s}$ )
- $V_{WIND} \in \mathbb{R}$  Relative wind speed ( $\frac{m}{s}$ )
- $\mathbf{V}(\mathbf{x}) \in \mathbb{R}$  Lyupanov Function
- $\mathbf{W}_i \in \mathbb{R}^{n_{ac} \times n_{ac}}$  Weight diagonal matrix FAL ( $\frac{1}{N^2}$ )
- $\mathbf{W}_{IAE} \in \mathbb{R}^{3 \times 3}$  Diagonal matrix penalising the pose error ( $(\frac{1}{m^2}, \frac{1}{m^2}, \frac{1}{rad^2})$ )
- $\mathbf{W}_{IATE} \in \mathbb{R}^{3 \times 3}$  Diagonal matrix penalising the thrust error ( $(\frac{1}{N}, \frac{1}{N}, \frac{1}{Nm})$ )
- $WP_{list} \in \mathbb{R}^{n \times 2}$  Waypoints list ( $m, m$ )
- $\mathbf{W}_\tau \in \mathbb{R}^{3 \times 3}$  Diagonal matrix penalising the thrust vector ( $(\frac{1}{N}, \frac{1}{N}, \frac{1}{Nm})$ )
- $x_d \in \mathbb{R}$  Desired position in  $\underline{f}_1$  ( $m$ )
- $x_{LOS} \in \mathbb{R}$  Half position of the longitudinal distance between the fore most and aft most point under water ( $m$ )
- $x_{L_{sub}} \in \mathbb{R}$  Center of the submerged lateral area ( $m$ )
- $\mathbf{x}_{OL} \in \mathbb{R}^{6 \times 1}$  Open loop state vector ( $\frac{m}{s}, \frac{m}{s}, \frac{rad}{s}, rad, RPS, rad$ )
- $X_u, X_v, X_r \in \mathbb{R}$  Ship model parameters
- $X_{\dot{u}}, X_{\dot{v}}, X_{\dot{r}} \in \mathbb{R}$  Added mass coefficients
- $X_{vr}, X_{rr}, X_{vv} \in \mathbb{R}$  Ship model parameters

$\mathbf{Y} \in \mathbb{R}^{2 \times 8}$  Lyapunov LMI matrix

$Y_u, Y_v, Y_r \in \mathbb{R}$  Ship model parameters

$Y_{\dot{u}}, Y_{\dot{v}}, Y_{\dot{r}} \in \mathbb{R}$  Added mass coefficients

$z \in \mathbb{R}$  Additional variables in lagrange multiplier problem

$z_{WL} \in \mathbb{R}$  Quota of the waterline with respect to the keel line ( $m$ )

$\alpha \in \mathbb{R}$  Azimuthal thrust angle ( $rad$ ) or ( $deg$ )

$\alpha_k \in \mathbb{R}$  Angle between  $\underline{n}_1$  and  $\underline{e}_1$  ( $deg$ )

$\dot{\alpha}_{max} \in \mathbb{R}$  Maximum rotation speed of azimuthal thruster ( $\frac{rad}{s}$ )

$\alpha_{rel_{R+1,I}} \in \mathbb{R}$  Relative bearing angle ( $deg$ )

$\alpha_{rel_{T,I}} \in \mathbb{R}$  Relative bearing angle between target and interceptor ( $deg$ )

$\alpha_{set} \in \mathbb{R}$  Azimuth angle setpoint ( $deg$ )

$\alpha_{t-1} \in \mathbb{R}^{n_{ac}}$  Actuator angles at the previous time step ( $deg$ )

$\beta \in \mathbb{R}$  Drift angle ( $deg$ )

$\beta_P \in \mathbb{R}$  Hydrodynamic pitch angle ( $-$ )

$\chi_{corr} \in \mathbb{R}$  It is the difference between  $\chi_{des}$  and  $\chi_T$  ( $deg$ )

$\chi_{des} \in \mathbb{R}$  Desired course angle in the CB heading law ( $deg$ )

$\chi_{\gamma_i} \in \mathbb{R}$  Operability index for each incoming direction ( $-$ )

$\chi_I \in \mathbb{R}$  Interceptor course angle ( $deg$ )

$\chi_T \in \mathbb{R}$  Target course angle ( $deg$ )

$\chi_{tot} \in \mathbb{R}$  Operability index ( $-$ )

$\delta \in \mathbb{R}$  Rudder angle ( $deg$ )

$\Delta\alpha \in \mathbb{R}$  Maximum actuator angle at each time step ( $deg$ )

$\Delta_{CB} \in \mathbb{R}$  Parameter of the CB heading law ( $deg$ )

$\Delta_{LOS} \in \mathbb{R}$  Component of distance vector between the interceptor and the desired position on  $\underline{e}_1$  ( $m$ )

$\epsilon \in \mathbb{R}$  Tuning parameter to adjust the azimuth behaviour ( $rad$ )

$\epsilon_{P_{\gamma_i}} \in \mathbb{R}$  Emission index for each incoming direction and for each pollutant ( $\frac{gP}{h}$ )

$\epsilon_{P_{tot}} \in \mathbb{R}$  Global emission index of each pollutant ( $\frac{gP}{h}$ )

$\boldsymbol{\eta} = [x, y, \psi]^T \in \mathbb{R}^3$  Vessel pose in  $\underline{n}$  frame ( $m, m, deg$ )

- $\eta(\alpha_i) \in \mathbb{R}$  Thruster's efficiency (-)  
 $\dot{\boldsymbol{\eta}} = [\dot{x}, \dot{y}, \dot{\psi}]^T \in \mathbb{R}^3$  Vessel velocity in the  $\underline{n}$  frame  $(\frac{m}{s}, \frac{m}{s}, \frac{deg}{s})$   
 $\boldsymbol{\eta}_D^* \in \mathbb{R}^2$  Desired position trajectory  $(m, m)$   
 $\eta_R \in \mathbb{R}$  Relative rotative efficiency (-)  
 $\boldsymbol{\eta}_{TR} \in \mathbb{R}^3$  Trajectory - pose time history  $(m, m, deg)$   
 $\eta_{TRP} \in \mathbb{R}$  Transmission efficiency of the shaftline (-)  
 $\boldsymbol{\Gamma} \in \mathbb{R}^{n_{acc} \times n_{acc}}$  Weight diagonal matrix FAL  $(\frac{1}{deg^2})$   
 $\gamma_{CURR} \in \mathbb{R}$  Wind angle of attack  $(deg)$   
 $\gamma_i \in \mathbb{R}$  Environmental coming direction  $(deg)$   
 $\gamma_{WAVE} \in \mathbb{R}$  Wave coming direction  $(deg)$   
 $\gamma_{WIND} \in \mathbb{R}$  Wind angle of attack  $(deg)$   
 $\lambda \in \mathbb{R}$  Lagrange multiplier  
 $\mu \in \mathbb{R}$  Peak limit LMI parameter  
 $\boldsymbol{\nu} = [u, v, r]^T \in \mathbb{R}^3$  Vessel velocity in the  $\underline{b}$  frame  $(\frac{m}{s}, \frac{m}{s}, \frac{deg}{s})$   
 $N_{\dot{u}}, N_{\dot{v}}, N_{\dot{r}} \in \mathbb{R}$  Added mass coefficients  
 $\dot{\boldsymbol{\nu}} = [\dot{u}, \dot{v}, \dot{r}]^T \in \mathbb{R}^3$  Vessel acceleration in the  $\underline{b}$  frame  $(\frac{m}{s^2}, \frac{m}{s^2}, \frac{deg}{s^2})$   
 $\boldsymbol{\nu}_R = [u_R, v_R, r]^T \in \mathbb{R}^3$  Relative speed between the ship and the current  $(\frac{m}{s}, \frac{m}{s}, \frac{deg}{s})$   
 $\boldsymbol{\nu}_{TR} \in \mathbb{R}^3$  Relative desire velocity time history  $(\frac{m}{s}, \frac{m}{s}, \frac{deg}{s})$   
 $\boldsymbol{\Omega}_{P_i} \in \mathbb{R}^2$   $i$ - Propeller position  $(m, m)$   
 $\omega \in \mathbb{R}$  Engine speed  $(\frac{rad}{s})$   
 $\boldsymbol{\Omega}_{AZ_i} \in \mathbb{R}^2$   $i$ - Azimuthal thruster position  $(m, m)$   
 $\omega_d \in \mathbb{R}$  Desired motor speed  $(\frac{rad}{s})$   
 $\boldsymbol{\Omega}_I \in \mathbb{R}^2$  Origin of  $\underline{h}_i$ -frame, vessel point  $(m, m)$   
 $\boldsymbol{\Omega}_{R+1} \in \mathbb{R}^2$  Proposed reference point in LOS guidance  $(dm, m)$   
 $\boldsymbol{\Omega}_R \in \mathbb{R}^2$  Origin of  $\underline{e}_i$ -frame, reference point  $(m, m)$   
 $\boldsymbol{\Omega}_T \in \mathbb{R}^2$  Origin of  $\underline{f}_i$ -frame, target point  $(m, m)$   
 $\boldsymbol{\Omega}_{WP_1} \in \mathbb{R}^2$  Position of the first waypoint  $(m, m)$   
 $\boldsymbol{\Omega}_{WP_2} \in \mathbb{R}^2$  Position of the second waypoint  $(m, m)$   
 $\phi \in \mathbb{R}$  Desired angle setpoint at each time step  $(deg)$   
 $\psi \in \mathbb{R}$  Interceptor heading angle  $(deg)$

- $\psi_d \in \mathbb{R}$  Desired heading (*deg*)  
 $\psi_{los} \in \mathbb{R}$  Angle between  $\underline{e}_1$  and the radius  $kL_{PP}$  (*deg*)  
 $\rho \in \mathbb{R}$  Water density ( $\frac{kg}{m^3}$ )  
 $\rho_{air} \in \mathbb{R}$  Air density ( $\frac{kg}{m^3}$ )  
 $\tau_1 \in \mathbb{R}$  Time constant of the first order reference model (*s*)  
 $\boldsymbol{\tau} = [X, Y, N]^T \in \mathbb{R}^3$  General forces and moment array ( $N, N, Nm$ )  
 $\boldsymbol{\tau}_{AZ} \in \mathbb{R}^3$  Azimuth thruster forces and moment array ( $N, N, Nm$ )  
 $\tau_{\alpha}^{AZ} \in \mathbb{R}$  Azimuth angle time constant (*s*)  
 $\tau_n^{AZ} \in \mathbb{R}$  Shaft line time constant (*s*)  
 $\boldsymbol{\tau}_{BT} \in \mathbb{R}^3$  Bow Thruster forces and moment array ( $N, N, Nm$ )  
 $\boldsymbol{\tau}_C \in \mathbb{R}^3$  Control action ( $N, N, Nm$ )  
 $\boldsymbol{\tau}_{ENV} \in \mathbb{R}^3$  Environmental forces and moment array ( $N, N, Nm$ )  
 $\boldsymbol{\tau}_{FB} \in \mathbb{R}^3$  Feedback control action ( $N, N, Nm$ )  
 $\boldsymbol{\tau}_{FF} \in \mathbb{R}^3$  Feedforward control action ( $N, N, Nm$ )  
 $\boldsymbol{\tau}_H \in \mathbb{R}^3$  Hull forces and moment array ( $N, N, Nm$ )  
 $\boldsymbol{\tau}_{HC} \in \mathbb{R}^3$  Cross Flow Drag forces and moment array ( $N, N, Nm$ )  
 $\boldsymbol{\tau}_{HL} \in \mathbb{R}^3$  Lift forces and moment array ( $N, N, Nm$ )  
 $\boldsymbol{\tau}_I \in \mathbb{R}^3$  Ideal Fluid forces and moment array ( $N, N, Nm$ )  
 $\boldsymbol{\tau}_P \in \mathbb{R}^3$  Actuator forces and moment array ( $N, N, Nm$ )  
 $\bar{\boldsymbol{\tau}}_{PD} \in \mathbb{R}^3$  Average of the forces and moment required by the PD controller in a previous fixed time interval ( $N, N, Nm$ )  
 $\boldsymbol{\tau}_{RB} \in \mathbb{R}^3$  Longitudinal and lateral forces and the moment acting on the vessel ( $N, N, Nm$ )  
 $\dot{\tau}^* \in \mathbb{R}$  Adimensional thrust derivative coefficient IADC ( $-$ )  
 $\boldsymbol{\tau}_{WIND} \in \mathbb{R}^3$  Forces and moment array ( $N, N, Nm$ )  
 $\theta \in \mathbb{R}$  Angle between  $\underline{n}_1$  and  $\underline{h}_1$  (*deg*)  
 $v \in \mathbb{R}$  Decay rate (*Hz*)  
 $\xi \in \mathbb{R}$  Angle between  $\underline{n}_1$  and  $\underline{d}_1$  (*deg*)  
 $\xi_{CB} \in \mathbb{R}$  CB speed law parameter (*m*)  
 $\xi_{old} \in \mathbb{R}$  Angle defined by the previous couple of waypoints (*deg*)  
 $\xi_{PP} \in \mathbb{R}$  PP speed law parameter (*m*)
-

$\zeta_{az} \in \mathbb{R}$  Azimuthal thrust coefficient ( $\frac{N}{s}$ )

$\zeta_{e_{jk}} \in \mathbb{R}$  Engine number turning on in each scatter diagram cell (-)

$\zeta_{jk} \in \mathbb{R}$  Function that states if the equilibrium in the cell  $jk$  is satisfied (-)

$\zeta_{RT} \in \mathbb{R}$  Hull resistance coefficient ( $\frac{kg}{s}$ )

# List of Acronyms

- ADS:** Automated Driving System
- ASV:** Autonomous Surface Vehicles
- CB:** Constant Bearing
- DDT:** Dynamic Driving Task
- DPCP:** Dynamic Positioning Capability Plot
- DOF:** Degree Of Freedom
- DP:** Dynamic Positioning
- EMSA:** European Maritime Safety Agency
- FAL:** Force Allocation Matrix
- GNC:** Guidance, Navigation, and Control
- GMTT30:** Global Marine Technology Trends 2030
- GNSS:** Global navigation satellite system
- GPS:** Global Positioning System
- HIL:** Human In the Loop
- HSD:** High-speed diesel engine
- IMO:** International Maritime Organization
- IMU:** Inertial Measurement Unit
- KPIs:** Key Performance Indicators
- LBSI:** Lean Burn Spark-Ignited
- LNG:** Liquefied Natural Gas
- LOA:** Levels Of Automation
- LOS:** Line-Of-Sight
- MASS:** Marine Autonomous Surface Ships
- MDO:** Marine Diesel Oil

**MSC:** Marine Safety Control

**ODD:** Operational Design Domain

**OEDR:** Object and Event Detection and Response

**PID:** Proportional Integrative Derivative

**PP:** Pure Pursuit

**PSV:** Platform Supply Vessel

**RM:** Reference Model

**RT-HIL:** Real time Hardware In the Loop

**SWAMP:** Shallow Water Autonomous Multipurpose Platform

**TAL:** Thrust Allocation Logic

**TK:** Track Keeping

**TT:** Target Tracking



# Bibliography

- [1] Aegis. <https://aegis.autonomous-ship.org/>.
- [2] Autoship. <https://www.autoship-project.eu/the-project/>.
- [3] BMT. global wave statistics. <http://www.globalwavestatisticsonline.com>. Accessed: 2022-09-20.
- [4] Moses. <https://moses-h2020.eu/>.
- [5] Definitions for autonomous merchant ships. Technical report, Norwegian Forum for Autonomous Ship, NFAS, 2017.
- [6] LR code for unmanned marine systems. Technical report, Lloyd's Register Group Limited, February 2017.
- [7] Taxonomy and definitions for terms related to driving automation systems for on-road motor vehicles. Technical report, SAE international, 2021.
- [8] Melih Akdağ, Petter Solnør, and Tor Arne Johansen. Collaborative collision avoidance for maritime autonomous surface ships: A review. *Ocean Engineering*, 250:110920, 2022.
- [9] A Alessandri, S Donnarumma, S Vignolo, M Figari, M Martelli, R Chiti, and L Sebastiani. System control design of autopilot and speed pilot for a patrol vessel by using LMIs. *Towards green marine technology and transport*, pages 577–584, 2015.
- [10] Angelo Alessandri, Silvia Donnarumma, Michele Martelli, and Stefano Vignolo. Motion control for autonomous navigation in blue and narrow waters using switched controllers. *Journal of Marine Science and Engineering*, 7(6):196, 2019.
- [11] Felipe Arditti, Felipe Lopes de Souza, Thiago de Castro Martins, and Eduardo Aoun Tannuri. Thrust allocation algorithm with efficiency function dependent on the azimuth angle of the actuators. *Ocean Engineering*, 105:206–216, 2015.
- [12] Felipe Arditti and Eduardo Aoun Tannuri. Experimental analysis of a thrust allocation algorithm for DP systems considering the interference between thrusters and thruster-hull. *IFAC Proceedings Volumes*, 45(27):43–48, 2012.
- [13] Xiangen Bai, Bohan Li, Xiaofeng Xu, and Yingjie Xiao. A review of current research and advances in unmanned surface vehicles. *Journal of Marine Science and Application*, 21(2):47–58, 2022.

- [14] Santiago Iglesias Baniela. The performance of a tunnel bow thruster with slow speed ahead: A revisited issue. *The Journal of Navigation*, 62(4):631–642, 2009.
- [15] Dimitri P Bertsekas. *Constrained optimization and Lagrange multiplier methods*. Academic press, 1996.
- [16] Marco Bibuli, Massimo Caccia, Lionel Lapierre, and Gabriele Bruzzone. Guidance of unmanned surface vehicles: Experiments in vehicle following. *IEEE Robotics & Automation Magazine*, 19(3):92–102, 2012.
- [17] Franco Blanchini, Fabrizio Dabbene, Gianfranco Fenu, Felice Andrea Pellegrino, and Erica Salvato. Model-free feedback control synthesis from expert demonstration. *IEEE Control Systems Letters*, 7:1604–1609, 2023.
- [18] Werner Blendermann. Parameter identification of wind loads on ships. *Journal of Wind Engineering and Industrial Aerodynamics*, 51(3):339–351, 1994.
- [19] Stephen Boyd, Laurent El Ghaoui, Eric Feron, and Venkataramanan Balakrishnan. *Linear matrix inequalities in system and control theory*. SIAM, 1994.
- [20] M. Breivik, V.E. Hovstein, and T.I. Fossen. Straight-line target tracking for unmanned surface vehicles. *Modeling, Identification and Control*, 29(4):131–149, 2008.
- [21] Morten Breivik. *Topics in guided motion control of marine vehicles*. PhD thesis, NTNU, 2010.
- [22] Morten Breivik and Thor I Fossen. Applying missile guidance concepts to motion control of marine craft. *IFAC Proceedings Volumes*, 40(17):349–354, 2007.
- [23] Edmund F Brekke, Egil Eide, Bjørn-Olav H Eriksen, Erik F Wilthil, Morten Breivik, Even Skjellaug, Øystein K Helgesen, Anastasios M Lekkas, Andreas B Martinsen, Emil H Thyri, et al. milliAmpere: An autonomous ferry prototype. In *Journal of Physics: Conference Series*, volume 2311, pages 12–29. IOP Publishing, 2022.
- [24] Sable Campbell, Wasif Naeem, and George W Irwin. A review on improving the autonomy of unmanned surface vehicles through intelligent collision avoidance manoeuvres. *Annual Reviews in Control*, 36(2):267–283, 2012.
- [25] John Carlton. *Marine propellers and propulsion*. Butterworth-Heinemann, 2018.
- [26] Matteo Cocetti, Silvia Donnarumma, Luca De Pascali, Matteo Ragni, Francesco Biral, Fabrizio Panizzolo, Pier Paolo Rinaldi, Alex Sassaro, and Luca Zaccarian. Hybrid nonovershooting set-point pressure regulation for a wet clutch. *IEEE/ASME Transactions on Mechatronics*, 25(3):1276–1287, 2020.
- [27] J. Curcio, J. Leonard, and A. Patrikalakis. SCOUT - a low cost autonomous surface platform for research in cooperative autonomy. In *Proceedings of OCEANS 2005 MTS/IEEE*, pages 725–729 Vol. 1, 2005.

- 
- [28] Jie Dang and Hans Laheij. Hydrodynamic aspects of steerable thrusters. Dynamic Positioning Conference, pages 1–33, 2004.
- [29] Alan Garnett Davenport. The application of statistical concepts to the wind loading of structures. *Proceedings of the Institution of Civil Engineers*, 19(4):449–472, 1961.
- [30] Christiaan De Wit. Optimal thrust allocation methods for dynamic positioning of ships. Master’s thesis, TU Delft, 2009.
- [31] DNV. Autonomous and remotely-operated ships. Technical report, 2018.
- [32] GL DNV. Assessment of station keeping capability of dynamic positioning vessels. Technical report, DNV GL AS, 2018.
- [33] DNV-GL. The ReVolt. a new inspirational ship concept. <https://www.dnv.com/maritime/autonomous-remotely-operated-ships/research-activities.html>.
- [34] Khac Duc Do and Jie Pan. *Control of ships and underwater vehicles: design for underactuated and nonlinear marine systems*. Springer Science & Business Media, 2009.
- [35] Silvia Donnarumma. *Low and High Speed Motion Control of a Vessel with Actuator Saturation*. PhD thesis, Università degli studi di Genova, 2016.
- [36] Silvia Donnarumma, Massimo Figari, Michele Martelli, Stefano Vignolo, and Michele Viviani. Design and validation of dynamic positioning for marine systems: A case study. *IEEE Journal of Oceanic Engineering*, 43(3):677–688, 2018.
- [37] C Draper. Control, navigation, and guidance. *IEEE Control Systems Magazine*, 1(4):4–17, 1981.
- [38] EMSA. Annual overview of marine casualties and incidents report. Technical report, 2023.
- [39] ENISA. Transport threat landscape. Technical report, 2023.
- [40] Bjørn-Olav Holtung Eriksen and Morten Breivik. Modeling, identification and control of high-speed ASVs: Theory and experiments. In *Sensing and control for autonomous vehicles: Applications to land, water and air vehicles*, pages 407–431. Springer, 2017.
- [41] Nicolò Faggioni. *Enabling technologies and decision support systems towards autonomous navigation of ships*. PhD thesis, Università degli studi di Genova, 2022.
- [42] Odd M Faltinsen. *Hydrodynamics of high-speed marine vehicles*. Cambridge university press, 2005.
- [43] F. C. Fickeisen and T. M. Stout. Analogue methods for optimum servomechanism design. *Transactions of the American Institute of Electrical Engineers, Part II: Applications and Industry*, 71(5):244–250, 1952.
-

- [44] Thor I Fossen. A survey on nonlinear ship control: From theory to practice. *IFAC Proceedings Volumes*, 33(21):1–16, 2000.
- [45] Thor I Fossen. *Handbook of marine craft hydrodynamics and motion control*. John Wiley & Sons, 2011.
- [46] Thor I Fossen, Morten Breivik, and Roger Skjetne. Line-of-sight path following of underactuated marine craft. *IFAC proceedings volumes*, 36(21):211–216, 2003.
- [47] The Nippon Foundation. The nippon foundation MEGURI2040 fully autonomous ship program. 2022.
- [48] Camilla Fruzzetti, Silvia Donnarumma, and Michele Martelli. Dynamic target chasing: parameters and performance indicators assessment. *Journal of Marine Science and Technology (Japan)*, 27(1):712 – 729, 2022.
- [49] Jawhar Ghommam and Maarouf Saad. Adaptive leader–follower formation control of underactuated surface vessels under asymmetric range and bearing constraints. *IEEE Transactions on Vehicular Technology*, 67(2):852–865, 2017.
- [50] Nan Gu, Dan Wang, Zhouhua Peng, Jun Wang, and Qing-Long Han. Advances in line-of-sight guidance for path following of autonomous marine vehicles: An overview. *IEEE Transactions on Systems, Man, and Cybernetics: Systems*, 53(1):12–28, 2022.
- [51] Xinghai Guo, Mingjun Ji, Ziwei Zhao, Dusu Wen, and Weidan Zhang. Global path planning and multi-objective path control for unmanned surface vehicle based on modified particle swarm optimization (PSO) algorithm. *Ocean Engineering*, 216:107693, 2020.
- [52] Sumaya Hamad, Yossra H. Ali, and Shaimaa H. Shaker. A survey of positioning systems for ships based on new categories. In *2020 13th International Conference on Developments in eSystems Engineering (DeSE)*, pages 189–194, 2020.
- [53] Ali Haseltala, Vittorio Garofano, Muhammad Raheel Afzal, Nicolás Faggioni, Shijie Li, Jialun Liu, Feng Ma, Michele Martelli, Yogang Singh, Peter Slaets, Xu You, and Rudy R Negenborn. The collaborative autonomous shipping experiment (CASE): Motivations, theory, infrastructure, and experimental challenges. In *International Ship Control Systems Symposium (iSCSS 2020)*. IMaReST, 2020.
- [54] Liang Hu, Huosheng Hu, Wasif Naeem, and Zidong Wang. A review on COLREGs-compliant navigation of autonomous surface vehicles: From traditional to learning-based approaches. *Journal of Automation and Intelligence*, 1(1):100003, 2022.
- [55] Yamin Huang, Linying Chen, Pengfei Chen, Rudy R Negenborn, and PHAJM Van Gelder. Ship collision avoidance methods: State-of-the-art. *Safety science*, 121:451–473, 2020.

- [56] Thomas Parke Hughes. *Elmer Sperry: inventor and engineer*. Johns Hopkins University Press, 1971.
- [57] IMO. Fourth greenhouse gas study 2020. <https://www.imo.org/en/ourwork/Environment/Pages/Fourth-IMO-Greenhouse-Gas-Study-2020.aspx>. Accessed: 2023-11-13.
- [58] IMO. Maritime safety committee (MSC), 99th session. <https://www.imo.org/en/MediaCentre/MeetingSummaries/Pages/MSC-99th-session.aspx>, 16–25 May 2018. Accessed: 2021-06-28.
- [59] IMO. COLREGs, -convention on the international regulations for preventing collisions at sea, 1972.
- [60] IMO. Maritime safety committee (MSC), 100th session. <https://www.imo.org/en/MediaCentre/MeetingSummaries/Pages/MSC-100th-session.aspx>, 3–7 December 2018. Accessed: 2021-06-28.
- [61] IMO. Maritime safety committee (MSC), 98th session. <https://www.imo.org/en/MediaCentre/MeetingSummaries/Pages/MSC-98th-session.aspx>, 7-16 June 2017. Accessed: 2021-06-28.
- [62] Economist impact. Global marine technology trends 2050. Technical report, 2023.
- [63] INAS. Autonomous ships test areas. <https://autonomous-ship.org/testarea.html>.
- [64] Tao Jiang, Rupert Henn, and Som Deo Sharma. Dynamic behavior of a tow system under an autopilot on the tug. In *International Symposium and Workshop on Forces Acting on a Manoeuvring Vessel (MAN'98)*, Val de Reuil, 1998.
- [65] Tor A. Johansen and Thor I. Fossen. Control allocation—a survey. *Automatica*, 49(5):1087–1103, 2013.
- [66] Gert Kuiper. *The Wageningen propeller series*. 1992.
- [67] Ismail Kurt and Murat Aymelek. Operational and economic advantages of autonomous ships and their perceived impacts on port operations. *Maritime Economics & Logistics*, 24(2):302–326, 2022.
- [68] Anastasios M Lekkas and Thor I Fossen. Integral LOS path following for curved paths based on a monotone cubic hermite spline parametrization. *IEEE Transactions on Control Systems Technology*, 22(6):2287–2301, 2014.
- [69] Zhihong Li, Di Zhang, Bing Han, and Chengpeng Wan. Risk and reliability analysis for maritime autonomous surface ship: A bibliometric review of literature from 2015 to 2022. *Accident Analysis & Prevention*, 187:107090, 2023.
- [70] Chenguang Liu, Xiumin Chu, Wenxiang Wu, Songlong Li, Zhibo He, Mao Zheng, Haiming Zhou, and Zhixiong Li. Human-machine cooperation research for navigation of maritime autonomous surface ships: A review and consideration. *Ocean Engineering*, 246:110555, 2022.
-

- [71] Zhixiang Liu, Youmin Zhang, Xiang Yu, and Chi Yuan. Unmanned surface vehicles: An overview of developments and challenges. *Annual Reviews in Control*, 41:71–93, 2016.
- [72] J. Lofberg. YALMIP: a toolbox for modeling and optimization in MATLAB. In *2004 IEEE International Conference on Robotics and Automation (IEEE Cat. No.04CH37508)*, pages 284–289, 2004.
- [73] A.M. Lyapunov. Probleme général de la stabilité du mouvement, vol. 17 of. *Annals of Mathematics Studies*, 1949.
- [74] IMCA M140. Specification for DP capability plots. <https://www.imca-int.com/product/specification-for-dp-capability-plots>. Accessed: 2023-11-13.
- [75] Kongsberg Maritime. Autonomous ship project, key facts about YARA birkeland. URL <https://www.km.kongsberg.com/ks/web/nokbg0240.nsf/AllWeb/4B8113B707A50A4FC125811D00407045>, 2017.
- [76] M. Martelli, N. Faggioni, and S. Donnarumma. A time-domain methodology to assess the dynamic positioning performances. *Ocean Engineering*, 247:110668, 2022.
- [77] Michele Martelli. *Marine propulsion simulation: methods and results*. Walter de Gruyter GmbH & Co KG, 2015.
- [78] Michele Martelli, Nicolò Faggioni, and Giovanni Berselli. Fuel saving in a marine propulsion plant by using a continuously variable transmission. *Proceedings of the Institution of Mechanical Engineers, Part M: Journal of Engineering for the Maritime Environment*, 233(4):1007–1021, 2019.
- [79] Michele Martelli, Diego Villa, Michele Viviani, Silvia Donnarumma, and Massimo Figari. The use of computational fluid dynamic technique in ship control design. *Ships and Offshore Structures*, 16(1):31–45, 2021.
- [80] Andreas B. Martinsen, Anastasios M. Lekkas, and Sébastien Gros. Reinforcement learning-based NMPC for tracking control of ASVs: Theory and experiments. *Control Engineering Practice*, 120:105024, 2022.
- [81] Izumi Masubuchi, Atsumi Ohara, and Nobuhide Suda. LMI-based controller synthesis: A unified formulation and solution. *International Journal of Robust and Nonlinear Control*, 8(8):669–686, 1998.
- [82] Francesco Mauro and Jasna Prpić-Oršić. Determination of a DP operability index for an offshore vessel in early design stage. *Ocean Engineering*, 195:106764, 2020.
- [83] Mojtaba Mehrzadi, Yacine Terriche, Chun-Lien Su, Muzaidi Bin Othman, Juan C. Vasquez, and Josep M. Guerrero. Review of dynamic positioning control in maritime microgrid systems. *Energies*, 13(12), 2020.
- [84] Anna Miller, Monika Rybczak, and Andrzej Rak. Towards the autonomy: Control systems for the ship in confined and open waters. *Sensors*, 21(7):2286, 2021.

- [85] Nicolas Minorsky. Directional stability of automatically steered bodies. *Journal of the American Society for Naval Engineers*, 34(2):280–309, 1922.
- [86] Apollonia Miola and Biagio Ciuffo. Estimating air emissions from ships: Meta-analysis of modelling approaches and available data sources. *Atmospheric Environment*, 45(13):2242–2251, 2011.
- [87] United Nations. Sustainable development goals. Technical report, 2023.
- [88] R.A.O. Nunes, M.C.M. Alvim-Ferraz, F.G. Martins, and S.I.V. Sousa. The activity-based methodology to assess ship emissions - a review. *Environmental Pollution*, 231:87–103, 2017.
- [89] Ilija Obradovic. Die abweichungsfläche bei schnellregelvorgängen beitrage zur theorie der schnellregelung. *Archiv für Elektrotechnik*, 36:382–390, 1942.
- [90] Oceana. Oceana - get closer to ocean. <https://www.oceanalpha.com/>.
- [91] Angelo Odetti, Gabriele Bruzzone, Marco Altosole, Michele Viviani, and Massimo Caccia. SWAMP, an autonomous surface vehicle expressly designed for extremely shallow waters. *Ocean Engineering*, 216:108205, 2020.
- [92] Peter Oltmann and Som Deo Sharma. Simulation of combined engine and rudder maneuvers using an improved model of hull-propeller-rudder interactions. Technical report, 1984.
- [93] Ülkü Öztürk, Melih Akdağ, and Tarık Ayabakan. A review of path planning algorithms in maritime autonomous surface ships: Navigation safety perspective. *Ocean Engineering*, 251:111010, 2022.
- [94] Raja Parasuraman, Thomas B Sheridan, and Christopher D Wickens. A model for types and levels of human interaction with automation. *IEEE Transactions on systems, man, and cybernetics-Part A: Systems and Humans*, 30(3):286–297, 2000.
- [95] Ruth G. Patterson, Emily Lawson, Vinay Udyawer, Gary B. Brassington, Rachel A. Groom, and Hamish A. Campbell. Uncrewed surface vessel technological diffusion depends on cross-sectoral investment in open-ocean archetypes: A systematic review of USV applications and drivers. *Frontiers in Marine Science*, 8, 2022.
- [96] Anders Aglen Pedersen. Optimization based system identification for the milliamper ferry. Master’s thesis, Norwegian University of Science and Technology (NTNU), Trondheim, Norway, 2019.
- [97] Benedetto Piaggio, Vittorio Garofano, Silvia Donnarumma, Angelo Alessandri, Rudy Negenborn, and Michele Martelli. Follow-the-leader guidance, navigation, and control of surface vessels: Design and experiments. *IEEE Journal of Oceanic Engineering*, pages 1–12, 2023.
- [98] Willard J Pierson Jr. The interpretation of wave spectrums in terms of the wind profile instead of the wind measured at a constant height. *Journal of geophysical research*, 69(24):5191–5203, 1964.
-

- [99] Mehdi Poornikoo and Kjell Ivar Øvergård. Levels of automation in maritime autonomous surface ships (MASS): A fuzzy logic approach. *Maritime Economics & Logistics*, 24(2):278–301, 2022.
- [100] Donald E Ridley. Observations on the effect of vessel speed on bow thruster performance. *Marine Technology and SNAME News*, 8(01):93–96, 1971.
- [101] Ørnulf Jan Rødseth and Hans-Christoph Burmeister. Developments toward the unmanned ship. In *Proceedings of International Symposium Information on Ships-ISIS*, volume 201, pages 30–31, 2012.
- [102] M Rolls-Royce. Remote and autonomous ships-the next steps. *Manchester, UK, Tech. Rep*, 2016.
- [103] Rolls Royce. Rolls-royce and Finferries demonstrate world’s first fully autonomous ferry. *Retrieved May, 21:2020*, 2018.
- [104] Monika Rybczak and Witold Gierusz. Maritime autonomous surface ships in use with LMI and overriding trajectory controller. *Applied Sciences*, 12(19), 2022.
- [105] Matteo Schiaretti, Linying Chen, and Rudy R Negenborn. Survey on autonomous surface vessels: Part I - a new detailed definition of autonomy levels. In *International Conference on Computational Logistics*, pages 219–233. Springer, 2017.
- [106] Matteo Schiaretti, Linying Chen, and Rudy R Negenborn. Survey on autonomous surface vessels: Part II - categorization of 60 prototypes and future applications. In *International Conference on Computational Logistics*, pages 234–252. Springer, 2017.
- [107] Agnes Schubert, Martin Kurowski, Michael Gluch, Olaf Simanski, and Torsten Jeinsch. Manoeuvring automation towards autonomous shipping. In *Proceedings of the 14th International Naval Engineering Conference INEC*, pages 1–8, October 2018.
- [108] RA Sheno, JA Bowker, Agnieszka S Dzielendziak, Artur Konrad Lidtke, G Zhu, F Cheng, D Argyos, I Fang, J Gonzalez, S Johnson, et al. Global marine technology trends 2030. Technical report, 2015.
- [109] Thomas B Sheridan and William L Verplank. Human and computer control of undersea teleoperators. Technical report, Massachusetts Inst of Tech Cambridge Man-Machine Systems Lab, 1978.
- [110] Neryahu A Shneydor. *Missile guidance and pursuit: kinematics, dynamics and control*. Elsevier, 1998.
- [111] Yogang Singh, Sanjay Sharma, Daniel Hatton, and Robert Sutton. Optimal path planning of unmanned surface vehicles. *Indian Journal of Geo-Marine Sciences*, 47(7):1325–1334, 2018.
- [112] Roger Skjetne, Mikkel E. N. Sørensen, Morten Breivik, Svern A. T. Værnø, Astrid H. Brodtkorb, Asgeir J. Sørensen, Øivind K. Kjerstad, Vincenzo Calabrò, and Bjørn Ole Vinje. AMOS DP research cruise 2016: Academic full-scale testing of experimental dynamic positioning control algorithms onboard



- r/v gunnerus. volume 1: Offshore Technology of *Offshore Mechanics and Arctic Engineering*, 06 2017.
- [113] O Smogeli, Nguyen Dong Trong, B Borhaug, and Luca Pivano. The next level DP capability analysis. In *Proceedings of Dynamic Positioning Conference*, 2013.
- [114] SNAME. Nomenclature for treating the motion of a submerged body through a fluid. *The Society of Naval Architects and Marine Engineers, Technical and Research Bulletin*, pages 1–5, 1950.
- [115] Rui Song, Yuanchang Liu, and Richard Bucknall. Smoothed A\* algorithm for practical unmanned surface vehicle path planning. *Applied Ocean Research*, 83:9–20, 2019.
- [116] Asgeir J Sørensen. A survey of dynamic positioning control systems. *Annual reviews in control*, 35(1):123–136, 2011.
- [117] Mikkel Eske Nørgaard Sørensen. *Topics in Nonlinear and Model-based Control of Ships*. PhD thesis, Norwegian University of Science and Technology (NTNU), Trondheim, Norway, 2021.
- [118] Mikkel Eske Nørgaard Sørensen and Morten Breivik. Comparing nonlinear adaptive motion controllers for marine surface vessels. *IFAC-PapersOnLine*, 48(16):291–298, 2015.
- [119] Jos F Sturm. Using SeDuMi 1.02, a MATLAB toolbox for optimization over symmetric cones. *Optimization methods and software*, 11(1-4):625–653, 1999.
- [120] CheeKuang Tam, Richard Bucknall, and Alistair Greig. Review of collision avoidance and path planning methods for ships in close range encounters. *The Journal of Navigation*, 62(3):455, 2009.
- [121] Nikola Tesla. Method of and apparatus for controlling mechanism of moving vessels or vehicles - US613809A. United States, 1898.
- [122] Emil H. Thyri, Glenn Bitar, and Morten Breivik. A 3 DOF path-following controller for a non-directionally stable vessel with slow thruster dynamics. *IFAC-PapersOnLine*, 54(16):288–294. 13th IFAC Conference on Control Applications in Marine Systems, Robotics, and Vehicles CAMS 2021.
- [123] Anete Vagale, Robin T Bye, Rachid Oucheikh, Ottar L Osen, and Thor I Fossen. Path planning and collision avoidance for autonomous surface vehicles II: a comparative study of algorithms. *Journal of Marine Science and Technology*, 26(4):1307–1323, 2021.
- [124] Anete Vagale, Rachid Oucheikh, Robin T Bye, Ottar L Osen, and Thor I Fossen. Path planning and collision avoidance for autonomous surface vehicles I: a review. *Journal of Marine Science and Technology*, pages 1–15, 2021.
- [125] Marialena Vagia, Aksel A Transeth, and Sigurd A Fjerdingen. A literature review on the levels of automation during the years. what are the different taxonomies that have been proposed? *Applied Ergonomics*, 53:190–202, 2016.
-

- [126] Thomas W Vaneck, Claudia D Rodriguez-Ortiz, Mads C Schmidt, and Justin E Manley. Automated bathymetry using an autonomous surface craft. *Navigation*, 43(4):407–419, 1996.
- [127] Jasmin Velagic, Zoran Vukic, and Edin Omerdic. Adaptive fuzzy ship autopilot for track-keeping. *Control Engineering Practice*, 11(4):433–443, 2003. MCMC00.
- [128] Bureau Veritas. Guidelines for autonomous shipping. Technical report, 2019.
- [129] Arthur Vrijdag and Michele Martelli. Parameter identification of a model scale ship drive train. *Journal of Marine Science and Engineering*, 9(3), 2021.
- [130] L Wang, Qing Wu, Jialun Liu, Shijie Li, and RR Negenborn. State-of-the-art research on motion control of maritime autonomous surface ships. *Journal of Marine Science and Engineering*, 7(12), 2019.
- [131] Wei Wang, David Fernández-Gutiérrez, Rens Doornbusch, Joshua Jordan, Tixiao Shan, Pietro Leoni, Niklas Hagemann, Jonathan Klein Schiphorst, Fabio Duarte, Carlo Ratti, and Daniela Rus. Roboat III: An autonomous surface vessel for urban transportation. *Journal of Field Robotics*, 40(8):1996–2009, 2023.
- [132] WMO. Manual on codes, volume I.1 – international codes - annex II to the WMO technical regulations - part A – alphanumeric codes. Technical report, 2019.
- [133] Haitong Xu and C Guedes Soares. Review of path-following control systems for maritime autonomous surface ships. *Journal of Marine Science and Application*, 22(2):153–171, 2023.
- [134] Qinping Yang. *Minimum decay rate of a family of dynamical systems*. Stanford University, 1992.
- [135] H Yasukawa and Y Yoshimura. Introduction of MMG standard method for ship maneuvering prediction. *Journal of Marine Science and Technology*, 20, 2015.
- [136] Raphael Zaccone. COLREG-compliant optimal path planning for real-time guidance and control of autonomous ships. *Journal of Marine Science and Engineering*, 9(4), 2021.
- [137] Raphael Zaccone, Massimo Figari, and Michele Martelli. An optimization tool for ship route planning in real weather scenarios. In *The 28th International Ocean and Polar Engineering Conference*, volume 2018-June, pages 738–744. International Society of Offshore and Polar Engineers, 2018.
- [138] Zeabuz. Launching the world’s first commercial, emission-free, autonomous passenger ferry in the heart of the city. ”<https://www.zeabuz.com/torghatten-and-zeabuz-make-history-in-stockholm/>”, 2023.
- [139] Ming Zhang, Hongxiang Ren, and Yi Zhou. Research on global ship path planning method based on improved ant colony algorithm. *IEEE Open Journal of Intelligent Transportation Systems*, 4:143–152, 2023.

- [140] Shaoze Zhang, Shaolong Yang, and Xianbo Xiang. Formation control of autonomous surface vehicle and experimental validation. *IFAC-PapersOnLine*, 52(24):278–282, 2019.
  - [141] Weicheng Zhang, Yanmin Xu, and Jinpeng Xie. Path planning of USV based on improved hybrid genetic algorithm. In *2019 European Navigation Conference (ENC)*, pages 1–7, 2019.
  - [142] Luman Zhao, Myung-Il Roh, et al. A thrust allocation method for efficient dynamic positioning of a semisubmersible drilling rig based on the hybrid optimization algorithm. *Mathematical Problems in Engineering*, 2015, 2015.
  - [143] Jing Zhou and Changyun Wen. *Adaptive Backstepping Control*, pages 9–31. Springer Berlin Heidelberg, Berlin, Heidelberg, 2008.
-